

*Mass Spectrometry Imaging for Food
Analysis – Method Development for
MALDI MS Imaging of Fresh and
Processed Food*

DISSERTATION

zur Erlangung des akademischen Grades eines
Doktors der Naturwissenschaften (Dr. rer. nat.)
in der Bayreuther Graduiertenschule für Mathematik und
Naturwissenschaften (BayNAT)
der Universität Bayreuth

vorgelegt von

Oliver Günther Wittek

aus *Nürnberg*

Bayreuth, 2024

Die vorliegende Arbeit wurde in der Zeit von Mai 2018 bis April 2024 (experimenteller Teil bis April 2022) in Bayreuth am Lehrstuhl für Bioanalytik und Lebensmittelanalytik unter Betreuung von Herrn Professor Dr. Andreas Römpp angefertigt.

Vollständiger Abdruck der von der Bayreuther Graduiertenschule für Mathematik und Naturwissenschaften (BayNAT) der Universität Bayreuth genehmigten Dissertation zur Erlangung des akademischen Grades eines Doktors der Naturwissenschaften (Dr. rer. nat.).

Form der Dissertation: Kumulative Dissertation

Dissertation eingereicht am: 22. April 2024

Zulassung durch das Leitungsgremium: 15. Mai 2024

Wissenschaftliches Kolloquium: 11. Oktober 2024

Amtierender Direktor: Prof. Dr. Jürgen Köhler

Prüfungsausschuss:

Prof. Dr. Andreas Römpp (Gutachter)

Prof. Dr. Susanne Baldermann (Gutachterin)

Prof. Dr. Stephan Clemens (Vorsitz)

Prof. Dr. Stephan Schwarzinger

Zusammenfassung

Bildgebende Massenspektrometrie mit matrixunterstützter Laserdesorption/Ionisation (MALDI MS imaging) ist eine analytische Technik von wachsender Bedeutung für verschiedene wissenschaftliche Gebiete. Die Anwendungsfelder in den Lebensmittelwissenschaften sind vielfältig und reichen von der Agrarforschung bis hin zu gesundheitsrelevanten Fragen der Lebensmittelsicherheit, für die MS imaging eingesetzt werden kann, um räumliche Verteilungen sowohl erwünschter als auch unerwünschter Verbindungen darzustellen. Die meisten bisherigen Veröffentlichungen konzentrierten sich auf die Visualisierung von Inhaltsstoffen in unverarbeiteten Lebensmitteln. Prozessierte Lebensmittel sind erst seit kurzem Gegenstand von MS imaging-Studien; Anwendungen zur Untersuchung exogener Bestandteile, wie Zusatzstoffe oder Kontaminanten, sind selten. Darüber hinaus gibt es aufgrund der bis dato begrenzten analytischen Möglichkeiten kaum Rechtsnormen, in denen Anforderungen an die räumliche Verteilung von Bestandteilen in Lebensmitteln aufgenommen sind.

Um zur Überwindung dieser Einschränkungen beizutragen, war das Ziel dieser Dissertation, die Leistungsfähigkeit von MALDI MS imaging für die Lebensmittelanalytik aufzuzeigen und das Potenzial zur Anwendung in den Lebensmittelwissenschaften, aber auch durch Lebensmittelunternehmer und Untersuchungsbehörden, hervorzuheben. Auf analytischer Ebene sollten hierzu Workflows zur Probenvorbereitung sowie Mess- und Datenanalysemethoden für verschiedene Lebensmittel und Analyten entwickelt werden. Hohe Massenauflösung und Massengenauigkeit waren bei allen Untersuchungen entscheidend, um hohe Messelektivität zu gewährleisten. Bei der Datenanalyse wurde nicht nur die bloße Darstellung räumlicher Analytverteilungen, sondern auch die Entwicklung tiefergehender Analyseansätze aus MS imaging-Daten angestrebt, insbesondere für gesetzlich regulierte Substanzen. Ein weiteres wichtiges Ziel war die Entwicklung einer dedizierten MS imaging-Methode für pflanzliches Gewebe zur räumlich aufgelösten ‚bottom-up‘ Identifizierung von Proteinen basierend auf akkurater Massendetektion.

Zunächst wurde eine Reihe repräsentativer Methoden für hochauflösendes MALDI MS imaging von Lebensmitteln entwickelt, um dessen breite Anwendbarkeit zu demonstrieren. Hardy Kiwi, Karotten, Weißwurst, Gouda-Käse und Lebkuchen repräsentierten sowohl unverarbeitete als auch prozessierte Lebensmittel pflanzlichen wie tierischen Ursprungs. Die untersuchten Substanzen umfassten hochgradig unpolare und polare endogene Bestandteile ebenso wie Zutaten, Kontaminanten und Lebensmittelzusatzstoffe. Mit dem kanzerogenen Acrylamid in Lebkuchen und dem Konservierungsstoff Natamycin in Gouda-Käse ist es erstmals gelungen, molekulare Verteilungen einer Kontaminante und eines Lebensmittelzusatzstoffs in prozessierten Lebensmitteln darzustellen. Zur Untersuchung des Diffusionsverhaltens von Natamycin in Gouda-Käse wurde ein neues Programm zur Datenverarbeitung entwickelt. Die Ergebnisse dieser Studie verdeutlichen das große Potenzial von MALDI MS imaging für die räumlich aufgelöste Analyse verschiedenster Lebensmittel.

Aufbauend auf den Grundlagen der ersten Veröffentlichung wurden die Protokolle zur Probenvorbereitung und -messung von Lebkuchen optimiert. Durch seine inhomogene und spröde Konsistenz stellt Lebkuchen eine herausfordernde Probe dar, die erhebliche Anpassungen im Workflow erforderte. Aufgrund der unebenen Oberfläche von Lebkuchenquerschnitten wurde Autofokussierung als neuer Bestandteil des Ionisierungsprozesses aufgenommen, um einen konstanten MALDI-Laserfokus zu gewährleisten. Sowohl abundante Nährstoffe als auch die gering konzentrierte Prozesskontaminante Acrylamid konnten identifiziert und ihre Verteilungen sichtbar gemacht werden. Ein Protokoll zum statistischen Vergleich der relativen Acrylamid-Intensitäten unterstützte die Beobachtung von erhöhter Acrylamid-Kontamination in Nussfragmenten. Weiterhin wurde zur Verbesserung der Nachweisselektivität von Acrylamid eine neue Methode zur *in situ*-Derivatisierung entwickelt. Für die Bewertung von Acrylamid-Reduktionsstrategien, die kürzlich in europäische Verordnungen aufgenommen wurden, können Informationen über die räumliche Verteilung von Acrylamid für Lebensmittelunternehmer wie auch Überwachungsbehörden von großem Nutzen sein. Diese Studie zeigt, dass MALDI MS imaging solche ergänzenden Informationen auch in anspruchsvollen, prozessierten Lebensmitteln liefern kann.

Neben dem Probenmaterial können auch Zielanalyten eine Herausforderung für erfolgreiches MS imaging darstellen; ein prominentes Beispiel hierfür sind Proteine. Im Bereich der Proteomik ist der ‚bottom-up‘ Ansatz eine bedeutende, ungerichtete Strategie zur Identifizierung von Proteinen, die die Messung von Peptiden nach enzymatischem Verdau nutzt, um Informationen über das Proteom abzuleiten; jedoch wurde sie bislang kaum auf Pflanzengewebe angewandt. Dies wurde durch die systematische Entwicklung

eines Protokolls für die Probenvorbereitung, den *in situ* tryptischen Verdau und hochauflösendes MALDI MS imaging am Beispiel von Kichererbsen ergänzt. Die Messungen ergaben unterschiedliche Verteilungsmuster in den Samenkompartmenten, für die insgesamt sechzehn Proteine anhand der akkuraten Massen ihrer tryptischen Peptide identifiziert werden konnten. In einem Anwendungsbeispiel aus dem Gebiet der Lebensmittelsicherheit wurde das toxische Protein Abrin in Paternostererbsen nachgewiesen und im Zusammenhang mit klinischen Berichten über Intoxikationen diskutiert. Diese Studie bildet die Grundlage für Untersuchungen von Proteinverteilungen in Pflanzenmatrices und eröffnet neue Möglichkeiten für die Pflanzenwissenschaften, zur Bewertung pflanzlicher Nährstoffqualität sowie der Sicherheit pflanzlicher Lebensmittel.

Insgesamt demonstrieren die vorgestellten Arbeiten die breite Anwendbarkeit von hochauflösendem MALDI MS imaging für verschiedenste Lebensmittel sowie Analyten. Bei sorgfältiger Methodenentwicklung können auch wenig abundante Verbindungen in herausfordernden Lebensmittelmatrices zuverlässig visualisiert werden. Für Pflanzenproteine wurde eine hochauflösende MALDI MS imaging-Methode zur bottom-up Identifizierung entwickelt. Die Arbeiten im Rahmen dieser Dissertation sollen verdeutlichen, dass MALDI MS imaging Methode der Wahl sein und chromatographiebasierte Analysen ergänzen kann, wenn räumliche Verteilungen von Bedeutung sind. Zudem kann MS imaging nicht nur für die Wissenschaft, sondern auch für Untersuchungsämter und Lebensmittelunternehmen zu Prozessüberwachungs- oder Qualitätskontrollzwecken von Interesse sein. Neben der Ausstattung der Untersuchungsämter mit entsprechenden Geräten und Expertise sollte die Implementierung gesetzlicher Anforderungen an die räumliche Verteilung bestimmter Zielanalyten in Rechtsnormen ein Ziel sein, um ein stetig steigendes Niveau an Lebensmittelsicherheit, -qualität und -authentizität zu gewährleisten.

Abstract

Matrix-assisted laser desorption/ionization (MALDI) mass spectrometry imaging (MS imaging) is a powerful analytical technique of increasing popularity in various scientific disciplines. Motivations in food science are diverse and range from agricultural developments to health-relevant food safety concerns, for which MS imaging can be applied to investigate spatial distributions of desired and undesired compounds. Most reports have focused on visualizing constituents in unprocessed food. Processed food has only recently become subject to MS imaging studies; applications targeting exogenous compounds, such as food additives or contaminants, are rare. Furthermore, requirements regarding the distribution of food-related compounds have hitherto scarcely been adopted into legal norms since analytical capabilities for such analyses have been limited.

Seeking to overcome these limitations, this dissertation aimed to demonstrate the value of MALDI MS imaging for food analysis and to stress its potential for use in the food sciences, by manufacturers and food authorities. To achieve this, sample preparation workflows, measurement methods and data analysis approaches were developed tailored to different kinds of food and analytes. In all measurements, high mass resolution and accuracy were crucial for high detection selectivity. Going beyond the mere visualization of distributions, in-depth data analysis approaches were to be designed for compounds underlying legal regulations. Another important goal was the development of a dedicated MS imaging method for the spatially resolved ‘bottom-up’ identification of proteins in plants based on accurate mass detection.

Initially, high-resolution MALDI MS imaging methods were developed for a selection of food samples to demonstrate its broad applicability. Samples of hardy kiwi, carrots, veal sausage, Gouda cheese and German gingerbread represented fresh and processed food of plant and animal origin. Highly nonpolar and polar constituents as well as ingredients, contaminants and food additives were detected and visualized. With the carcinogen acrylamide in gingerbread and the preservative natamycin in Gouda cheese, distributions of a contaminant and a food additive have been revealed in processed food for the first time. To investigate the penetration behavior of natamycin into Gouda cheese, a new data processing tool was developed. Overall, the results show the great potential of MS imaging for the spatially resolved investigation of various foodstuffs.

Expanding upon the foundations laid in the first publication, protocols for sample preparation and measurement of German gingerbread were optimized. Since inhomogeneous, brittle gingerbread constitutes a challenge for sample preparation, substantial modifications to the workflow were necessary. The uneven surface of gingerbread cross-sections required autofocusing as part of the ionization process to ensure a constant MALDI-laser focus. Major nutrients and the low-abundant contaminant acrylamide were identified and visualized. A statistical protocol based on relative acrylamide intensities substantiated the observation of higher acrylamide contamination within nut fragments. Furthermore, to achieve higher detection selectivity, a novel *in situ* derivatization protocol for acrylamide was developed. For evaluating acrylamide mitigation strategies adopted into European regulations, knowledge about its spatial distribution can be valuable to manufacturers and food authorities. This study demonstrates that MALDI MS imaging can provide such complementary information even in challenging processed food.

Besides the sample material, target analytes can be challenging in MS imaging analysis as well; a prominent example for such challenging analytes are proteins. In the field of proteomics, the bottom-up approach is a fundamental identification strategy including enzymatic protein digestion and analysis of peptides to deduce untargeted information on the proteome. However, it has rarely been applied to plant tissue yet. This was addressed by systematically developing a protocol for preparation, *in situ* tryptic digestion and high-resolution MALDI MS imaging of chickpea seeds. Measurements revealed different distribution patterns across seed compartments, for which a total of sixteen proteins were identified by accurate mass detection of tryptic peptides. In a food safety application, the toxic protein abrin was detected in seeds of crab’s eye vine and contextualized with human intoxication reports. This study lays the foundation for investigations on protein distributions in plant matrices, offering new possibilities for plant sciences and the assessment of crop quality and safety.

Overall, this work demonstrates the broad applicability of high-resolution MALDI MS imaging for various food samples and analytes. Given thorough method development, even low-abundant compounds

in challenging food matrices could be reliably visualized. For plant proteins, a high-resolution MALDI MS imaging method for bottom-up protein identification and visualization has been developed. All work as part of this dissertation seeks to demonstrate that MS imaging can be the method of choice and complement chromatography-based methods when spatial distributions matter. Moreover, it can not only be of interest to analytical scientists, but also to food authorities as well as to manufacturers for process monitoring or quality control reasons. Providing food authorities with MS imaging instrumentation and expertise alongside the implementation of spatial distribution requirements into legal norms should be a future objective to ensure an ever-increasing level of food safety, quality and authenticity.

Contents

Zusammenfassung	I
Abstract	III
List of Tables	VI
List of Figures	VII
1 Introduction	1
1.1 Mass spectrometry imaging	1
1.1.1 (Atmospheric pressure-) Matrix-assisted laser desorption/ionization	1
1.1.2 High mass resolution MS imaging	2
1.1.3 Autofocusing AP-SMALDI for MS imaging	4
1.1.4 Sample preparation for MALDI MS imaging	5
1.1.5 Data analysis	7
1.2 MS imaging of food	8
1.2.1 Motivations for MS imaging of food	8
1.2.2 Applications in food crops and raw food materials	10
1.2.3 Applications in processed food of animal and plant origin	11
1.3 Previous work and status built upon	12
2 Results	13
2.1 Synopsis	13
2.1.1 MALDI MS imaging of various substance classes in fresh and processed food	13
2.1.2 Autofocusing MALDI MS imaging for food with uneven surfaces	17
2.1.3 Spatially resolved identification of plant proteins by MALDI MS imaging	21
2.2 Author contributions	26
3 Scientific publications and manuscripts	27
3.1 MALDI mass spectrometry imaging: From constituents in fresh food to ingredients, contaminants and additives in processed food	28
3.2 Autofocusing MALDI MS imaging of processed food exemplified by the contaminant acrylamide in German gingerbread	52
3.3 MALDI MS imaging of chickpea ceeds (<i>Cicer arietinum</i>) and crab's eye vine (<i>Abrus precatorius</i>) after tryptic digestion allows spatially resolved identification of plant proteins	74
4 Conclusions and outlook	111
5 Publication list	X
6 Danksagung	XII
7 (Eidesstattliche) Versicherungen und Erklärungen	XIII

List of Tables

1	Selection of MS imaging applications on unprocessed food, subdivided by plant/animal origin and the predominant motivation brought forward in the respective publications. . .	10
2	Overview of methodological details in sample preparation and measurement of traditional German gingerbread for the first and second publication.	18

List of Figures

1	Overview of the optical laser system of the AP-SMALDI ion source (TransMIT GmbH). Reprinted with the kind permission of Prof. Bernhard Spengler.	2
2	Quadrupole Orbitrap mass spectrometer schematic overview. Reprinted from Kaufmann et al. 2018 ¹⁶ with written permission of John Wiley & Sons Inc.	4
3	General sample preparation workflow for AP-MALDI MS imaging by example of hardy kiwi.	5
4	Basic MS imaging data analysis protocol by example of hardy kiwi (<i>A. arguta</i>), following up the sample preparation and measurement workflow described in section 1.1.4. Single pixel mass spectra of three candidate signals are displayed with the corresponding relative mass errors, mass resolutions R and molecular structures. Upon selecting a target m/z -value, analyte peaks are retrieved from all mass spectra and processed into an ion image with the brightness reflecting peak intensities. Ion images normalized to the TIC were generated for the lipid TG(54:9) K-adduct (red), the phytochemical quercetin (blue) and disaccharide K-adducts (green). Note that the structure of sucrose is displayed exemplary for the green signal, although the ion image includes all disaccharide K-adducts with the respective sum formula. Single ion images can be overlaid in an RGB ion image and juxtaposed with a microscopy image.	14
5	matrix-assisted laser desorption/ionization (MALDI) mass spectrometry (MS) imaging of constituents in fresh food (carrots, A and B) and processed food (veal sausage, C). A , B : Juxtaposed microscopy images with the respective ion images of β -carotene in orange carrot and cyanidin in purple carrot, each with the respective molecular structures. C : RGB overlay and molecular structures of constituents of varying polarity in German veal sausage: Disaccharide Na-adducts (red), cholesterol ($[M - H_2O + H]^+$, blue) and PC(36:4) Na-adduct (green). Note that the structure of sucrose is displayed exemplary for the red signal, although the ion image includes all disaccharide Na-adducts with the respective sum formula.	15
6	MALDI MS imaging of the process contaminant acrylamide in traditional German gingerbread as an example for highly processed food. A : Single ion image of protonated acrylamide, m/z 72.04439, pixel size 200 μm . B : Microscopy image of the measured section with annotated ingredients.	15
7	MALDI MS imaging for penetration analysis of natamycin into sections of Gouda cheese. A : Molecular structure of the detected natamycin Na-adduct. B : Single pixel MALDI mass spectrum on Gouda cheese with annotated signals of protonated natamycin ($m/z_{theor.} = 666.31202$) and natamycin Na-adduct ($m/z_{theor.} = 688.29396$) with the corresponding relative mass error and mass resolution R . C : Ion image of sphingomyelin SM(d34:1) Na-adduct, $m/z_{theor.} = 725.55680$ and resultant calculated cheese edge highlighted in yellow. D : Ion image of natamycin Na-adduct and calculated cheese edge from C . E : Distance map from the edge into the cheese bulk for the calculation of penetration depth values. F : Plot of mean natamycin intensities against the distance from the edge ('penetration plot') including exponential fit displayed in red.	17
8	Autofocusing MS imaging of German gingerbread. A : 3D ion image of disaccharide K-adducts, m/z 381.07937, TIC-normalized. z -coordinates were retrieved from AF-laser data. The pink line represents an exemplary profile through high and low regions on the sample surface. B : Line scans of the surface profile and total height difference (Δ) along the pink line shown in A , based on digital microscopy data (top) and AF-laser data (bottom). . . .	19
9	Representative MALDI-MS/MS spectrum and fragmentation scheme for protonated acrylamide on German gingerbread. Isolation window: m/z 72.0 \pm 0.2, scan range: m/z 50–80, HCD: 60.	19

10	Distribution analysis of acrylamide in German gingerbread. A: Microscopy image of the measurement area. B: Ion image of acrylamide, m/z 72.04439, TIC-normalized. C: ROI-mask generated for sample surface stratification into ROI „nuts“ and „other“. D: Boxplots of backtransformed ($x^{0.25}$ -transformation) acrylamide abundance values for both ROI, $***t(247) = 16.93, p < .001$	20
11	Sample preparation workflow for bottom-up protein MALDI MS imaging of plant tissue. Compared to established protocols for animal tissue, soaking and water spray were newly introduced. The ‘alarm clock’-symbol indicates that the sprays are performed in immediate succession. The ‘moon’-symbol indicates a controlled overnight incubation.	22
12	Necessity for high mass resolution for selective peptide visualization. A: Zoomed-in single pixel mass spectrum with indicated mass resolution R of tryptic peptide CPGR (ammonium adduct), m/z 449.22893, and its neighboring peak. B: MMA-plot of the respective peaks in A . C: Ion image of tryptic peptide CPGR (ammonium adduct). D: Ion image of the neighboring peak.	23
13	MALDI MS imaging of tryptic peptides with different distributions throughout a chickpea seed cross-section. A: Microscopic image of the measured sample. B: Overlay of tryptic peptide EFVR K-adduct, m/z 588.25426 (red), protein A0A1S2XHJ1 and tryptic peptide VGVKNR Na-adduct, m/z 807.48112 (green), protein A0A1S2YYM1. C: Overlay of tryptic peptide SHGVK K-adduct, m/z 565.24946 (red), protein A0A1S2YX55 and tryptic peptide KKWVIHIER NH ₄ -adduct, m/z 1225.75283 (green), protein A0A1S2XNP5. . . .	24
14	MALDI-MS/MS mean spectrum ($n = 34$ single spectra) of tryptic peptide NDVSYVPR K-adduct, m/z 974.43436, HCD: 35. Molecular ion and fragment ions are indicated in the spectrum together with their relative mass error and in the adjacent molecular structure with the respective cleavage site.	24

Abbreviations

kDa kilo-Dalton.

m mass.

m/z mass-to-charge ratio.

ppm parts per million.

AF autofocusing.

AP atmospheric pressure.

APCI atmospheric pressure chemical ionization.

DART direct analysis in real time.

DESI desorption electrospray ionization.

DHB 2,5-dihydroxybenzoic acid.

EC European Community.

EEC European Economic Community.

EU European Union.

FT-ICR fourier-transform ion cyclotron resonance.

FWHM full peak width at half intensity maximum.

GC gas chromatography.

HCD higher-energy collisional dissociation.

HPLC-DAD high-performance liquid chromatography coupled to diode array detection.

HPLC-UV high-performance liquid chromatography coupled to ultraviolet detection.

HRMS high-resolution mass spectrometry.

IHC immunohistochemistry.

IM ion mobility spectrometry.

LA-ICP laser-ablation inductively coupled plasma.

LAESI laser-ablation electrospray ionization.

LC liquid chromatography.

LDI Laser desorption/ionization.

LGL Bavarian Health and Food Safety Authority.

MALDI matrix-assisted laser desorption/ionization.

MMA mass measurement accuracy.

MRI magnetic resonance imaging.

MS mass spectrometry.

MS/MS tandem mass spectrometry.

nano-PALDI nanoparticle-assisted laser desorption/ionization.

PC phosphatidylcholine.

RF radio frequency.

RGB red, green and blue.

RMSE root-mean square error.

ROI region of interest.

SIM single ion monitoring.

SIMS secondary-ion mass spectrometry.

SMALDI scanning MALDI.

ssp. subspecies.

TG triglyceride.

TIC total ion current.

TOF time-of-flight.

ULT ultra-low temperature.

UV ultraviolet.

var. variety.

1 Introduction

1.1 Mass spectrometry imaging

Mass spectrometry imaging (MS imaging) is a powerful analytical technique, which links mass spectrometric data to defined locations on the surface of (biological) samples and thus allows for resolving the molecular complexity in a two-dimensional manner. In contrast to ‘classical’ MS techniques coupled to chromatographic separation, such as gas chromatography (GC) or liquid chromatography (LC), sample homogenization and analyte extraction are omitted, or the latter at least performed in a way that retains analytes’ original spatial distribution across the sample. By MS imaging, both endogenous and exogenous compounds can be simultaneously detected, visualized, and characterized based on their mass, without the need for labeling or staining.¹ The only mandatory requirements are ionizability of the compounds of interest and their presence in concentrations relevant to the instrument sensitivity. The possibility to selectively analyze individual chemical compounds is a distinguishing feature of MS imaging compared to other visualizing analytical techniques, such as histological staining, immunohistochemistry (IHC) or spectroscopic methods. However, MS imaging is not per se linked to superior selectivity; this aspect is further elaborated in section 1.1.2 and is an essential part of the second publication (section 3.2). MS imaging can be performed as an untargeted analytical approach — with the limitation of more or less determinant steps in sample preparation, such as the choice of matrix when using MALDI — since it offers the possibility of a retrospective analysis by use of a candidate analyte list or simply browsing through *mass-to-charge ratio* (m/z)-values to observe interesting analyte distributions without prior knowledge of the sample. This is of particular interest in protein MS imaging and elaborated in section 1.1.4 as well as in the third publication (section 3.3).

‘MS images’ (or ‘ion images’) constitute two-dimensional heatmaps, which elucidate both the spatial distributions and the relative abundances of ionizable compounds using color scales. Usually, MS images are presented in combination with images recorded by optical microscopy to link spatial molecular features to anatomical structures of the sample. More and more tools for MS imaging data processing are becoming available, enabling in-depth statistical analysis and data interpretation. A selection of data analysis tools used for this dissertation is presented in section 1.1.5.

Mass spectrometers can, in principle, be equipped with different MS imaging-compatible ion sources. Among an ever-increasing list of ionization methods, the most popular ones today are MALDI under vacuum as well as under atmospheric pressure (AP), secondary-ion mass spectrometry (SIMS), desorption electrospray ionization (DESI) and laser-ablation inductively coupled plasma (LA-ICP), all possessing individual advantages and limitations for specific research goals (see also applications described in sections 1.2.2 and 1.2.3). Since all MS imaging analyses as part of this dissertation were performed using AP-MALDI, this technique will be further elaborated in the following section.

1.1.1 (Atmospheric pressure-) Matrix-assisted laser desorption/ionization

The principle of MALDI was first published by Karas and Hillenkamp in 1988² and is today by far the most commonly used ionization technique in MS imaging.¹ MALDI is a soft ionization method producing mostly singly-charged ions directly from solid samples. A surplus of highly light-absorbing chemicals – the matrix – is used to assist the ionization process by shielding analytes from direct laser exposure and facilitating the energy transfer to analytes. For MALDI MS imaging, the matrix is commonly applied by (re-)sublimation or in a pneumatic spray, causing analyte molecules to be extracted from the sample surface and co-crystallized. Laser desorption/ionization (LDI) without a matrix works very well for chromophore-containing compounds such as anthocyanins,³ struggles, however, to ionize compounds lacking a chromophore. Matrices used for ultraviolet (UV)-MALDI are crystalline organic solids with a chromophore capable of absorbing UV light. Many common UV-MALDI matrices contain a delocalized π -electron system. More details are provided in section 1.1.4.

Upon MALDI-laser irradiation, both matrix molecules and analytes are co-desorbed while the matrix inhibits excessive destructive heating of the analytes.⁴ Georgiou and Hillenkamp described the laser ablation during MALDI as „a very fast boiling off of the material“ and at the same time point out that highly complex phenomena lie beyond this simplification.⁵ To date, though MALDI is very commonly

applied in analytical chemistry and several plausible theories explaining the desorption/ionization process of analyte molecules have been published,^{6,7} the entire process — in particular the desorption/ionization — is yet not fully understood. It is consensus that there is no singular pathway of ion formation; instead, depending on multiple factors, such as the types of matrix and analytes and the pH on the sample surface, ions are preformed within matrix crystals and/or formed after desorption in the gas phase to a varying extent.⁸

An advantage for the investigation of water-containing biological samples is conferred by AP-MALDI, a subtype of MALDI using ion sources which are not operating under vacuum atmosphere. With AP-MALDI, samples are analyzed in their native state without morphological changes at ambient pressure and temperature. Moreover, a lower degree of fragmentation is observed in AP-MALDI MS imaging experiments compared to vacuum MALDI due to the rapid collisional cooling of desorbed ions, which occurs at atmospheric pressure.⁹ As part of this dissertation, AP scanning MALDI (SMALDI) ionization has been used for all MS imaging work done. The term ‘scanning’ refers to the ionization mode with the MALDI-laser scanning the sample surface pixel by pixel (also known as ‘microprobe mode’). A schematic representation of the MALDI-laser system is provided in Figure 1. From the laser source, the beam passes an assembly of mirrors, lenses, and filters to adjust the laser energy and at the same time direct it into the ion source. There, an objective lens refocuses the laser beam onto the sample target attached to an x/y/z-movable sample stage. This construction, i.e., the orthogonal orientation of the MALDI-laser and the ion trajectory passing through the centrally drilled 45° mirror, is a distinguishing feature of the TransMIT AP-SMALDI ion sources.¹⁰ As described in more detail in section 1.3, Prof. Römpp’s research group has considerable experience in AP-MALDI MS imaging.¹¹

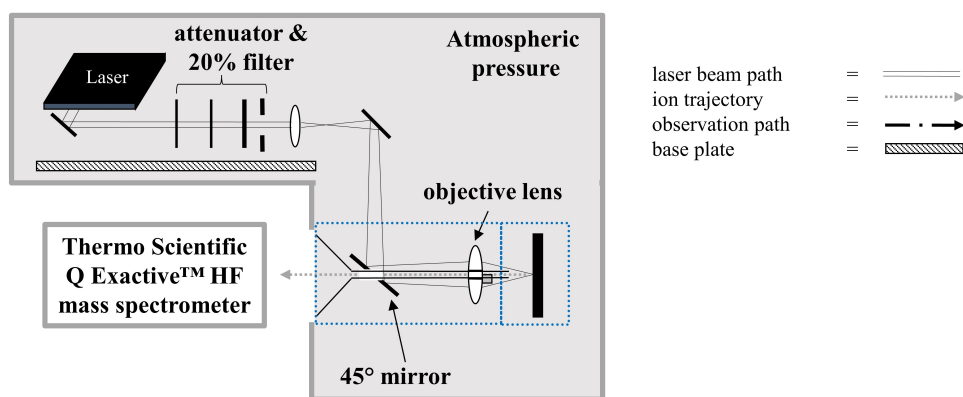


Figure 1: Overview of the optical laser system of the AP-SMALDI ion source (TransMIT GmbH). Reprinted with the kind permission of Prof. Bernhard Spengler.

1.1.2 High mass resolution MS imaging

A fundamental performance indicator in mass spectrometry is the mass resolution R . It is defined by the full peak width at half intensity maximum (FWHM) and calculated from the m/z difference ($\Delta m/z$) at 50 % peak intensity for a given mass (m) or m/z -value,⁸ see equation 1.

$$R = \frac{m}{\Delta m} = \frac{m/z}{\Delta(m/z)} \quad (1)$$

The mass resolution thus describes the narrowness of a peak in a mass spectrum and is predominantly influenced by the type of mass analyzer. The threshold for the distinction between low and high resolution MS is not universally defined since the boundary of achievable mass resolution has been constantly pushed by the development of modern instruments. Additionally, the necessary level of mass resolution is always dependent on the mass range, the complexity of the analyzed sample and the desired selectivity of the experiment.

Another important key figure in mass spectrometry is mass accuracy. It is usually reported as the

relative mass error to the theoretical m/z -value of a compound (calculated based on its sum formula). In contrast to the absolute mass error, which constitutes the mere difference in measured and theoretical m/z , the relative mass error is expressed in parts per million (*ppm*) relative to a given m/z and calculated according to equation 2.⁸

$$\frac{\delta m}{m} = \left(\frac{m/z_{\text{measured}} - m/z_{\text{theoretical}}}{m/z_{\text{theoretical}}} \right) \times 10^6 \quad (2)$$

Besides the general requirement of high mass accuracy for reliably determining the elemental composition of an unknown compound, mass accuracy is a very useful quality control parameter in an MS imaging experiment. A scatter plot of the relative mass errors (positive and negative) for a given m/z -value in the mass spectra of all pixels against the respective signal intensities is commonly referred to as mass measurement accuracy (MMA) plot. It can, for instance, reveal a systematic deviation to a hypothesized theoretical m/z -value or the inclusion of multiple compound peaks into one image bin. A desirable MMA plot exhibits a ‘fir tree’-shape with its center near the theoretical m/z -value (i.e., 0 *ppm* relative mass error) and all data points within the set image bin. The root-mean square of all (n) relative mass errors (RMSE, see equation 3) is commonly used to summarize the overall mass accuracy for a given compound.

$$RMSE_{m/z} = \sqrt{\sum_1^n \frac{(\delta m/z - m/z_{\text{theoretical}})^2}{n}} \quad (3)$$

Thorough calibration of the mass spectrometer is a crucial prerequisite for high mass accuracy. Mass spectrometers need to be calibrated externally on a regular basis using standard material with well-defined masses.⁸ Additionally, internal mass calibration is often used during an MS experiment to supplement the external mass calibration and further increase mass accuracy. By use of a ubiquitous substance with known mass, such as a matrix cluster ion, each mass spectrum can be corrected by the corresponding relative mass error. All MS measurements presented in this work were conducted using both external and internal mass calibration and profited from a systematic investigation thereof;¹² more details are provided in section 1.3.

Whenever it is referred to high-resolution mass spectrometry (HRMS) in this dissertation, this includes both high mass resolution (R typically 240,000 at m/z 200) and mass accuracy (RMSE < 1.5 *ppm*). Considering the molecular complexity of the investigated biological samples, combining high mass resolution and mass accuracy is beneficial for the identification of compounds of interest by reducing false-positive assignments, e.g., in database searches following untargeted analysis (see section 2.1.3 and third publication, section 3.3) or the determination of possible elemental compositions. Due to the plethora of compounds in biological tissues as well as — in case of MALDI ionization — the matrix and its various cluster forms, a highly selective detection of analytes by use of accurate masses, isotopic patterns and/or *in situ* fragmentation experiments provides more reliable mass spectral data and thus an increased confidence level. In case of MS imaging in particular, high mass resolution and mass accuracy render a selective presentation of analytes’ spatial distributions.¹³

The selectivity of MS imaging experiments mainly depends on the mass resolution provided by the instrument. The initial uniqueness of time-of-flight (TOF) mass analyzers following MALDI ionization does not exist anymore since TOF mass resolution is sometimes insufficient for applications with complex biological samples.¹⁴ Other modern high-resolution mass analyzers are nowadays coupled to MALDI sources besides TOF, such as fourier-transform ion cyclotron resonance (FT-ICR) and Orbitrap instruments. The latter was used for all MS experiments in this dissertation and is introduced in more detail hereinafter.

The orbital trapping mass spectrometer was developed by Makarov in 2000¹⁵ and gained widespread adoption in the field of MS since. A simplified schematic description of such an instrument is provided in Figure 2.

Following the entry of ionized substances through the ion transfer tube, the ion beam is focused and subsequently directed through one or more quadrupoles (indicated in blue in Figure 2). This part is responsible for the elimination of uncharged molecules and an optional preselection of certain m/z -values

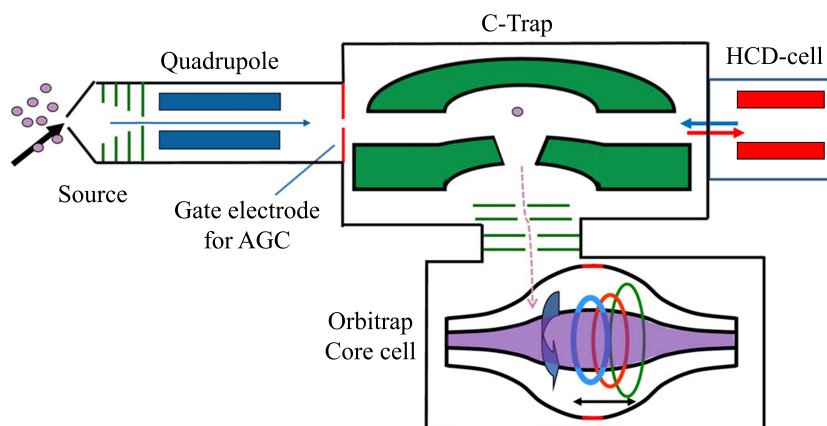


Figure 2: Quadrupole Orbitrap mass spectrometer schematic overview. Reprinted from Kaufmann et al. 2018¹⁶ with written permission of John Wiley & Sons Inc.

in a quadrupole mass filter, e.g., for single ion monitoring (SIM) or targeted tandem mass spectrometry (MS/MS) experiments. The following C-Trap, highlighted in green in Figure 2, is a bent multipole working in radio frequency (RF)-mode only, which is filled with nitrogen as a bath gas to slow down and trap incoming ions by collisional cooling.¹⁶ After a short time period referred to as ‘C-Trap injection time’, ion packets are accelerated into the Orbitrap, which constitutes the actual mass analyzer. The Orbitrap is characterized by the combination of a split outer barrel-shaped and a central spindle-shaped electrode, the latter depicted in violet color in Figure 2. Ions enter from the C-Trap, indicated by the dashed violet arrow, at a slight offset to the Orbitrap’s symmetry plane (‘equator’). Within the void between the two electrodes, they are both accelerated towards the equator and forced to orbit around the central electrode. The slighter the difference in m/z of two ions, the more oscillations are necessary for physical separation, which is why measurements at very high mass resolution take longer time. Oscillation frequencies of the orbiting ions along the symmetry axis of the Orbitrap are dependent only on their m/z -ratios and recorded as a current.¹⁵ Using Fourier transformation, acquired raw voltage/time data are transformed and further processed to mass spectra with the m/z -ratio on the abscissa. For MS/MS experiments, a higher-energy collisional dissociation (HCD)-cell for optional fragmentation analyses is located next to the C-trap. It is filled with (nitrogen) gas particles to collide with analyte ions and induce fragmentation. From the HCD-cell, ions can then be redirected into the C-Trap as indicated by the red and blue arrows in Figure 2.

The relevance of mass spectrometry as an analytical technique for food analysis and in particular the benefits of HRMS are emphasized in recent reviews.^{17,18} As already mentioned, a Quadrupole-Orbitrap MS instrument (QExactive HF, Thermo Fisher Scientific) coupled to an AP-SMALDI ion source was used for all MS imaging work done as part of this dissertation. All assignments of compounds to m/z -values presented in this work are based on accurate mass, i.e., mass accuracy better than 1.5 ppm relative mass error. This high level of selectivity is particularly important due to the complexity of food samples and the lack of reduction measures, such as chromatographic separation, preceding mass spectrometric analysis in MS imaging,¹¹ which is highlighted in all three publications.

1.1.3 Autofocusing AP-SMALDI for MS imaging

In common MS imaging experiments, a flat sample surface is crucial for constant MALDI conditions throughout the measurement. Sometimes, it is hard to produce perfectly flat surfaces, especially when samples are difficult to section due to an inhomogeneous texture or the presence of cavities. According to Bjarnholt et al., surface topology is an often overlooked, but serious issue for MS imaging results.⁹ When using a fixed MALDI-laser focus, differences in ionization efficiency caused by the sample surface topology can be partly compensated by setting a larger ablation area (defocus) of the MALDI-laser, as was done in the first publication (section 3.1). An elegant recent add-on to keep measurement conditions (laser focus and fluence) constant despite an uneven sample surface is the introduction of an additional

continuous-wave autofocusing (AF)-laser positioned at a 35° angle to the transfer capillary axis.¹⁹ This feature was realized in a special MALDI source (AP-SMALDI5 AF, TransMIT GmbH, Giessen, Germany). Autofocusing is performed by adjusting the relative position of the AF-laser at each pixel position prior to irradiation by the MALDI-laser. To investigate irregular surfaces with height differences up to hundreds of μm , such as plant leaves²⁰ or, as shown in the second publication, sections of gingerbread, an AF-ion source is highly beneficial and becomes increasingly necessary with higher lateral resolution. Ion images resulting from AF MALDI MS imaging are sometimes referred to as ‘3D ion images’. Since there is also 3D MS imaging as a technique for visualizing multiple sample layers, it is important to differentiate these terms. 3D ion images presented in this work represent the topology of the sample based on the recorded z-positions of the sample stage at each pixel after adjustment by autofocusing.

1.1.4 Sample preparation for MALDI MS imaging

1.1.4.1 General workflow

The ultimate goal of a typical AP-MALDI MS imaging experiment is to create ion images representing the molecular composition of a given sample in its current state. Despite what this subsection’s title might imply, there is no universal sample preparation procedure. The ‘general workflow’ described hereinafter consists of the most common steps in sample preparation for AP-MALDI MS imaging and is depicted in Figure 3. In any case, it is indispensable to adapt the protocol to the properties of the respective sample by optimizing parameters or extension by additional preparation steps (see following section).

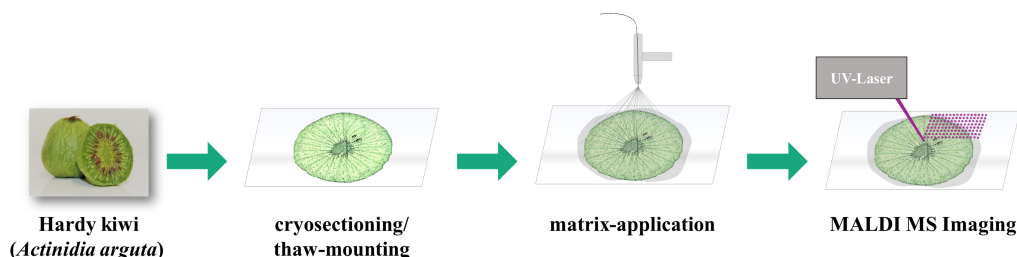


Figure 3: General sample preparation workflow for AP-MALDI MS imaging by example of hardy kiwi.

Usually, the first task is to produce thin sections of the sample (typically 10 - 100 μm). The most common method for this is cryosectioning, with the frozen sample being introduced into the chilled chamber of a cryomicrotome and attached to a movable stage in front of a cutting blade. With every up-and-down rotation of the stage, it also moves towards the sharp blade for a well-defined increment, determining the thickness of the sections. These can be thaw-mounted onto an appropriate slide and then stored in frozen state until further processing.

For MALDI MS imaging, a chemical matrix needs to be applied prior to the measurement. Here, both the choice and deposition method of the matrix are crucial steps in method development. While most analyte molecules are non-absorbing in the near-UV, it is essential for the matrix to absorb light at the MALDI-laser emission wavelength. Some MALDI matrices, such as 2,5-dihydroxybenzoic acid (DHB), can be applied for a wide spectrum of analytes of high and low mass, which is why DHB has been proven suitable for all measurements in this dissertation. Technically, both an effective analyte extraction/matrix co-crystallization and the formation of crystals smaller than the desired laser focal point diameter need to be achieved. For all experiments as part of this dissertation, samples were covered with matrix by spray application: The matrix was dissolved in a mixture of an organic solvent and water and then nebulized in a spray nozzle, which was either fixed above the revolving sample plate (semiautomatic application, see first publication, section 3.1) or movable/programmable as part of a spray chamber (automated application, see second and third publication, sections 3.2 and 3.3). In the pneumatic spray setup, solvent droplets assist the extraction of analyte molecules from the sample surface; upon evaporation of the solvent, the matrix crystallizes and incorporates the analytes. Optimizing spray parameters often strikes a balance between efficient analyte extraction, resulting in potentially higher analyte abundance, and best possible retention of analytes’ spatial arrangements, i.e., not to cause dislocation.

After mounting the matrix-covered sample onto the movable stage of the AP-SMALDI chamber, parameters for the stage (e.g., step size and raster size), the MALDI-laser (e.g., laser focus and energy) and the mass spectrometer (e.g., acquisition mode, mass range and polarity) are set. As already described in section 1.1.2, internal mass calibration was performed during the measurement using homogeneously distributed matrix cluster ions.¹² During the measurement, the stage moves in increments defined by the step size following each irradiation event until the entire raster is measured.

In AP-MALDI, molecular ions generated in positive ion mode are usually protonated or adducts with alkali metal (Na^+ , K^+) or ammonium (NH_4^+) cations.²¹ The types and relative proportions of ions (protonated or adduct), which are detected in a particular experiment, are strongly influenced by the presence of adduct-forming cations in/on the sample, as encountered for instance in the first publication for natamycin in Gouda cheese, which was applied as a sodium salt and consequently detected as the corresponding adduct in MALDI MS imaging experiments. Notably, distributions encountered in MS images depend strongly on the ionizability of the respective analyte and can be influenced by local suppression effects exerted by interfering compounds. Especially in heterogeneous samples, inconsistent ion suppression cannot be ruled out and might require data normalization as described in section 1.1.5.

1.1.4.2 Special requirements for plant (food) samples

Due to fundamental differences in cell morphology between animal and plant cells, plant material often has different requirements regarding preparation steps or parameters than commonly used animal tissues, such as mouse brain or pig liver. There are several important aspects to consider in sample preparation when attempting to analyze samples of plant origin by MS imaging, which are discussed in the following.

In general, sectioning plant samples in a cryomicrotome is not trivial because, depending on the organ (e.g., root, stem, leaf, fruit, or seed), the tissue might be very hard and brittle, or contain large vacuoles.^{22,23} If the sample texture is too firm for immediate cryosectioning, preparative soaking might be necessary beforehand. This can be performed either by rinsing and keeping samples moist,²⁴ placing them on wet filter paper,²⁵ bubbling in water²⁶ or soaking them in an appropriate medium (see third publication, section 3.3). In the next step, samples need to be frozen, which is often done gently by placing the sample in an ultra-low temperature (ULT)-freezer instead of (damaging) rapid deep-freezing by submersion in liquid nitrogen.^{23,27} To prevent delicate samples from deformation or rupture upon cryosectioning, they can be embedded in a stabilizing medium, such as gelatin or carboxymethyl cellulose. Although embedding is also commonly used for fragile animal tissue, it is essential for many plant organs due to the rigid plant cell wall and the high water content, which make them prone to crack formation or detachment of sample parts. The cryomicrotome's temperature settings, sample orientation towards the cutting blade, and sectioning speed need to be adjusted to the specific type of sample. There is no universal tendency when comparing sectioning protocols for plant and animal tissue. However, it has often been found that for plant organs, a slightly higher thickness (i.e., 35–100 μm) needs to be set to obtain sections of good and reproducible quality.^{28–30} A popular method for the preparation of thin sections of delicate samples, which makes use of a double-sided (conductive) adhesive tape, was described by Kawamoto.³¹ This tape is fixed onto the sample surface in the cryomicrotome immediately before sectioning and thus ensures maintaining sections' integrity. However, this method is not applicable for protocols involving a subsequent washing step (see following section) since a sample section might detach from the tape when it comes into contact with organic solvents. Despite the described measures to facilitate cryosectioning even for challenging samples, some samples still remain which are not suitable for the cryosectioning process. For these samples, alternative methods need to be developed to produce sections or flat surfaces. Reported methods include the use of a dicer and a shaver for turmeric roots,³² a cutting blade for roasted coffee beans,³³ or an electric cutting-disk as presented in the first (section 3.1) and second publication (section 3.2).

The variety of different histological features in plant tissues, including phloem and xylem, cells with large vacuoles, stone and oil cells, might not only be responsible for their behavior in sectioning, but also for the crystallization behavior of the MALDI matrix.⁹ Many plant samples in their native state are rich in water and, as dry thin sections, show a tendency to absorb liquid applied to their surface. It is thus not surprising that the matrix application protocol needs to meet these requirements. Compared to

the mentioned typical animal tissues, higher amounts of MALDI matrix tend to be necessary for plant samples to achieve a complete coating with matrix crystals and avoid uncoated sample surface, ensuring constantly efficient analyte ionization.

1.1.4.3 MALDI MS imaging of proteins

In an experimental context, the term ‘proteomics’ constitutes the determination of the qualitative and quantitative composition of all proteins in biological samples as opposed to ‘protein analysis’, which focuses on individual proteins and the determination of their molecular properties.³⁴ In the field of MS imaging, such analyses usually cover the mass spectrometric identification of (multiple) proteins together with the elucidation of their spatial distributions across the surface of a biological sample. As for chromatography-based in-solution proteomics, two fundamental strategies for protein identification can be distinguished also when applying an MS imaging setup: Top-down and bottom-up.

The top-down protein identification strategy is characterized by a direct analysis of intact proteins in the mass spectrometer.³⁵ Identification based solely on the mass of the intact protein is not reliable, especially in mass ranges exceeding 30 *kDa* due to the decreasing detection sensitivity.³⁶ Therefore, MS/MS experiments are obligatory in top-down proteomics to support the hypothesized protein assignment. In MALDI MS imaging, however, proteins merely carry a single charge, which leads to inefficient fragmentation and less informative MS/MS spectra.

The bottom-up protein identification approach relies on an enzymatic digestion of proteins prior to the MS measurement, resulting in smaller peptides.³⁷ This enables the identification of proteins indirectly based on their ‘peptide fingerprint’. By computational *in-silico* digestion of database protein entries, theoretical peptide masses are matched with the observed accurate masses from the MS imaging experiment and subsequently assigned to the corresponding protein(s). Therefore, the bottom-up approach is especially advantageous for larger proteins that are usually not accessible through direct top-down MS imaging. Trypsin is by far the most popular protease used in bottom-up proteomics and nearly all analytical optimization work has been done using trypsin.³⁸ It is both an efficient and specific endopeptidase, which generates peptides with a C-terminal arginine or lysine, making it ideally suitable for bottom-up proteomics. Therefore, trypsin was used for all protein MS imaging as part of this dissertation as well. Due to the artificial expansion of the molecular complexity through enzymatic digestion, ensuring high selectivity is particularly important for bottom-up protein MS imaging measurements. Schober et al. published the first MS imaging experiments using an orbital trapping mass spectrometer for the detection of tryptic peptides with accurate mass and pointed out that high mass resolution and mass accuracy are crucial for a selective detection and presentation of spatial features in MS imaging of mammalian tissue.^{13,39} In contrast to MALDI-IHC as another highly selective spatially-resolved protein identification strategy, bottom-up protein MS imaging is considered an untargeted approach, which is not restricted to a selection of target proteins. This aspect has been taken up and emphasized by the example of chickpea seeds in the third publication (section 3.3) and is further discussed in the results section 2.1.3.

General possibilities and challenges in MS imaging of proteins were reviewed by Han et al.⁴⁰ Specifically for plant tissues, Grassl et al. provide practical aspects to consider for sample preparation and *in situ* digestion.²⁷ For instance, enzymatic digestion is usually preceded by washing steps to prevent denaturation or deactivation of the proteolytic enzymes used as well as to prevent ion suppression effects exerted by salts, lipids and saccharides (the latter mostly in plant tissue).²⁴ With this, however, comes the risk of decreased spatial resolution due to analyte diffusion, which is one of the major challenges in bottom-up protein MS imaging. Therefore, to minimize this risk and to avoid analyte loss, washing protocols should be kept as short as possible²³ and enzyme (spray) application parameters need to be optimized thoroughly. Further general technical aspects, which are also applicable for protein MS imaging, have already been addressed in the previous section.

1.1.5 Data analysis

As with sample preparation, there is no generally harmonized procedure for data analysis in MS imaging; instead, it needs to be tailored to the specific research question to be answered and might include

additional calculations, quality control steps or statistical analyses. The essential steps in data analysis, which have been applied to experiments as part of this work, are briefly described in the following.

Digital microscopy was used for quality control during sample preparation, so as to verify section integrity, the morphology of matrix crystals or the laser burn pattern after the measurement. Furthermore, overview images were recorded since ion images are typically compared to a corresponding optical image of the sample by superimposition or juxtaposition. After every MS imaging experiment, proprietary Thermo Fisher Scientific ‘RAW’ data were converted into the open file format imzML⁴¹ using open access imzML converters, e.g., the jimzml converter.⁴² Validation of the created imzML files was done using imzML Validator⁴³ to complement the imzML data file with additional information necessary for data analysis and further processing. Ion images of a defined bin width (± 3 ppm) were generated based on the imzML file using MSiReader,⁴⁴ SpectralAnalysis⁴⁵ or Mirion;⁴⁶ the latter was also able to process RAW data directly and was further used for the generation of 3D ion images. Complementary MS/MS measurements were analyzed and processed using Thermo XCalibur QualBrowser.

If in a measurement the total ion current (TIC) is expected (or encountered) to be substantially susceptible to the sample morphology, normalization methods should be applied to MS imaging data to at least partially account for such effects.⁴⁷ For instance, normalization to the TIC is necessary for heterogeneous samples such as highly processed food comprising multiple ingredients (see second publication, section 3.2). This function is available in all mentioned MS imaging data processing tools. Whenever the generation of MMA plots was conducted for the verification of satisfactory mass accuracy, the in-house programmed software ‘imzML Analyzer’ was chosen.⁴⁸ Apart from the already mentioned generation of ion images, SpectralAnalysis⁴⁵ was used as a basis for the semiautomatic penetration tool (next to a dedicated MATLAB program) presented in the first publication as well as for the creation and export of regions of interest in the second publication.

For the identification and visualization of proteins from MS imaging data, as done for the third publication, a dedicated data analysis approach was necessary. This was supported by a series of in-house coded programs currently under development in Prof. Römpp’s group. Based on a list of peptide candidates, a protein identification strategy including both spatial patterns and the assignment of peptides to their corresponding proteins was used, which was conceived by Prof. Römpp.²¹ The Excel add-in ‘Pepcalc’ was used for the calculation of molecular masses and sum formulae from peptide one-letter codes.⁴⁹ For the interpretation of tryptic peptide MS/MS spectra, mMass v5.5.0 was chosen.⁵⁰

1.2 MS imaging of food

As presented in the following sections, numerous reports on the application of MS imaging to food samples have been published within the last decade. Recent reviews summarize and categorize these applications, focusing on technical aspects,^{51,52} on target analyte groups⁵³ or specifically on (edible) plants.^{54–56} In the following subsection, fundamental motivations for the use of MS imaging for food samples are discussed, followed by the presentation of selected applications, with a general differentiation between unprocessed/raw food (crops) and processed food of animal and plant origin.

1.2.1 Motivations for MS imaging of food

Mass spectrometry in general is extensively used as an analytical technique to ensure food safety.¹⁷ Indeed, food safety is an important motivation for researchers to use MS imaging and is commonly referred to in publications.^{57–60} In the context of food safety, there are various types of undesired compounds which need to be regulated and controlled. These mainly include residues^{f1}, such as pesticides and veterinary drugs, and contaminants^{f2}, which in turn can be subdivided into heavy metals (e.g., lead, cadmium), agricultural contaminants (e.g., mycotoxins, pyrrolizidine and tropane alkaloids), process contaminants (e.g., nitrosamines or acrylamide) and persistent environmental contaminants (e.g., dioxins or per- and polyfluorinated alkyl substances). Distribution analyses of such undesired compounds in food can be

^{f1}Regulation (EC) 1107/2009 of the European Parliament and of the Council of 21 October 2009 concerning the placing of plant protection products on the market and repealing Council Directives 79/117/EEC and 91/414/EEC

^{f2}Council Regulation (EEC) 315/93 of 8 February 1993 laying down Community procedures for contaminants in food

valuable in addition to quantitative information from homogenates whenever the substances in question are expected to be inhomogeneously distributed or even concentrated in hotspots. This added knowledge may help manufacturers in optimizing production processes for an effective reduction of exposure. For instance, by imaging pesticide distributions in/on crops, a possible reduction potential could be assessed on a sub-millimeter scale, thereby simultaneously considering sufficient surface treatment and avoiding diffusion into the mesocarp. In case of contaminants, distribution analyses could contribute to the optimization of food processing steps, as described by example of acrylamide in gingerbread in the second publication (section 2.1.2), or to assess a possible post-harvest removal of contaminated crop parts. For all these applications, MS imaging may be the method of choice, especially when distributions cannot be easily elucidated by sample dissection and separate analysis due to small-scale (approximately $< 5\text{ mm}$) and/or complex distributions or when analytes are difficult to detect by spectroscopic imaging techniques. To date, spatial distributions of undesired compounds in food are investigated solely out of scientific interest. Even though in the European Union (EU) legal norms have been adopted for residues and contaminants, they focus very strongly on concentrations in the homogenate, but scarcely take spatial distributions into account. Given a widespread equipment of food authorities (and commercial food laboratories) with MS imaging instrumentation, legal requirements could be defined in a more differentiated manner than by merely laying down overall concentration limits, particularly in food comprising non-edible parts, such as rind, peel, coating, etc.

Next to food safety, motivations for food quality and authenticity spark the development of MS imaging methods. Biomarker distributions could for example be used to determine food quality or the geographical origin of crops. The detection of transglutaminase-treated meat products based on different constituents' distribution patterns constitute a conceivable MS imaging application for food authenticity reasons. A recent study used MS imaging to differentiate the type of farming (e.g., wild vs. farmed animal products, further discussion see section 1.2.2). In food technology as well as nutritional sciences, knowledge about the location of desired/beneficial constituents, such as nutrients, vitamins, phytochemicals, or minerals, can be helpful, especially in the context of food processing to prevent the loss or degradation of such substances.

In the field of agricultural sciences, understanding metabolic processes through spatiotemporal changes in plant seeds and sprouts during dormancy and/or germination is a typical motivation to use MS imaging²² (for further details, see section 1.2.2). Other examples might be the investigation of metabolic responses to wounding or other types of stress induced in food crops or insights into molecular changes between transgenic and wild agricultural products, e.g., spatial differences in the proteome subsequent to genetic modification. Most commonly, such studies aim to make food crops more resistant to external (phytosanitary, climatic or other) influences or to increase their yield. However, by use of MS imaging, also the interfaces to food safety and nutrition could be examined when it comes to health- or nutritionally relevant changes in constituents' distributions as a result of genetic modifications.

Recently, the application of MS imaging for food microbiology has been advocated for in a review article by Zou et al.⁶¹ Possible applications might be the detection and identification of desired and pathogenic microorganisms directly in/on food (surfaces), on food surface blots or crude extracts. Time-consuming cultivation of such microorganisms could be shortened if by MS imaging colonies of less than 1 mm in diameter can be identified, localized and counted directly on the sample surface (e.g., broiler skin) in a spatially resolved setup.

As presented in the first publication (section 3.1), MS imaging offers the possibility to visualize a very large range of chemical compounds in one measurement, which can help in identifying relations/interferences of different compounds without prior knowledge ('untargeted'). Thus, irrespective of the listed fields of research, MS imaging can be beneficial for explaining molecular processes underlying observed phenomena.

1.2.2 Applications in food crops and raw food materials

The vast majority of MS imaging applications in food have dealt with unprocessed^{f3} food materials or food crops. Although the term ‘food MS imaging’ might indicate that actual food is sampled, it is often not edible parts which are chosen as target samples, but for instance other plant organs or crops at an early development stage. This wide definition of the term ‘food MS imaging’ is important to keep in mind and is a result from the various motivations for MS imaging in the food context (see section 1.2.1). A selection of applications using actual food as a sample is provided in Table 1, in conjunction with the respective predominant motivation and analytical technique.

Table 1: Selection of MS imaging applications on unprocessed food, subdivided by plant/animal origin and the predominant motivation brought forward in the respective publications.

	Predominant motivation	Sample	Analytes	Technique	Reference
Plant food	Agricultural sciences	wheat seed	lipids, carbohydrates	MALDI-Orbitrap MS imaging	22
		nightshades	metabolites	MALDI-TOF MS imaging	62
		green and red tomato	tomatine, esculeoside A	MALDI-TOF MS imaging	63
		tomato	steroidal glycoalkaloids	MALDI-FT-ICR MS imaging	64
	Food safety	rye ergot body	ergot alkaloids	LAESI-TOF MS imaging	57
		potato tuber	glycoalkaloids	MALDI-TOF MS imaging	58
		soybean seed and sprout	organochlorines	MALDI-TOF MS imaging	59
		cucumber	procymidone	nano-PALDI-FT-ICR MS imaging	60
	Nutritional sciences	grape	nutrients, anthocyanins	MALDI-Orbitrap MS imaging	28
		barley grain	Fe, Zn	LA-ICP MS imaging	65
nuts		lipids	DESI- IM-TOF MS imaging	24	
Animal food	Food authenticity	sea bream (fish)	anserine, carnitine	MALDI-TOF MS imaging	66
	Food quality	bovine muscle	phospholipids, triglycerides, cholesterol	MALDI-TOF MS imaging	67
	Nutritional sciences	raw pork chops	phosphatidylcholines	MALDI-TOF MS imaging	68
		raw broiler meat	cholesterol, vitamin E	TOF-SIMS	69

Studies from the perspective of agricultural sciences predominantly investigated the influence of plant development, fruit ripening, stress induction or genetic modifications on the distribution of value-determining constituents/metabolites or marker compounds. The first MS imaging study with high mass resolution ($R > 50,000$ at m/z 200) and high spatial resolution in plants was conducted by Prof. Römpp’s

^{f3}The term ‘unprocessed’ is used according to the definition in Art. 2 No. 1 lit. n Regulation (EC) 852/2004 of the european parliament and of the council of 29 April 2004 on the hygiene of foodstuffs

group using wheat seeds, oilseed rape and rice roots.²² Especially in agricultural sciences, analyses often include non-edible parts of crops, which are nonetheless important for holistic approaches. For instance, Bhandari et al. investigated the pathosystem of wheat stems and the fungus *Fusarium graminearum* after inoculation of young roots.⁷⁰ From the food safety perspective, studies mainly investigated edible parts of food or spatially close parts with a risk for contamination, e.g., ergot alkaloids in rye ergot bodies.⁵⁷ As mentioned in section 1.2.1 as well as the first and second publication, analytical targets are mostly undesired compounds, such as contaminants^{71,72} and residues.^{59,73} Interestingly, already the first report on MS imaging in plant science used the technique to study pesticide uptake into soy plants.⁷⁴ Nutritional science studies mainly focus on the elucidation of nutrient distributions in ripe fruit/cereals or raw meat. Occasionally, scientists investigated samples in different ripening stages with regards to nutrient distributions.⁶⁵ Such applications are, however, often closely related to agricultural sciences and sometimes not unequivocally classifiable. For food authenticity reasons, Goto-Inoue et al. applied MS imaging for the differentiation of wild and farmed sea fish based on the well-known marker compounds anserine and carnitine.⁶⁶ Moreover, they suggest the use of biomarkers' distributions for determining the geographic origin of fish samples. Yet, the added value of MS imaging compared to quantitative MS of dissected red and white muscle tissue does not entirely come across in this study. Dyer et al. used MS imaging to determine the food quality of bovine muscle tissue.⁶⁷ Distributions of phosphatidylethanolamines and lysophosphatidylcholines revealed oxidative degradation mechanisms that progress from the outer parts into the interior of the muscle.

MS imaging of proteins in food has already been mentioned as a challenging task from a technical point of view. Publications on MS imaging of proteins in food of animal origin are difficult to find, because samples such as mouse kidney are not considered food but model tissues for proof-of-concept studies. The emphasis of such studies often lies in technical aspects, such as method development and/or validation. In food of plant origin, few studies were published applying MALDI-TOF MS imaging at low mass resolution for the detection of small proteins: Cavatorta et al. showed the distribution of Pru P3 allergen protein (approximately 9 *kDa*) in peach peel, which constitutes a typical food safety topic.⁷⁵ In tomato, distributions of small lipid transfer proteins (7 – 9 *kDa*) were detected.⁷⁶ A recent study used protein fragments (10 *kDa*) to obtain spatial information on proteins in soybean.²⁶ A notable exception regarding the protein size is a recent publication using caffeic acid as a matrix for top-down MALDI-TOF MS imaging of large proteins (up to 200 *kDa*) in germinating soybeans.⁷⁷ In section 2.1.3 and the third publication, these publications are put into context with regards to protein identification strategies.

1.2.3 Applications in processed food of animal and plant origin

The term 'processing' in this dissertation conforms to the legal definition laid down in Regulation (EC) 852/2004^{f4} as „any action that substantially alters the initial product“, including, inter alia, heating, curing, maturing, drying and extraction. In general, processed food has scarcely been subject to MS imaging studies so far. With respect to sample preparation, processed food often poses a greater challenge due to an altered texture resulting from the mixture of multiple ingredients, processing and/or preparation steps. Especially for a reliable detection of minor compounds, such as most food additives, residues, contaminants, or low abundant constituents in complex processed food, high mass resolution and mass accuracy are often crucial to ensure sufficient selectivity.

The first reported application of MS imaging of processed food used an in-house built gas desorption unit coupled to an atmospheric pressure chemical ionization (APCI) source and a linear ion trap mass spectrometer to generate an MS/MS image of the contaminant melamine on a cross-section of cooked egg with an approximate pixel size of 250 μm .⁷⁸ Dry-cured ham muscle is another type of processed food subject to MS imaging investigation. Though dry-curing substantially changes the texture of ham, it is still suitable for sectioning in a cryomicrotome. In two publications, endogenous peptides were measured and visualized by MALDI-TOF MS imaging to evaluate peptide oxidation⁷⁹ and proteolytic activity⁸⁰ as food quality parameters within such muscle tissue. Roasted coffee beans are an example for processed food, which cannot be sectioned in a cryomicrotome due to their hard and brittle texture. Instead, Fowble et al. used razor blades to cut the samples into halves and measured the uneven cutting planes

^{f4}Art. 2 No. 1 lit. m Regulation (EC) 852/2004 of the European Parliament and of the Council of 29 April 2004 on the hygiene of foodstuffs

using laser ablation direct analysis in real time (DART)-TOF MS imaging to trace volatile compounds.³³ Lastly, a recent article by Cao et al. claimed to conduct MALDI-TOF MS imaging of vegetable oils for authentication.⁸¹ Though vegetable oils are doubtlessly processed food and the shown mass spectrometric analyses of lipids appear to be scientifically substantiated, no spatial information is provided in the results and thus there is no difference to standard MALDI MS. In a recent review on MS imaging of insects, the authors directly refer to possible future applications with edible insects in the context of food safety.⁸² Although the review does not list publications on insects which are currently admitted as novel food in the EU, it argues that MS imaging can provide valuable information on metabolites' distributions in insects. This might spark new applications for edible insects in the future. These few examples demonstrate that MS imaging of processed food, particularly with high mass resolution and mass accuracy, is a scientific niche that has yet to be fully explored and the results presented in the first and second publication (sections 3.1 and 3.2) are pushing the boundaries of the field.

1.3 Previous work and status built upon

While the presented work on food MS imaging and the resulting publications describe considerable improvements in terms of practical aspects of sample preparation as well as the scientific results of the experiments performed, needless to say it benefited greatly from the valuable experience of the work group around Prof. Römpp in MS imaging of biological samples over the past decade.^{11,83} Since large parts of the work for this dissertation concentrated on food of plant origin, the work group's profound experience on the preparation and measurement of plant (food) samples^{22,28} was particularly valuable. For successful and high-quality MALDI MS imaging experiments, many key prerequisites have been addressed by (former) colleagues without which the described achievements would not have been possible. Starting with the provided MS imaging instrumentation, the considerable development work of Prof. Spengler's work group in Giessen, including Prof. Römpp at that time, resulted in the unique high-resolution AP scanning microprobe MALDI source, which was later commercialized by TransMIT GmbH. The AP-SMALDI source is known for its applicability at high spatial resolution down to a few micrometers pixel size for a vast range of samples, especially for complex and delicate biological samples both of animal origin (e.g., down to 10 μm in mouse kidney,⁸⁴ 5 μm in mouse lung⁸⁵ and 5 μm in zebrafish⁸⁶) as well as samples of plant origin (e.g., 10 μm in roots of peony⁵² and down to 5 μm in wheat seeds²²). In combination with Orbitrap MS instruments working at high mass resolution (R typically 240,000 at m/z 200) and mass accuracy (RMSE < 1.5 ppm), the resulting setup provides both high lateral resolution and high mass resolution, which is a key element in the work of Prof. Römpp's group and became known as „high resolution in mass and space (HR²)“ MS imaging.^{11,84} The broad applicability of these developments offer the possibility for a systematic transfer to other types of challenging samples and/or analytes and built the foundation for the achievements described in this dissertation. Profound preliminary work on internal mass calibration for MALDI MS imaging was helpful to ensure high mass accuracy.¹²

The first Orbitrap-MS imaging experiments of peptides following tryptic digestion of mammalian tissues by Schober et al. provided important findings, especially on the necessity of high mass accuracy and mass resolution for reliable bottom-up proteomics in MS imaging as well as the beneficial effect of complementary LC-MS/MS measurements for protein identification.^{13,39} Moreover, these and following efforts on manual trypsin spray application for mammalian tissue^{21,87} laid the basis for the successful development of a sample preparation workflow for plant tissue, including an automated trypsin spray method, as presented in the third publication. The chosen strategy for protein identification profited from profound development work and findings from experiments on mammalian tissues.²¹

To handle MS imaging data and perform in-depth data analysis as described in section 1.1.5, the common open-source data format (imzML) was co-developed by Prof. Römpp and contributed to the standardization and consolidation of MS imaging data, irrespective of the initial proprietary instrument software.^{41,88} Lastly, powerful and partially tailor-made software solutions for handling data presented in the publications were developed by (former) colleagues, enabling conversion⁴² and validation⁴³ of imzML data as well as profound data visualization⁴⁵ and analysis.⁴⁸

2 Results

2.1 Synopsis

This dissertation constitutes a compilation of three scientific publications, which have all been accepted and published in renowned, peer-reviewed journals. Towards the overall goal of demonstrating the analytical potential of MALDI MS imaging for the field of food analysis, these three publications highlight multiple key aspects:

In the first publication, MALDI MS imaging is presented to the food science community as a versatile analytical technique for a wide range of food samples supported by dedicated workflows and data analysis approaches for fresh and processed food samples of plant and animal origin. Both major constituents, such as carbohydrates, lipids and phytochemicals, as well as minor compounds underlying legal regulations, such as a food contaminant and a food additive, have been selected as target analytes for investigation and visualization.

Highly processed food can be very challenging for successful MALDI MS imaging analysis. In the pursuit of developing the analytical technique for its application not only for scientific reasons, but also by manufacturers and food authorities, it is necessary to find new ways to overcome such difficulties posed by ‘real-life’ samples. Expanding upon the first MALDI MS imaging measurement of acrylamide in German gingerbread in the first publication, several decisive methodological advancements, in-depth data analysis steps and practical aspects of quality control in MS imaging are presented in the second publication.

Proteins constitute a challenging, but no less important group of analytes in food; motivations for investigation of their distributions reach from nutritional studies to health-relevant food safety issues. Since reports on protein distributions in plant tissue using MS imaging are scarce and restricted to top-down measurement settings and/or low mass resolution, a high-resolution MALDI MS imaging method for the spatially resolved ‘bottom-up’ identification of proteins in plants was developed by example of chickpea seeds in the third publication. The developed workflow was finally used for the food safety-related investigation of the toxic protein abrin in seeds of crab’s eye vine.

A detailed description of all three publications is given in the following subsections of this synopsis, pointing out the respective motivations, methodological approaches and scientific results. Subsequent to the scientific manuscripts including supplementary information in section 3, general concluding remarks and an outlook based on the findings of all publications are provided in section 4.

2.1.1 MALDI MS imaging of various substance classes in fresh and processed food

The following details are part of the first publication entitled *„MALDI mass spectrometry imaging: from constituents in fresh food to ingredients, contaminants and additives in processed food“*.

In this study, MALDI MS imaging is portrayed as an analytical method for food samples. It demonstrates the versatility of high-resolution MALDI MS imaging for the visualization of constituents, ingredients, contaminants and food additives. The selection of food matrices spans food of plant and animal origin as well as both fresh/unprocessed and processed food. For each food category in conjunction with the target analytes, an MS imaging workflow was optimized and tailored sample preparation protocols are presented to meet the specific sample properties and challenges.

By means of a MALDI MS imaging analysis of hardy kiwi (*Actinidia arguta*), which is a grape-sized hairless fruit of green colored peel and flesh, the basic measurement and data analysis procedure was explained (see Figure 4). A thin section of 30 μm was produced in a cryomicrotome and covered with DHB matrix prior to the measurement with a step size of 45 μm and a mass range of m/z 250–1000. The MS signals of three representative constituents of different molecular structures and physicochemical properties, namely disaccharides as a carbohydrate, quercetin as a phytochemical/polyphenol and the lipid glyceryl trilinolenate TG(54:9), were chosen for the generation of ion images. As shown in single ion images in Figure 4, the lipophilic triglyceride proved to be present exclusively in the interior of the seed while quercetin was detected in the peel and disaccharides were highly abundant in the pericarp.

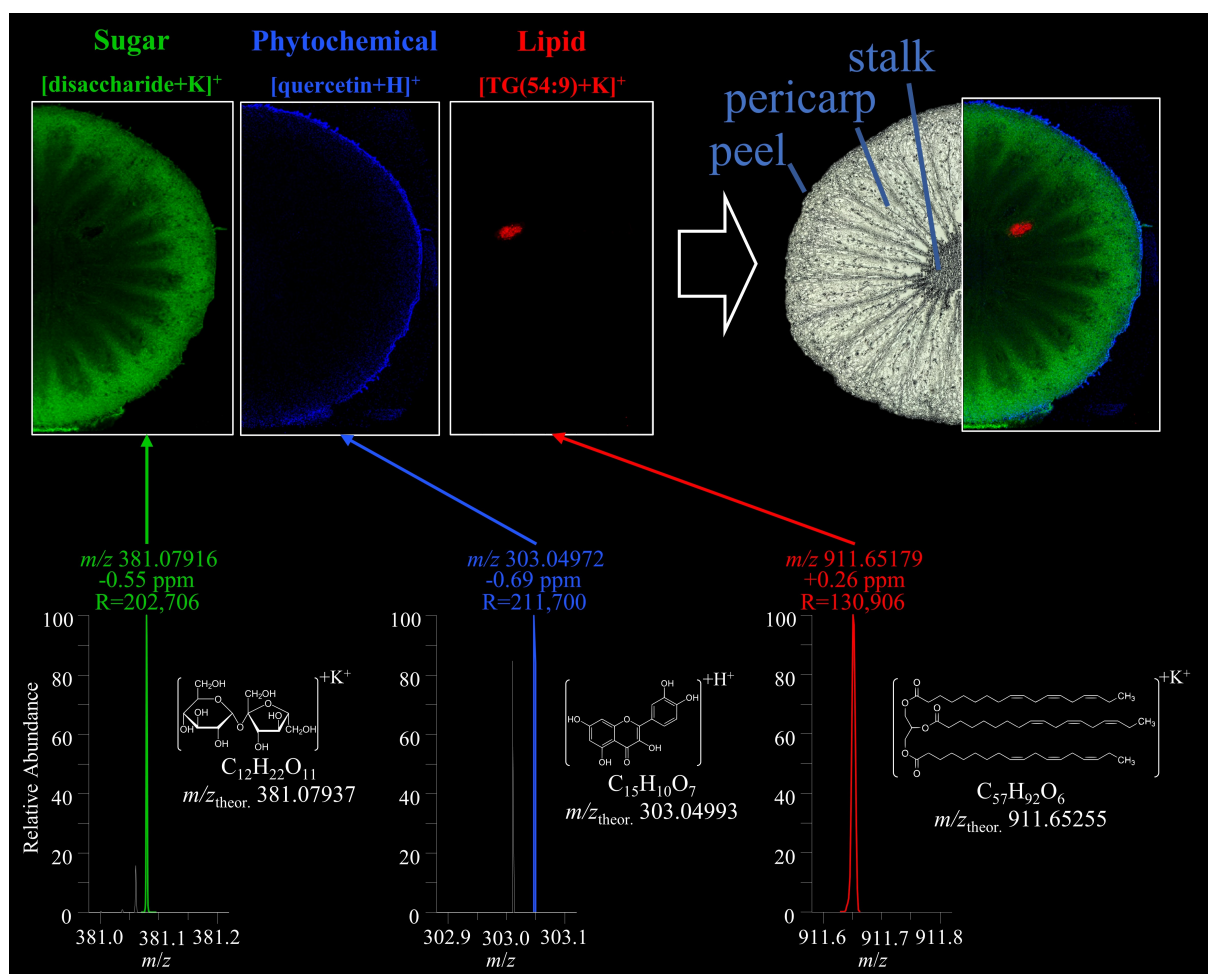


Figure 4: Basic MS imaging data analysis protocol by example of hardy kiwi (*A. arguta*), following up the sample preparation and measurement workflow described in section 1.1.4. Single pixel mass spectra of three candidate signals are displayed with the corresponding relative mass errors, mass resolutions R and molecular structures. Upon selecting a target m/z -value, analyte peaks are retrieved from all mass spectra and processed into an ion image with the brightness reflecting peak intensities. Ion images normalized to the TIC were generated for the lipid TG(54:9) K-adduct (red), the phytochemical quercetin (blue) and disaccharide K-adducts (green). Note that the structure of sucrose is displayed exemplary for the green signal, although the ion image includes all disaccharide K-adducts with the respective sum formula. Single ion images can be overlaid in an RGB ion image and juxtaposed with a microscopy image.

A red, green and blue (RGB) overlay of those three ion images and co-registration with the microscopic image of the hardy kiwi demonstrated the possibility to link the distributions of mass spectrometric signals to anatomical structures such as peel, pericarp, seeds or stalk. Besides, the respective values for mass resolution R (FWHM) and relative mass deviation (in ppm) were provided in the mass spectra to introduce the terms and illustrate their significance for highly selective data visualization.

Carrots (*Daucus carota*) have been chosen as representatives for raw food of plant origin with optically visible structures of β -carotene and, in case of purple carrots (*Daucus carota* ssp. *sativus* var. *atrorubens* Alef.), anthocyanins. The well-known provitamin β -carotene, which is abundant in orange carrots, is a challenging analyte due to its highly nonpolar structure and thus a low ionization efficiency with MALDI ionization. Nonetheless, the radical cation of β -carotene could be detected and a successful retention of the spatial distribution was observed when compared to the microscopic image (Figure 5A). In purple carrots, the visible coloring of the outer core and cortex could be reproduced by visualizing cyanidin as a representative anthocyanidin (Figure 5B). Also structures invisible to the naked eye can be unraveled using MS imaging, which was demonstrated by means of German veal sausage as an example for processed food of animal origin with a dramatically altered texture compared to the primary ingredients (e.g., trimmed

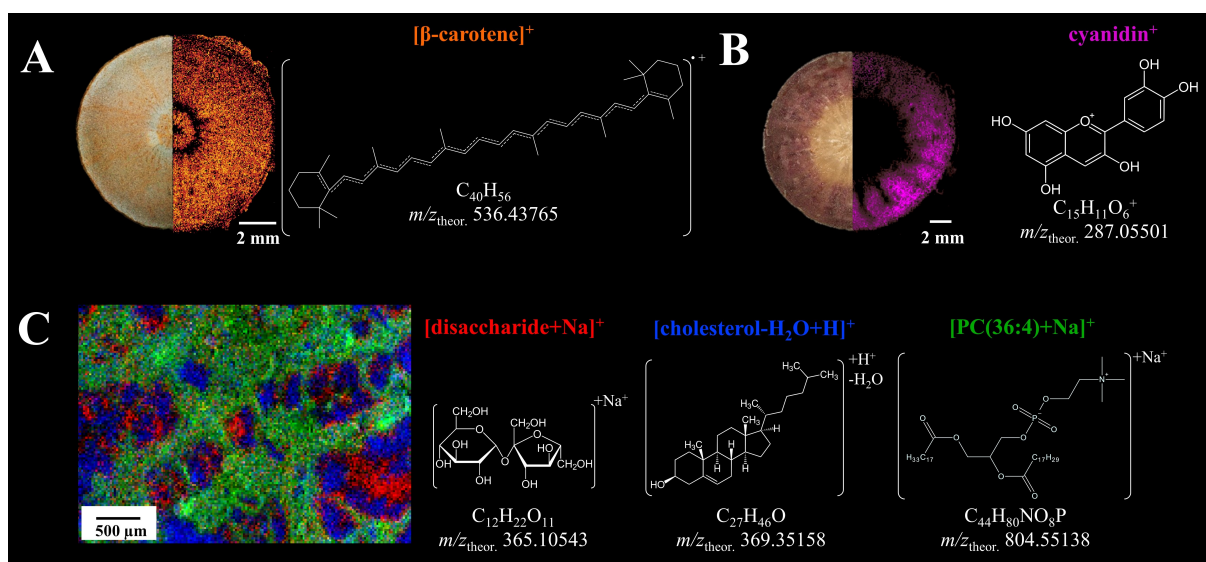


Figure 5: MALDI MS imaging of constituents in fresh food (carrots, **A** and **B**) and processed food (veal sausage, **C**). **A, B:** Juxtaposed microscopy images with the respective ion images of β -carotene in orange carrot and cyanidin in purple carrot, each with the respective molecular structures. **C:** RGB overlay and molecular structures of constituents of varying polarity in German veal sausage: Disaccharide Na-adducts (red), cholesterol ($[M - H_2O + H]^+$, blue) and PC(36:4) Na-adduct (green). Note that the structure of sucrose is displayed exemplary for the red signal, although the ion image includes all disaccharide Na-adducts with the respective sum formula.

veal, high-fat pork, bacon, herbs and spices). Water-soluble regions could be clearly distinguished from fat-soluble areas by visualization of lipophilic and hydrophilic constituents as marker compounds. In an RGB overlay shown in Figure 5C, signals of disaccharides and cholesterol showed nearly complementary distributions while the signal of phosphatidylcholine PC(36:4) covered the entire surface. Moreover, herbal particles could be highlighted within the sample by tracing chlorophyll derivatives as characteristic markers for plant material; corresponding ion images are presented in the publication's supplementary material.

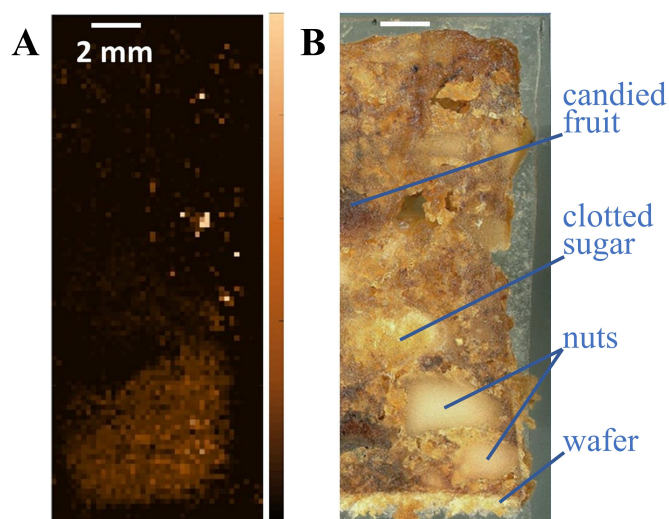


Figure 6: MALDI MS imaging of the process contaminant acrylamide in traditional German gingerbread as an example for highly processed food. **A:** Single ion image of protonated acrylamide, m/z 72.04439, pixel size 200 μm . **B:** Microscopy image of the measured section with annotated ingredients.

Traditional German gingerbread as an example for highly processed food of plant origin is prone to the formation of the carcinogenic process contaminant acrylamide. A highly contaminated gingerbread

sample was acquired from the Bavarian Health and Food Safety Authority (LGL) and used for the first application of MS imaging for a contaminant in processed food. Technical aspects regarding the sectioning method, matrix application and laser energy were reported. A novel sectioning method was introduced using an electric cutting disk since gingerbread is impossible to cut in a cryomicrotome due to its brittle texture. This cutting method produced stable sections of approximately 2 mm thickness. The remaining unevenness of the surface, however, influences the ionization efficiency during the MALDI process when a fixed laser focus is used. This variation was reduced by setting a larger laser ablation area (defocused) and choosing the average distance between laser optics and the lowest vs. highest spot on the uneven sample surface. Acrylamide signal intensities could be increased by doubling the number of laser pulses per pixel (60 compared to 30 for other measurements) together with an increased C-trap injection time of 1000 ms. Two alternating scan intervals of m/z 50–165 and m/z 250–1000 were set within one measurement, with a final pixel size of 200 μm . From these datasets, distributions of disaccharides and acrylamide were visualized. While disaccharides were present throughout the sample surface, increased acrylamide abundances were found in regions of and around nut fragments close to the wafer (see Figure 6). These results lead to the assumption that proximity to the baking tray might promote the formation of acrylamide; yet, this assumption sparked further investigations into the distribution of acrylamide in gingerbread, which are described in the second publication (section 3.2) and in section 2.1.2.

By example of Gouda cheese as processed food of animal origin, an MS imaging workflow was developed with the aim of detecting and visualizing the antifungal preservative natamycin (molecular structure and sum formula see Figure 7A), a food additive which is admitted for Gouda as a semi-hard cheese with a maximum level of 1 mg/dm^2 and a penetration limit of 5 mm from the surface^{f5}. Next to characteristic compounds for coating layers and cheese bulk, signals of protonated natamycin and its Na-adduct were detected, whereas the natamycin Na-adduct was the most abundant (Figure 7B). Its identity was confirmed by matching MALDI-MS/MS analyses on Gouda cheese and on natamycin standard. Natamycin proved to be present on the surface and a certain distance into the cheese bulk. To accurately determine the penetration depth of natamycin into the cheese independent of the surface topography, and to thereby validate the existing official method based on high-performance liquid chromatography coupled to diode array detection (HPLC-DAD)^{f6}, a versatile penetration analysis tool was developed in MATLAB (R2016b). In a multi-step protocol, the matrix edge (in this specific case the cheese edge) is determined based on a reference signal (e.g., a characteristic cheese lipid, Figure 7C) prior to the calculation of mean intensities for a target signal (in this case natamycin, Figure 7D) for all pixels with the same lateral distance from the edge (Figure 7E). By plotting these intensity values against the distance from the edge into the cheese bulk, the diffusion behavior of a target signal can be investigated (Figure 7F). In case of natamycin, signal intensities in four cheese samples decreased exponentially and penetration depths did not exceed 1000 μm . By this first report of a food additive’s distribution by MS imaging, knowledge about the diffusion behavior of natamycin into cheese could be expanded. These results could, in a next step, contribute to the discussion about updating the natamycin maximum level and/or the penetration limit laid down in Regulation (EC) 1333/2008^{f7}.

To sum up, this publication constitutes a compilation of MALDI MS imaging approaches for very different kinds of food matrices as well as both endogenous and exogenous target compounds. In general, dedicated workflows needed to be developed for each type of food due to varying physicochemical properties; particularly processed food proved to pose a higher challenge due to brittle texture and/or the presence of multiple ingredients. In samples of hardy kiwi, carrots and German veal sausage, both highly nonpolar and polar constituents could be detected, and their spatial distributions visualized. The reports on successful MS imaging of a contaminant (i.e., acrylamide in German gingerbread) and a food additive (i.e., natamycin in Gouda cheese) in processed food were the first of their kind. By example of natamycin in Gouda cheese, the penetration of a legally regulated food additive was investigated, showing that MS imaging data analysis may go beyond the mere display of MS signals in ion images and contribute to the reevaluation of legal requirements. All presented applications support the great potential of MS imaging for the field of food analysis by complementing established analytical methods

^{f5}Art. 4(1) in conjunction with Annex II Cat. 01.7.2 Regulation (EC) 1333/2008 of the European Parliament and of the Council of 16 December 2008 on food additives

^{f6}Method L 03.00–41/2 §64(1) Lebensmittel- und Futtermittelgesetzbuch (LFGB) in conjunction with technical rule L 03.00–41/2:2020–02

^{f7}Regulation (EC) 1333/2008 of the European Parliament and of the Council of 16 December 2008 on food additives

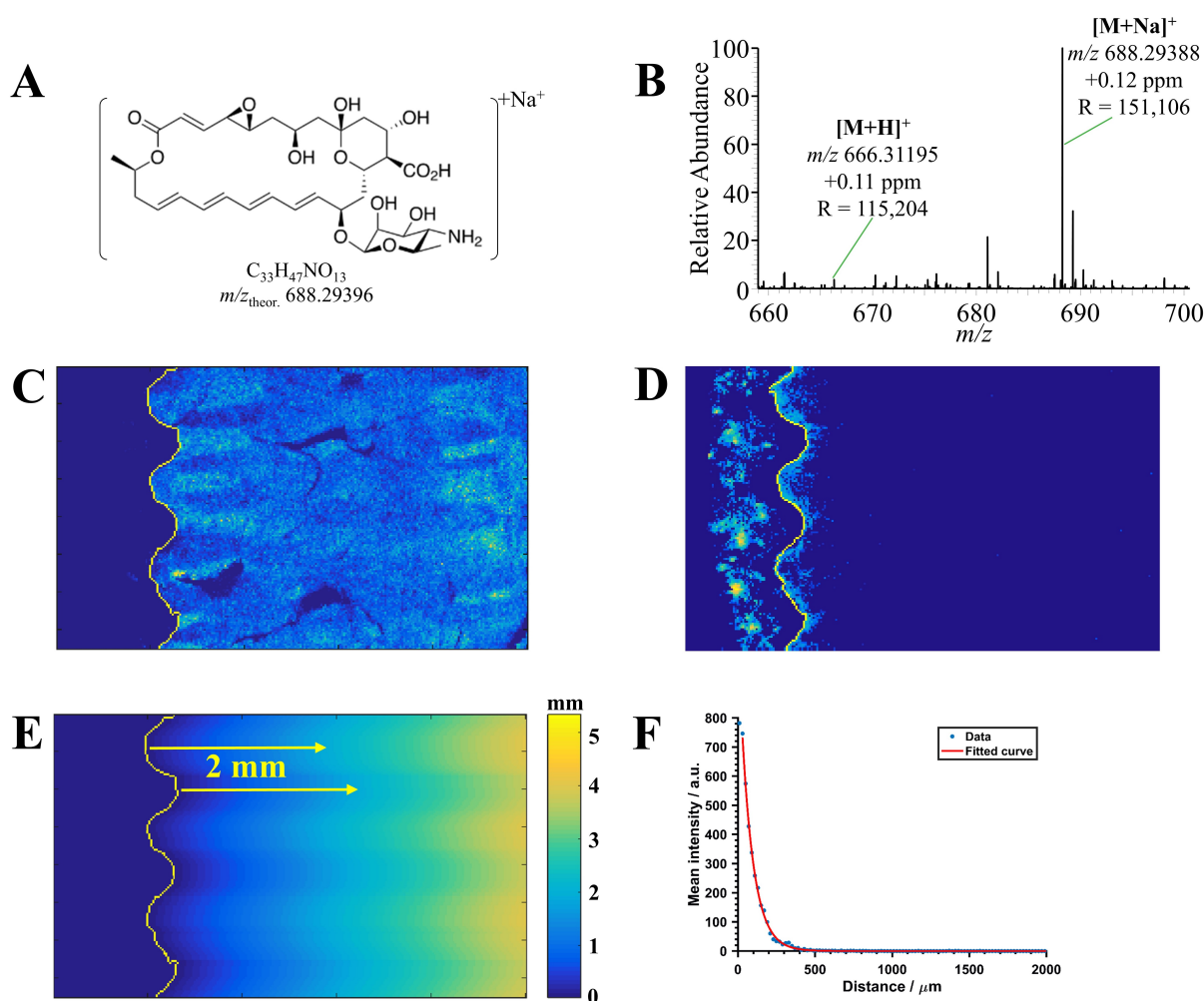


Figure 7: MALDI MS imaging for penetration analysis of natamycin into sections of Gouda cheese. **A:** Molecular structure of the detected natamycin Na-adduct. **B:** Single pixel MALDI mass spectrum on Gouda cheese with annotated signals of protonated natamycin ($m/z_{theor.} = 666.31202$) and natamycin Na-adduct ($m/z_{theor.} = 688.29396$) with the corresponding relative mass error and mass resolution R . **C:** Ion image of sphingomyelin SM(d34:1) Na-adduct, $m/z_{theor.} = 725.55680$ and resultant calculated cheese edge highlighted in yellow. **D:** Ion image of natamycin Na-adduct and calculated cheese edge from **C**. **E:** Distance map from the edge into the cheese bulk for the calculation of penetration depth values. **F:** Plot of mean natamycin intensities against the distance from the edge ('penetration plot') including exponential fit displayed in red.

and provide the impetus towards an implementation of MS imaging methods for substances underlying legal regulations.

2.1.2 Autofocusing MALDI MS imaging for food with uneven surfaces

The following details are part of the second publication entitled „Autofocusing MALDI MS imaging of processed food exemplified by the contaminant acrylamide in German gingerbread“.

For the carcinogenic process contaminant acrylamide, several international legal norms have been established in the last years aiming to mitigate its exposure to consumers by effective reduction strate-

gies^{f8,f9,f10,f11}. For the evaluation of such strategies, however, it is not only quantitative data in homogenized samples, but also the contaminant’s spatial distribution and knowledge about possible hotspots, which are of interest to manufacturers, food safety authorities and legislative bodies. Therefore, building on the foundations laid in the first publication and under particular consideration of high selectivity in detection, a detailed workflow for the preparation and measurement of traditional German gingerbread as an example of brittle, inhomogeneous processed food using MALDI MS imaging is reported. For this purpose, a decisive new development was the autofocusing function prior to AP-SMALDI ionization, which may account for sample height variations and enables MS imaging with a consistently focused MALDI-laser despite uneven surfaces.

Table 2: Overview of methodological details in sample preparation and measurement of traditional German gingerbread for the first and second publication.

First publication		Second publication	
–60 °C (sample and cutting-disk)	sectioning	–80 °C (sample and cutting-disk)	2 mm section thickness
2 mm section thickness		2 mm section thickness	
30 mg/ml DHB	matrix spray	40 mg/ml DHB	automated spray
70 % acetone + 0.1 % TFA		50 % methanol + 0.4 % TFA	
semiautomatic spray			
AP-SMALDI10 source	MALDI process	AP-SMALDI5 AF source	100 µm pixel size
nitrogen laser, 337 nm		solid-state laser, 343 nm	
fixed MALDI-laser		autofocusing MALDI	
60 laser pulses		50 laser pulses	
1000 ms injection time		500 ms injection time	
200 µm pixel size			

Methodological differences between the gingerbread preparation and measurement protocols of the first and second publication are summarized in Table 2. The sectioning method using an electric micro-saw, which was presented in the first publication, was further optimized with both sample and cutting disk consistently frozen at –80 °C at all times except for the immediate cutting process to avoid sample deformation and heating. 2 mm sections were produced and subjected to an automated matrix application. Unlike the semiautomatic protocol described in the first publication, here, the MALDI matrix was sprayed by a robotic device based on an array of parameters such as nozzle temperature, flow rate and nozzle velocity. The automated application procedure helps to objectify the matrix spray and improves inter-laboratory reproducibility. As a novel development for the measurement, an additional triangulation laser (AF-laser) under a 35° angle allowed for an adjustment of the MALDI-laser focus prior to irradiation of each pixel and thereby kept desorption/ionization conditions constant throughout the analysis despite a certain topography of the surface. Due to the autofocusing option, the increase of injection time and laser shots described in the first publication is no longer necessary and sufficient acrylamide signal intensity could be obtained even at smaller pixel sizes (i.e., 100 µm). Notably, this limit in spatial resolution is not caused by the instrument setup, which is known for its applications at 5 µm pixel size and below (see also section 1.3), but by the exceptionally dry gingerbread surface, which in turn requires high MALDI-laser energy settings and thus larger ablation areas. The reduction from 200 µm pixel size

^{f8}Commission Regulation (EU) 2017/2158 of 20 November 2017 establishing mitigation measures and benchmark levels for the reduction of the presence of acrylamide in food

^{f9}Commission Recommendation (EU) 2013/647 of 8 November 2013 on investigations into the levels of acrylamide in food

^{f10}Commission Recommendation (EU) 2019/1888 of 7 November 2019 on the monitoring of the presence of acrylamide in certain foods

^{f11}Food & Drug Administration. Guidance for Industry: Acrylamide in Foods. (FDA-2013-D-0715), (2013). <https://www.fda.gov/regulatory-information/search-fda-guidance-documents/guidance-industry-acrylamide-foods>.

as reported in the first publication to 100 μm resulted in a 4-fold data-per-area ratio and consequently allowed more profound (statistical) data analysis.

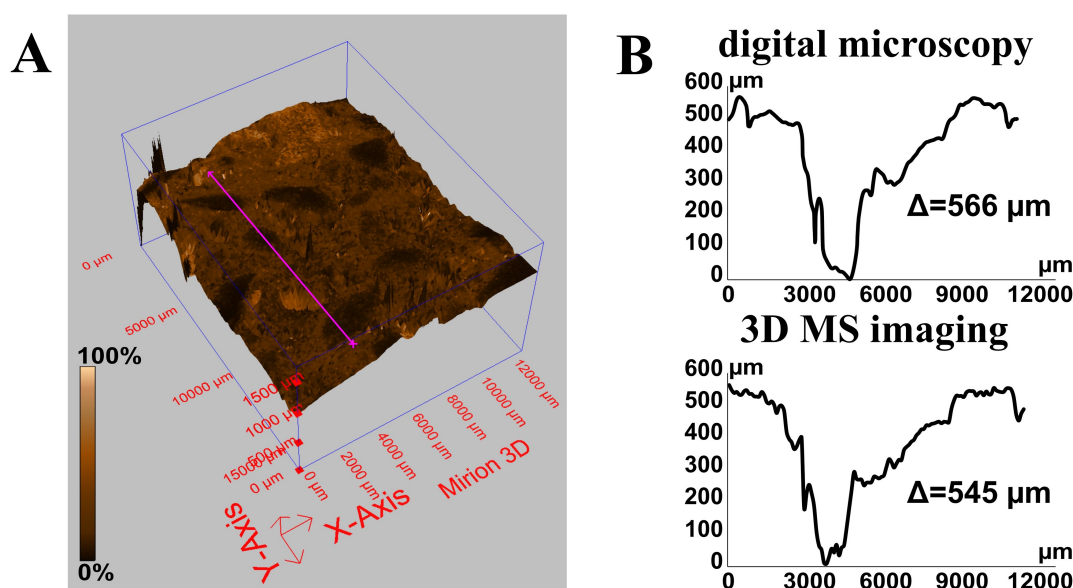


Figure 8: Autofocusing MS imaging of German gingerbread. **A:** 3D ion image of disaccharide K-adducts, m/z 381.07937, TIC-normalized. z-coordinates were retrieved from AF-laser data. The pink line represents an exemplary profile through high and low regions on the sample surface. **B:** Line scans of the surface profile and total height difference (Δ) along the pink line shown in **A**, based on digital microscopy data (top) and AF-laser data (bottom).

Using this analytical approach, constituents were visualized with higher spatial resolution and thus a substantial increase in contrast compared to previous gingerbread MS images. All measurements were carried out at high mass resolution ($R = 240,000$ at m/z 200) and mass accuracy (RMSE < 1.5 ppm). As expected, the lipophilic PC(36:3) was predominantly detected in nut fragment regions and the disaccharide signal was highly abundant throughout the measured area except for nut fragments, as shown in Figure 8A. A comparison of the topographies recorded by the triangulation laser and the digital microscope showed very good correlation, as expressed by an exemplary line scan across low and high regions on the z-axis depicted in Figure 8B. This proved that the AF-laser is a suitable tool to reliably account for height differences during the measurement.

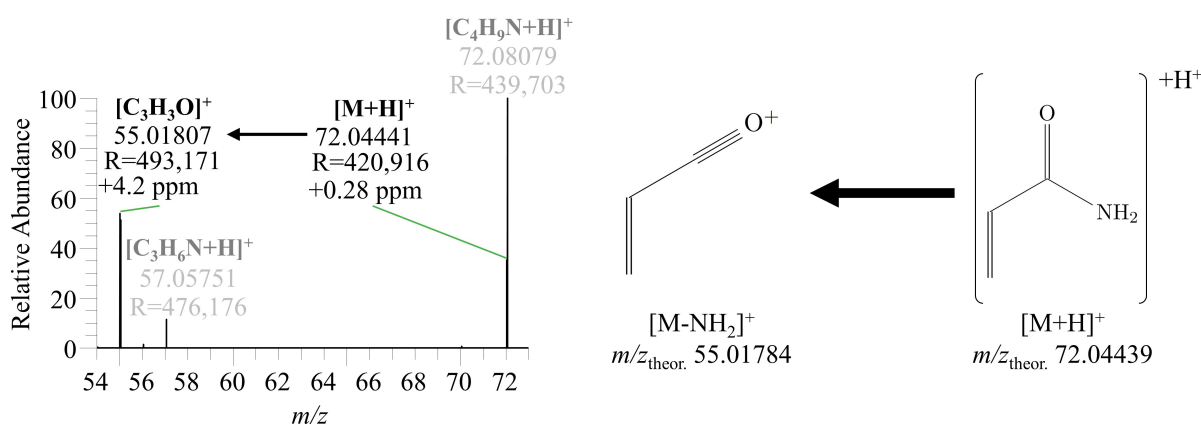


Figure 9: Representative MALDI-MS/MS spectrum and fragmentation scheme for protonated acrylamide on German gingerbread. Isolation window: m/z 72.0 ± 0.2 , scan range: m/z 50–80, HCD: 60.

With an average acrylamide concentration of 3,200 $\mu\text{g}/\text{kg}$ in the gingerbread sample, its signal was detected throughout the entire section except for a bulk of clotted sugar and within candied fruit (see

Figure 10A, B). A close neighboring peak at m/z 72.08082 to the acrylamide signal at theoretical m/z 72.04439 emphasizes the necessity of high mass resolution in this context to reliably resolve those peaks. The assignment of acrylamide to the corresponding MS signal is supported by matching MALDI-MS/MS results showing the characteristic loss of ammonia and formation of the $C_3H_3O^+$ -fragment both on gingerbread (shown in Figure 9) as well as in analytical standard. The presumption of higher signal intensities within nut fragments based on visual appearance in the MS image was further investigated by the creation of complementary region of interest (ROI) masks for nut regions and all remaining sample surface, as shown in Figure 10C, followed by a separate export and comparison of acrylamide abundance data. Indeed, nut fragments show significantly higher acrylamide intensities compared to the remaining dough (two-sided t-test, $p < 0.001$), as indicated by the boxplots provided in Figure 10D. The higher contamination of nut regions might be due to a higher content of polyunsaturated lipids and formation through the lipid pathway and/or the lower water activity combined with a higher heat capacity of nuts, fostering the formation of acrylamide.

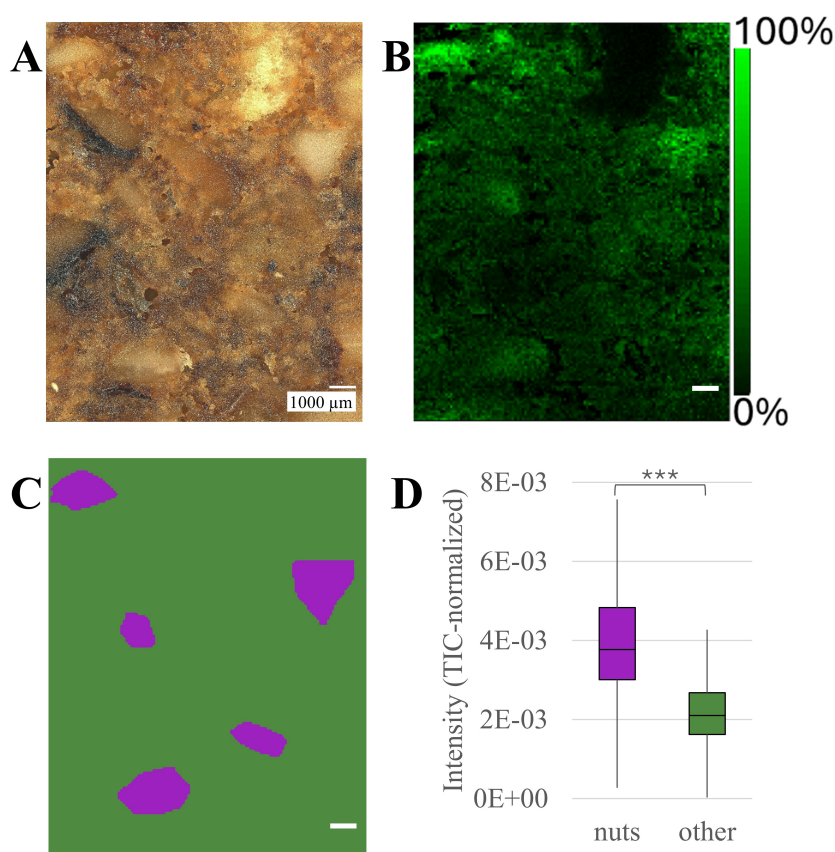


Figure 10: Distribution analysis of acrylamide in German gingerbread. **A:** Microscopy image of the measurement area. **B:** Ion image of acrylamide, m/z 72.04439, TIC-normalized. **C:** ROI-mask generated for sample surface stratification into ROI „nuts“ and „other“. **D:** Boxplots of backtransformed ($x^{0.25}$ -transformation) acrylamide abundance values for both ROI, $***t(247) = 16.93, p < .001$.

A great deal of effort has been put into the confirmation of acrylamide’s origin from the sample itself and not being an artifact resulting from sample preparation. For this, quality control aspects have been evaluated and complementary experiments were conducted: First, a putative formation of acrylamide in the course of sectioning was evaluated by measuring a gingerbread section which was cut in frozen state with a sharp knife. Since acrylamide was detected throughout this sample as well, substantial artifact formation during sectioning could be excluded. Secondly, the MALDI process was identified as a critical step of high energy deposition to surface areas which are immediately measured. The influence of MALDI on the putative formation of acrylamide was evaluated in a proof-of-concept study using the surface of freshly baked pancakes. Pancakes constitute another type of processed food prone to the formation of

acrylamide and are listed in the recent Commission Recommendation (EU) 2019/1888^{f12} to be monitored by food business operators and authorities in the member states. A suitable approach to prove the origin of acrylamide from pancake surface is *in situ* derivatization prior to the measurement and a targeted search for the adduct. Derivatization was performed by an additional spray of alkaline thiosalicylic acid solution before application of the MALDI matrix. The derivatization product could be detected with a similar distribution to underivatized acrylamide, confirming the origin of acrylamide from the sample itself.

In summary, the applicability of autofocusing MALDI MS imaging for ‘real-life’ processed food samples was demonstrated in this publication by example of traditional German gingerbread, an exceptionally brittle and heterogeneous type of processed food. To achieve this, an advanced sample preparation workflow was developed based on foundational work reported in the first publication. The study found that autofocusing MALDI MS imaging is effective in compensating for variations caused by uneven surfaces. Next to the display of major gingerbread constituents, the distribution of the low-abundant contaminant acrylamide was shown, with in-depth statistical analysis supporting its formation preferably, however not exclusively, within nut fragments. Lastly, quality control aspects regarding the origin of acrylamide signal have been given special consideration in this publication. Amongst the supplementary experiments for this purpose is the first report of an *in situ* analyte derivatization in food prior to MS imaging. To conclude, both food safety authorities and the food industry could profit from MS imaging as an analytical technique for (legally required) acrylamide monitoring to gain further insights into the formation and distribution of acrylamide in susceptible food such as traditional German gingerbread.

2.1.3 Spatially resolved identification of plant proteins by MALDI MS imaging

The following details are part of the third publication entitled „MALDI MS imaging of chickpea seeds (*Cicer arietinum*) and crab’s eye vine (*Abrus precatorius*) after tryptic digestion allows spatially resolved identification of plant proteins“.

MS imaging of proteins in plants has so far been conducted only using low mass resolution instruments and has, with one exception being the detection of a 198 *kDa* protein in soybean, been restricted to small proteins (< 20 *kDa*) or protein fragments (< 10 *kDa*) (see section 1.2.2). *In situ* tryptic digestion and spatially resolved untargeted protein identification in mammalian tissue by MALDI MS imaging is already commonly used in biomedical research, however, it has rarely been applied to plant tissue. On the contrary, the need for development of bottom-up protein MS imaging for plant tissue has been expressed by several authors in the early 2010’s^{27,89,90} since it had hitherto been unsuccessful to establish such a protocol. Merely one MS imaging article could be found, in which tryptic digestion was applied to samples of both animal and plant origin using one universal workflow without dedicated method development or adjustments accounting for differences between animal and plant tissue and without further measures to support the assignment of the detected MS signals to proteins.⁷⁷ In this context, it is important to note that only substantiated assignments of MS signals to distinct proteins are of high scientific value; marking an MS signal as ‘protein’ merely based on its intact mass without further evidence is not considered sufficient for reliable identification (see also section 1.1.4.3). The present publication shows the first results of MALDI MS imaging of proteins in plant (food) tissue after *in situ* tryptic digestion with high mass accuracy (RMSE < 1.5 *ppm*) and mass resolution ($R = 240,000$ at m/z 200, $R_{min} > 60,000$). Each step in the preparation of plant seeds for MS imaging was carefully evaluated, including newly introduced steps in the workflow, as well as the procedure and parameters for protein identification based on detected peptides. Finally, the developed method was applied to seeds of crab’s eye vine (*Abrus precatorius*) for targeted analysis and visualization of the toxic protein abrin.

The development of a sample preparation workflow tailored to delicate chickpea (*Cicer arietinum*) seeds as an example for protein-rich plant (food) was the first task reported in this publication; the resulting procedure is depicted schematically in Figure 11 and is briefly described in the following. Seeds were soaked in 30 % aqueous ethylene glycol for one week at room temperature to facilitate sectioning in a cryomicrotome. Due to a tendency of water-rich plant tissue towards shrinkage, deformation, or loss of the seed coat upon sectioning, samples needed to be embedded in 5 % gelatin beforehand. Stable

^{f12}Commission Recommendation (EU) 2019/1888 of 7 November 2019 on the monitoring of the presence of acrylamide in certain foods

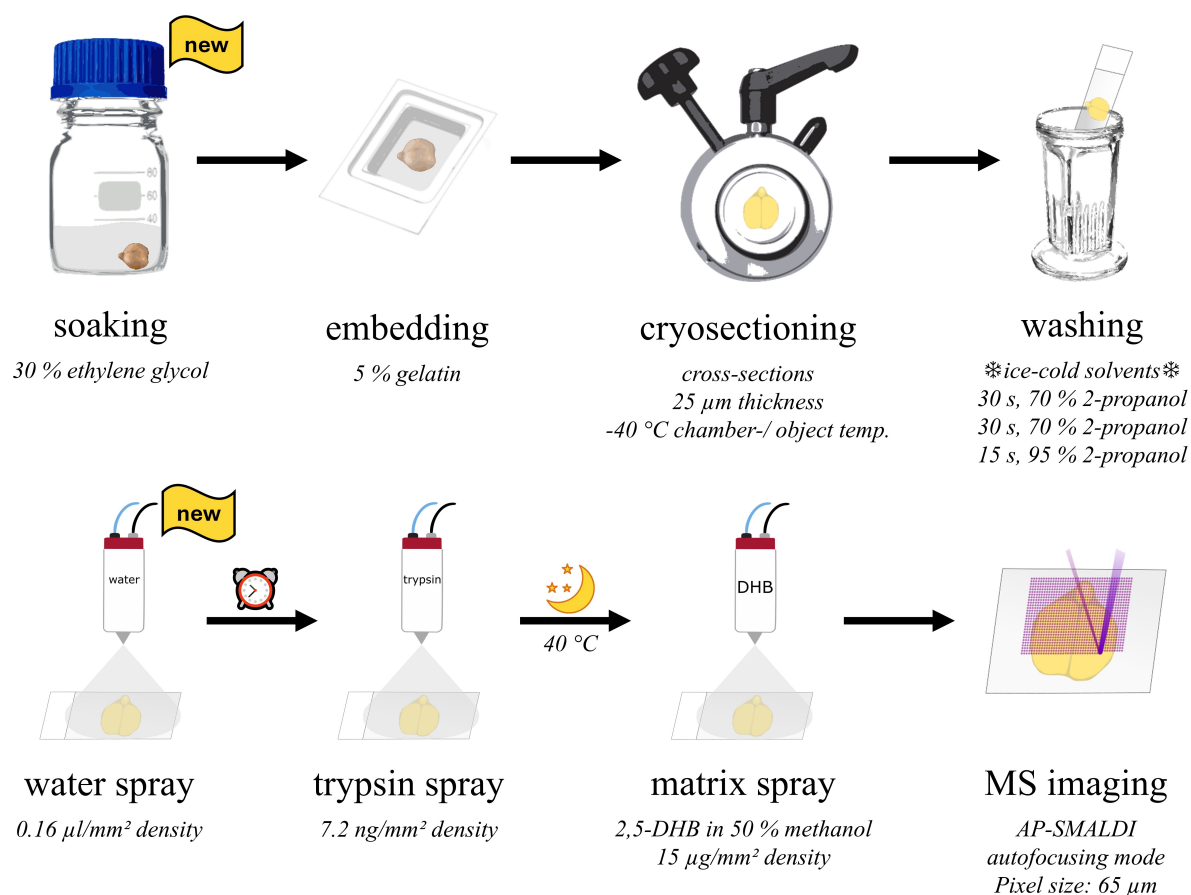


Figure 11: Sample preparation workflow for bottom-up protein MALDI MS imaging of plant tissue. Compared to established protocols for animal tissue, soaking and water spray were newly introduced. The ‘alarm clock’-symbol indicates that the sprays are performed in immediate succession. The ‘moon’-symbol indicates a controlled overnight incubation.

sections were acquired by careful sectioning at 25 μm thickness and -40°C cryostat temperature. To effectively remove interfering compounds, such as salts, lipids, and particularly saccharides (as opposed to animal tissue), sample sections are typically subjected to a washing step. An isopropanol-based protocol developed by Grassl et al. proved to be suitable for this purpose,²⁷ also considering possible protein delocalization in this step. After tissue washing, an additional short spray of water was found necessary to saturate the absorbent plant tissue prior to enzyme spray application to prevent absorption of trypsin from the surface. Digestion was performed in a 40°C tempered humid chamber overnight. Subsequently, DHB matrix was applied with a final calculated matrix density of $15 \mu\text{g}/\text{mm}^2$. Parameters for the automated sprays of water, trypsin and DHB were carefully evaluated and reported. MS imaging measurements were carried out in positive ion mode in the mass range m/z 400–1600 with a pixel size of 65 μm , which constitutes a higher spatial resolution than in all previous MS imaging studies on proteins in plants.

In general, the use of HRMS is of utmost importance in bottom-up proteomics for a reliably selective assignment of peptides by accurate mass due to the artificial expansion of sample complexity through enzymatic digestion. This aspect is emphasized in the publication by zoomed-in mass spectra showing peaks very close to the target tryptic peptide signals. Moreover, an example for a tryptic peptide with a close neighboring peak is given in Figure 12A and B, whose distribution differ greatly (Figure 12C and D) and would adulterate an MS image generated at low mass resolution. Resulting from the described workflow and downstream filtering by relative mass error ($< 1.5 \text{ ppm}$) as well as measure of spatial chaos (≥ 0.96),⁹¹ signals of tryptic peptides were visualized and could be sorted into four major distribution patterns when compared to the microscopic image: Presence throughout all seed compartments as indi-

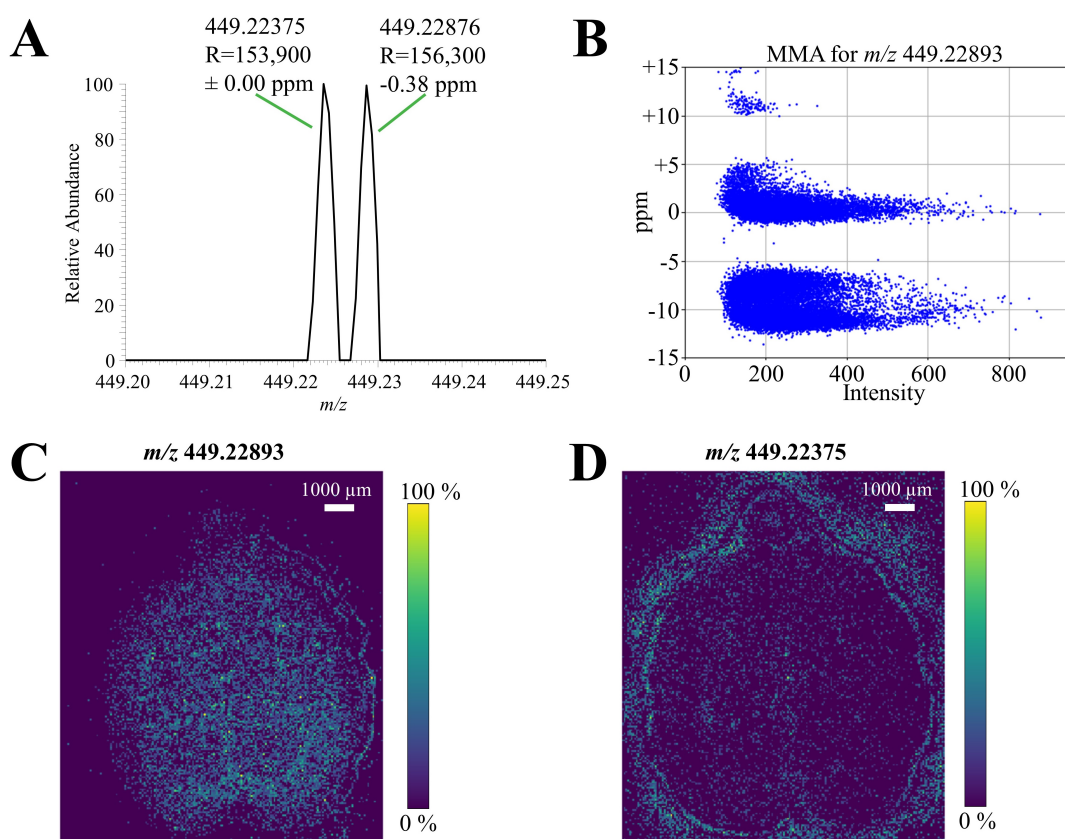


Figure 12: Necessity for high mass resolution for selective peptide visualization. **A:** Zoomed-in single pixel mass spectrum with indicated mass resolution R of tryptic peptide CPGR (ammonium adduct), m/z 449.22893, and its neighboring peak. **B:** MMA-plot of the respective peaks in **A**. **C:** Ion image of tryptic peptide CPGR (ammonium adduct). **D:** Ion image of the neighboring peak.

cated by tryptic peptide EFVR K-adduct in Figure 13B (red), across cotyledons and radicle as indicated by tryptic peptide VGVIKNR Na-adduct in Figure 13B (green), only within cotyledons as indicated by tryptic peptide SHGVK K-adduct in Figure 13C (red), and primarily in the testa/seed coat as indicated by tryptic peptide KKWVIHIER NH_4 -adduct in Figure 13C (green). This shows that the presented MS imaging approach is suitable for the disclosure of different tryptic peptide distributions in plant seeds.

Complementary LC-MS/MS measurements with a subsequent protein database search are an elegant way to generate a sample-specific list of candidate proteins for identification in MS imaging data. For a reliable identification of proteins in MS imaging, no generally agreed procedure has been laid down so far. Thus, as already described in section 1.1.5, requirements for protein identification in this publication were based on the concept of ‘predominant distributions’ of peptide candidates together with a minimum number of two detected peptides per protein and with at least one peptide being unique within the LC-MS/MS-based protein dataset.²¹ Generating meaningful *in situ* MALDI-MS/MS spectra of tryptic peptides is challenging due to the very low peptide abundances. Nevertheless, with an added *in situ* analyte recrystallization step directly on chickpea sections, the identity of selected tryptic peptides could be supported by successful MALDI-MS/MS measurements; a representative spectrum is depicted together with the molecular structure of the respective tryptic peptide in Figure 14. A total of sixteen proteins were identified and visualized for three of the mentioned distribution patterns: Seven were present throughout the entire section, eight were distributed across cotyledons and radicle, one protein was found only within cotyledons. It is important to note that this number results from applying such strict identification criteria and, for instance, a total of 189 proteins would be reported with the hypothetical requirement of only one unique peptide assigned to a protein. Moreover, the majority of identified proteins was larger

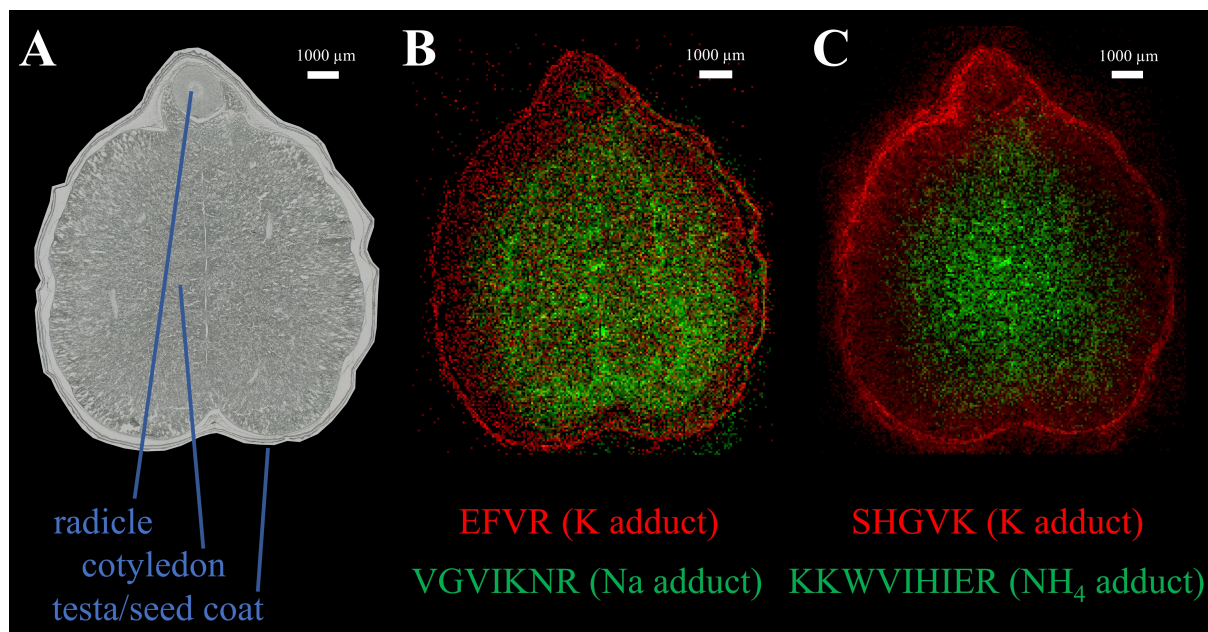


Figure 13: MALDI MS imaging of tryptic peptides with different distributions throughout a chickpea seed cross-section. **A:** Microscopic image of the measured sample. **B:** Overlay of tryptic peptide EFVR K-adduct, m/z 588.25426 (red), protein A0A1S2XHJ1 and tryptic peptide VGVIKNR Na-adduct, m/z 807.48112 (green), protein A0A1S2YYM1. **C:** Overlay of tryptic peptide SHGVK K-adduct, m/z 565.24946 (red), protein A0A1S2YX55 and tryptic peptide KKWVIHIER NH_4 -adduct, m/z 1225.75283 (green), protein A0A1S2XNP5.

than 30 kDa and would thus not have been readily identifiable using top-down protein MS imaging, as explained in section 1.1.4.3.

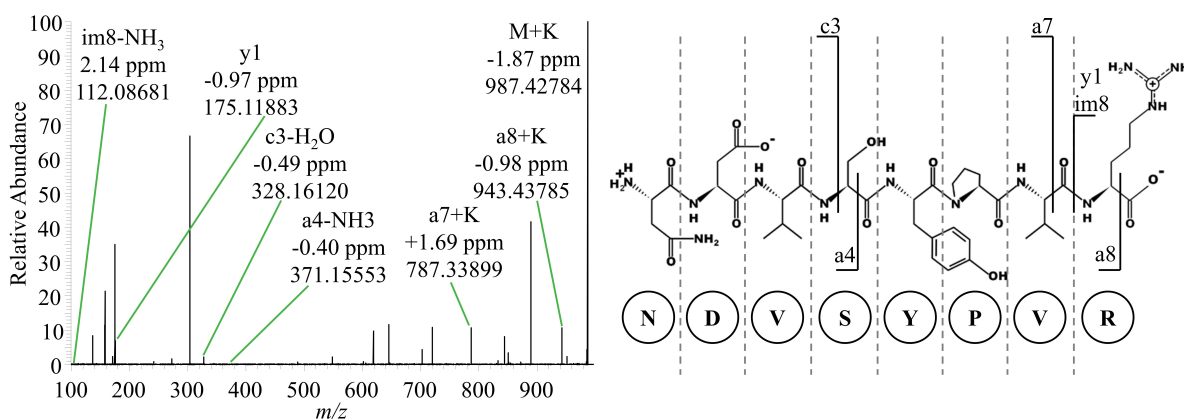


Figure 14: MALDI-MS/MS mean spectrum ($n = 34$ single spectra) of tryptic peptide NDVSYPR K-adduct, m/z 974.43436, HCD: 35. Molecular ion and fragment ions are indicated in the spectrum together with their relative mass error and in the adjacent molecular structure with the respective cleavage site.

Another promising analytical technique for the visualization of protein distributions with exceptional selectivity is MALDI MS imaging after immunosorbent addition of antibodies to proteins on the sample surface, which is referred to as MALDI-IHC. Such antibodies used for MALDI-IHC carry a photocleavable mass-tag, which is detached upon desorption/ionization and detected in the mass spectrometer.⁹² Though this is a highly elegant strategy to overcome the drawbacks of top-down (molecular mass limitation) and bottom-up proteomics (increased sample complexity), such antibodies need to be designed for specific proteins and constrict the approach to few targets. As already mentioned in section 1.1.4.3, bottom-up protein MS imaging as applied in this publication is on the other hand considered an untargeted

proteomics approach, which does not include a preselection of proteins prior to the measurement (apart from a certain restriction by the comprehensiveness of the underlying protein database).

The developed workflow was finally used for a food safety-related application for the spatially resolved detection of abrin in seeds of crab's eye vine. These seeds are small and attractively colored in black and red, which is why they are frequently used to produce 'natural jewelry' in their countries of provenance. However, they are known to contain the highly toxic 60 *kDa* protein abrin (the term subsumes four isoforms a, b, c and d). A recent report on the presence of such seeds in oriental pepper mixtures⁹³ as well as several case reports on abrin intoxication by ingestion of crab's eye vine seeds^{94–96} substantiate this topic as a matter of health and food safety. To directly investigate the distribution of abrin, the developed MS imaging method for chickpea seeds was transferred to seeds of crab's eye vine in a targeted measurement setup. Two unique peptides of abrin-a could be detected, which were both evenly distributed throughout all seed compartments including the seed coat. Grinding off seed coat particles in a pepper mill as well as suction on intact or drilled seeds as part of 'natural jewelry' can thus already lead to a certain exposure to abrin. Therefore, these results support recommendations to withhold such jewelry from the market and emphasize the need for monitoring of oriental pepper mixtures.

To sum up, the results presented in this study demonstrate that, also in plant samples, proteins can be visualized and identified based on accurate mass detection of their tryptic peptides. Emphasizing the possibility for untargeted analysis, the bottom-up MS imaging approach is clearly distinguished from antibody-based targeted imaging techniques, such as multiplexed MALDI-IHC. In contrast to the top-down approach, bottom-up protein MS imaging is not restricted in protein size. As a consequence, the chosen procedure including *in situ* enzymatic digestion provides unique information by enabling access to the spatial distribution and identity of larger proteins (> 30 *kDa*) in plant tissues in an untargeted manner. Compared to state-of-the-art bottom-up protein MS imaging of mammalian tissues, which looks back at more than a decade of developmental work, the presented application on plant tissues naturally lags behind in the number of identified proteins and spatial resolution. This might at least partially derive from fundamental differences in cell morphology between plants and animals including the presence and distribution of proteins. Nevertheless, the present study laid the foundation for further optimization of the workflow (including, for instance, the use of alternative enzymes) and future studies on protein distributions in plant matrices. Knowledge on the distributions of proteins in plants or food of plant origin can be decisive for understanding biological processes since proteins constitute indispensable molecules in living systems which are involved in innumerable pathways. As a consequence, the application of bottom-up protein MS imaging holds great potential for all plant- and food-related scientific disciplines and motivations, as exemplified by the targeted elucidation of the distribution of the toxic protein abrin in seeds of crab's eye vine as a food safety-related application.

2.2 Author contributions

First Publication

Kokesch-Himmelreich, J.*; **Wittek, O.***; Race, A. M.; Rakete, S.; Schlicht, C.; Busch, U.; Römpp, A. MALDI mass spectrometry imaging: From constituents in fresh food to ingredients, contaminants and additives in processed food. *Food Chemistry* **2022**, *385*, 132529. (* equal contribution)

A.R. conceived the study, provided funding and necessary instrumentation. O.W. acquired contaminated German gingerbread; Gouda cheese was provided by C.S. and U.B. A.R. acquired samples of veal sausage. Experiments on hardy kiwi and German gingerbread were designed by J.K.-H., A.R. and O.W.; O.W. conducted measurements and data analysis. Experiments on carrots, veal sausage and Gouda cheese were designed by J.K.-H., S.R. and A.R.; J.K.-H. and S.R. conducted measurements. C.S. provided additional HPLC-UV measurement data on natamycin in Gouda cheese, which was processed by J.K.-H. A.M.R. developed the penetration analysis MATLAB tool. Data analysis of Gouda cheese was performed by J.K.-H. and A.M.R. O.W. conducted data analysis for carrots and veal sausage in close collaboration with J.K.-H. and complementary data analysis of Gouda cheese for manuscript revision. J.K.-H. and O.W. created figures and tables for the manuscript in coordination with A.R. The original draft of the manuscript was written by J.K.-H., A.R. and O.W. Manuscript revisions were incorporated by A.R. and O.W. All authors reviewed the manuscript.

Second Publication

Wittek, O.; Römpp, A. Autofocusing MALDI MS imaging of processed food exemplified by the contaminant acrylamide in German gingerbread. *Scientific Reports* **2023**, *13*, 5400.

A.R. provided funding and necessary instrumentation for the automated spray and the autofocusing SMALDI source. O.W. acquired contaminated German gingerbread and prepared pancake samples. Experiments for the development and optimization of methodology and data analysis were designed by O.W. in close coordination with A.R. O.W. performed all practical work on sample preparation, method development, measurements and data processing. O.W. created all figures and tables for the manuscript in coordination with A.R. The manuscript was written and reviewed by O.W. and A.R.

Third Publication

Wittek, O.; Jahreis, B.; Römpp, A. MALDI MS imaging of chickpea seeds (*Cicer arietinum*) and crab's eye vine (*Abrus precatorius*) after tryptic digestion allows spatially resolved identification of plant proteins. *Analytical Chemistry* **2023**, *95*, 14972–1498.

A.R. initiated the study, acquired funding, managed and supervised the project. B.J. established the digestion workflow for mammalian tissue, which served as a basis for this study, as well as the trypsin activity test. O.W. acquired seeds of chickpea and crab's eye vine and performed a first experiment in collaboration with B.J. Subsequent experiments for the development and optimization of methodology and data analysis were designed by O.W. in coordination with A.R. O.W. performed practical work on sample preparation, method development, measurements and data processing. B.J. generated pictures for Table S4 and performed supporting MALDI-MS/MS measurements for Figure S13 and Table S3. O.W. created all figures and tables for the manuscript in coordination with A.R. The manuscript was written by A.R. and O.W. All authors reviewed the manuscript.

3 Scientific publications and manuscripts

3.1 MALDI mass spectrometry imaging: From constituents in fresh food to ingredients, contaminants and additives in processed food

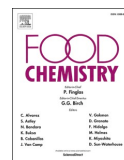
Food Chemistry 385 (2022) 132529



Contents lists available at ScienceDirect

Food Chemistry

journal homepage: www.elsevier.com/locate/foodchem



MALDI mass spectrometry imaging: From constituents in fresh food to ingredients, contaminants and additives in processed food

Julia Kokesch-Himmelreich^{a,1}, Oliver Wittek^{a,1}, Alan M. Race^{a,2}, Sophie Rakete^{a,3},
Claus Schlicht^b, Ulrich Busch^b, Andreas Römpf^{a,*}

^a Bioanalytical Sciences and Food Analysis, University of Bayreuth, Bayreuth, Germany
^b Bavarian Health and Food Safety Authority, Oberschleißheim, Germany

ARTICLE INFO

Keywords:

MALDI mass spectrometry imaging
Processed food
Penetration analysis tool
Diffusion
Additives
Natamycin
Contaminants
Acrylamide
Beta-carotene
Anthocyanins

ABSTRACT

Mass Spectrometry imaging (MS imaging) provides spatial information for a wide range of compound classes in different sample matrices. We used MS imaging to investigate the distribution of components in fresh and processed food, including meat, dairy and bakery products. The MS imaging workflow was optimized to cater to the specific properties and challenges of the individual samples. We successfully detected highly nonpolar and polar constituents such as beta-carotene and anthocyanins, respectively. For the first time, the distributions of a contaminant and a food additive were visualized in processed food. We detected acrylamide in German gingerbread and investigated the penetration of the preservative natamycin into cheese. For this purpose, a new data analysis tool was developed to study the penetration of analytes from uneven surfaces. Our results show that MS imaging has great potential in food analysis to provide relevant information about components' distributions, particularly those underlying official regulations.

1. Introduction

Mass spectrometry is extensively used for the analysis of food (Dominguez, Garrido Frenich, & Romero-González, 2020; Medina, Pereira, Silva, Perestrelo, & Cámara, 2019). It is ideally suited to address the complexity of food samples and to quantify a wide range of compounds. These studies are almost exclusively based on homogenized samples, which are commonly separated by chromatography before mass spectral detection.

However, in some cases, the identification and quantification of compounds is not sufficient, and the spatial distribution of one or more analytes is also relevant. The combination of mass spectrometry and spatial information is accessible by mass spectrometry imaging (MS imaging), which has gained substantial interest over the last 20 years in the analytical community, but has so far not been fully explored for food analysis. MS imaging enables the visualization of spatial distributions for a wide range of chemical compounds in complex biological samples

(Römpf & Spengler, 2013). The most widely used ionization technique is matrix-assisted laser desorption/ionization (MALDI).

The MALDI MS imaging measurement procedure is briefly explained by the example of a hardy kiwi (*Actinidia arguta*) in Fig. 1. Commonly, thin sections of the sample are obtained and sprayed with a suitable matrix solution to obtain the incorporation of the analytes in small matrix crystals (co-crystallization). The matrix-coated surface of the sample is scanned in a grid-like pattern with a laser to desorb and ionize the analytes (Fig. 1A). For each laser spot on the sample section, a full mass spectrum is acquired (segments shown in Fig. 1B). An 'ion image' or 'MS image' can be generated by picking an m/z value of interest and displaying all pixels containing the selected signal in a predefined color, where the brightness of the color corresponds to the intensity of the ion signal (Fig. 1C). Thus, the combination of mass spectrometric detection and spatially resolved analysis provides information about both the presence and the relative intensities of an analyte on the sample surface. Commonly, up to three ion channels are overlaid yielding a multicolor

* Corresponding author at: Chair of Bioanalytical Sciences and Food Analysis, University of Bayreuth, Universitätsstraße 30, 95447 Bayreuth, Germany.

E-mail addresses: Julia.Kokesch-Himmelreich@uni-bayreuth.de (J. Kokesch-Himmelreich), Oliver.Wittek@uni-bayreuth.de (O. Wittek), alan.race@uni-marburg.de (A.M. Race), Sophie.Rakete@med.uni-muenchen.de (S. Rakete), Claus.Schlicht@lgl.bayern.de (C. Schlicht), Ulrich.busch@lgl.bayern.de (U. Busch), Andreas.Roempp@uni-bayreuth.de (A. Römpf).

¹ The respective authors contributed equally to the preparation of this manuscript.

² Present address: Alan Race: Institute of Medical Bioinformatics and Biostatistics, Philipps University of Marburg, Marburg, Germany.

³ Present address: Sophie Rakete: Institute of Laboratory Medicine, University Hospital, LMU Munich, 81377 Munich, Germany.

<https://doi.org/10.1016/j.foodchem.2022.132529>

Received 16 July 2021; Received in revised form 20 January 2022; Accepted 19 February 2022

Available online 22 February 2022

0308-8146/© 2022 The Authors. Published by Elsevier Ltd. This is an open access article under the CC BY-NC-ND license (<http://creativecommons.org/licenses/by-nc-nd/4.0/>).

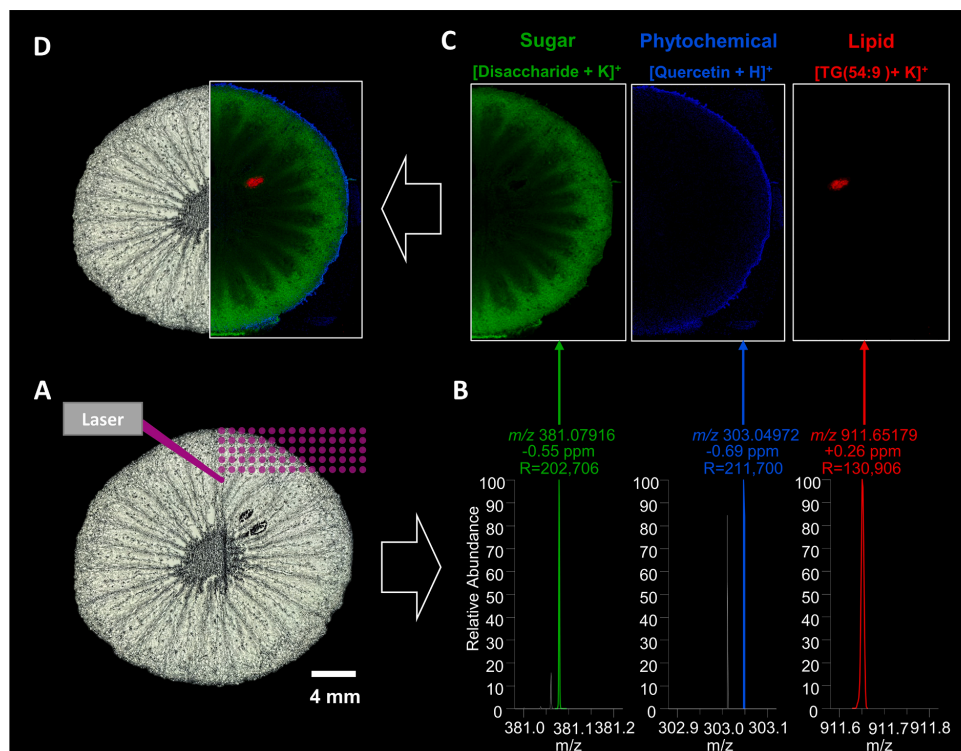


Fig. 1. MS imaging of hardy kiwi (*A. arguta*). A: Optical image of kiwi section and schematic explanation of the MS imaging process. B: Single pixel mass spectra of three selected analytes with their corresponding mass deviation (in ppm) and mass resolution R (full width at half maximum, FWHM). C: Corresponding single ion images, pixel size 45 μm , MS images were normalized to the total ion current (TIC). D: RGB MS image of the lipid TG(54:9) $[\text{M} + \text{K}]^+$, m/z 911.65255, red), the disaccharide $[\text{M} + \text{K}]^+$, m/z 381.07937, green) and the phytochemical Quercetin $[\text{M} + \text{H}]^+$, m/z 303.04993, blue).

ion image (RGB MS image, Fig. 1D, right), which can be directly compared to the optical image (Fig. 1D, left). In the present example, the signals of a disaccharide, a phytochemical and a triglyceride, all compounds of interest in food analysis, were chosen to be visualized in the kiwi fruit. Details on these food constituents and their identification are discussed in the Results section. This example shows that the combination of MS images and the corresponding optical image can be used to discuss the potential function or effect of a given analyte. It is important to note that different compound classes can be visualized simultaneously - and without the need for labelling - despite their potentially varying physical and chemical properties.

MALDI MS imaging in general has been successfully used for analyzing metabolites, drug compounds, lipids and proteins in biological samples (Spengler, 2015). MS imaging methods were also developed for analyzing constituents in fresh plant-based food, e.g. wheat grain (Bhandari, Wang, Friedt, Spengler, Gottwald, & Römpf, 2015) rice (Yoshimura & Zaima, 2020), tomatoes (Bednarz, Roloff, & Niehaus, 2019), grape (Berisha et al., 2014) and strawberries (Wang, Yang, Chaurand, & Raghavan, 2021). Applications for animal-based food include raw chicken-meat (E. Marzec, Wojtysiak, Połtowicz, Nowak, & Pedrys, 2016), pork chops (Enomoto, Furukawa, Takeda, Hatta, & Zaima, 2020) and fish (Goto-Inoue, Sato, Morisasa, Igarashi, & Mori, 2019). MS imaging for food analysis has been reviewed with a focus on application examples (Yoshimura and Zaima, 2020) and technical details (Handberg, Chingin, Wang, Dai, & Chen, 2015; Li et al., 2016).

Only very limited data are available for mass spectrometry imaging

of processed food. Maslov et al. recently investigated the peptide distribution in dry-cured ham muscle (Rešetar Maslov, Svirikova, Allmaier, Marchetti-Deschmann, & Kraljević Pavelić, 2019). Almost all previously published studies focus on endogenous constituents in food. A notable exception is the study by (Nielen & van Beek, 2014) that includes imaging of pesticides (as a residue in food) and mycotoxins in food plants using laser-ablation electrospray ionization (LAESI). Minor substances such as toxic reaction products, residues, contaminants or food additives are also of interest in the context of food safety and authenticity. Studies applying MS imaging for food safety reasons are rare so far and focused on unprocessed fresh food, such as glycoalkaloids in potato tubers (Deng, He, Feng, Zhang, & Zhang, 2021) or organochlorines in soybean seeds and sprouts (Yang et al., 2020). In the EU, most processed food is subject to regulations regarding maximum levels of residues, contaminants and food additives. In some cases, the spatial distribution is also regulated, e.g. for the food additive natamycin. Such components have not been analyzed previously using MS imaging and are described in this work for the first time.

In this study, we want to show the versatility of high-resolution MALDI MS imaging for visualizing the distribution of constituents, ingredients, contaminants and additives. This includes food of both plant and animal origin. We optimized the MS imaging workflow to cater to the specific properties and challenges of the individual samples. Especially for imaging experiments of processed food that consist of multiple ingredients with varying physical and chemical properties, sample preparation procedures differ from established protocols.

We show the distribution of constituents of hardy kiwi, different carrot species (food plants) and German veal sausage (processed meat-based food). We also developed an MS imaging protocol for traditional German gingerbread as an example for highly processed food of plant origin to reveal the spatial distribution of the food contaminant acrylamide. As an example for food additives, we investigated the distribution of the preservative natamycin in cheese, which diffuses from the surface into the cheese. In this case, we have developed a novel analysis approach to assess the penetration from the surface into the cheese in more detail.

2. Methods

2.1. Samples

Samples of hardy kiwi (*Actinidia arguta*) as well as orange and purple carrots (*Daucus carota* ssp. *sativus* var. *atrorubens* Alef.) were purchased at a local supermarket.

German veal sausage ("Weißwurst") was provided by the Max Rubner Institute (Kulmbach, Germany). Samples of Gouda cheese with varying natamycin concentrations (see Table S1, supplementary material), the natamycin standard (2.5 % aqueous suspension, Sigma Aldrich, Dreieich, Germany) and acrylamide-contaminated gingerbread (3,200 µg/kg determined by GC-MS) were provided by the Bavarian Health and Food Safety Authority (LGL, Germany).

2.2. Sectioning

Frozen samples were sectioned with a cryostat (Leica CM3050, Wetzlar, Germany) at $-15\text{ }^{\circ}\text{C}$ - $-25\text{ }^{\circ}\text{C}$ object temperature. Section thickness for the food samples were as follows: Kiwi 30 µm, orange carrot 100 µm, purple carrot 50 µm, German veal sausage 16 µm and Gouda cheese varied between 14 µm and 16 µm. Sections were thaw-mounted on adhesion object slides (SuperFrost Plus™, Thermo Scientific™) and stored at $-80\text{ }^{\circ}\text{C}$ (gouda cheese at $-20\text{ }^{\circ}\text{C}$) until analysis. Gingerbread-sections of 2 mm thickness were cut off the frozen gingerbread using an electric micro saw (Dremel® 8220, Breda, Netherlands) with a cooled cutting-disk and stored at $-80\text{ }^{\circ}\text{C}$ until analysis.

2.3. MALDI MS imaging

30 mg 2,5-Dihydroxybenzoic acid (DHB, Sigma Aldrich, Dreieich, Germany) were dissolved in 1 mL acetone/water (1:1, Carl Roth, Karlsruhe, Germany) and 0.1 % trifluoroacetic acid (Sigma Aldrich, Dreieich, Germany). 170–200 µL DHB matrix solution was applied to the sections using a home-built pneumatic sprayer system with a nitrogen pressure of 0.7–0.75 bar, a flow rate of 10–15 µL/min and a distance of 10 cm between nozzle and target. Detailed information per sample is given in Table S2 (supplementary material). The section and matrix quality was checked before and after matrix application with a digital microscope (Keyence VHX-5000, Osaka, Japan).

Mass spectrometric data were acquired with an AP-SMALDI10 ion source (TransMIT GmbH, Giessen, Germany) coupled to a Q-Exactive-HF Orbitrap mass spectrometer (Thermo Fisher Scientific, Bremen, Germany). The MALDI source is equipped with a 60 Hz Nitrogen laser ($\lambda = 337\text{ nm}$) and one scan event consisted of 30 laser pulses corresponding to an injection time of the mass spectrometer of 500 ms. The laser was focused down to a spot size of 10 µm and the energy on the target varied between 0.5 µJ and 2.0 µJ. For the gingerbread samples, analyses were performed with 12.5 µJ laser energy, 60 laser shots per pixel and an injection time of 1000 ms.

All MS imaging measurements were performed in positive ion mode with a mass resolution of $R = 240,000$ at m/z 200 ($R = 120,000$ at m/z 200 for German veal sausage sample). Matrix clusters were used as lock masses for the appropriate mass range to gain a mass accuracy

typically better than 1.5 ppm (Treu & Römpf, 2021). The m/z ranges varied for each application and are given in Table S3 (supplementary material) as well as raster and pixel size for the corresponding imaging experiments.

On Gouda sections MS/MS experiments were also performed. The details are provided in Figs. S7 and S8 (supplementary material).

2.4. Data analysis

MS data were analyzed with the QualBrowser of the Thermo Xcalibur 4.0 software. Tentative compound identification was based on accurate mass unless stated otherwise. MS imaging data were converted to the open file format imzML (Schramm et al., 2012) using 'imzML Converter' (Version 2.0.4) (Race, Styles, & Bunch, 2012) and 'imzML Validator' (Race & Römpf, 2018), MSiReader 1.0 (Bokhart, Nazari, Garrard, & Muddiman, 2018) and Mirion (Paschke et al., 2013) (version 3.2.64.12) were used to generate MS images with a selected m/z window of ± 2.5 ppm. Preprocessing steps (such as normalization) are indicated in the corresponding figure caption. Detailed penetration analysis of natamycin was performed using our newly developed semiautomatic penetration tool based on SpectralAnalysis (Race, Palmer, Dexter, Steven, Styles, & Bunch, 2016) and written in MATLAB (R2016b), which consists of two parts: i) Lipid based edge detection to determine the interface ii) calculation of penetration plots. More details are given in the result section (Fig. 5) and in Fig. S10 (supplementary material).

3. Results and discussion

In the following, we demonstrate the power of applying mass spectrometry imaging to food science applications. The examples range from ingredients, contaminants and additives in samples as diverse as plant and animal-based, fresh and processed food. Motivation and specific experimental protocols for each application are discussed in the respective section.

3.1. Constituents in fresh plant-based food

3.1.1. Hardy kiwi

The hardy kiwi (*Actinidia arguta*) is an essentially hairless grape-sized fruit with edible peel and an intense sweet and sour taste reminding of tropical fruit (Hallett & Sutherland, 2005; Fisk, McDaniel, Strik, & Zhao, 2006). Apart from its nutritional value, it contains several health-promoting bioactive constituents, such as vitamin C, polyunsaturated fatty acids and polyphenols (Kim, Beppu, & Kataoka, 2009; Nishiyama, Yamashita, Yamanaka, Shimohashi, Fukuda, & Oota, 2004; Park et al., 2011). One half of a 30 µm thin cross section of a hardy kiwi was sectioned at $-24\text{ }^{\circ}\text{C}$ without prior embedding and analyzed in positive ion mode with a step size of 45 µm and a mass range of m/z 250–1000 (Fig. 1A). The mass spectral signals shown in Fig. 1B were acquired from a single pixel. The MS images in Fig. 1C show the distributions of the lipid glyceryl trilinolenate (TG(54:9), $[M + K]^+$, m/z 911.65255, red) dihexoses ($[M + K]^+$, m/z 381.07937, green) and the anthocyanin quercetin ($[M + H]^+$, m/z 303.04993, blue). The combination of these single ion images (RGB MS image) and the optical image (Fig. 1D) shows that the structure of the sample was retained throughout sample preparation and data acquisition. The distribution of the imaged constituents can be directly linked to structures in the hardy kiwi. These compounds – and all other compounds reported in this study – were identified by accurate mass, i.e. mass accuracy was better than 1.5 ppm. This high specificity of the mass spectral data is particularly important in mass spectrometry imaging measurements as the complexity of the (food) sample cannot be reduced by chromatographic separation (Römpf and Spengler, 2013). The $[M + K]^+$ -adduct of the lipid TG(54:9) (m/z 911.65255), for example, was detected in the single MS spectrum in Fig. 1B with a mass deviation of 0.26 ppm. The mass accuracy for the whole measurement can be determined as the root mean square error

(RMSE) of the mass deviation for each individual spectrum containing the targeted ion. The calculated RMSE for all pixels in this RGB MS image were 1.14 ppm (3427 spectra), 0.80 ppm (32705 spectra) and 0.55 ppm (127821 spectra) for the signals of glyceryl trilinolenate (m/z 911.65255, red), quercetin (m/z 303.04993, blue) and dihexose (m/z 381.07937, green), respectively. This allows for reliable compound identification and an image generation with a bin width of ± 2.5 ppm. This provides specific information on the distribution of analytes and significantly reduces the risk of interference by neighboring peaks. As expected, dihexoses (Fig. 1D, green) were found with high intensities in the pericarp of the hardy kiwi. Glyceryl trilinoleate (Fig. 1D, red) is the most abundant triglyceride in kiwi seed oil (Piombo et al., 2006), which supports our assignment. Due to the different cutting planes of the seeds, the relative abundance of the lipid varies between the two seeds in the measured section. Kiwi fruit contain an average of 2660 mg/100 g total phenolic content and the peel in particular is rich in polyphenols (Baranowska-Wójcik & Szwałgier, 2019; Kim et al., 2009). This is consistent with the high intensities of quercetin (Fig. 1C, blue), found here in the peel. Similar distributions of additional anthocyanins such as cyanidin and pelargonidin are shown in Fig. S1 (supplementary material). The example of the hardy kiwi shows that MS imaging provides the combination of specific molecular information with spatial information, which can be used to link the distributions of components to specific functions or metabolic processes. This information can be obtained for a wide range of compound classes with different physicochemical properties as shown in the following examples.

3.1.2. Carrots

Carrots are popular root vegetables and valued for their high content of beta-carotene (approx. 7.6 mg/100 g) (Souci, Fachmann, & Kraut, 2008). Typical orange carrots have a very firm texture and don't require embedding. However, carrots are hard to section in frozen state, because thin sections tend to form cracks very easily. Therefore, a 100 μm thick cross section of an orange-colored carrot was obtained at a relatively high cryostat temperature of -15 °C and analyzed in positive ion mode with a step size of 50 μm and a mass range of m/z 100–1500. Using MALDI MS imaging it was possible to detect beta-carotene ($[\text{M}]^+$, m/z 536.43820). The MS image is shown with the corresponding optical image of the carrot in Fig. 2A. The single pixel mass spectrum of beta-carotene is shown next to the MS image in Fig. 2A and a mass deviation of 0.52 ppm was determined for the shown signal. The RMSE for the whole measurement is 1.29 ppm (35981 spectra). Carotenes are highly nonpolar and therefore difficult to detect in MALDI experiments due to their low ionization efficiency. However, the beta-carotene distribution is visibly comparable to the orange-colored regions in the optical image and thus confirms our results. Apart from the well-known orange-colored variety, differently colored carrots are also cultivated, such as yellow or purple varieties. Purple carrots (*Daucus carota* ssp. *sativus* var. *atrorubens* Alef.) have an attractive purple-colored outer core and cortex due to high concentrations of anthocyanins. We could detect these anthocyanins in an MS imaging measurement of a 50 μm cross section and reconstruct the purple ring in the cross section as an MS image of cyanidin ($[\text{M}]^+$, m/z 287.05557, RMSE: 1.02 ppm (2100 spectra)). The MS image is shown with the corresponding optical image in Fig. 2B. A previous study used Raman mapping to gain insight into compartment-specific differences in carotenogenesis in orange- and purple-colored carrots (Baranska, Baranski, Schulz, & Nothnagel, 2006). They were able to differentiate three different carotenoids based on Raman spectroscopy. However, their assessment of anthocyanins (as a compound class) was based only on visual color perception. In contrast, MS imaging can provide information not only on the spatial distribution, but also on specific molecule identities for a wide range of compound classes.

3.2. Ingredients in animal-based processed food

Using MS imaging, it is not only possible to investigate constituents

in fresh, but also in processed food. Homogenizing a mixture of ingredients is a common method in food processing, resulting in dramatically altered physicochemical properties that have to be taken into account for MS imaging analysis – especially for sample preparation. German veal sausage is produced by mincing trimmed rosé veal with a low content of fat and tendons, high-fat pork and bacon with the optional addition of herbs and spices such as parsley, onion, pepper and mace (Lebensmittelbuch-Kommission, 2019). Consequently, regions of low fat content can be found in direct proximity to high-fat regions and shreds of connective tissue. These high-fat regions influenced the sample preparation process. Sectioning was performed at -25 °C without embedding and the matrix application was optimized towards a 'wetter' spray for an enhanced analyte extraction (higher flow rate: 0.15 $\mu\text{L}/\text{min}$). Using this adapted MS imaging workflow, the low-fat and high-fat regions can be clearly distinguished by visualizing water-soluble and fat-soluble constituents as shown in Fig. 2C. In this example, the m/z of water-soluble disaccharide ($[\text{M} + \text{Na}]^+$, m/z 365.10544, RMSE: 0.68 ppm (24394 spectra), red) and the fat-soluble cholesterol ($[\text{M}-\text{H}_2\text{O} + \text{H}]^+$, m/z 369.35158, RMSE: 0.62 ppm (27491 spectra), blue) show nearly complementary distributions. The lipid PC(36:4) ($[\text{M} + \text{Na}]^+$, m/z 804.55138, RMSE: 1.23 ppm (30549 spectra), green), a phosphatidylcholine naturally occurring in biological membranes, covers the entire tissue. The 16 μm thin section in Fig. 2C was imaged with a pixel size of 20 μm in the mass range of m/z 200–900. Single ion images of all constituents shown in the RGB overlay of Fig. 2C are provided in Fig. S2 (supplementary material). In addition, ingredients of plant origin could be localized by tracing the m/z of chlorophyll-derivatives originating from added herbs, as shown in Fig. S3 (supplementary material). This shows that not only optically visible structures can be reproduced by MS imaging also in processed food, but also invisible tissue regions can be distinguished by tracing suitable marker compounds. MS imaging could be useful to further investigate topics such as customer deception and food fraud in meat products, e.g. in the context of structured meat. Meat binding in this case is so far investigated by histological techniques and more recently by LC-MS (Jira & Schwägele, 2017). Our proposed method could combine the respective information of these two approaches (spatial and molecular) in one experiment and thus provide further insight.

3.3. Contaminants in plant-based processed food

In addition to constituents shown in the previous examples, the distributions of minor components, such as contaminants, are of interest in food analysis. As laid down in Codex Alimentarius and adopted by EU legislation, food contaminants are legally defined as substances that are unintentionally added to food during the production chain, which includes primary production, preparation and packaging^{4,5}. A prominent example is the carcinogen acrylamide, which is formed from the naturally occurring constituents asparagine and reducing sugars, when prepared at low moisture and temperatures higher than 120 °C (Stadler et al., 2002). The occurrence of acrylamide in food is continuously under discussion, especially since the new Regulation (EU) 2017/2158, establishing mitigation measures and benchmark levels, entered into force⁶. Fig. 3 presents results of a newly developed MS imaging workflow for the investigation of the acrylamide distribution in traditional German gingerbread. Due to its very dry and hard texture, the standard

⁴ Joint FAO/WHO Codex Alimentarius Commission. GENERAL STANDARD FOR CONTAMINANTS AND TOXINS IN FOOD AND FEED. CXS 193-1995, Section 1.2.2

⁵ Art. 1 (1) Regulation (EEC) 315/93 of 8 February 1993 laying down Community procedures for contaminants in food

⁶ Commission Regulation (EU) 2017/2158 of 20 November 2017 establishing mitigation measures and benchmark levels for the reduction of the presence of acrylamide in food

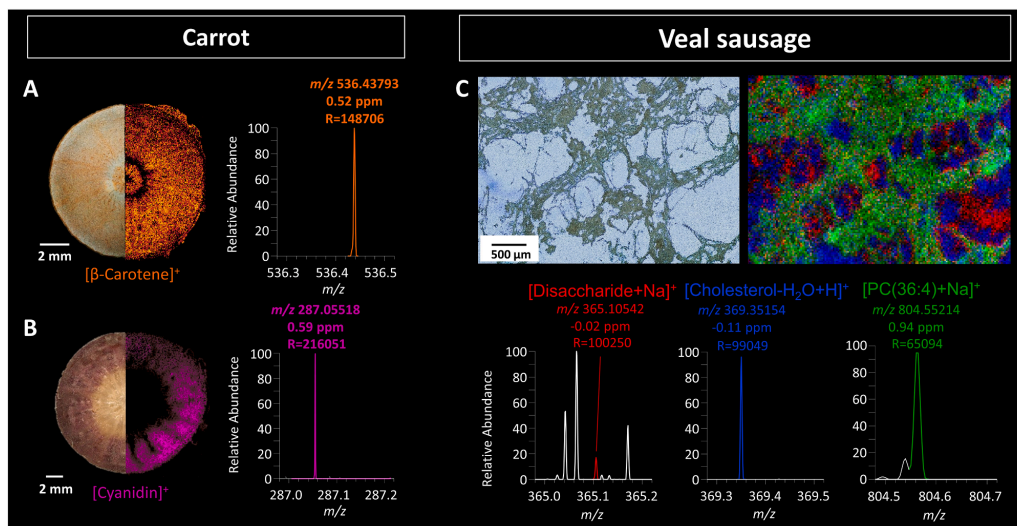


Fig. 2. MS imaging of constituents in carrot species and veal sausage: A: Orange carrot: Overlay of optical image and single ion image of beta-Carotene ($[\text{M}]^+$, m/z 536.43765, orange), pixel size 50 μm . B: Purple carrot: Overlay of optical image and single ion image of Cyanidin ($[\text{M}]^+$, m/z 287.05501, purple), pixel size 80 μm . C: Optical image and RGB MS image of three constituents of veal sausage: Disaccharide ($[\text{M} + \text{Na}]^+$, m/z 365.10544, red), PC(36:4) ($[\text{M} + \text{Na}]^+$, m/z 804.55138, green) and cholesterol ($[\text{M}-\text{H}_2\text{O} + \text{H}]^+$, m/z 369.35158, blue), pixel size 20 μm .

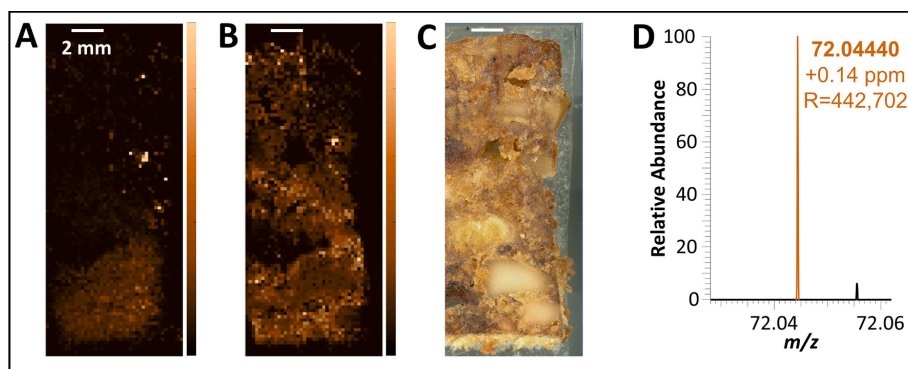


Fig. 3. MS imaging of German gingerbread. A: MS image of process contaminant acrylamide ($[\text{M} + \text{H}]^+$, m/z 72.04439, mass range m/z 50–165, pixel size 200 μm . B: MS image of Disaccharide ($[\text{M} + \text{K}]^+$, m/z 381.07937, mass range m/z 250–1000, pixel size 200 μm , MS spectrum shown in Fig. S13 (supplementary material). C: optical image. D: Single pixel mass spectrum of acrylamide.

cryosectioning procedure was not applicable for the gingerbread samples. Instead, we developed a sectioning protocol using an electric micro saw to obtain sections of approx. 2000 μm thickness. To prevent acrylamide from forming during the sectioning process, both the gingerbread sample and the cutting disk were cooled down to -60 $^{\circ}\text{C}$ before each sectioning operation.

The solvent system was adapted to a higher proportion of acetone (see Table S2, supplementary material) to gain a better matrix crystallization on the gingerbread sections. The thickness and texture of the sections led to an uneven/rough surface which can influence the ionization efficiency during the MALDI process while rastering across the sample with the laser. We addressed this problem by choosing the average distance between the lowest and highest sample regions and the laser optics. For an enhanced ion signal, the injection time was raised to

1000 ms, while 60 laser pulses were applied per pixel. Two alternating scan intervals of m/z 50–165 and m/z 250–1000, respectively, were set to cover a large m/z range with high mass resolution and optimized ion intensities for all analytes of interest. In Fig. 3C, a gingerbread section is shown which was prepared and measured with the described optimized MS imaging workflow at 200 μm pixel size. Our results show nearly ubiquitous presence of disaccharides throughout the sample surface, demonstrated in Fig. 3B by the potassium adduct ($[\text{M} + \text{K}]^+$, m/z 381.07937, RMSE: 0.71 ppm (3397 spectra), for MS spectrum see Fig. S13, supplementary material), indicating the success of the established workflow. Furthermore, sufficient intensity for the spatially resolved detection of acrylamide ($[\text{M} + \text{H}]^+$, m/z 72.04439, RMSE: 0.93 ppm (2208 spectra) Fig. 3D) was achieved. The contaminant was predominantly detected in the region around nuts and close to the wafer

(Fig. 3A). As indicated above, acrylamide is formed predominantly under low moisture and high temperature conditions. Consequently, the observed distribution of acrylamide might result from higher temperatures and/or lower moisture of the gingerbread occurring in regions in close proximity to the baking tray. The successful elucidation of the acrylamide distribution in German gingerbread is the first MS imaging study of a contaminant in processed food and also demonstrates the analytical capability of MS imaging for the detection of low-abundant food components.

3.4. Additives in animal-based processed food

In contrast to contaminants, food additives are intentionally added during the production process to obtain certain properties such as color or extended shelf-life of the processed food. In some cases, not only a concentration limit is defined for food additives, but the location of a regulated component in the sample is also specified. A prominent example is the antifungal drug natamycin, which is approved as a preservative in the European Union (E235). According to Regulation (EC) 1333/2008, natamycin may be added to meat products as well as hard and semi-hard cheeses⁷. Gouda is a prominent example for a semi-hard cheese with dry-matter between 49 % and 57 % and a minimal maturation of 5 weeks⁸. Apart from the maximum level of 1 mg/dm² on the cheese surface, the regulation states a penetration limit of 5 mm for natamycin⁹. Official food analyses in Germany are listed in the Official Collection of Methods according to § 64 of the German Foodstuffs and Feed Code (LFGB)¹⁰. Based on the official method, natamycin is extracted from a cheese slice close to the surface and from the bulk (Fig. S4, supplementary material) with methanol, separated by HPLC on a LiChrospher® 100 RP-18 (5 µm) LiChroCART® 125-4 column (125 × 4,0 mm; 5 µm) (Merck, Darmstadt, Germany) using an isocratic eluent mixture of 75 %V methanol and 25 %V 22.2 mM aqueous KH₂PO₄ (pH 4.45). Natamycin was detected by DAD (scan range λ = 220 – 400 nm) with an absorbance maximum at λ = 303 nm). This method allows quantification (external standard calibration), but does not provide spatial information. In cooperation with the *Bavarian Health and Food Safety Authority* (LGL), we have therefore developed a MALDI MS imaging workflow to investigate the natamycin penetration into cheese sections. A schematic description of the workflow can be found in Fig. S5 (supplementary material). Special care must be taken while sectioning the cheese samples to avoid cross-contamination of natamycin from the surface towards the cheese bulk. The sectioning process of cheese in general is very challenging, due to its high lipid content and varying textures between different cheeses. Furthermore, the presence of holes in certain cheese varieties can easily cause cracks during sectioning. The high lipid content would normally lead to lower cutting temperatures, but the texture of certain Goudas was too brittle if the temperatures were too low. This caused problems while sectioning and made thaw-mounting on glass slides impossible. Therefore, the cutting temperature needed to be optimized separately for every cheese sample. Analogous to our previous study on drug compound imaging in mouse model tissue, the glass slides were warmed from behind by finger contact in the area of the section in order to ensure proper sample mounting (Treu, Kokesch-Himmelreich, Walter, Holscher, & Römpp, 2020).

In the optical image of a Gouda section (16 µm thickness) in Fig. 4A,

two layers of coating and the cheese region can be seen. The MS imaging experiment shown in Fig. 4B was conducted with a pixel size of 20 µm in the mass range of m/z 200–800. We were able to detect characteristic compounds for the three different sample regions, e.g. two coating compounds in blue and green, and one lipid in the cheese bulk in red (see Fig. S6, supplementary material, for single ion images). The lipid could be identified as SM(d34:1) ($[M + Na]^+$, m/z 725.55680, RMSE 0.58 ppm (55198 spectra)), see Fig. S7 (supplementary material) for MS/MS spectrum. The RGB MS image matches the optical image very well, which shows that the imaging workflow was successfully developed and retains the structure of the sample.

Furthermore, using MS imaging it is possible to visualize the distribution of natamycin, which is not visible in the optical image. The distribution of the sodiated natamycin adduct ($[M + Na]^+$, m/z 688.29396) is shown in Fig. 4C as an overlay with the optical image. It can be observed that natamycin occurs in this sample mainly in the rind of the cheese. The sodium adduct ($[M + Na]^+$) showed the highest intensity in comparison to the protonated ion ($[M + H]^+$) and the potassium adduct ($[M + K]^+$) in all of our measurements. This can be explained by the industrial application of natamycin on cheese as an aqueous sodium solution and the natural occurrence of sodium in cheese.

In Fig. 4D, a single pixel mass spectrum from the measurement in Fig. 4C is shown in the mass range of m/z 650–700. The $[M + H]^+$ signal (m/z 666.31202) and the $[M + Na]^+$ adduct (m/z 688.29396) were detected with a mass deviation of 0.11 ppm and 0.12 ppm, respectively. Over the whole measurement, a mass accuracy ≤ 1 ppm could be obtained (RMSE: 0.94 ppm in 1190 spectra and 0.63 ppm in 5199 spectra, respectively). For additional confirmation, MS/MS spectra of the $[M + Na]^+$ adduct in cheese were acquired (Fig. 4E). Four characteristic product ions were detected, which match the MS/MS spectra of the pure natamycin standard (Fig. S8, supplementary material) and thus confirm the identity of natamycin in the Gouda sample.

In addition, a Gouda sample with no declared natamycin – confirmed by the HPLC-DAD reference method – was imaged. In the corresponding MS image of this sample no natamycin signal was present (Fig. S9, supplementary material). This combination of accurate mass detection, on-sample MS/MS fragmentation and verification with a blank sample as shown here by the example of natamycin provides for an additional level of certainty for the identification of food components.

Using the MS imaging approach, we could confirm the presence of natamycin in multiple cheese samples. Different spatial distributions of natamycin were observed in each sample. One example is shown in Fig. 5A, where the sodiated natamycin signal ($[M + Na]^+$, m/z 688.29396) is shown in green and the lipid SM(d34:1) (corresponding to the lipid in Fig. 4B) is shown in red in an optical overlay. Here, natamycin was detected not only in the rind, but also in the coating of the cheese. Application methods for natamycin onto the cheese surface vary between producers; it can be applied onto the cheese surface before the coating or premixed with the coating, explaining the observed differences.

The determination of the penetration of an analyte in the MS image is not straightforward. A simple approach to determine the penetration of natamycin into the cheese would be the use of line scans. Two examples are shown in Fig. 5B + C; the intensity of natamycin is plotted against the x-direction of the image (given in µm). Comparing the two line scans it becomes clear that a single line scan is not representative for the whole cheese section. Due to the rough surface of the cheese, and the noisy line scans, it is difficult to determine the edge of the cheese bulk and the exact depth of penetration, which strongly influences data interpretation.

Similar problems have been described in the literature in case of a drug penetration study in human skin (Bonnel et al., 2018) and 3D cell cultures (Machalkova et al., 2019). Bonnel et al used a semi-automated workflow to correlate the drug concentration to a certain depth in the skin based on a user-defined region of interest. Machalkova et al. evaluated penetration depths of the investigated drug in the 3D cell culture

⁷ Art. 4 (1) in conjunction with Annex II Cat. 01.7.2 Regulation (EC) 1333/2008 of the European Parliament and of the Council of 16 December 2008 on food additives.

⁸ § 7 in conjunction with Appx. 1 KäseV (1965)

⁹ Art. 4 (1) in conjunction with Annex II Cat. 01.7.2 Regulation (EC) 1333/2008 of the European Parliament and of the Council of 16 December 2008 on food additives.

¹⁰ method L 03.00-41/2 § 64(1) Lebensmittel- und Futtermittelgesetzbuch (LFGB) in conjunction with technical rule L 03.00-41/2:2020-02

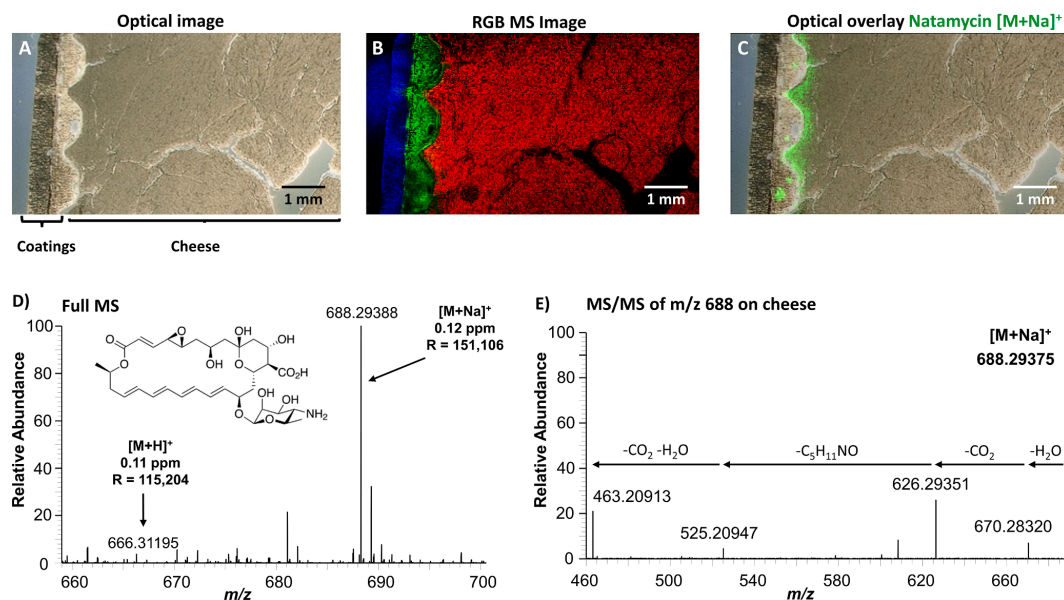


Fig. 4. MS imaging of Gouda cheese A: Optical image of a Gouda cheese section. B: RGB MS image of characteristic compounds for the coatings, m/z 719.48576 (blue) corresponding to PG32:2 ($[M + H]^+$) and m/z 775.55420 (green) with possible elemental composition $C_{40}H_{60}O_{12}$ ($[M + Na]^+$), as well as the lipid SM(d34:1) ($[M + Na]^+$, m/z 725.55680, red) in the cheese bulk. MS spectra of all compounds are shown in Fig. S6 (supplementary material); an MS/MS spectrum of SM(d34:1) can be found in Fig. S7 (supplementary material). MS imaging measurement was acquired with a pixel size of 20 μ m. C: Overlay of natamycin signal ($[M + Na]^+$, green) and optical image. D: Single MS spectrum acquired from natamycin on the Gouda cheese, $[M + H]^+$ at m/z 666.31202 and $[M + Na]^+$ at m/z 688.29396 are highlighted with their corresponding mass deviation in ppm and mass resolution R (FWHM). E: Averaged MS/MS spectrum of $[M + Na]^+$ (isolation window: m/z 688.3 \pm 0.2) at NCE = 25.

with the MALDI MS imaging supported by complementary information from laser scanning confocal microscopy. In contrast, we developed a data analysis approach that solely relies on MS data and includes an automated identification of the region of interest (interface between cheese and coating). This workflow is briefly explained in the following and more details can be found in Fig. S10 (supplementary material).

As a first step, we use the lipid signal, shown in Fig. 5A, which occurred in all our investigated cheese samples to generate a mask for the cheese (Fig. 5D). For generating this mask, image-processing techniques were used to remove noise and fill in gaps to be able to determine a smooth cheese edge (Fig. 5E). Therefore, it is possible to differentiate between natamycin pixels on cheese and off cheese (Fig. 5F). Natamycin signals in the coating ('off cheese') are not considered for the following analysis since they are not in the cheese.

After edge detection, the lateral distance to the edge is calculated for every pixel in the cheese region and can be plotted as a 'distance map' (Fig. 5G). The mean intensity of the natamycin signal is then calculated for all pixels with the same lateral distance from the edge. The mean intensity values were plotted against the distance in μ m to generate a penetration plot, shown in Fig. 5H. The zero value on the x-axis represents the cheese surface (the edge in the distance map). Data points close to the edge show the highest natamycin intensity, with the intensity decreasing with higher distances from the edge. This trend can be expressed in an exponential function and the fit equation describes the diffusion of natamycin into the cheese bulk. Every step in the data analysis workflow and the corresponding figures and graphs are automatically generated in one run by the developed data analysis tool.

Additional Gouda samples with different natamycin concentrations from different producers (Table S1, supplementary material) were analyzed in the same way. The penetration plots of four samples are depicted in Fig. 6A-D. Sample Gouda D corresponds to the penetration

plot shown in Fig. 5H. The penetration plots show that natamycin diffused into the cheese in all cases, however, different penetration behaviors could be observed for the four examples. To compare the four cheese samples, penetration depths at 50% of the maximum intensity value ($I_{\max 50}$) were calculated using the fit equations. The comparison of these $I_{\max 50}$ values is shown in Fig. 6E.

In order to assess the reproducibility of our approach, two additional (serial) sections from the same cheese were measured and analyzed in case of Gouda D. All three penetration plots of the neighboring sections show the same trend and the penetration depths are comparable (Fig. S11, supplementary material). In Fig. 6E, the mean value of ($85 \pm 11 \mu$ m) is shown for these three replicates of Gouda D. The relative standard deviation of 13 % indicates that our approach can be applied with reasonable reproducibility to determine the penetration depths. The $I_{\max 50}$ values can be used to compare the diffusion behavior of natamycin in different samples. Gouda A shows the highest value, and Gouda C the lowest. The penetration analysis shows that none of the investigated cheese samples exceeded the penetration limit of 5 mm of the applicable EU regulation. Apart from the penetration analysis, our approach allows comparing mean intensities in a defined area of multiple sections and samples. The HPLC-DAD results from the first 2 mm of the cheese, which were measured by LGL, are given in Fig. S12 (supplementary material). The MS imaging results follow the same trend (highest signal in Gouda A and lowest signal in Gouda D) as the homogenate analysis from the HPLC-DAD reference method, while providing additional spatial information as discussed above.

With our MS imaging workflow, we were able to determine the spatial distribution of natamycin in cheese samples. This constitutes the first spatially resolved detection of a food additive in food. The crucial advantage compared to the routine HPLC analysis (which has a "spatial resolution" of 5 mm) is the investigation of natamycin penetration in

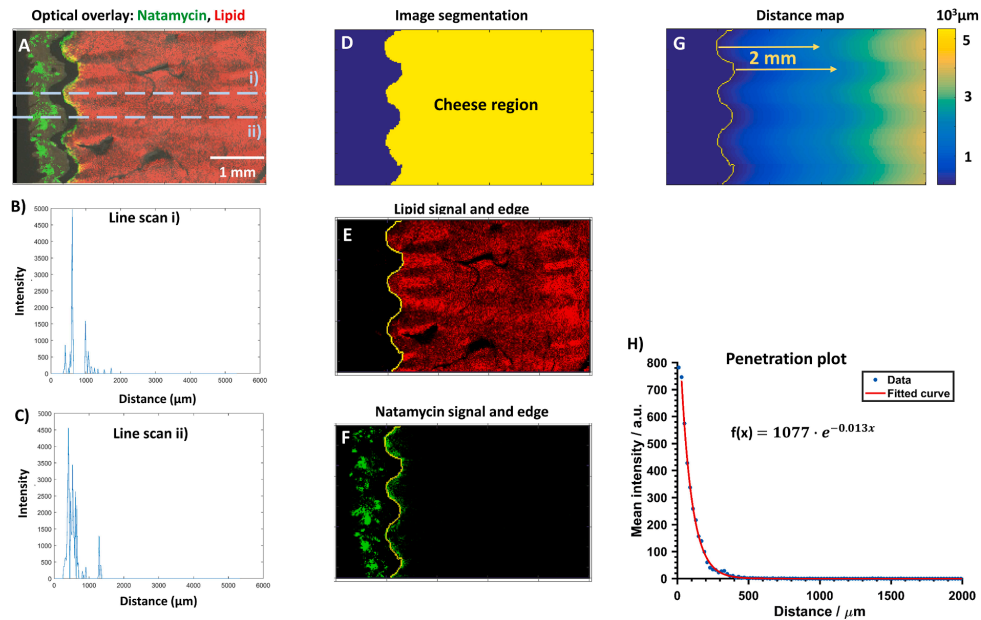


Fig. 5. Description of developed method for determining the cheese edge and then calculating a 'penetration plot' for natamycin into the cheese. A: Overlay of lipid SM(d34:1) $[M + Na]^+$, m/z 725.55680 in red, natamycin $[M + Na]^+$, m/z 688.29396 in green and optical image. B + C: Line scans, showing the intensity of natamycin against the lateral distance in μm . D: Image segmentation. E: Lipid signal and calculated edge from D panel. F: Natamycin signal displayed with edge from D panel. G: Distance map from edge of cheese surface. H: Penetration plot of natamycin into cheese including exponential fit. The mean intensity of the natamycin signal is given for a certain distance from the surface of the cheese in x-direction.

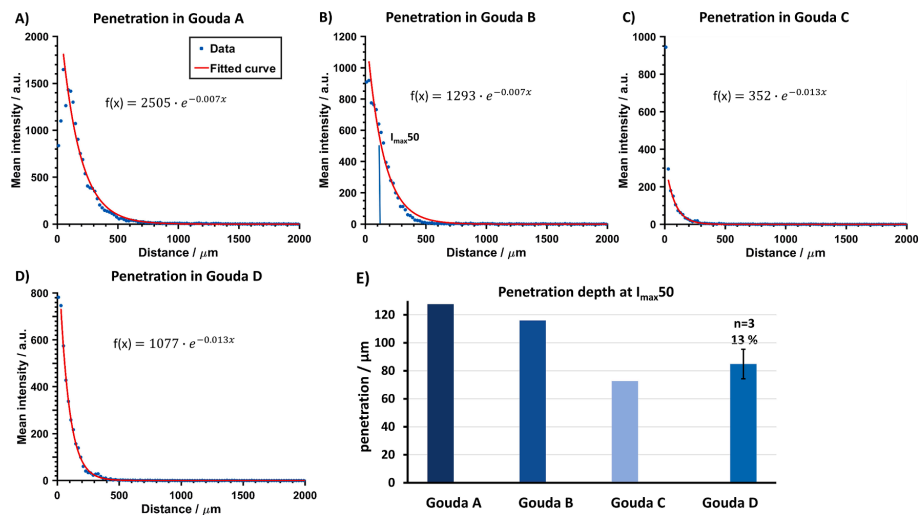


Fig. 6. Comparison of natamycin penetration in Gouda samples A, B, C and D. A-D: Penetration plots for different Gouda samples. Mean intensity against distance from the surface in μm . E: Comparison of penetration depth at 50% of maximum intensity ($I_{\text{max},50}$). For Gouda D the mean of three neighboring sections with standard deviation is shown, relative error 13 %.

much more detail and independent of uneven surfaces. With our advanced data analysis approach, it was possible to compare the natamycin penetration between different cheese samples. This penetration is most likely dependent on the application method for natamycin, which varies between brushing, dipping, spraying and addition to the brine (Kammerlehner, 2015). Therefore, our MS imaging approach confirms the current penetration limit of 5 mm as technically feasible. Moreover, the described penetration analysis could contribute to the discussion about a possible reduction of the permitted penetration limit and thereby less exposure of consumers to natamycin, which would be in line with Article 11 of Regulation (EC) 1333/2008 stating that for food additives “the level of use shall be set at the lowest level necessary to achieve the desired effect”¹¹.

4. Conclusions

MS imaging can be used for a wide range of food-related applications. Our results show that the unique combination of molecular and spatial information can provide the distribution of different compound classes in various food sample matrices. We were able to detect highly nonpolar compounds such as triglycerides in the hardy kiwi and beta-carotene in the orange carrot. We could also visualize the distribution of very polar compounds such as disaccharides and anthocyanins in hardy kiwi and purple carrot. Our data include not only fresh plant-based food, but also processed food comprising meat, dairy and bakery products. The specific properties of each sample required the development of a dedicated workflow. In the case of processed food, the workflow is more challenging due to the fragile and heterogeneous texture of the samples as they consist of multiple ingredients with varying physical and chemical properties. The properties of the processed food samples in our study ranged from lipid-rich (veal sausage/cheese) to very dry (gingerbread). We successfully visualized different distributions of food constituents (disaccharides, lipids), even in highly homogenized samples such as the German veal sausage.

In addition to constituents, we also investigated minor components of processed food, i.e. a food additive and a contaminant. Our investigations of acrylamide in gingerbread and natamycin in cheese are the first MS imaging analyses of a contaminant and a food additive distribution in processed food. Natamycin was detected in varying distributions between the investigated cheese samples. With this example, we also showed that MS imaging goes beyond mere visualization of compounds, and can provide additional information on the penetration behavior of food additives. The developed data analysis approach can be used as a general tool to investigate diffusion processes by MS imaging in a wide range of other applications. In conclusion, our results show that MS imaging has great potential to complement established methods in food analysis by providing deeper information about spatial distributions of food components, in particular those underlying official regulations.

5. Funding sources

This work was supported by the Deutsche Forschungsgemeinschaft (DFG) INST 91/373-1-FUGG and the TechnologieAllianzOberfranken (TAO).

CRedit authorship contribution statement

Julia Kokesch-Himmelreich: Investigation, Methodology, Writing – original draft. **Oliver Wittke:** Investigation, Methodology, Writing – original draft. **Alan M. Race:** Software, Methodology. **Sophie Rakete:** Investigation, Visualization. **Claus Schlicht:** Investigation, Validation.

Ulrich Busch: Validation. **Andreas Römpf:** Conceptualization, Methodology, Writing – review & editing.

Declaration of Competing Interest

The authors declare that they have no known competing financial interests or personal relationships that could have appeared to influence the work reported in this paper.

Acknowledgements

We would like to thank Holger Zorn (Justus Liebig University Gießen, Germany) for initial discussions on the topic of natamycin MS imaging and Jan Lauter for first experiments on sample preparation. We would also like to thank Holger Knapp and Jennifer Mels from the *Bavarian Health and Food Safety Authority* (LGL, Erlangen, Germany) for providing the gingerbread samples and the Max Rubner-Institute (MRI, Kulmbach, Germany) for providing the German veal sausage.

Appendix A. Supplementary data

Supplementary data to this article can be found online at <https://doi.org/10.1016/j.foodchem.2022.132529>.

References

- Baranowska-Wójcik, E., & Sz wajgier, D. (2019). Characteristics and pro-health properties of mini kiwi (*Actinidia arguta*). *Horticulture, Environment, and Biotechnology*, 60(2), 217–225. <https://doi.org/10.1007/s13580-018-0107-y>
- Baranska, M., Baranski, R., Schulz, H., & Nothnagel, T. (2006). Tissue-specific accumulation of carotenoids in carrot roots. *Planta*, 224(5), 1028–1037. <https://doi.org/10.1007/s00425-006-0289-x>
- Bednarz, H., Roloff, N., & Niehaus, K. (2019). Mass Spectrometry Imaging of the Spatial and Temporal Localization of Alkaloids in Nightshades. *Journal of Agriculture and Food Chemistry*, 67(49), 13470–13477. <https://doi.org/10.1021/acs.jafc.9b01155>
- Berisha, A., Dold, S., Guenther, S., Desbenoit, N., Takats, Z., Spengler, B., & Römpf, A. (2014). A comprehensive high-resolution mass spectrometry approach for characterization of metabolites by combination of ambient ionization, chromatography and imaging methods. *Rapid Communications in Mass Spectrometry*, 28(16), 1779–1791. <https://doi.org/10.1002/rcm.6960>
- Bhandari, D. R., Wang, Q., Friedt, W., Spengler, B., Gottwald, S., & Römpf, A. (2015). High resolution mass spectrometry imaging of plant tissues: Towards a plant metabolite atlas. *Analyst*, 140(22), 7696–7709. <https://doi.org/10.1039/C5AN01065A>
- Bokhart, M. T., Nazari, M., Garrard, K. P., & Muddiman, D. C. (2018). MSIReader v1.0: Evolving Open-Source Mass Spectrometry Imaging Software for Targeted and Untargeted Analyses. *Journal of The American Society for Mass Spectrometry*, 29(1), 8–16. <https://doi.org/10.1007/s13361-017-1809-6>
- Bonnel, D., Legouffe, R., Eriksson, A. H., Mortensen, R. W., Pamelard, F., Stauber, J., & Nielsen, K. T. (2018). MALDI imaging facilitates new topical drug development process by determining quantitative skin distribution profiles. *Analytical and Bioanalytical Chemistry*, 410(11), 2815–2828. <https://doi.org/10.1007/s00216-018-0964-3>
- Deng, Y., He, M., Feng, F., Feng, X., Zhang, Y., & Zhang, F. (2021). The distribution and changes of glycoalkaloids in potato tubers under different storage time based on MALDI-TOF mass spectrometry imaging. *Talanta*, 221, Article 121453. <https://doi.org/10.1016/j.talanta.2020.121453>
- Domínguez, I., Garrido Frenich, A., & Romero-González, R. (2020). Mass spectrometry approaches to ensure food safety. *Analytical Methods*, 12(9), 1148–1162. <https://doi.org/10.1039/c9ay02681a>
- E. Marzec, M., Wojtyśiak, D., Połtowicz, K., Nowak, J., & Pedrys, R. (2016). *Study of cholesterol and vitamin E levels in broiler meat from different feeding regimens by TOF-SIMS*.
- Enomoto, H., Furukawa, T., Takeda, S., Hatta, H., & Zaima, N. (2020). Unique Distribution of Diacyl-, Alkylacyl-, and Alkenylacyl-Phosphatidylcholine Species Visualized in Pork Chop Tissues by Matrix-Assisted Laser Desorption/Ionization–Mass Spectrometry Imaging. *Foods*, 9(2), 205. <https://www.mdpi.com/2304-8158/9/2/205>.
- Fisk, C. L., McDaniel, M. R., Strik, B. C., & Zhao, Y. (2006). Physicochemical, Sensory, and Nutritive Qualities of Hardy Kiwifruit (*Actinidia arguta* ‘Ananasnaya’) as Affected by Harvest Maturity and Storage. *Journal of Food Science*, 71(3), S204–S210. <https://doi.org/10.1111/j.1365-2621.2006.tb15642.x>
- Goto-Inoue, N., Sato, T., Morisasa, M., Igarashi, Y., & Mori, T. (2019). Characterization of Metabolite Compositions in Wild and Farmed Red Sea Bream (*Pagrus major*) Using Mass Spectrometry Imaging. *Journal of Agriculture and Food Chemistry*, 67(25), 7197–7203. <https://doi.org/10.1021/acs.jafc.9b03205>

¹¹ Art. 11 (1) lit. a Regulation (EC) 1333/2008 of the European Parliament and of the Council of 16 December 2008 on food additives.

- Hallett, I. C., & Sutherland, P. W. (2005). Structure and Development of Kiwifruit Skins. *International Journal of Plant Sciences*, 166(5), 693–704. <https://doi.org/10.1086/431232>
- Handberg, E., Chingin, K., Wang, N., Dai, X., & Chen, H. (2015). Mass spectrometry imaging for visualizing organic analytes in food. *Mass Spectrometry Reviews*, 34(6), 641–658. <https://doi.org/10.1002/mas.21424>
- Jira, W., & Schwägele, F. (2017). A sensitive high performance liquid chromatography-tandem mass spectrometry method for the detection of microbial transglutaminase in different types of restructured meat. *Food Chemistry*, 221, 1970–1978. <https://doi.org/10.1016/j.foodchem.2016.11.148>
- Kammerlehner, J. (2015). *Käsetechnologie*. (3 ed.): B&L Mediengesellschaft mbH & Co. KG.
- Kim, J. G., Beppu, K., & Kataoka, I. (2009). Varietal differences in phenolic content and astringency in skin and flesh of hardy kiwifruit resources in Japan. *Scientia Horticulturae*, 120(4), 551–554. <https://doi.org/10.1016/j.scienta.2008.11.032>
- Lebensmittelbuch-Kommission, D. (2019). *Leitsätze des Deutschen Lebensmittelbuchs für Fleisch und Fleischerzeugnisse*. Zuletzt geändert durch die Bekanntmachung vom 17.04.2019. (p. 319). GMBI.
- Li, Bin, Dunham, Sage J. B., Dong, Yonghui, Yoon, Sohee, Zeng, Maomao, & Sweedler, Jonathan V. (2016). Analytical capabilities of mass spectrometry imaging and its potential applications in food science. *Trends in Food Science & Technology*, 47, 50–63. <https://doi.org/10.1016/j.tifs.2015.10.018>
- Machalkova, M., Pavlatovska, B., Michalek, J., Pruska, A., Stepka, K., Necasova, T., ... Navratilova, J. (2019). Drug Penetration Analysis in 3D Cell Cultures Using Fiducial-Based Semiautomatic Coregistration of MALDI MSI and Immunofluorescence Images. *Analytical Chemistry*, 91(21), 13475–13484. <https://doi.org/10.1021/acs.analchem.9b02462>
- Medina, S., Pereira, J. A., Silva, P., Perestrelo, R., & Cámara, J. S. (2019). Food fingerprints – A valuable tool to monitor food authenticity and safety. *Food Chemistry*, 278, 144–162. <https://doi.org/10.1016/j.foodchem.2018.11.046>
- Nielen, M. W., & van Beek, T. A. (2014). Macroscopic and microscopic spatially-resolved analysis of food contaminants and constituents using laser-ablation electrospray ionization mass spectrometry imaging. *Analytical and Bioanalytical Chemistry*, 406(27), 6805–6815. <https://doi.org/10.1007/s00216-014-7948-8>
- Nishiyama, I., Yamashita, Y., Yamanaka, M., Shimohashi, A., Fukuda, T., & Oota, T. (2004). Varietal Difference in Vitamin C Content in the Fruit of Kiwifruit and Other Actinidia Species. *Journal of Agricultural and Food Chemistry*, 52(17), 5472–5475. <https://doi.org/10.1021/jf049398z>
- Park, H.-M., Son, M.-W., Kim, D.-H., Kim, S.-H., Kim, S.-H., Kwon, H.-C., & Kim, S.-Y. (2011). Fatty Acid Components of Hardy Kiwifruit (*Actinidia arguta*) as IL-4 Production Inhibitor. *Biomolecules and Therapeutics*, 19. <https://doi.org/10.4062/biomolther.2011.19.1.126>
- Paschke, C., Leisner, A., Hester, A., Maass, K., Guenther, S., Bouschen, W., & Spengler, B. (2013). Mirion—a software package for automatic processing of mass spectrometric images. *Journal of the American Society for Mass Spectrometry*, 24(8), 1296–1306. <https://doi.org/10.1007/s13361-013-0667-0>
- Piombo, G., Barouh, N., Barea, B., Boulanger, R., Brat, P., Pina, M., & Villeneuve, P. (2006). Characterization of the seed oils from kiwi (*Actinidia chinensis*), passion fruit (*Passiflora edulis*) and guava (*Psidium guajava*). *OCL*, 13(2–3), 195–199. <https://doi.org/10.1051/ocl.2006.0026>
- Race, A. M., Palmer, A. D., Dexter, A., Steven, R. T., Styles, I. B., & Bunch, J. (2016). SpectralAnalysis: Software for the Masses. *Analytical Chemistry*, 88(19), 9451–9458. <https://doi.org/10.1021/acs.analchem.6b01643>
- Race, A. M., & Römpf, A. (2018). Error-Free Data Visualization and Processing through imzML and mzML Validation. *Analytical Chemistry*, 90(22), 13378–13384. <https://doi.org/10.1021/acs.analchem.8b03059>
- Race, A. M., Styles, I. B., & Bunch, J. (2012). Inclusive sharing of mass spectrometry imaging data requires a converter for all. *Journal of Proteomics*, 75(16), 5111–5112. <https://doi.org/10.1016/j.jpro.2012.05.035>
- Rešetar Maslov, D., Svirikova, A., Allmaier, G., Marchetti-Deschmann, M., & Kraljević Pavelić, S. (2019). Optimization of MALDI-TOF mass spectrometry imaging for the visualization and comparison of peptide distributions in dry-cured ham muscle fibers. *Food Chemistry*, 283, 275–286. <https://doi.org/10.1016/j.foodchem.2018.12.126>
- Römpf, A., & Spengler, B. (2013). Mass spectrometry imaging with high resolution in mass and space. *Histochemistry and Cell Biology*, 139(6), 759–783. <https://doi.org/10.1007/s00418-013-1097-6>
- Schramm, T., Hester, A., Klinkert, I., Both, J. P., Heeren, R. M., Brunelle, A., ... Römpf, A. (2012). imzML—a common data format for the flexible exchange and processing of mass spectrometry imaging data. *Journal of Proteomics*, 75(16), 5106–5110. <https://doi.org/10.1016/j.jpro.2012.07.026>
- Souci, S. W., Fachmann, W., & Kraut, H. (2008). *Food Composition and Nutrition Tables. (7th revised and completed edition ed.)*. Stuttgart: Medpharm Scientific Publ.
- Spengler, B. (2015). Mass Spectrometry Imaging of Biomolecular Information. *Analytical Chemistry*, 87(1), 64–82. <https://doi.org/10.1021/ac504543v>
- Stadler, R. H., Blank, I., Varga, N., Robert, F., Hau, J., Guy, P. A., ... Riediker, S. (2002). Acrylamide from Maillard reaction products. *Nature*, 419(6906), 449–450. <https://doi.org/10.1038/419449a>
- Treu, A., Kokesch-Himmelreich, J., Walter, K., Holscher, C., & Römpf, A. (2020). Integrating High-Resolution MALDI Imaging into the Development Pipeline of Anti-Tuberculosis Drugs. *Journal of the American Society for Mass Spectrometry*. <https://doi.org/10.1021/jasms.0c00235>
- Treu, A., & Römpf, A. (2021). Matrix ions as internal standard for high mass accuracy MALDI mass spectrometry imaging. *Rapid Communications in Mass Spectrometry*, e9110. <https://doi.org/10.1002/rcm.9110>
- Wang, J., Yang, E., Chaurand, P., & Raghavan, V. (2021). Visualizing the distribution of strawberry plant metabolites at different maturity stages by MALDI-TOF imaging mass spectrometry. *Food Chemistry*, 345, Article 128838. <https://doi.org/10.1016/j.foodchem.2020.128838>
- Yang, X., Leng, X., Qi, Y., Zhang, J., Jiang, R., Li, W., & Zhong, H. (2020). Monitoring of adsorption and transfer of organochlorines in soybean seeds and sprouts with mass spectrometry imaging. *Analytica Chimica Acta*, 1130, 10–19. <https://doi.org/10.1016/j.aca.2020.07.011>
- Yoshimura, Y., & Zaima, N. (2020). Application of Mass Spectrometry Imaging for Visualizing Food Components. *Foods*, 9(5). <https://doi.org/10.3390/foods9050575>

Supplementary material

MALDI mass spectrometry imaging: from constituents in fresh food to ingredients, contaminants and additives in processed food

Julia Kokesch-Himmelreich ^{a,‡}, Oliver Wittek ^{a,‡}, Alan M. Race ^a, Sophie Rakete ^a,
Claus Schlicht ^b, Ulrich Busch ^b, Andreas Römpf ^{a,*}

a Bioanalytical Sciences and Food Analysis, University of Bayreuth, Bayreuth, Germany

b Bavarian health and food safety authority, Oberschleißheim, Germany

Julia.Kokesch-Himmelreich@uni-bayreuth.de

Oliver.Wittek@uni-bayreuth.de

alan.race@uni-marburg.de

Sophie.Rakete@med.uni-muenchen.de

Claus.Schlicht@lgl.bayern.de

Ulrich.busch@lgl.bayern.de

Andreas.Roempp@uni-bayreuth.de

[‡]The respective authors contributed equally to the preparation of this manuscript

*Corresponding author:

Andreas Römpf,

Chair of Bioanalytical Sciences and Food Analysis, University of Bayreuth

Universitätsstraße 30, 95447 Bayreuth

Andreas.roempp@uni-bayreuth.de

0049-921-553662

1. Material and Methods

Table S1: Gouda samples provided by the LGL (Bavarian health and food safety authority). Shown natamycin concentrations were measured by the LGL using the HPLC-DAD reference method. All listed samples were also investigated in this study by MS imaging.

Sample	Natamycin declaration	mg/dm ² Surface	mg/dm ² Bulk
Gouda Blank	no	< 0.01	< 0.01
Gouda A	yes	0.57	< 0.01
Gouda B	yes	0.42	< 0.01
Gouda C	yes	0.11	< 0.01
Gouda D	yes	0.38	< 0.01

Table S2: Sample preparation: Detailed information of sectioning and spraying parameters for all samples in this study. *The gingerbread sample and the cutting disk were cooled to -60 °C before sectioning. [Sectioning of gingerbread](#) was not performed in a cryostat, please see the “methods” section in the main paper.

Sample	Sectioning		Spray Parameters				
	OT/°C	thickness/μm	DHB Solution	Ratio	Flow rate/μl/min	gas pressure/bar	Volume/mL
Hardy Kiwi	-24	30	Aceton/H2O + 0.1% TFA	1:1	10	0.7	175
Orange carrot	-15	100	Aceton/H2O + 0.1% TFA	1:1	10	0.7	175
Purple carrot	-24	50	Aceton/H2O + 0.1% TFA	1:1	10	0.7	175
Veal sausage	-25	16	Aceton/H2O + 0.1% TFA	1:1	15	0.7	170
Gouda	-20	14/16	Aceton/H2O + 0.1% TFA	1:1	10	0.7	170
Gingerbread	-60*	2000	Aceton/H2O + 0.1% TFA	70:30	10	0.7	200

Table S3: Detailed data acquisition parameters for MALDI MS imaging. The gingerbread section was measured in an alternating scanning mode (Treu, Kokesch-Himmelreich, Walter, Holscher, & Römpp, 2020) with a step size of 100 μm x 200 μm (XxY). Every second scan event was measured with one of the given mass ranges (m/z 50-165 or m/z 250-1000). This leads to a pixel size of 200 μm in the MS images.

Sample	Raster size	Step size	mass range
Hardy Kiwi	320x540	45	250-1000
Orange carrot	237x237	50	100-1500
Purple carrot	244x216	80	200-800
Veal sausage	240x170	20	200-900
Gouda A	340x185	20	200-800
Gouda B	310x145	20	200-800
Gouda C	330x175	20	200-800
Gouda D	315x150	20	200-800
Gouda blank	285x235	20	200-800
Gingerbread	43x104	100x200	50-165 / 250-1000

2. Results and discussion:

Constituents in fresh plant-based food

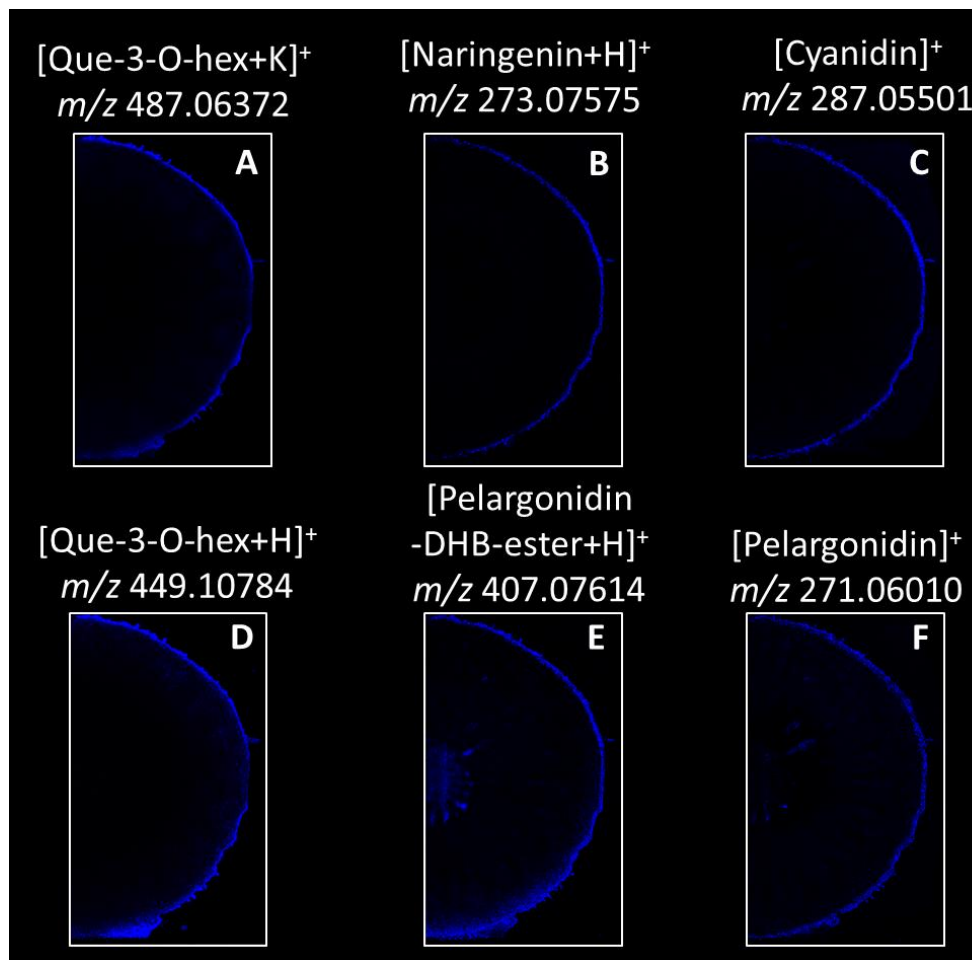


Figure S1: Distributions of additional anthocyanin signals in hardy kiwi (Figure 1). All depicted analytes show high intensities in the peel, pelargonidin is also detectable in the stem (E,F).

Ingredients in animal-based processed food

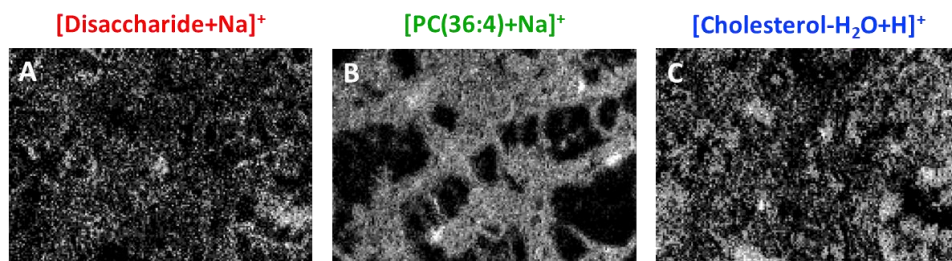


Figure S2: Single ion images for the RGB MS image of three constituents of German veal sausage in Figure 2C. A: Disaccharide ($[M+Na]^+$, m/z 365.10544), B:PC(36:4) ($[M+Na]^+$, m/z 804.55138), and C: Cholesterol ($[M-H_2O+H]^+$, m/z 369.35158).

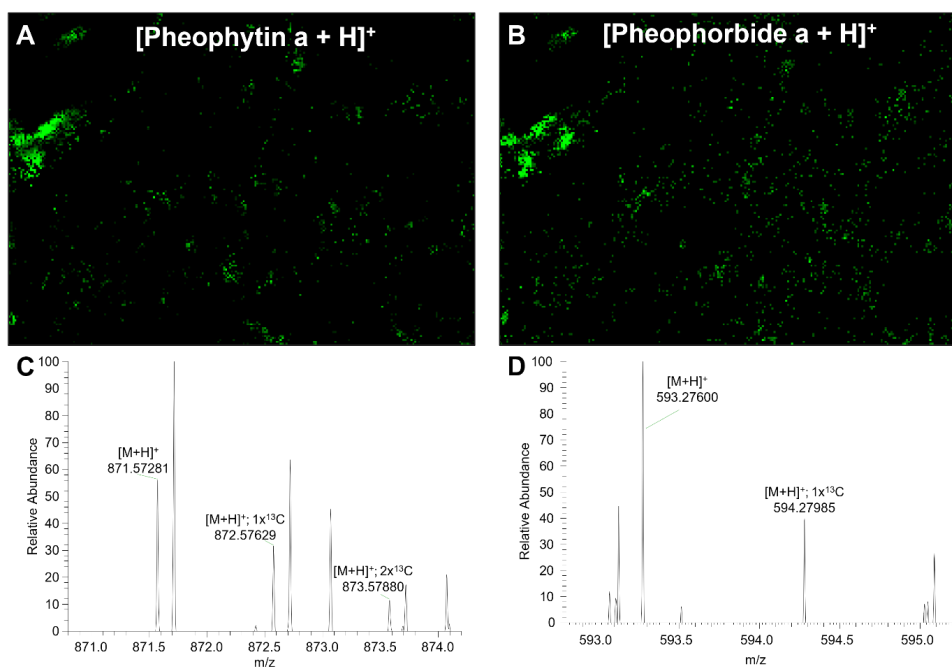


Figure S3: Distribution of chlorophyll-derivatives originating from added herbs in German veal sausage in Figure 2C. A: Pheophytin a ($[M+H]^+$, m/z 871.57319) and B: Pheophorbide a ($[M+H]^+$, m/z 593.27584). C and D: Single pixel mass spectra of pheophytin a and pheophorbide a, respectively. Spectra show the monoisotopic peak and corresponding isotope peak(s).

Additives in animal-based processed food

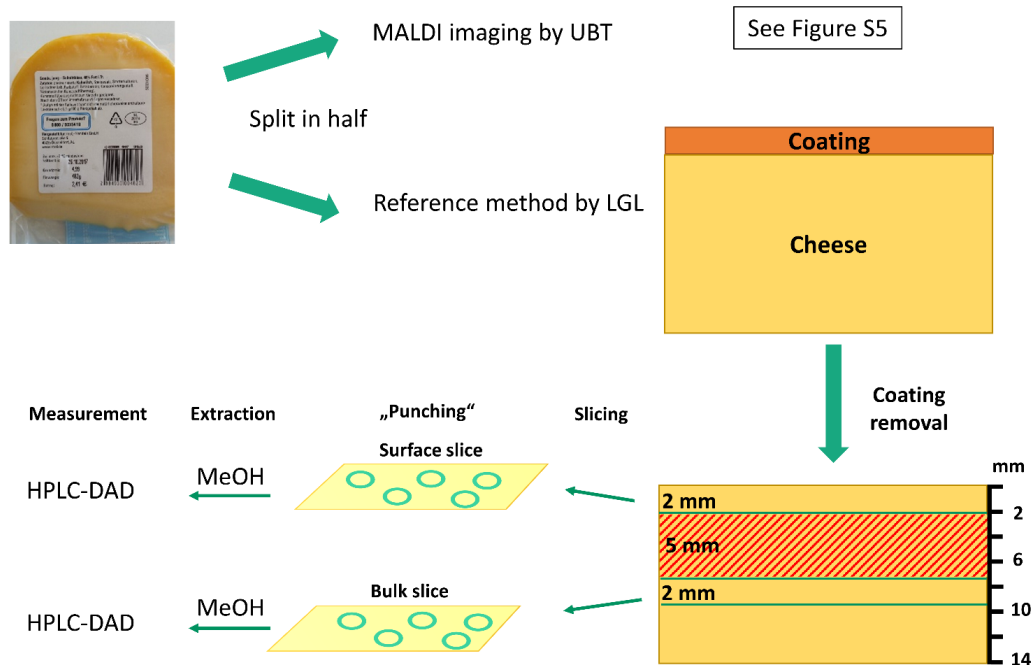


Figure S4: HPLC-DAD reference method for quantification of natamycin: Adapted from § 64 LFGB - German Food and Feed Code.

The cheese samples were split in half. One half was shipped on ice to the University of Bayreuth for MALDI imaging analysis. The other half was investigated using the HPLC-DAD reference method by the LGL. After removing the coating of the cheese, a slice of 2 mm was set aside for further analysis, another 5 mm were discarded and another slice of 2 mm was used also for further analysis. The first slice was collected to determine the surface concentration and the second as reference for the bulk concentration. From both slices 5 tablets were punched out and subjected to methanol extraction followed by HPLC-DAD analysis. Separation was performed on a LiChrospher® 100 RP-18 (5 µm) LiChroCART® 125-4 column (125 x 4,0 mm; 5 µm) with an isocratic eluent mixture of 75 %V methanol and 25 %V 22.2 mM aqueous KH₂PO₄ (pH 4.45). The DAD scan range was set to λ = 220 – 400 nm, peak absorbance maximum for quantification was set to λ = 303 nm. Quantification was based on an external calibration using natamycin standard.

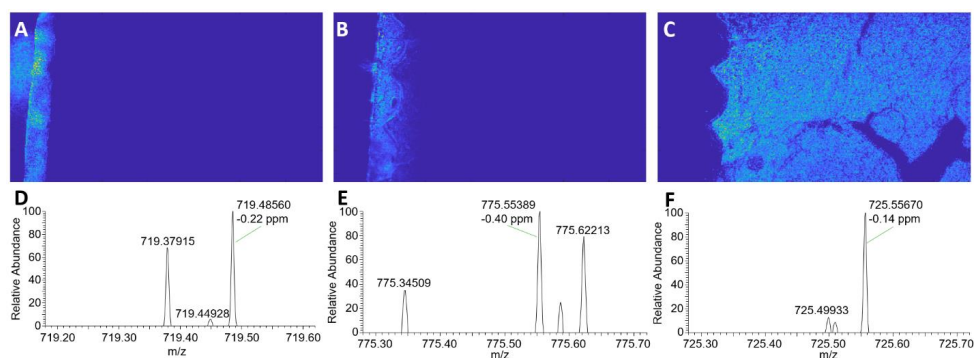


Figure S6: Single ion images of the RGB MS image in Figure 4B: Characteristic compounds for the coatings PG32:2 ($[M+H]^+$, m/z 719.48576 (A), $C_{40}H_{80}O_{12}$ $[M+Na]^+$, m/z 775.55420 (B) and the lipid SM(d34:1) ($[M+Na]^+$, m/z 725.55680) (C). Representative mass spectra of the respective compounds above are given in (D), (E) and (F).

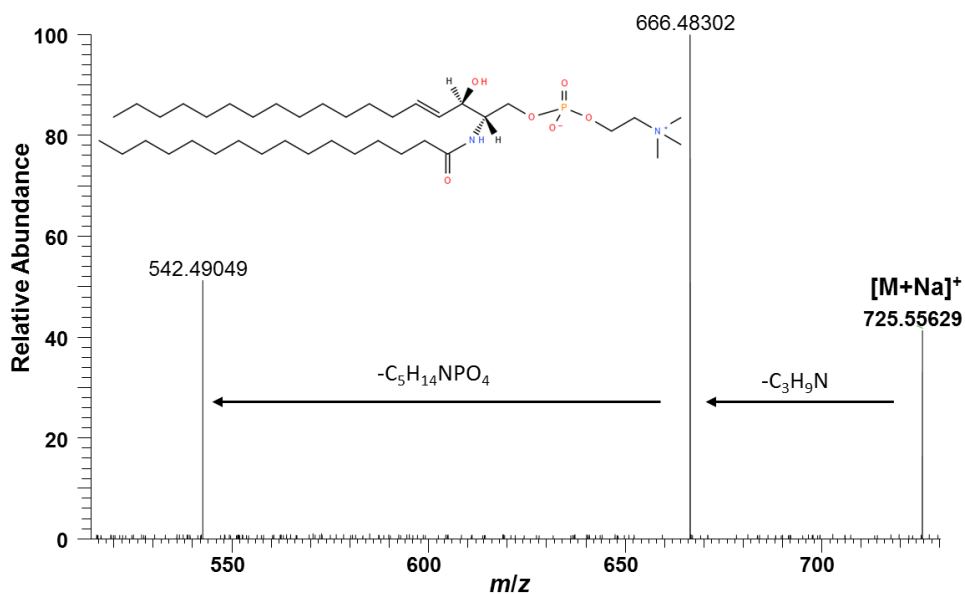


Figure S7: Average MS/MS spectrum of lipid signal m/z 725.55680 in Figure 4B (HCE = 25, isolation window = $m/z \pm 0.2$). The two characteristic neutral losses of C_3H_9N and $C_5H_{14}NPO_4$ confirm the lipid species sphingomyelin. Therefore we annotated the signal with the database result SM(d34:1) (lipidmaps.org).

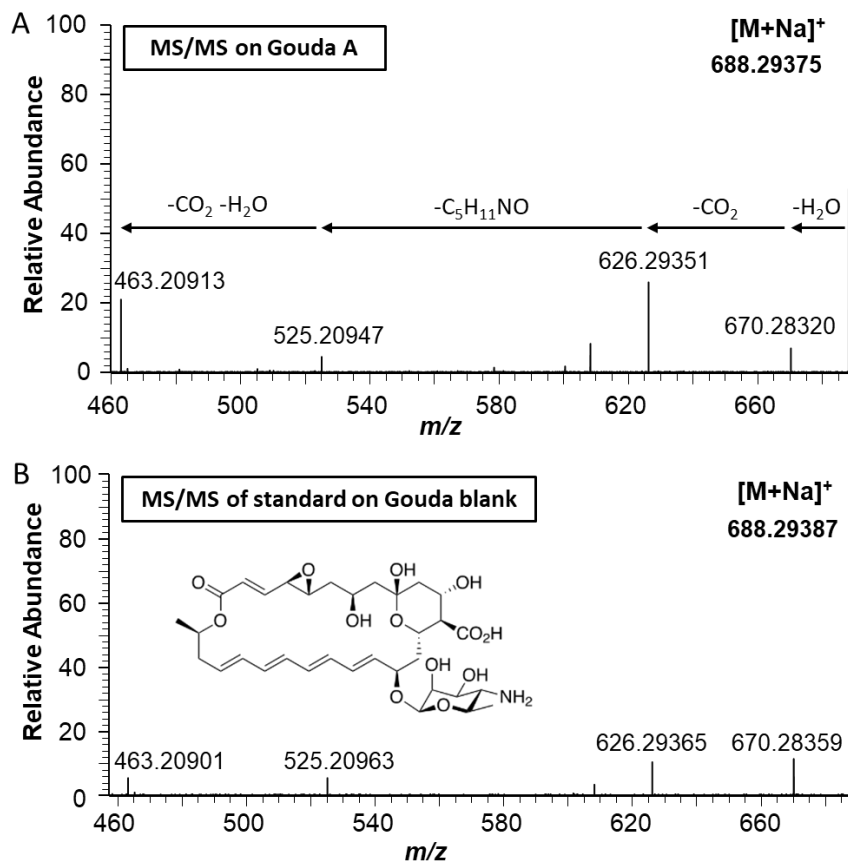


Figure S8: Comparison of MS/MS spectra of natamycin: A: MS/MS of natamycin hot spot on Gouda sample A (HCE = 25, isolation window = $m/z \pm 0.2$). B: MS/MS of natamycin standard. A 2.5 % aqueous natamycin suspension was diluted in methanol/water (50:50, v/v) and pipetted on a Gouda blank section. DHB was applied as for all other cheese samples. For MS/MS experiments an isolation window of $m/z \pm 0.2$ and a collision energy of 20 was used. The same fragment ions could be detected with slightly different intensities, which can be explained by the different collision energies. In combination with the high mass accuracy in the full MS spectrum (see Figure 4) the signal at m/z 668 can be unequivocally identified as the sodiated natamycin.

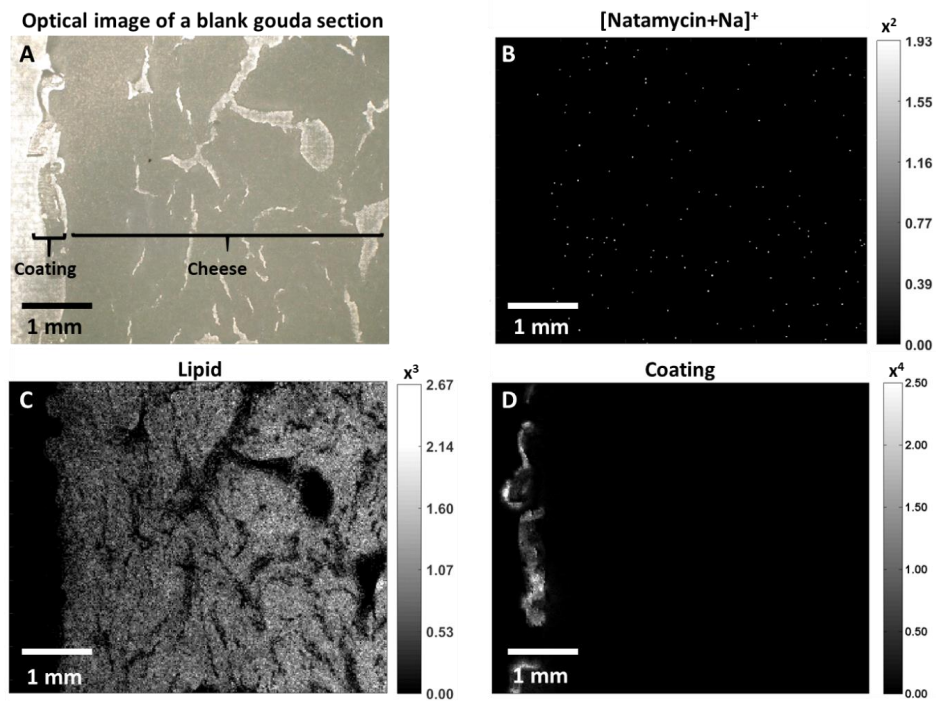


Figure S9: MS imaging of blank Gouda section: A) optical image, B) Natamycin signal ($[M+Na]^+$, m/z 688.29396), C) Distribution of lipid SM(d34:1) ($[M+Na]^+$, m/z 725.55660), D) coating signal m/z 512.40041. The lipid and coating distribution match the optical image well. No natamycin could be detected in this Gouda section.

Penetration analysis

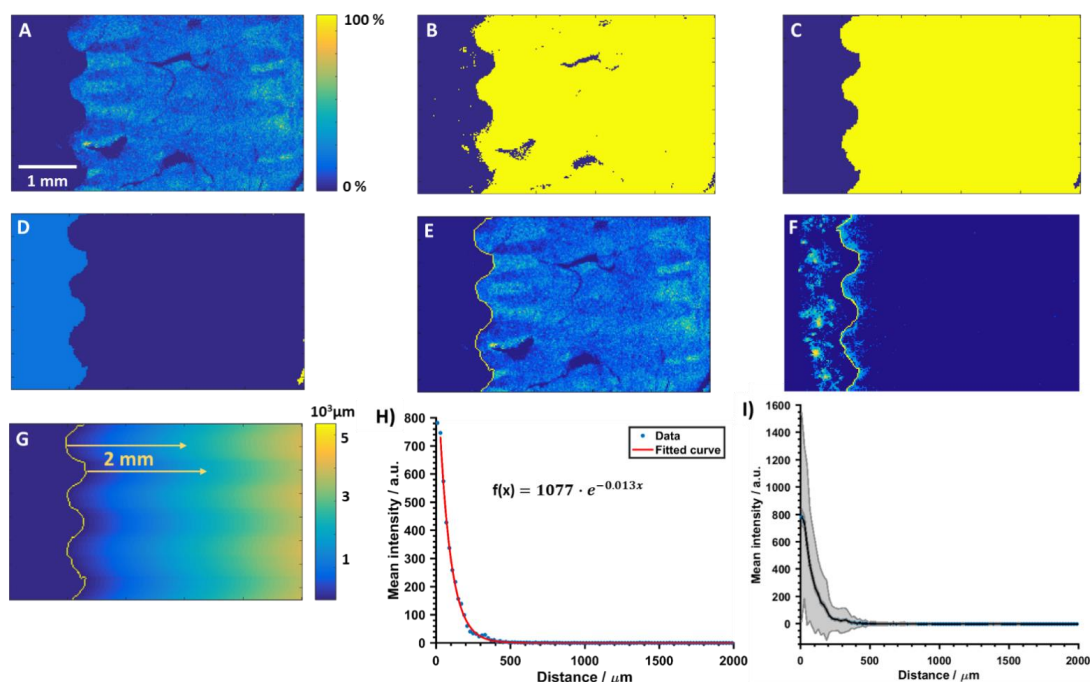


Figure S10: Detailed developed data analysis approach.

An ion image representing a lipid signal which is only present in the cheese region was generated (Fig S10A). The ion image was then thresholded to form a binary mask (Figure S10B). Small features were removed using the mathematical morphology opening (erosion followed by dilation) with a disk-shaped structuring element (radius = 3) leaving a binary mask of the cheese bulk. Holes in the binary image were then filled, with the largest continuous remaining area forming the cheese mask (Figure 10C). The inverse of this mask formed the 'off cheese' mask (Figure S10D). The cheese boundary was defined as the edge between the cheese and off-cheese masks and is shown with the lipid signal in Figure S10E and with the natamycin signal in Figure S10F. Using the cheese boundary, it is possible to calculate the distance (Euclidean distance in the 'x' direction) from the cheese edge of every pixel within the cheese region, shown pictorially in the distance map in Figure (S10G). The intensity of the analyte of interest at every pixel within the cheese can be combined with the distance information (binned at the pixel size of 20 μm) and was averaged (mean intensity) for a certain distance to form a penetration curve (Figure S10H). Each data point represents the mean intensity of natamycin for all pixels with this certain distance. An exponential function was then fit to this data and the standard error calculated (shown in shaded area in Figure S10I). Figure S10I shows that the first pixels have the highest error. As the first pixel in the distance plot is at the cheese edge, it is possible that this covers both 'off' and 'on' cheese regions, and so was omitted from the exponential curve fitting process.

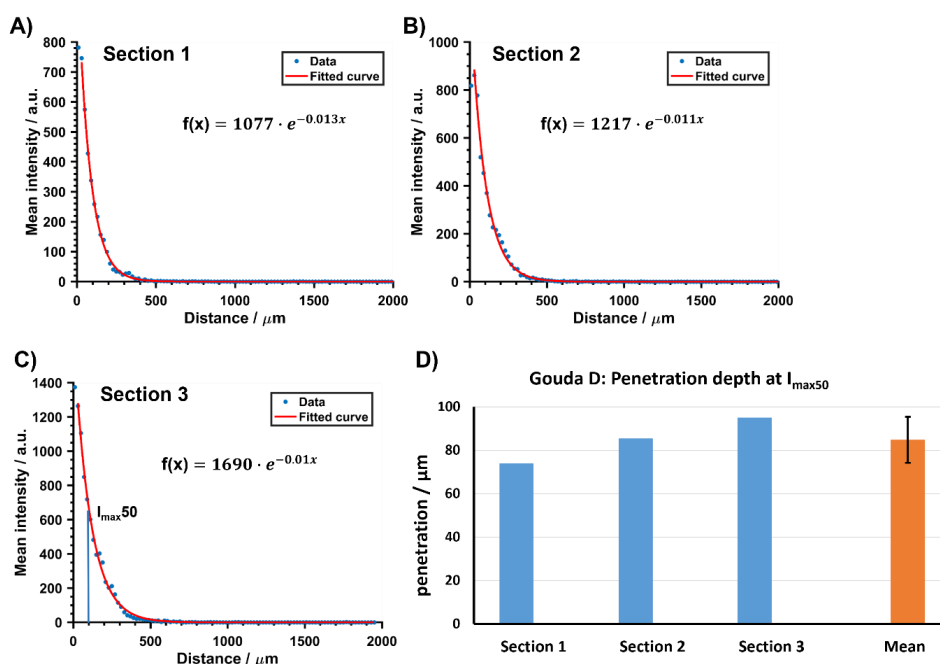


Figure S11: Penetration curves for three neighboring sections of Gouda D. A) Penetration curve including exponential fit and equation of section 1 (same as Figure 5H and 6D). B) Penetration curve including exponential fit and equation of section 2 of the same cheese. C) Penetration curve including exponential fit and equation of section 3 of the same cheese. D: Comparison of calculated $I_{\max 50}$ values and calculated mean and standard deviation for all three sections. A relative error of 13% was calculated and shows the good reproducibility of the whole workflow.

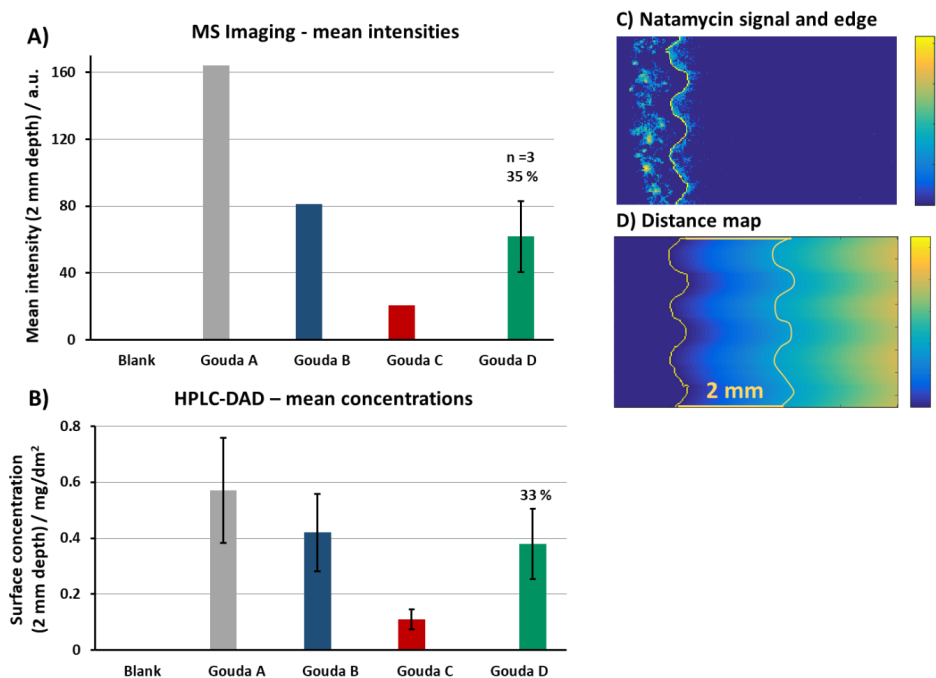


Figure S12: Comparison of natamycin signal intensities among Gouda cheese samples. A: Mean intensities of natamycin of all pixels in the first 2 mm on cheese in the MS imaging experiments for all four cheese samples. Gouda sample D is shown as mean of three serial sections, with a relative standard deviation of 35%. B: Surface concentrations of natamycin in the first 2 mm found by HPLC-DAD measurements after homogenization (reference method). All values have a relative standard deviation of 33%. C: Natamycin signal and edge for Gouda D, section 1. D: Distance map with edge and 2 mm line for Gouda D, section 1.

The mean intensities of natamycin from the imaging experiments for the first 2 mm of the four Gouda cheese sections are shown in Figure S12A. For the MALDI-MS imaging results of Gouda D the mean of three neighboring sections is shown with a relative standard deviation of 35%. In Figure S12 C the natamycin signal for section 1 of Gouda D is depicted with the calculated edge. In Figure S12D the distance map is shown with a second line at 2 mm after the edge. The mean of the natamycin intensities were calculate for all pixels in the first 2 mm after the edge. For comparison, the HPLC-DAD results from the first 2 mm of the cheese, which were measured by LGL are depicted in Figure S12B. The HPLC-DAD results are shown with a relative standard deviation of 33%. This high relative error results from the low intensities and a low recovery rate. The relative standard deviation was calculated with a different line of LC-experiments. The MS imaging results follow the same trend as the homogenate analysis from the HPLC-DAD reference method.

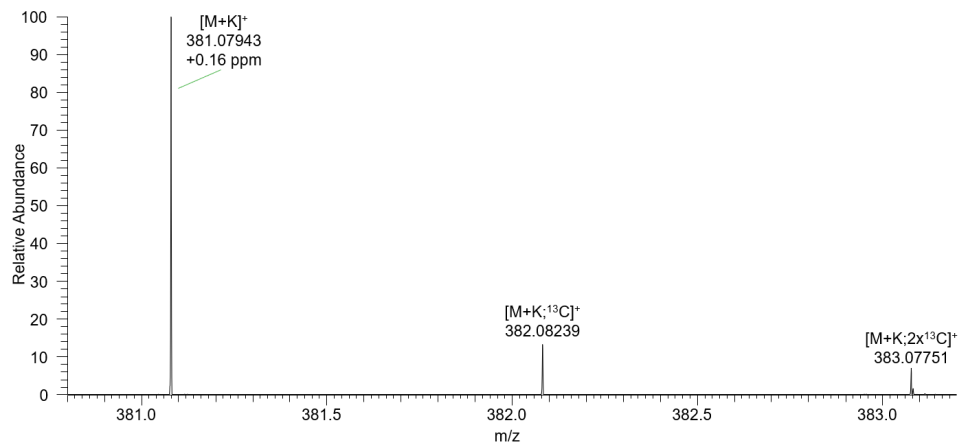


Figure S13: Single pixel mass spectrum of disaccharide $[M+K]^+$, m/z 381.07937 and the corresponding ^{13}C -isotope signals

References

- Bokhart, M. T., Nazari, M., Garrard, K. P., & Muddiman, D. C. (2018). MSiReader v1.0: Evolving Open-Source Mass Spectrometry Imaging Software for Targeted and Untargeted Analyses. *Journal of the American Society for Mass Spectrometry*, 29(1), 8-16.
- Race, A. M., Palmer, A. D., Dexter, A., Steven, R. T., Styles, I. B., & Bunch, J. (2016). SpectralAnalysis: Software for the Masses. *Anal Chem*, 88(19), 9451-9458.
- Race, A. M., & Römpp, A. (2018). Error-Free Data Visualization and Processing through imzML and mzML Validation. *Anal Chem*, 90(22), 13378-13384.
- Race, A. M., Styles, I. B., & Bunch, J. (2012). Inclusive sharing of mass spectrometry imaging data requires a converter for all. *Journal of Proteomics*, 75(16), 5111-5112.
- Schramm, T., Hester, A., Klinkert, I., Both, J. P., Heeren, R. M., Brunelle, A., Laprevote, O., Desbenoit, N., Robbe, M. F., Stoeckli, M., Spengler, B., & Römpp, A. (2012). imzML--a common data format for the flexible exchange and processing of mass spectrometry imaging data. *J Proteomics*, 75(16), 5106-5110.
- Treu, A., Kokesch-Himmelreich, J., Walter, K., Holscher, C., & Römpp, A. (2020). Integrating High-Resolution MALDI Imaging into the Development Pipeline of Anti-Tuberculosis Drugs. *J Am Soc Mass Spectrom*.

3.2 Autofocusing MALDI MS imaging of processed food exemplified by the contaminant acrylamide in German gingerbread

www.nature.com/scientificreports

scientific reports


 Check for updates

OPEN **Autofocusing MALDI MS imaging of processed food exemplified by the contaminant acrylamide in German gingerbread**

Oliver Wittke  & Andreas Römpf 

Acrylamide is a toxic reaction product occurring in dry-heated food such as bakery products. To meet the requirements laid down in recent international legal norms calling for reduction strategies in food prone to acrylamide formation, efficient chromatography-based quantification methods are available. However, for an efficient mitigation of acrylamide levels, not only the quantity, but also the contaminant's distributions are of interest especially in inhomogeneous food consisting of multiple ingredients. A promising tool to investigate the spatial distribution of analytes in food matrices is mass spectrometry imaging (MS imaging). In this study, an autofocusing MALDI MS imaging method was developed for German gingerbread as an example for highly processed and instable food with uneven surfaces. Next to endogenous food constituents, the process contaminant acrylamide was identified and visualized keeping a constant laser focus throughout the measurement. Statistical analyses based on relative acrylamide intensities suggest a higher contamination of nut fragments compared to the dough. In a proof-of-concept experiment, a newly developed *in-situ* chemical derivatization protocol is described using thiosalicylic acid for highly selective detection of acrylamide. This study presents autofocusing MS imaging as a suitable complementary method for the investigation of analytes' distributions in complex and highly processed food.

Acrylamide is a toxic reaction product, which is under debate due to its presence in a variety of heated foodstuffs, especially in carbohydrate-rich food¹. As a Maillard-reaction product it is formed mainly during dry heating above 120 °C (frying, baking or roasting) of food containing its precursors, namely the amino acid asparagine and reducing sugars^{2,3}. The cause of increasing concern about the presence of acrylamide in food lies in its toxic and carcinogenic properties, mainly exerted by its epoxidation product glycidamide^{4,5}. Acrylamide is declared as "probably carcinogenic to humans" by the International Agency for Research on Cancer (IARC)⁶ and the harmonized classification and labelling (CLP) approved by the European Union lists the substance as carcinogenic, mutagenic and toxic to reproduction (Reg. (EC) 1232/2008)⁷. In the context of food and with respect to human studies⁸, acrylamide's carcinogenicity is, however, considered inconclusive by the European Food Safety Authority's Panel on Contaminants in the Food Chain (EFSA CONTAM Panel)⁹. In the light of reports on an endogenous level of acrylamide in the human bloodstream¹⁰ and recent scientific recommendations towards the definition of a tolerable daily intake (TDI)¹¹, the discussion about acrylamide in food and the necessity of mitigation measures has been sparked once more. Nevertheless, since acrylamide is considered a food contaminant, international legislation introduced guidelines and strategies to reduce its amount in foodstuffs¹². While the US Food and Drug Administration (FDA) released a Guidance document for the industry in 2016¹³, the EU passed Regulation (EU) 2017/2158¹⁴, which entered into force on April 11, 2018. Among the food listed in these legal norms, gingerbread is a prominent example since it is prone to acrylamide formation during baking^{15,16}. Next to possible approaches to reduce acrylamide in gingerbread, a benchmark level of 800 µg/kg was set by the Commission¹⁷. Traditional German gingerbread ('Elisenlebkuchen') is an exquisite spiced sweet product consisting of less than 10% cereal products and at least 25% almonds, walnuts and/or hazelnuts¹⁸, thus providing the necessary acrylamide precursors. Another, less prominent, example for potentially acrylamide-rich food is pancakes. Although not falling within the scope of the respective Regulation, pancakes might contain significant levels of acrylamide and could therefore be relevant contributors to the dietary exposure to acrylamide, which is why they are listed in Commission Recommendation (EU) 2019/1888 as food to be monitored regularly regarding

Bioanalytical Sciences and Food Analysis, University of Bayreuth, Universitaetsstrasse 30, 95447 Bayreuth, Germany.  email: andreas.roempf@uni-bayreuth.de

www.nature.com/scientificreports/

the presence of acrylamide¹⁹. Since pancakes are often prepared by customers at home, i.e., in uncontrolled conditions compared to industrial baking, the investigation of acrylamide formation is of high interest from a food safety point of view. In addition, pancakes constitute a suitable model system for mass spectrometry imaging investigation of acrylamide formation in food.

To reliably determine the amounts of acrylamide in food, powerful analytical methods are needed. Currently, mass spectrometry-based methods after Carrez precipitation, Quechers extraction and chromatographic separation are most common for acrylamide analysis, some also include derivatization strategies prior to or after chromatographic separation^{8,20}. However, these techniques require homogenization and provide no information on the spatial distribution of acrylamide throughout the food sample. For the development of efficient mitigation measures tailored to the specific food product, it is not only the mere quantity of acrylamide, which is of interest to manufacturers, but also knowledge about the distribution and possible hotspots. A promising analytical tool to fill this gap is mass spectrometry imaging (MS imaging). MS imaging is a rapidly evolving technique in (bio-) analytical chemistry which links mass spectrometric data to defined locations throughout the surface of an analyzed biological sample. In medicine as well as in animal and plant biology, MS imaging has steadily developed into a sophisticated technology with numerous applications^{21–24}. The rapid expansion of MS imaging in these fields has also sparked applications in food analysis. The majority focused on the localization of constituents in unprocessed fresh food using matrix-assisted laser desorption/ionization (MALDI) as ionization technique²⁵. Moreover, fresh food samples have also been investigated using desorption electrospray ionization (DESI)²⁶, laser-ablation electrospray ionization (LAESI)²⁷ and secondary ion mass spectrometry (SIMS)²⁸. Advancements of MS imaging in the field of food analysis were reviewed by Yoshimura et al.²⁹. In recent years, also processed food with an altered texture compared to the respective raw product became subject to MS imaging studies, such as dry-cured ham³⁰ and roasted coffee beans³¹. Due to alterations of the native cell structure during processing steps, such as cooking, baking, roasting or drying, processed food usually poses a greater challenge regarding sample preparation. Well-established preparation protocols might need to be adapted or even replaced by suitable alternatives, especially when attempting to image low abundant analytes, such as acrylamide. For instance, cryosectioning, as the standard method for the preparation of sample sections for MS imaging, is not suitable for inhomogeneous samples such as German gingerbread. Cryosectioning has been successfully applied to obtain thin sections of food both of animal and plant origin, such as dried ham muscle³² or wheat grains³³. However, its success often depends on a compact tissue structure or at least a firm sample texture. Thus, for samples with an altered and delicate texture, an alternative sectioning method is needed. Apart from the challenge of preparing processed food samples and successfully visualizing low abundant components with MALDI MS imaging, the selectivity of acrylamide detection constitutes another challenge. Commonly applied measures to ensure high selectivity in MS imaging experiments are high mass accuracy and *in-situ* MS/MS experiments³³. In liquid chromatography methods, another common tool to enhance selectivity is derivatization of the target analytes prior to or following chromatographic separation³⁴. For acrylamide detection in HPLC, derivatization protocols using D-cysteine^{35,36}, 2-naphthalenethiol^{37,38} and thiosalicylic acid (TSA)^{39,40} have been published. All derivatization reagents contain a thiol group which reacts with the double bond of acrylamide to form a Michael adduct. Analogous to HPLC, various protocols for on-tissue chemical derivatization (OTCD) have been described for MS imaging methods of both animal- and plant-based samples^{41,42}. However, existing protocols are almost exclusively used to enhance the ionization yield of poorly ionizable analytes⁴³. Gaining higher selectivity has scarcely been the primary motivation for the development of derivatization strategies in MS imaging so far.

We have recently published an extensive study on MS imaging experiments tailored to both fresh and processed food including first MS imaging results of the additive natamycin and the contaminant acrylamide in processed food⁴⁴. In the respective study, we describe the proof-of-concept for detection of acrylamide in a gingerbread cross-section with a lateral resolution of 200 μm using a fixed MALDI-laser. In the present study, we go one step further by using an additional autofocusing laser (AF-laser), which allows adjusting the laser focus for each pixel position and thereby keep measurement conditions constant throughout the entire analysis⁴⁵. By resetting the focus prior to each pixel acquisition, enhanced signal intensities can be obtained resulting in MS images with higher contrast. In addition, measurement in AF-mode allows for smaller pixel sizes, in this case 100 μm . The resulting higher number of pixels per area produces a larger data basis and enables more profound (statistical) analyses on analyte distributions, which are presented in our study by endogenous constituents and the contaminant acrylamide in German gingerbread. All measurements are based on a sample preparation workflow for MS imaging of brittle, inhomogeneous food samples, which is described in detail below. Additionally, we consider quality control aspects regarding the possible acrylamide formation during sample preparation and analysis. In this context, we identified the critical steps for artifact formation and conducted complementary measurements. To increase the selectivity of acrylamide detection beyond accurate mass and *in-situ* MALDI-MS/MS, a new derivatization method for acrylamide on the surface of pancakes was developed.

Results and discussion

Development of a sample preparation workflow. The sample preparation workflow for MS imaging of German gingerbread is illustrated in Fig. 1 and described in detail in the following. Highly processed food with soft and/or brittle texture, especially when consisting of multiple separate ingredients, is not suitable for the cryosectioning process³¹. German gingerbread is a typical example belonging to this group of challenging processed food. We recently developed an alternative sectioning method using an electric micro-saw⁴⁴, which was further optimized in the present study. The entire sample was frozen at $-80\text{ }^{\circ}\text{C}$, resulting in a firm structure less prone to deformation. Cutting disks of the micro-saw were thoroughly dried and cooled down to $-80\text{ }^{\circ}\text{C}$ prior to sectioning. It has been proven best to keep both the sample and the cutting disks under dry ice at all times except for the immediate sectioning and to use a fresh cutting disk for each section. With this approach, sections of

www.nature.com/scientificreports/

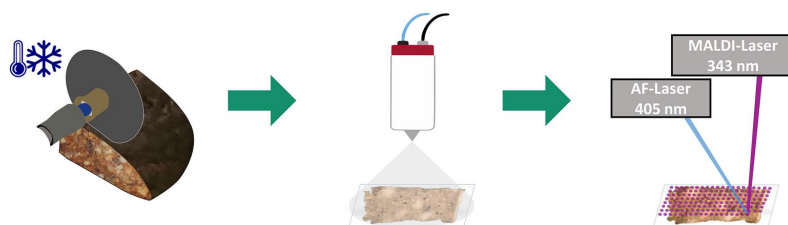


Figure 1. Sample preparation of German gingerbread for MALDI MS imaging experiments. Sections of approx. 2 mm thickness are cut off deep-frozen gingerbread with an electric micro-saw. Sections are glued to an object slide and covered with the MALDI matrix 2,5-dihydroxybenzoic acid (DHB) using an automated spraying system. The sample is then introduced into an AP-SMALDI5 AF ion source for the autofocusing (AF) MALDI MS imaging measurement. The AF-laser at $\lambda = 405$ nm ensures a constant focus of the MALDI-laser throughout the uneven sample surface.

approx. 2 mm thickness could be prepared. For both a homogeneous matrix deposition and reproducible spraying conditions, 2,5-dihydroxybenzoic acid (DHB) matrix was applied onto the gingerbread sections using an HTX M5 Sprayer (HTX Technologies, Chapel Hill, USA) as automated spraying device. To cater to the specific needs of the lipid-rich sample surface, the matrix spray was performed under ‘dry’ conditions, i.e., at a relatively high nozzle-temperature of 85 °C. The matrix density resulting from the parameters set for the automatic sprayer is 23.3 $\mu\text{g}/\text{mm}^2$, which is comparatively high and at least partly due to the rough section surface. Although when conducted by an experienced operator the section surface is visibly flat and even, a certain topography of around 800 μm in z-direction remained unavoidable (see Fig. 2d). However, when measuring in autofocusing mode (AF-mode), the position of the AF-laser in the MALDI-source is adjusted to the z-position of the current pixel to be irradiated; thus, changes in the topography of the sample surface can be compensated so that the MALDI-laser has a constant focus resulting in high quality mass spectra. The energy and focus settings of the MALDI-laser needed to be optimized as well for gingerbread samples. With the improvement of autofocusing, the standard injection time of 500 ms is sufficient for adequate analyte abundance. Setting an overall defocus and an increased C-trap injection time as done in our initial study⁴⁴ is no longer necessary. For gingerbread measurements, the energy density was approx. 7000 $\mu\text{J}/\text{mm}^2$ with 50 applied laser pulses per pixel. Lower laser energy settings, however, resulted in a loss of acrylamide signal. Based on the ablation area caused by the MALDI-laser, measurements with a step size of 100 μm were performed in AF-mode compared to 200 μm in regular setup⁴⁴. It is important to note that spatial resolution in this study is not limited by instrumentation. The identical setup is routinely used to perform high-quality MS imaging at 5 μm pixel size, e.g., of drug compounds and lipids in mouse lung tissue⁴⁶. Instead, the pixel size is limited by the very dry and inhomogeneous properties of the gingerbread sample, which lead to low ionization efficiency and higher signal variation. Consequently, the number of compounds detected in this study is lower compared to typical MS imaging experiments of, e.g., mammalian tissue. Nevertheless, the presented modifications to the sample preparation workflow lay the groundwork for successful autofocusing MALDI MS imaging of German gingerbread.

Using this approach, several gingerbread constituents could be detected and visualized with a substantial increase in contrast. Lipids, such as phosphatidylcholines (PC), are expected to be present in lipophilic areas of the sample, such as nut fragments. PC 36:3 $[\text{M} + \text{K}]^+$, i.e., the potassium adduct of a PC comprising 36 carbon atoms with 3 unsaturated bonds⁴⁷, depicted in Fig. 2b, for instance shows distinct hotspots in nut fragment areas visible in the microscope image (Fig. 2a). The distribution of disaccharide potassium adduct, shown in Fig. 2c, indicates nearly ubiquitous presence of sugar throughout the surface with reduced intensities, e.g., within nut fragments and elevated intensities in a piece of candied fruit and a region of clotted sugar near the upper margin of the image (see supplementary, Fig. S3a). The identity of disaccharide $[\text{M} + \text{K}]^+$ could be confirmed by matching MS/MS-spectra with sucrose standard (see supplementary, Fig. S1). In addition, MS images of tri-, tetra- and pentasaccharides (all K adducts) are provided in Fig. S9d–f. The oligosaccharides show consistent distributions with disaccharide, present in candied fruit, clotted sugar and dough.

The topology of the sample surface is depicted in a microscopic 3D optical overlay together with an exemplary line scan across low and high regions on the z-axis (Fig. 2d). A comparison of the 3D MS image of disaccharide $[\text{M} + \text{K}]^+$ (Fig. 2e) to the microscopic 3D optical overlay (Fig. 2d) shows that the overall topology of the surface could be reproduced by the AF-laser. Moreover, an analogous line scan based on AF-laser data (Fig. 2e, inserted diagram) has a similar profile and comparable overall Δz to the microscopy-based line scan (Fig. 2d, inserted diagram). These results demonstrate the applicability of the AF-laser for uneven surfaces of around 800 μm in depth and the success of autofocusing MALDI MS imaging of German gingerbread with the described parameters.

MS imaging of the process contaminant acrylamide. In addition to the spatially resolved detection of major constituents, also minor components can be visualized in highly processed food by MALDI MS imaging. In the present example, the distribution of the process contaminant acrylamide is given in Fig. 3a. The average amount of acrylamide in the sample determined by gas chromatography coupled to mass spectrometry (GC–MS) was 3,200 $\mu\text{g}/\text{kg}$ (detailed method description is provided in the supplementary material). With a

www.nature.com/scientificreports/

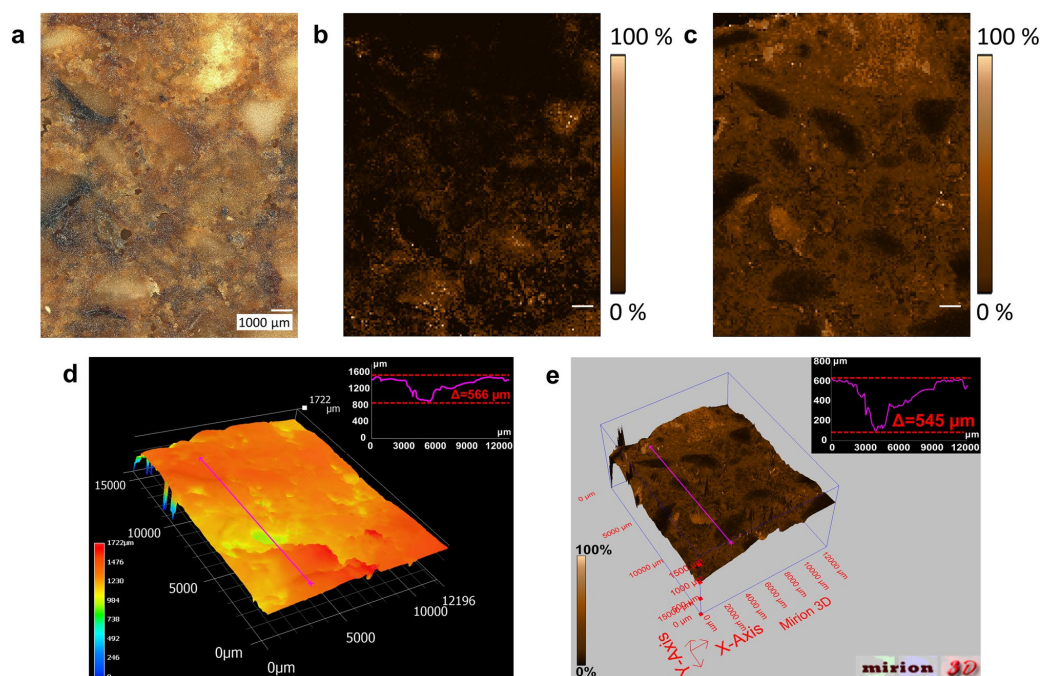


Figure 2. Autofocusing (AF) MALDI MS imaging of German gingerbread. Raster size: 128×161 pixels, pixel size: $100 \mu\text{m}$ (a) microscope image of German gingerbread section. (b) MS image of PC 36:3 $[\text{M} + \text{K}]^+$, m/z 822.54096, TIC-normalized. (c) MS image of disaccharide $[\text{M} + \text{K}]^+$, m/z 381.07937, TIC-normalized. (d) microscopic 3D depth-composition optical overlay with integrated linescan, Z axis is based on microscopic data. (e) 3D MS image of disaccharide $[\text{M} + \text{K}]^+$, m/z 381.07937, TIC-normalized, Z-axis is based on AF-laser focus data. Gray-scale MS images of the presented analytes and higher saccharides are provided in supplementary, Fig. S9.

benchmark level of $800 \mu\text{g}/\text{kg}$ set by Commission Regulation (EU) 2017/2158¹⁴, the sample exceeded this level fourfold. Acrylamide could be detected as its $[\text{M} + \text{H}]^+$ at m/z 72.04439 with high mass accuracy as indicated by the mass measurement accuracy (MMA) plot shown in Fig. 3b. Across all 20,363 pixels, in which acrylamide signal could be detected, the root mean square mass error (RMSE) was 0.61 ppm. In case of acrylamide, high mass resolution is crucial due to a neighboring peak at m/z 72.08082, as depicted in the single pixel mass spectrum in Fig. 3c. These results could be reproduced in an additional section from the same sample (see supplementary, Fig. S4a–d). The assignment of acrylamide is supported by MALDI-MS/MS experiments on gingerbread surface (Fig. 3d) and of acrylamide standard mixed with DHB matrix on glass (see supplementary, Fig. S2) Both MS/MS spectra show the characteristic fragment signal at its theoretical m/z 55.01784 corresponding to the loss of NH_3 . In the MS image shown in Fig. 3a, acrylamide signal is detected in all regions across the section except for the sugar bulk on the top edge of the measurement area and within regions of candied fruit. Judging from the visible intensity distribution, some areas putatively corresponding to nut fragments seem to show higher acrylamide intensities. This observation is addressed in more detail below.

In MS imaging with a fixed MALDI-laser focus, uneven surfaces influence the ionization efficiency during the MALDI process. We reduced this effect by using a larger laser ablation area (defocused) in our previous study⁴⁴. By autofocusing prior to each pixel, it is now possible to perform MS imaging with a consistently focused MALDI-laser and, given an adjusted laser energy density, sufficient analyte intensities can still be obtained despite smaller areas of ionized sample compared to defocused measurements. The presented measurements were conducted with a step size of $100 \mu\text{m}$ without oversampling, i.e., with a MALDI-laser ablation diameter smaller than the step size, thus avoiding multiple irradiations of a given area. Considering the sample size of approx. $12 \times 15 \text{ mm}$, this lateral resolution enables more detailed and reliable analyses of analyte distributions across different ingredients compared to previous measurements with a fixed MALDI-laser and $200 \mu\text{m}$ step size⁴⁴. To support the visible tendency towards higher acrylamide abundances in nut regions, the measurement area was stratified into regions of interest (ROI) comprising distinct nut fragments and an inverted ROI for the remaining sample surface. However, this surface stratification could not simply be based on the optical image since some ingredients, such as sugar agglomerates, might have a similar appearance to nut fragments. Therefore, an evaluation of the optical image was combined with MS imaging information resulting from triglyceride

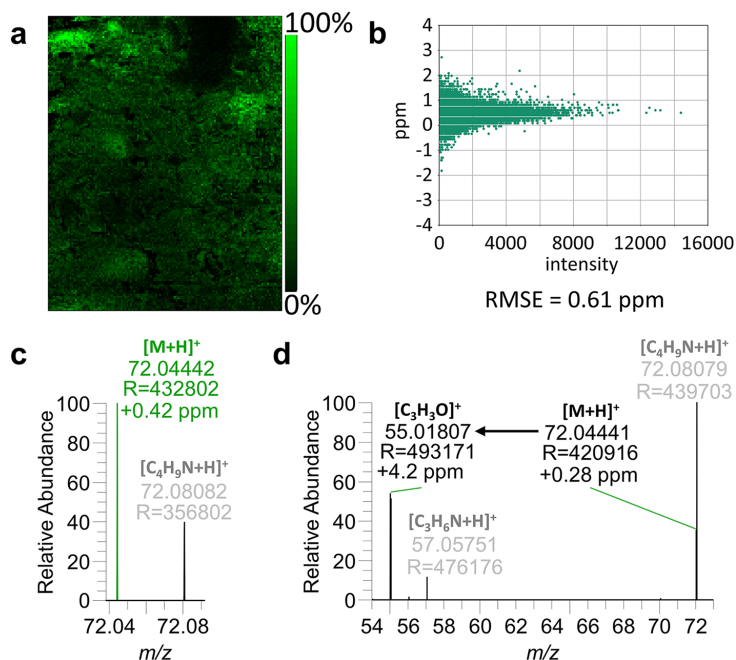


Figure 3. MS imaging of acrylamide in German gingerbread. (a) MS image of acrylamide $[M+H]^+$, m/z 72.04439, TIC-normalized. (b) Mass measurement accuracy plot and RMSE value for the acrylamide signal. (c) single pixel mass spectrum of acrylamide (d) *in-situ* MALDI-MS/MS spectrum showing the characteristic fragment at m/z 55.01807, isolation window: m/z 72.0 \pm 0.2, scan range: m/z 50–80, HCD: 60.

signals typical for nuts. The step-by-step procedure for stratification of gingerbread surface into the ROI “nuts” and “other” is visualized in supplementary, Fig. S3. First, candidate “nut” regions were determined based on visual perception in the optical image (Fig. 4a). In a second step, only regions showing elevated intensities in a sum image of the triglycerides TG 52:3, TG 52:4, TG 54:5, TG 54:6 and TG 57:10 (all $[M+K]^+$) were retained, whereas the remaining candidate regions were discarded. The so defined “nut” regions across the sample surface were compiled and exported as one ROI “nuts”; the inverted ROI, i.e., all pixels not assigned to the “nuts” ROI,

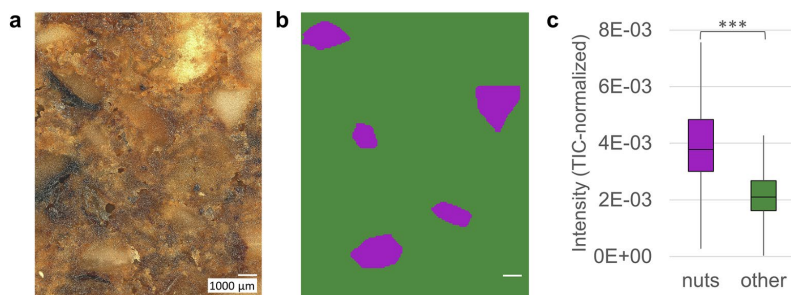


Figure 4. Acrylamide intensity distribution on German gingerbread. (a) microscope image of German gingerbread section. (b) Surface stratification into regions of interest (ROI) “nuts” based on sum image of triglycerides TG 52:3, TG 52:4, TG 54:5, TG 54:6 and TG 57:10 and “other”; more details are provided in Fig. S3. Export of abundance data of acrylamide m/z 72.04439 \pm 2.5 ppm for both ROI. (c) Boxplot of backtransformed intensity values stratified into ROI “nuts” and “other”; two-sided t-Test was performed on $x^{0.25}$ -transformed intensity values; *** $t(247) = 16.93$, $P < .001$.

www.nature.com/scientificreports/

were exported as “other”. A binary image showing the masks for both ROI is given in Fig. 4b. From these ROI, the acrylamide $[M + H]^+$ TIC-normalized intensity values of each pixel were exported as separate datasets. In Fig. 4c, boxplots of the “nuts” and “other” ROI are depicted showing higher acrylamide intensities within the nuts. This finding is supported by a two-sided t-test of the $x^{0.25}$ -transformed datasets, proving significantly higher acrylamide intensities within the “nuts” ROI than in the remaining section ($P < 0.001$). Data transformation was necessary to obtain Gaussian distributions within the datasets. In the replicate measurement of the contaminated gingerbread, shown in supplementary, Fig. S4, this protocol was applied as well leading to an analogous result. The higher acrylamide intensities in nut regions may have several possible causes. First, there is a lipid pathway for the formation of acrylamide, which is directly linked to the unsaturation of fatty acids⁴⁹. As previously mentioned and demonstrated in supplementary, Fig. S10, polyunsaturated fatty acids are more abundant in nut regions. Our MS imaging approach allows direct coregistration to the acrylamide distribution in the same measurement, depicted in Fig. 3a, suggesting that this compound class could foster the formation of acrylamide. Secondly, the combination of reduced water activity and a higher heat capacity within nut fragments could further contribute to acrylamide formation. Since acrylamide is formed preferably at low water activity⁵⁰, nut regions might present suitable conditions due to their high fat- and comparatively low water-content. The present results indicate that acrylamide might form preferably, however not exclusively, within regions in and around nut fragments. These findings are in accordance with our previously published two-dimensional MALDI MS imaging of German gingerbread⁴⁴. High acrylamide concentrations of 885 $\mu\text{g}/\text{kg}$ in average have been found previously in roasted almonds, whereas roasted hazelnuts contained much less acrylamide⁵¹. For the sake of producing safe food, it seems likely that not only the size of nut fragments, but also the type and size during roasting are crucial regarding the mitigation of acrylamide in gingerbread⁵². As a further step, a section of German gingerbread with relatively low acrylamide levels (174 $\mu\text{g}/\text{kg}$, determined by GC-MS) has been measured. Images and MMA-plot of the market sample are shown in supplementary, Fig. S5a–c. A comparison of the acrylamide intensities in the presented measurements, depicted in supplementary, Fig. S5d, shows a lower intensity range in the analysis of the market sample compared to the analyses of the contaminated sample and thus proves the applicability of MALDI MS imaging for the analysis not only of heavily contaminated samples, but also of regular market samples. Therefore, the presented protocol can be used as a complementary method to established chromatography-based methods for the analysis of acrylamide in food to gain further insight into the formation process of acrylamide, which is of interest for food safety authorities as well as the food industry.

Quality control aspects in MS imaging of acrylamide. As described in the previous section, the identity of the detected acrylamide signal has been confirmed by an *in-situ* MALDI-MS/MS-experiment. However, a confirmation of the origin of acrylamide from the contaminated sample itself and not being an artifact resulting from sample preparation or measurement cannot be covered by MS/MS alone. Since acrylamide forms at elevated temperatures, the critical steps in this protocol are sample sectioning and the MALDI-process. Here we present strategies for both steps to exclude the risk of detecting artificially formed acrylamide.

By thorough cooling of both the gingerbread sample and the cutting disk to -80°C , acrylamide formation resulting from elevated temperatures during the sectioning process has already been addressed. For verification, a measurement of the same sample was sectioned in frozen state with a sharp knife. This method induces no significant heat during the sectioning process and thus artificial production of acrylamide can be excluded. However, sectioning with a knife produces a rougher surface and more cracks. Nonetheless, acrylamide signal could be detected throughout this sample as well with high mass accuracy, as demonstrated in supplementary, Fig. S6. This confirms the presence of acrylamide independent of the sectioning method and excludes artifacts by sample preparation.

Another potential source for acrylamide is the MALDI-process in which the laser deposits energy and thus leads to local increase of temperature at the site of desorption. To confirm that the detected acrylamide signal is not an artifact occurring during this process, we conducted a proof-of-principle experiment on *in-situ* derivatization of acrylamide. Contrary to most previously published studies using derivatization for MS imaging^{41–43,53}, the scope is not to enhance the detection limit, but to detect acrylamide on food surfaces with high selectivity. A similar approach has been used for minor bioactive lipids in mouse brain⁵⁴.

TSA was chosen as derivatization agent for acrylamide based on an established derivatization strategy developed for LC-MS/MS analysis³⁹. Alkaline conditions are necessary for an efficient addition of the nucleophilic thiol group to the α,β -unsaturated carbonyl function of acrylamide (see Fig. 5b). Therefore, TSA could not directly be prepared in aqueous methanol, but needed to be dissolved in aqueous NaOH at $\text{pH} = 10$ first and subsequently mixed 50/50 (v/v) with methanol. The derivatization solution was sprayed onto the sample surface using an automated HTX M5 Sprayer. A surface density of 10.3 $\mu\text{g}/\text{mm}^2$, calculated from the spray parameters, turned out to be the best balance to ensure efficient derivatization and at the same time avoid signal suppression. In contrast to TSA, the MALDI matrix DHB was dissolved in aqueous trifluoroacetic acid (TFA) at $\text{pH} = 1$ and made up with methanol (final mixture 50:50, v/v) to provide an acidic environment on the sample surface and thereby ensure an efficient ionization for MS experiments in positive ion mode. Since excessive crystallized TSA on the sample surface exerts an additional matrix effect by absorbing laser energy, the DHB matrix density was reduced compared to underivatized samples to 16.8 $\mu\text{g}/\text{mm}^2$. Given the two successive sprays under varying pH-conditions (Fig. 5a), acrylamide derivatization for MALDI MS imaging is not trivial, but needed to be adjusted to meet the respective requirements of the derivatization reagent and an efficient MALDI-process. The laser energy density was reduced to approx. 460 $\mu\text{J}/\text{mm}^2$ to avoid fragmentation of the labile derivatization product.

In our gingerbread samples, acrylamide levels were sufficient for the detection of its protonated ion, but too low for the derivatization product to be detected (see supplementary, Fig. S7). Consequently, we used freshly prepared pancakes as a model for acrylamide-containing food matrix to demonstrate the feasibility of the

www.nature.com/scientificreports/

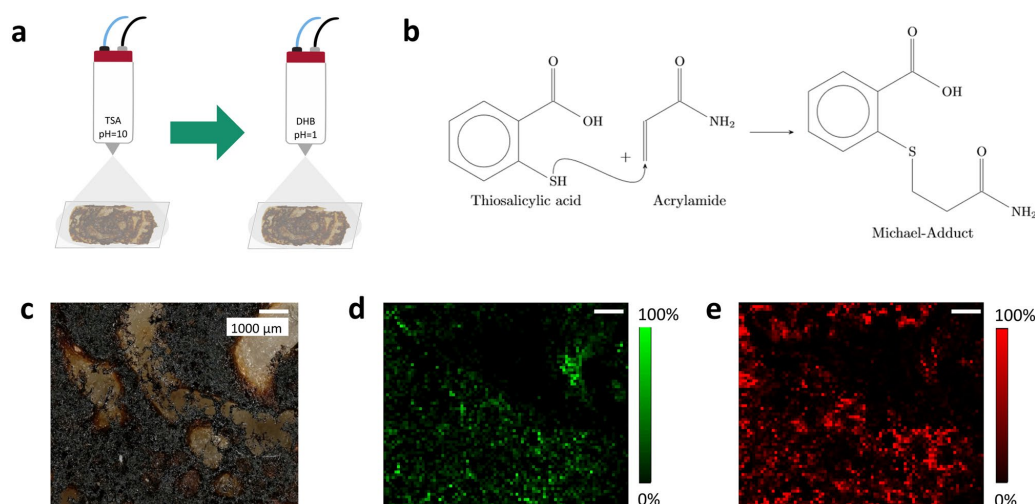


Figure 5. *in-situ* Derivatization of acrylamide on pancake surface. Raster size: 89×75 pixels, pixel size: $100 \mu\text{m}$. (a) Scheme of the sample preparation: Application of thiosalicylic acid in alkaline solution followed by 2,5-dihydroxybenzoic acid in acidic solution. (b) Derivatization reaction of thiosalicylic acid and acrylamide. (c) Microscope image of the measured pancake surface. (d) MS image of acrylamide $[M + H]^+$, m/z 72.04439. (e) MS image of the Michael-adduct $[M + Na]^+$, m/z 248.03519 (isotope distribution, see supplementary, Fig. S8).

derivatization method. In Fig. 5c, an optical image of the measured pancake surface is presented. The acrylamide $[M + H]^+$ signal at m/z 72.04439 was detected analogous to gingerbread samples with an RMSE = 0.57 ppm (2596 spectra), the corresponding MS image is provided in Fig. 5d. Acrylamide is distributed throughout vast parts of pancake surface. With a similar distribution, the TSA-acrylamide adduct $[M + Na]^+$ at m/z 248.03519 could be detected on pancake surface (Fig. 5e). To confirm the identity of the sodiated TSA-acrylamide adduct, mass spectra showing ^{13}C - and ^{34}S -isotope distributions of both the adduct formed from acrylamide standard on glass and from pancake surface are shown in supplementary, Fig. S8.

The detection of TSA-acrylamide adduct confirms that the detected acrylamide originates from the sample itself and is not a result of the ionization process. In addition, this derivatization approach covers the entire sample area, in contrast to commonly conducted *in-situ* MALDI-MS/MS experiments to confirm the identity of analytes, which are typically limited to a small representative area on the measured surface.

Conclusions

MALDI MS imaging of German gingerbread as an example of processed food has been optimized by introducing autofocusing of the MALDI-laser to adjust for height differences of the sample with an uneven surface. The contaminant acrylamide was successfully detected and identified in sections of German gingerbread by means of accurate mass and MS/MS measurements. A comparison of acrylamide intensities in different sample compartments revealed significantly higher intensities in regions containing nuts. In addition, by identifying critical steps for unintended acrylamide formation and complementary measurements including a new proof-of-principle approach for *in-situ* derivatization of acrylamide, we present measures to reduce the risk of artifacts during sample preparation and the MALDI-process.

Materials and methods

Sample material. Traditional German gingerbread was provided by the Bavarian Health and Food Safety Authority (LGL). The sample contained $3,200 \mu\text{g}/\text{kg}$ acrylamide previously determined by GC-MS in official analyses (for the method description, see supplementary material). Furthermore, a reference sample of traditional German gingerbread was purchased on a local market.

For the investigation of derivatized acrylamide, pancakes were prepared from a mixture of wheat flour, glucose and water with added asparagine (1.5%). The dough was baked in a pan without using oil until a dark-brown surface emerged.

Chemicals and standards. HPLC-Grade methanol and water were purchased from Carl Roth (Karlsruhe, Germany). 2,5-Dihydroxybenzoic acid (DHB), 2-Sulfanylbenzoic acid (thiosalicylic acid, TSA), sucrose and acrylamide analytical standard were purchased from Sigma Aldrich (Dreieich, Germany). Adhesive glass slides (Menzel Gläser, SuperFrost) were purchased from VWR (Darmstadt, Germany).

www.nature.com/scientificreports/

Sample sectioning. Whole gingerbreads were first cut into quarters using a sharp knife and then frozen at -80°C . If applicable, the chocolate coating was removed from the frozen sample with a knife prior to sectioning. Sections of 2–3 mm thickness were acquired using an electric micro saw (Dremel 8220, Breda, Netherlands). Gingerbread sections were always freshly prepared at the day of analysis.

TSA application. Thiosalicylic acid (TSA) was applied using an HTX M5 Sprayer (HTX Technologies, Chapel Hill, USA). The spray solution was prepared as follows: 154 mg TSA were weighed into a glass beaker and suspended in 3 mL water. By adding 1 M NaOH, the suspension was brought to $\text{pH} = 10$ and then filled up to 5 mL. Under these alkaline conditions, TSA is completely dissolved. The solution is finally made up to 10 mL with methanol and loaded into the sample loop of the sprayer. 20 passes were sprayed onto the sample surface with a flow rate of 50 $\mu\text{L}/\text{min}$, a spray nozzle velocity of 750 mm/min and 50°C nozzle temperature. Track spacing was set to 2 mm in a criss-cross (CC) scan-pattern.

Matrix application. For the application of DHB matrix, the HTX M5 Sprayer was used as well. The matrix solution was prepared in methanol/water (1:1, (v/v)) to a final concentration of 40 mg/mL and 30 mg/mL for gingerbread and pancake samples, respectively, and acidified with 0.4 % TFA. For gingerbread samples, 14 passes were sprayed onto the sample surface with a flow rate of 100 $\mu\text{L}/\text{min}$, a spray nozzle velocity of 1200 mm/min and 85°C nozzle temperature. For the pancake samples, the DHB solution was sprayed onto the sample directly after the derivatization using the same spraying system with minimal time delay due to a manual flushing step of the system. 16 passes were sprayed with a flow rate of 70 $\mu\text{L}/\text{min}$, a velocity of 1000 mm/min and 80°C nozzle temperature. Track spacing was always set to 2 mm in a criss-cross (CC) scan-pattern.

AF-MALDI MS imaging measurements. All MALDI MS imaging measurements were conducted using a quadrupole-orbitrap mass spectrometer QExactive HF (Thermo Fisher Scientific GmbH, Bremen, Germany) coupled to the atmospheric pressure autofocusing MALDI imaging source AP-SMALDI5 AF (TransMIT GmbH, Gießen, Germany)⁴⁵. Apart from the diode-pumped solid-state laser (MALDI-laser, $\lambda = 343\text{ nm}$) operating at a repetition rate of 100 Hz and oriented orthogonally to the sample surface, the ion source is equipped with a triangulation laser (AF-laser, $\lambda = 405\text{ nm}$), which is directed at the same spot as the MALDI laser, but from a 35° angle relative to the MS transfer capillary axis⁴⁵. All measurements were carried out in positive ion mode with a fixed C-trap injection time of 500 ms and 50 laser shots per pixel at a mass resolution of 240,000 @ m/z 200 full width at half maximum (FWHM). To ensure high mass accuracy ($< 1.5\text{ ppm RMSE}$), an online mass calibration before and internal mass calibration during each measurement were performed using homogeneously distributed matrix cluster ions⁵⁵. On gingerbread samples, the two m/z ranges 70–280 and 250–1000 were scanned successively and with shifted x- and y-coordinates ($0.5 \times$ step size) to cover both the mass range of small (e.g., acrylamide) and larger analytes, such as sugars and lipids. For the pancake samples, only one measurement with an m/z range 70–280 was conducted.

Data analysis. Optical images and depth composition heatmaps of the samples were created using a Keyence VHX-5000 digital microscope (Keyence Corporation, Osaka, Japan). Analysis of MS and MS/MS data was conducted in QualBrowser, a tool within the Thermo Xcalibur v4.0.27.10 software package. Following MS imaging experiments, proprietary Thermo “RAW” files were converted to imzML using RAW2IMZML converter v1.3R85 (TransMIT GmbH, Gießen, Germany) and validated with imzML Validator v1.0.2⁵⁶. 2D and 3D ion images were generated based on a bin width of $\pm 3\text{ ppm}$ using Mirion 3D v3.3.64.11⁵⁷. For the visualization of gingerbread ingredients, a customized “ginger” colormap was created (available for download, see supplementary information). SpectralAnalysis was used for the creation and export of regions of interest (ROI)⁵⁸; whereas the export of acrylamide abundance data was performed in MSiReader v1.01x⁵⁹. The generation of MMA plots and RMSE calculation were conducted using an in-house programmed imzML Analyzer v2.3.3 software. Statistical analyses were performed in IBM SPSS Statistics v26.0.0.0. The level of significance was defined as $P \leq 0.05$.

Data availability

Further data are available from the corresponding author on request.

Received: 8 January 2023; Accepted: 21 March 2023

Published online: 03 April 2023

References

1. Tareke, E., Rydberg, P., Karlsson, P., Eriksson, S. & Törnqvist, M. Analysis of acrylamide, a carcinogen formed in heated foodstuffs. *J. Agric. Food Chem.* **50**, 4998–5006. <https://doi.org/10.1021/jf020302f> (2002).
2. Mottram, D. S., Wedzicha, B. L. & Dodson, A. T. Acrylamide is formed in the Maillard reaction. *Nature* **419**, 448–449. <https://doi.org/10.1038/419448a> (2002).
3. Stadler, R. H. *et al.* Acrylamide from Maillard reaction products. *Nature* **419**, 449–450. <https://doi.org/10.1038/419449a> (2002).
4. Besaratinia, A. & Pfeifer, G. P. Genotoxicity of acrylamide and glycidamide. *J. Natl. Cancer Inst.* **96**, 1023–1029. <https://doi.org/10.1093/jnci/djh186> (2004).
5. Calleman, C. J., Bergmark, E. & Costa, L. Acrylamide is metabolized to glycidamide in the rat: evidence from hemoglobin adduct formation.
6. International Agency for Research on Cancer. *Some Industrial Chemicals: IARC Monographs on the Evaluation of Carcinogenic Risks to Humans*. 560 (1994).

www.nature.com/scientificreports/

7. Annex VI Part 3 Table 3.1 Regulation (EC) 1232/2008 of the European Parliament and of the Council of 16 December 2008 on classification, labelling and packaging of substances and mixtures, amending and repealing Directives 67/548/EEC and 1999/45/EC, and amending Regulation (EC) 1907/2006
8. Cantrell, M. S. & McDougal, O. M. Biomedical rationale for acrylamide regulation and methods of detection. *Compr. Rev. Food Sci. Food Saf.* **20**, 2176–2205. <https://doi.org/10.1111/1541-4337.12696> (2021).
9. Chain, E. P. O. C. I. T. F. Scientific opinion on acrylamide in food. *EFSA J.* <https://doi.org/10.2903/j.efsa.2015.4104> (2015).
10. Goempel, K. *et al.* Biomarker monitoring of controlled dietary acrylamide exposure indicates consistent human endogenous background. *Arch. Toxicol.* **91**, 3551–3560. <https://doi.org/10.1007/s00204-017-1990-1> (2017).
11. Eisenbrand, G. Revisiting the evidence for genotoxicity of acrylamide (AA), key to risk assessment of dietary AA exposure. *Arch. Toxicol.* **94**, 2939–2950. <https://doi.org/10.1007/s00204-020-02794-3> (2020).
12. Joint FAO/WHO Expert Committee on Food Additives (JECFA). *CODE OF PRACTICE FOR THE REDUCTION OF ACRYLAMIDE IN FOODS*. (CAC/RCP 67-2009), 11 (2009). https://www.fao.org/fao-who-codexalimentarius/sh-proxy/en/?lnk=1&url=https%253A%252F%252Fworkspace.fao.org%252Fsites%252Fcodex%252Fstandards%252FCAC%2BRC%2B67-2009%252FCXP_067e.pdf.
13. Food & Drug Administration. *Guidance for Industry: Acrylamide in Foods*. (FDA-2013-D-0715), (2013). <https://www.fda.gov/regulatory-information/search-fda-guidance-documents/guidance-industry-acrylamide-foods>.
14. Commission Regulation (EU) 2017/2158 of 20 November 2017 establishing mitigation measures and benchmark levels for the reduction of the presence of acrylamide in food
15. Hoenicke, K. & Gatermann, R. Studies on the stability of acrylamide in food during storage. *J. AOAC Int.* **88**, 268–273 (2005).
16. Arvanitoyannis, I. S. & Dionisopoulou, N. Acrylamide: formation, occurrence in food products, detection methods, and legislation. *Crit. Rev. Food Sci. Nutr.* **54**, 708–733. <https://doi.org/10.1080/10408398.2011.606378> (2014).
17. Art. 1 (1) in conjunction with Annex IV Regulation (EU) 2017/2158
18. *Leitsätze für Feine Backwaren vom 17./18. September 1991 (Beilage Nr. 86b zum BAnz. Vom 8. Mai 1992, GMBL Nr. 17 S. 325 vom 8. Mai 1992), zuletzt geändert am 09.01.2010 (BAnz. Nr. 16 vom 29.01.2010, GMBL Nr. 5/6 S. 120 ff. vom 04.02.2010)*
19. *Recital 3 in conjunction with Annex Commission Recommendation (EU) 2019/1888 of 7 November 2019 on the monitoring of the presence of acrylamide in certain foods*
20. Mousavi, K. A., Fakhri, Y., Nematollahi, A., Seilani, F. & Vasseghian, Y. The concentration of acrylamide in different food products: A global systematic review, meta-analysis, and meta-regression. *Food Rev. Int.* **5**, 1–19. <https://doi.org/10.1080/87559129.2020.1791175> (2020).
21. Šcupáková, K. *et al.* Cellular resolution in clinical MALDI mass spectrometry imaging: the latest advancements and current challenges. *Clin. Chem. Lab. Med.* **58**, 914–929. <https://doi.org/10.1515/cklm-2019-0858> (2020).
22. Bhandari, D. R. *et al.* High resolution mass spectrometry imaging of plant tissues: towards a plant metabolite atlas. *Analyst* **140**, 7696–7709. <https://doi.org/10.1039/c5an01065a> (2015).
23. Neumann, E. K., Do, T. D., Comi, T. J. & Sweedler, J. V. Exploring the fundamental structures of life: non-targeted, chemical analysis of single cells and subcellular structures. *Angewandte Chemie (International ed. in English)* **58**, 9348–9364. <https://doi.org/10.1002/anie.201811951> (2019).
24. Schnackenberg, L. K., Thorn, D. A., Barnette, D. & Jones, E. E. MALDI imaging mass spectrometry: An emerging tool in neurology. *Metab. Brain Dis.* **37**, 105–121. <https://doi.org/10.1007/s11011-021-00797-2> (2022).
25. Bednarz, H., Roloff, N. & Niehaus, K. Mass Spectrometry Imaging of the Spatial and Temporal Localization of Alkaloids in Nightshades. *J. Agric. Food Chem.* **67**, 13470–13477. <https://doi.org/10.1021/acs.jafc.9b01155.s001> (2019).
26. Hou, J. *et al.* Spatial lipidomics of eight edible nuts by desorption electrospray ionization with ion mobility mass spectrometry imaging. *Food Chem.* **371**, 130893. <https://doi.org/10.1016/j.foodchem.2021.130893> (2022).
27. Da Silva, L. G. *et al.* Laser ablation electrospray ionization mass spectrometry imaging as a new tool for accessing patulin diffusion in mold-infected fruits. *Food Chem.* **373**, 131490. <https://doi.org/10.1016/j.foodchem.2021.131490> (2022).
28. Marzec, M. E., Wojtyśiak, D., Połowicz, K., Nowak, J. & Pedrys, R. Study of cholesterol and vitamin E levels in broiler meat from different feeding regimens by TOF-SIMS. *Biointerphases* **11**, 02A326. <https://doi.org/10.1116/1.4943619> (2016).
29. Yukihiro, Y. & Zaima, N. Application of mass spectrometry imaging for visualizing food components. *Foods (Basel, Switzerland)* **9**, 74 (2020).
30. Gallego, M., Mora, L. & Toldrá, F. Differences in peptide oxidation between muscles in 12 months Spanish dry-cured ham. *Food Res. Int. (Ottawa, Ont.)* **109**, 343–349. <https://doi.org/10.1016/j.foodres.2018.04.045> (2018).
31. Fowble, K. L., Okuda, K., Cody, R. B. & Musah, R. A. Spatial distributions of furan and 5-hydroxymethylfurfural in unroasted and roasted Coffea arabica beans. *Food Res. Int. (Ottawa, Ont.)* **119**, 725–732. <https://doi.org/10.1016/j.foodres.2018.10.052> (2019).
32. Rešetar Maslov, D., Svirikova, A., Allmaier, G., Marchetti-Deschamann, M. & Kraljević, P. S. Optimization of MALDI-TOF mass spectrometry imaging for the visualization and comparison of peptide distributions in dry-cured ham muscle fibers. *Food Chem.* **283**, 275–286. <https://doi.org/10.1016/j.foodchem.2018.12.126> (2019).
33. Boughton, B. A., Thinagarani, D., Sarabia, D., Bacic, A. & Roessner, U. Mass spectrometry imaging for plant biology: A review. *Phytochem. Rev.* **15**, 445–488. <https://doi.org/10.1007/s11101-015-9440-2> (2016).
34. Qi, B.-L. *et al.* Derivatization for liquid chromatography-mass spectrometry. *TrAC Trends Anal. Chem.* **59**, 121–132. <https://doi.org/10.1016/j.trac.2014.03.013> (2014).
35. Lim, H.-H. & Shin, H.-S. A new derivatization approach with D-cysteine for the sensitive and simple analysis of acrylamide in foods by liquid chromatography-tandem mass spectrometry. *J. Chromatogr. A* **1361**, 117–124. <https://doi.org/10.1016/j.chroma.2014.07.094> (2014).
36. Yang, S. *et al.* Thiol-ene click derivatization for the determination of acrylamide in potato products by capillary electrophoresis with capacitively coupled contactless conductivity detection. *J. Agric. Food Chem.* **67**, 8053–8060. <https://doi.org/10.1021/acs.jafc.9b01525> (2019).
37. Martínez, E., Rodríguez, J. A., Bautista, M., Rangel-Vargas, E. & Santos, E. M. Use of 2-naphthalenethiol for derivatization and determination of acrylamide in potato crisps by high-performance liquid chromatographic with fluorescence detection. *Food Anal. Methods* **11**, 1636–1644. <https://doi.org/10.1007/s12161-018-1150-0> (2018).
38. Faraji, M., Hamdamali, M., Aryanasab, F. & Shabaniyan, M. 2-Naphthalenethiol derivatization followed by dispersive liquid-liquid microextraction as an efficient and sensitive method for determination of acrylamide in bread and biscuit samples using high-performance liquid chromatography. *J. Chromatogr. A* **1558**, 14–20. <https://doi.org/10.1016/j.chroma.2018.05.021> (2018).
39. Jezussek, M. & Schieberle, P. A new LC/MS-method for the quantitation of acrylamide based on a stable isotope dilution assay and derivatization with 2-mercaptobenzoic acid Comparison with two GC/MS methods. *J. Agric. Food Chem.* **51**, 7866–7871. <https://doi.org/10.1021/jf0349228> (2003).
40. Oellig, C., Gottstein, E. & Granvogl, M. Analysis of acrylamide in vegetable chips after derivatization with 2-mercaptobenzoic acid by liquid chromatography-mass spectrometry. *Eur. Food Res. Technol.* **248**, 937–946. <https://doi.org/10.1007/s00217-021-03898-5> (2022).
41. Dueñas, M. E., Larson, E. A. & Lee, Y. J. Toward mass spectrometry imaging in the metabolomics scale: increasing metabolic coverage through multiple on-tissue chemical modifications. *Front. Plant Sci.* **10**, 860. <https://doi.org/10.3389/fpls.2019.00860> (2019).

www.nature.com/scientificreports/

42. Merdas, M. *et al.* On-tissue chemical derivatization reagents for matrix-assisted laser desorption/ionization mass spectrometry imaging. *J Mass Spectr* **56**, e4731. <https://doi.org/10.1002/jms.4731> (2021).
43. Harkin, C. *et al.* On-tissue chemical derivatization in mass spectrometry imaging. *Mass Spectrom. Rev.* <https://doi.org/10.1002/mas.21680> (2021).
44. Kokesch-Himmelreich, J. *et al.* MALDI mass spectrometry imaging: from constituents in fresh food to ingredients, contaminants and additives in processed food. *Food Chem.* <https://doi.org/10.1016/j.foodchem.2022.132529> (2022).
45. Kompauer, M., Heiles, S. & Spengler, B. Autofocusing MALDI mass spectrometry imaging of tissue sections and 3D chemical topography of nonflat surfaces. *Nat. Methods* **14**, 1156–1158. <https://doi.org/10.1038/nmeth.4433> (2017).
46. Kokesch-Himmelreich, J. *et al.* Do anti-tuberculosis drugs reach their target?—high-resolution matrix-assisted laser desorption/ionization mass spectrometry imaging provides information on drug penetration into necrotic granulomas. *Anal. Chem.* **94**, 5483–5492. <https://doi.org/10.1021/acs.analchem.1c03462> (2022).
47. Liebis, G. *et al.* Update on LIPID MAPS classification, nomenclature, and shorthand notation for MS-derived lipid structures. *J. Lipid. Res.* **61**, 1539–1555. <https://doi.org/10.1194/jlr.s120001025> (2020).
48. Buchberger, A. R., DeLaney, K., Johnson, J. & Li, L. Mass spectrometry imaging: A review of emerging advancements and future insights. *Anal. Chem.* **90**, 240–265. <https://doi.org/10.1021/acs.analchem.7b04733> (2018).
49. Daniali, G., Jinap, S., Hajeb, P., Sanny, M. & Tan, C. P. Acrylamide formation in vegetable oils and animal fats during heat treatment. *Food Chem.* **212**, 244–249. <https://doi.org/10.1016/j.foodchem.2016.05.174> (2016).
50. Biedermann, M., Biedermann-Brehm, S., Noti, A. & Grob, K. Methods for determining the potential of acrylamide formation and its elimination in raw materials for food preparation, such as potatoes. *Mitt. Lebensmittelunters. Hyg.* **93**, 653–667 (2002).
51. Amrein, T. M. *et al.* Acrylamide in roasted almonds and hazelnuts. *J. Agric. Food Chem.* **53**, 7819–7825. <https://doi.org/10.1021/jf051132k> (2005).
52. Weisshaar, R. Acrylamide in bakery products—results from model experiments. *DEUTSCHE LEBENSMITTEL-RUNDSCHAU* **100**, 92 (2004).
53. Enomoto, H., Sensu, T., Yumoto, E., Yokota, T. & Yamane, H. Derivatization for detection of abscisic acid and 12-oxo-phytyldienoic acid using matrix-assisted laser desorption/ionization imaging mass spectrometry. *Rapid Commun. Mass Spectrom.* **RCM 32**, 1565–1572. <https://doi.org/10.1002/rcm.8200> (2018).
54. Iwama, T. *et al.* Development of an on-tissue derivatization method for MALDI mass spectrometry imaging of bioactive lipids containing phosphate monoester using phos-tag. *Anal. Chem.* **93**, 3867–3875. <https://doi.org/10.1021/acs.analchem.0c04479> (2021).
55. Treu, A. & Römpf, A. Matrix ions as internal standard for high mass accuracy matrix-assisted laser desorption/ionization mass spectrometry imaging. *Rapid Commun. Mass Spectrom.* **35**, e9110. <https://doi.org/10.1002/rcm.9110> (2021).
56. Race, A. M. & Römpf, A. Error-free data visualization and processing through imzML and mzML validation. *Anal. Chem.* **90**, 13378–13384. <https://doi.org/10.1021/acs.analchem.8b03059> (2018).
57. Paschke, C. *et al.* Mirion—a software package for automatic processing of mass spectrometric images. *J. Am. Soc. Mass Spectrom.* **24**, 1296–1306. <https://doi.org/10.1007/s13361-013-0667-0> (2013).
58. Race, A. M. *et al.* SpectralAnalysis: Software for the masses. *Anal. Chem.* **88**, 9451–9458. <https://doi.org/10.1021/acs.analchem.6b01643> (2016).
59. Bokhart, M. T., Nazari, M., Garrard, K. P. & Muddiman, D. C. MSiReader v1.0: Evolving open-source mass spectrometry imaging software for targeted and untargeted analyses. *J. Am. Soc. Mass Spectrom.* **29**, 8–16. <https://doi.org/10.1007/s13361-017-1809-6> (2018).

Acknowledgements

This study was supported by the Deutsche Forschungsgemeinschaft (DFG, German Research Foundation), Project Number 491183248, 391977956-SFB 1357, INST 91/373-1-FUGG as well as the TechnologieAllianzOberfranken (TAO). The authors are grateful to Holger Knapp and Jennifer Mels from the Bavarian Health and Food Safety Authority (LGL, Erlangen, Germany) for providing the gingerbread samples and conducting GC-MS reference measurements.

Author contributions

O.W. and A. R. designed experiments O.W. conducted measurements A.R. provided methodology, infrastructure and funding. O.W. and A.R. wrote the manuscript.

Funding

Open Access funding enabled and organized by Projekt DEAL.

Competing interests

The authors declare no competing interests.

Additional information

Supplementary Information The online version contains supplementary material available at <https://doi.org/10.1038/s41598-023-32004-w>.

Correspondence and requests for materials should be addressed to A.R.

Reprints and permissions information is available at www.nature.com/reprints.

Publisher's note Springer Nature remains neutral with regard to jurisdictional claims in published maps and institutional affiliations.

www.nature.com/scientificreports/



Open Access This article is licensed under a Creative Commons Attribution 4.0 International License, which permits use, sharing, adaptation, distribution and reproduction in any medium or format, as long as you give appropriate credit to the original author(s) and the source, provide a link to the Creative Commons licence, and indicate if changes were made. The images or other third party material in this article are included in the article's Creative Commons licence, unless indicated otherwise in a credit line to the material. If material is not included in the article's Creative Commons licence and your intended use is not permitted by statutory regulation or exceeds the permitted use, you will need to obtain permission directly from the copyright holder. To view a copy of this licence, visit <http://creativecommons.org/licenses/by/4.0/>.

© The Author(s) 2023

Autofocusing MALDI MS Imaging of processed food exemplified by the contaminant acrylamide in German gingerbread

Oliver Wittek, Andreas Römpf

Bioanalytical Sciences and Food Analysis, University of Bayreuth, Universitätsstrasse 30, D-95440 Bayreuth, Germany

Supplementary

GC-MS reference method for acrylamide quantification

After soaking the sample in warm water, turbids are removed from the extract using Carrez precipitation. The clarified extract is treated with a bromination reagent and concentrated by solid phase extraction (SPE). The derivatized acrylamide is eluted from the column with ethyl acetate, concentrated by evaporation and then analyzed by GC-MS. Quantification is performed via external calibration under consideration of initially added deuterated internal standard acrylamide-d₃. The limit of quantification is 33 µg/kg.

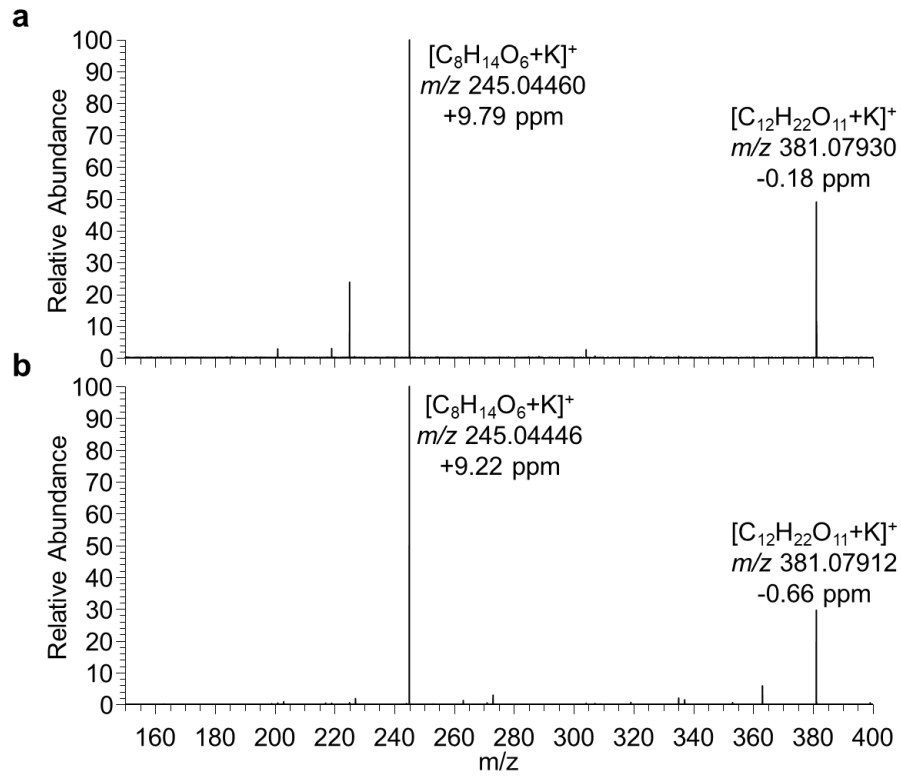


Fig. S1: Average MALDI-MS/MS spectra of (a) putative disaccharide $[M+K]^+$ on gingerbread, theoretical m/z 381.07937 (n=47 single spectra), isolation window: m/z 381.1 \pm 0.2 at NCE = 31 and (b) sucrose standard $[M+K]^+$ on glass, theoretical m/z 381.07937 (n=84 single spectra), isolation window: m/z 381.1 \pm 0.2 at NCE = 20.

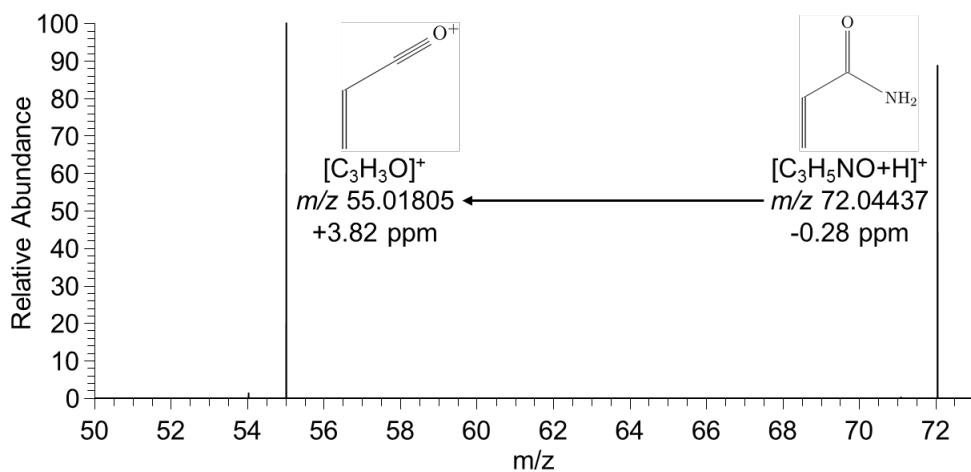


Fig. S2: Average MALDI MS/MS spectrum of acrylamide standard (n=42 single spectra). Isolation window: m/z 72.0 \pm 0.2 at $NCE_{HCD} = 50$.

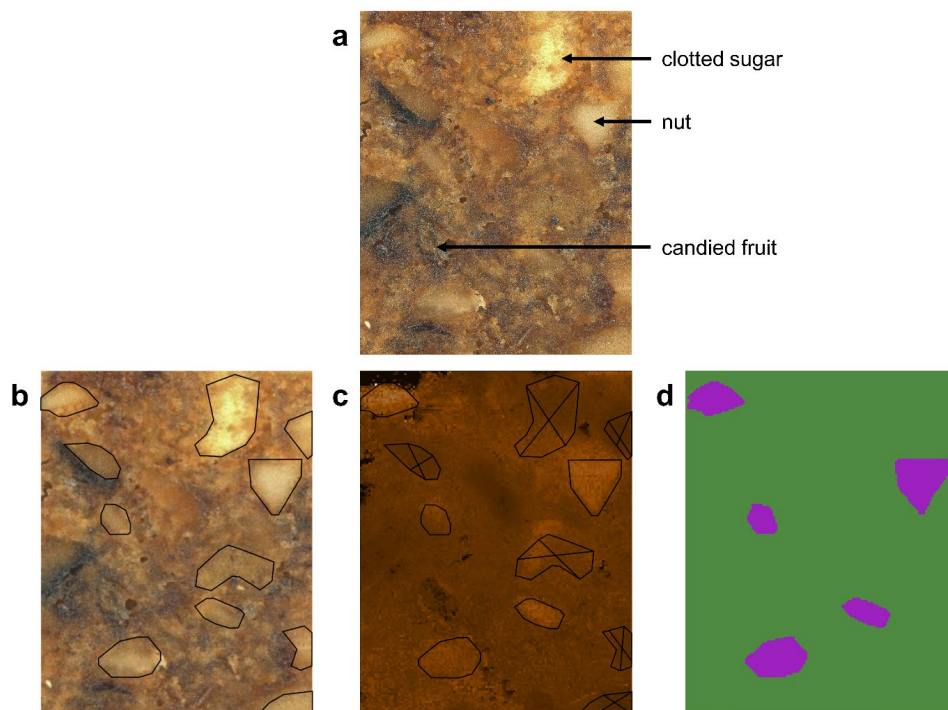


Fig. S3: Step-by-step procedure for stratification of gingerbread surface into ROI “nuts” and “other”. (a) optical image with annotated ingredients. (b) optical image with potential nut fragments based on visual perception. (c) sum image of triglycerides TG 52:3, TG 52:4, TG 54:5, TG 54:6 and TG 57:10 (all [M+K]⁺), generated in Mirion⁵², with overlaid candidate “nuts” ROI; regions with no visibly elevated triglyceride intensity were crossed out. (d) ROI mask for export of acrylamide abundance data; ROI “nuts” is depicted in pink, ROI “other” in green, performed in SpectralAnalysis⁵³. Export of abundance data of acrylamide m/z 72.04439 ± 2.5 ppm for both ROI, performed in MSiReader v1.01x⁵⁴.

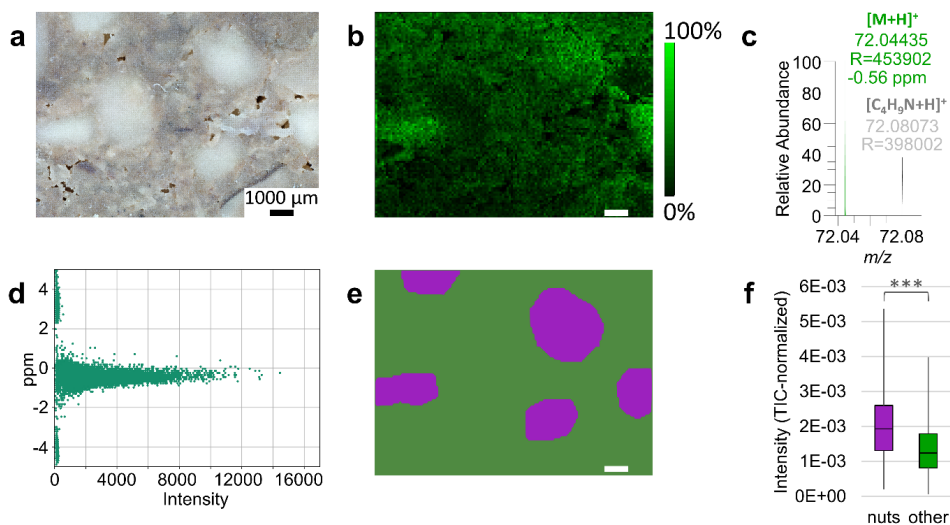


Fig. S4: MS imaging of a replicate contaminated German gingerbread sample. (a) optical image after measurement. (b) MS image of acrylamide [M+H]⁺, m/z 72.04439, TIC-normalized. Image dimensions are 127x94 pixels with a step size of 100 μm and an m/z range of 70-280. (c) single pixel mass spectrum of acrylamide signal together with mass resolution $R = 453902$ and relative mass error of -0.56 ppm. (d) mass measurement accuracy plot of m/z 72.04439, $RMSE = 0.52$ ppm ($n=11896$ peaks). (e) binary image showing ROI "nuts", based on optical image and sum image of triglycerides TG 52:3, TG 52:4, TG 54:5, TG 54:6 and TG 57:10, and "other". (f) Boxplot of backtransformed intensity values stratified into ROI „nuts“ and „other“; two-sided t-Test was performed on $x^{0.5}$ -transformed intensity values; *** $t(3087)=32.26$, $p<.001$.

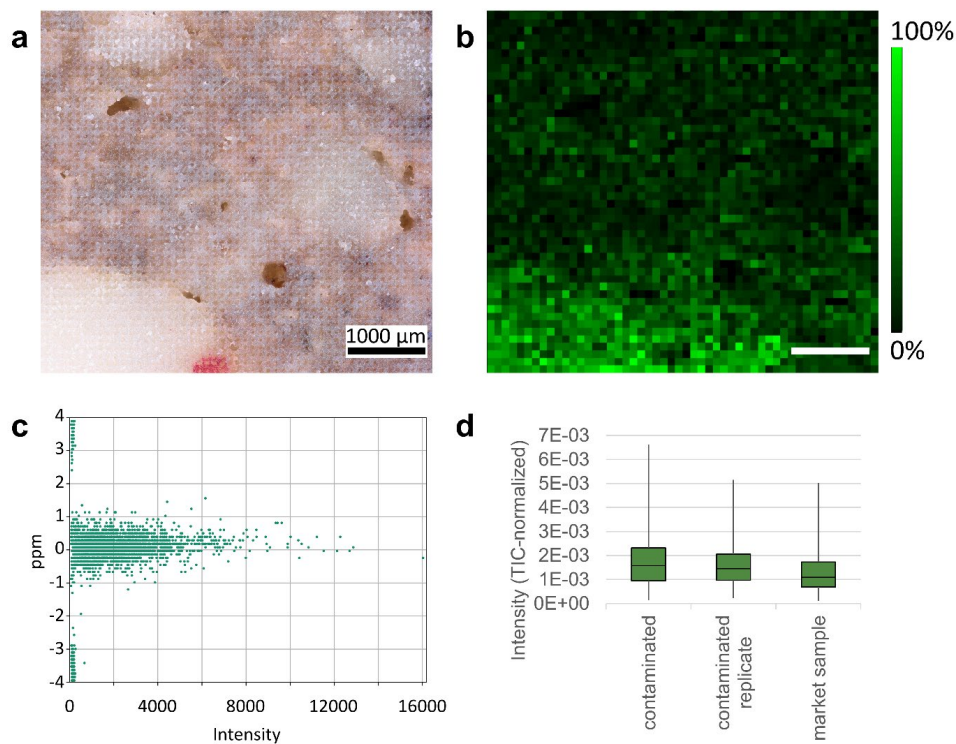


Fig. S5: MS imaging of a gingerbread market sample. The mean acrylamide amount determined by the GC-MS reference method is 174 µg/kg. (a) optical image after measurement. (b) MS image of acrylamide $[M+H]^+$, m/z 72.04439, TIC-normalized. Image dimensions are 52x48 pixels with a step size of 100 µm and an m/z range of 70-280. (c) mass measurement accuracy plot of m/z 72.04439, RMSE = 0.37 ppm ($n=2469$ peaks). (d) Boxplot of backtransformed acrylamide intensity values of entire measurements. Comparison of acrylamide intensities between the contaminated sample, shown in Fig. 3, the replicate measurement, shown in Fig. S8, and the market sample.

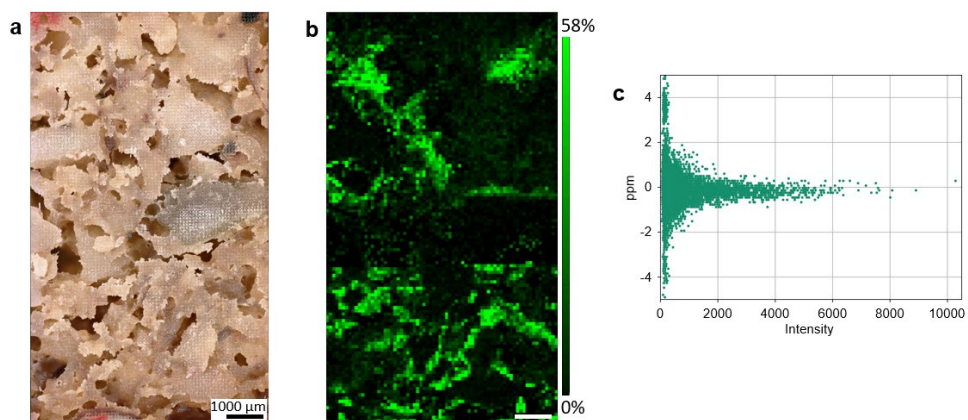


Fig. S6: MS imaging experiment of a gingerbread section cut with a knife. (a) optical image. (b) MS image of acrylamide $[M+H]^+$, m/z 72.04439, TIC-normalized. Image dimensions are 72x127 pixels with a step size of 90 µm and an m/z range of 70-280. (c) mass measurement accuracy plot of m/z 72.04439, RMSE = 0.67 ppm.

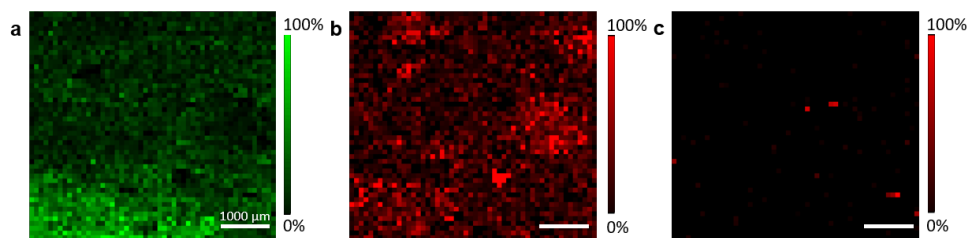


Fig. S7: In-situ derivatization of acrylamide on German gingerbread (measurement see Fig. S7). **(a)** MS image of acrylamide analogous to Fig. S7b. **(b)** Indexed MS image of TSA $[M+H]^+$, m/z 155.01613; $[M+Na]^+$, m/z 176.99807; $[M+K]^+$, m/z 192.97201 and $[M+NH_4]^+$, m/z 172.04268, TIC-normalized. **(c)** Indexed MS image of the Michael-adduct $[M+H]^+$, m/z 226.05324; $[M+Na]^+$, m/z 248.03519; $[M+K]^+$, m/z 264.00912 and $[M+NH_4]^+$, m/z 243.07979, TIC-normalized.

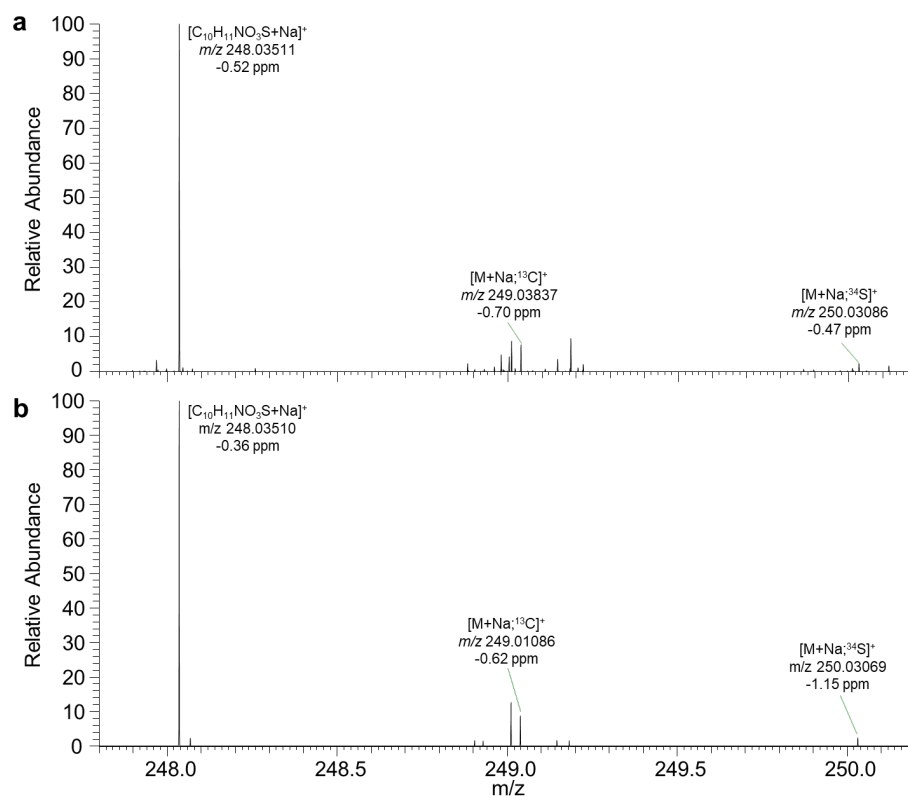


Fig. S8: Isotope distribution of the Michael-adduct, sum formula $[C_{10}H_{11}NO_2S+Na]^+$ (theoretical m/z 248.03519). **(a)** Average spectrum (n=102 single spectra) of the derivatization product formed from acrylamide standard on glass with sprayed TSA. **(b)** Single spectrum of the derivatization product formed on pancake sprayed with TSA and DHB.

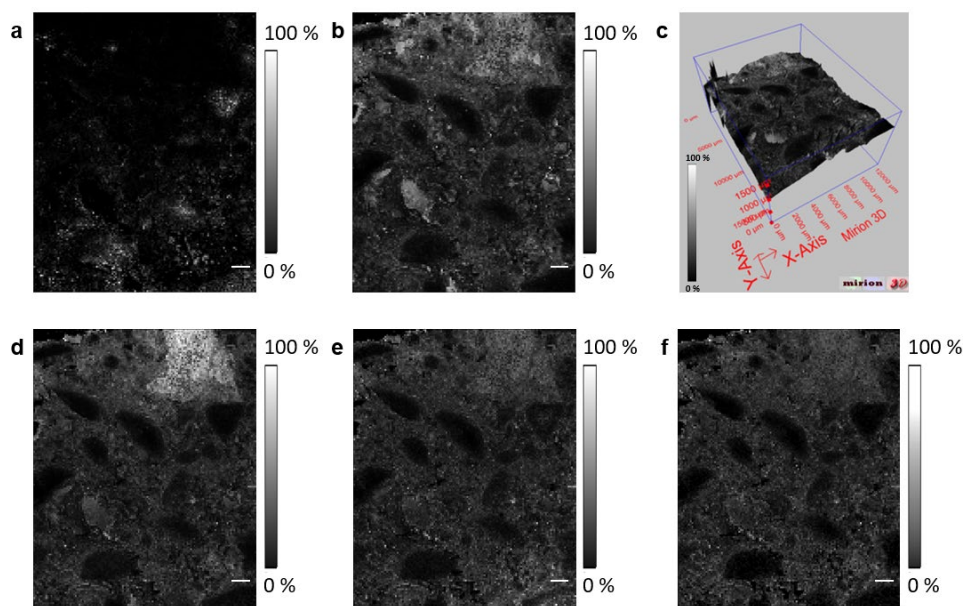


Fig. S9: Gray-scale MS images corresponding to Fig. 2. (a) MS image of PC 36:3 [M+K]⁺, m/z 822.54096, TIC-normalized. (b) MS image of disaccharide [M+K]⁺, m/z 381.07937, TIC-normalized. (c) 3D MS image of disaccharide [M+K]⁺, m/z 381.07937, TIC-normalized, Z-axis is based on AF-laser focus data. (d) MS image of trisaccharide [M+K]⁺, m/z 543.13219, TIC-normalized. (e) MS image of tetrasaccharide [M+K]⁺, m/z 705.18502, TIC-normalized. (f) MS image of pentasaccharide [M+K]⁺, m/z 867.23784, TIC-normalized.

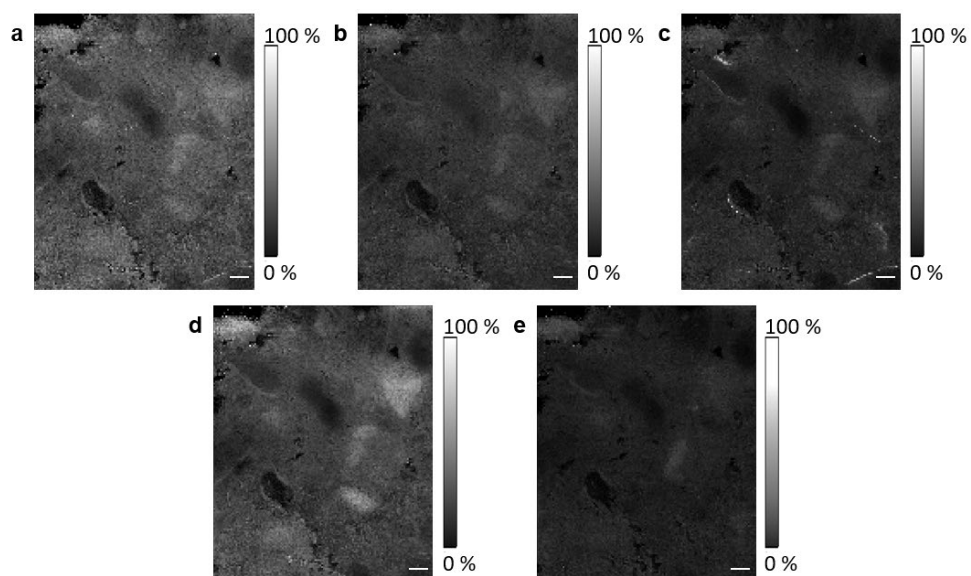


Fig. S10: Single-channel gray-scale MS images corresponding to Fig. S3. (a) MS image of TG 52:4 [M+K]⁺, m/z 893.69950, TIC-normalized. (b) MS image of TG 52:3 [M+K]⁺, m/z 895.71510, TIC-normalized. (c) MS image of TG 54:6 [M+K]⁺, m/z 917.69950, TIC-normalized. (d) MS image of TG 54:5 [M+K]⁺, m/z 919.71510, TIC-normalized. (e) MS image of TG 57:10 [M+K]⁺, m/z 935.70990, TIC-normalized.

3.3 MALDI MS imaging of chickpea seeds (*Cicer arietinum*) and crab's eye vine (*Abrus precatorius*) after tryptic digestion allows spatially resolved identification of plant proteins

MALDI MS Imaging of Chickpea Seeds (*Cicer arietinum*) and Crab's Eye Vine (*Abrus precatorius*) after Tryptic Digestion Allows Spatially Resolved Identification of Plant Proteins

Oliver Wittek, Bastian Jahreis, and Andreas Römpp*

Cite This: *Anal. Chem.* 2023, 95, 14972–14980

Read Online

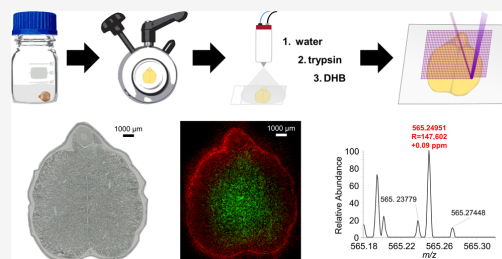
ACCESS |

Metrics & More

Article Recommendations

Supporting Information

ABSTRACT: Matrix-assisted laser desorption/ionization mass spectrometry (MALDI MS) imaging following in situ enzymatic digestion is a versatile analytical method for the untargeted investigation of protein distributions, which has rarely been used for plants so far. The present study describes a workflow for in situ tryptic digestion of plant seed tissue for MALDI MS imaging. Substantial modifications to the sample preparation procedure for mammalian tissues were necessary to cater to the specific properties of plant materials. For the first time, distributions of tryptic peptides were successfully visualized in plant tissue using MS imaging with accurate mass detection. Sixteen proteins were visualized and identified in chickpea seeds showing different distribution patterns, e.g., in the cotyledons, radicle, or testa. All tryptic peptides were detected with a mass resolution higher than 60,000 as well as a mass accuracy better than 1.5 ppm root-mean-square error and were matched to results from complementary liquid chromatography-MS/MS (LC-MS/MS) data. The developed method was also applied to crab's eye vine seeds for targeted MS imaging of the toxic protein abrin, showing the presence of abrin-a in all compartments. Abrin (59 kDa), as well as the majority of proteins visualized in chickpeas, was larger than 50 kDa and would thus not be readily accessible by top-down MS imaging. Since antibodies for plant proteins are often not readily available, in situ digestion MS imaging provides unique information, as it makes the distribution and identification of larger proteins in plant tissues accessible in an untargeted manner. This opens up new possibilities in the field of plant science as well as to assess the nutritional quality and/or safety of crops.



INTRODUCTION

Mass spectrometry imaging (MS imaging) is an analytical technique, which allows for resolving the spatial and molecular complexity of biological samples. Distributions of both endogenous and exogenous compounds can be identified and visualized based on their mass, without the need for labeling or staining.¹ The first report on MS imaging in plant science used the technique to study the uptake of pesticides into soya plants.² Since then, MS imaging has been an emerging field of research in plant biology with an increasing number of applications, e.g., focusing on lipids,³ metabolites,^{4,5} and contaminants.⁶ In this context, resulting from increasing interest in food safety, quality, and nutrition, we have recently published a variety of tailored sample preparation protocols for MS imaging of (processed) food, including the visualization of carotenoids and anthocyanins in carrots.⁷ Scientific advancements in plant^{8–10} and food MS imaging,¹¹ including food of plant origin, are regularly reviewed.

As indispensable components in living systems and major nutrients in the human diet, proteins are of extraordinary scientific interest. Mass spectrometry has been extensively used for proteome investigation both in animal (including human)¹²

and plant tissue.¹³ The analytical power of mass spectrometry is demonstrated in the recent publication on a quantitative atlas of the *Arabidopsis thaliana* proteome.¹⁴ Using MS imaging, the identification of proteins in a sample can be complemented by their spatial distribution. Despite a variety of developments in animal tissues,¹⁵ plant proteins have rarely been the focus of MS imaging studies. So far, only low-mass-resolution MALDI MS imaging techniques have been used to investigate proteins in plants. Visualized proteins are typically relatively small, i.e., lipid-transfer proteins in tomato (<9 kDa),¹⁶ an allergen protein in peach (<9.1 kDa),¹⁷ and sweet proteins in *Capparis masaiikai* seeds (<18.1 kDa).¹⁸ A notable exception is the report of a signal at 198 kDa in soybean, however, without further identification of the protein.¹⁸ A very recent study used the approach of detecting lower mass

Received: June 4, 2023

Accepted: September 5, 2023

Published: September 26, 2023



fragments (<10 kDa) to obtain information about larger proteins.¹⁹ In general, reliable protein identification is challenging with lower-mass-resolution time-of-flight (TOF) mass analyzers used in all previous studies on plant proteins.

Therefore, alternative methods have been developed to investigate the spatial distribution of proteins. The most recent approach for multiplexed MS imaging of proteins is MALDI-IHC, utilizing highly specific immunohistochemical (IHC) binding of antibodies or lectins carrying a photocleavable mass tag.²⁰ However, this approach is targeted, i.e., it requires functionalized antibodies, which are not broadly available for plant proteins yet.

Another strategy for protein identification is the analysis of peptides resulting from controlled in situ enzymatic protein digestion.²¹ This approach can be especially useful for larger proteins, which are typically not accessible by direct top-down MS imaging. In this bottom-up approach, proteins present on the sample surface are enzymatically digested in situ using a protease (most commonly trypsin). MALDI MS imaging is then used to measure the resulting proteotypic peptides, as these smaller compounds are easier to detect and identify than large intact proteins. Spatial distributions of proteins are determined based on their corresponding peptides. Due to the extraordinary complexity of biological tissue, especially after artificial expansion by enzymatic digestion, the use of a high-resolution mass analyzer is required for a reliable assignment of peptides by accurate mass.²² Identification results can often be improved by additional LC-MS/MS measurements.²¹ In an earlier study, we described such an approach for 25 μm pixel size in mammalian tissue and proposed a protein identification strategy based on a combination of "predominant distributions" of tryptic peptides and the detection of at least two peptides per protein.²³ MS imaging of tryptic peptides in mammalian tissue is already commonly used for spatially resolved untargeted protein identification in biomedical research.²⁴ However, it has rarely been applied to plant tissue. Some MS imaging studies have been conducted focusing on endogenous peptides in plant organs, such as roots,²⁵ leaves,²⁶ and petals²⁷ without digestion. On a technical basis, Grassl et al. provided useful information on the sample preparation for in situ enzymatic digestion but did not present measurement results.²⁸ Yet several authors mention the need for the development of a bottom-up MS imaging method in plants²⁹ or emphasize this as an unresolved challenge.^{28,30}

In this study, a sample preparation workflow for untargeted MALDI MS imaging of proteins in plants after tryptic digestion was developed by the example of seeds. Substantial modifications to the established workflow were necessary to cater to the requirements of plant tissue. Chickpea seeds, as an important food crop, were used as a model system because of their high protein content. The results constitute one of the first reports of MS imaging of proteins after enzymatic digestion in plants. Proteins were identified and localized based on the accurate mass of their corresponding tryptic peptides and complementary LC-MS/MS data. The developed method was also applied to a targeted investigation of the toxic protein abrin and its distribution within seeds of crab's eye vine. Our results are put into the context of reports on intoxication through the ingestion of crab's eye vine seeds after different forms of preprocessing, such as drilling or powdering.

MATERIALS AND METHODS

Sample Materials, Chemicals, and Enzymes. Organic, raw, and dried chickpea seeds were purchased from a local market, and all experiments were conducted with seeds from this package. Dried crab's eye vine seeds were provided by the Chemical and Veterinary Investigation Office (CVUA) Karlsruhe. 2,5-Dihydroxybenzoic acid (DHB, 98%), α -cyano-4-hydroxycinnamic acid (CHCA), trifluoroacetic acid (TFA, Chromasolv for HPLC), *N* α -benzoyl-L-arginine 4-nitroanilide hydrochloride ($\geq 99\%$), DL-dithiothreitol ($\geq 99\%$), Iodoacetamide ($\geq 99\%$), and ammonium bicarbonate (ReagentPlus $\geq 99\%$) were purchased from Sigma-Aldrich GmbH (Taufkirchen, Germany). Urea ($\geq 99.5\%$, pro analysis 'p.a.'), TRIS ($\geq 99.3\%$), formic acid ($\geq 98\%$, p.a.), ethylene glycol ($\geq 99.5\%$), and 2-propanol (HPLC-Grade) were obtained from Carl Roth GmbH (Karlsruhe, Germany). Gelatin, methanol, and water (both HiPerSolv Chromanorm) were purchased from VWR Chemicals (Darmstadt, Germany). Trypsin (sequencing grade, modified) was obtained from Promega (Madison, WI).

Protein Extraction, In-Solution Digestion, and LC-MS/MS. For protein extraction and subsequent digestion, the protocols described by Bose et al. for cereal grains³¹ and Schober et al. for mouse brain tissue²¹ were modified for chickpeas and crab's eye vine. The procedure is described in the Supporting Information. An UltiMate 3000 nano-LC (Thermo Scientific, Bremen, Germany) coupled to a Q Exactive HF-X mass spectrometer (Thermo Scientific, Bremen, Germany) was used for analysis. Parameters for both chromatographic separation and mass spectrometric detection are listed in Table S1. Protein results were filtered by 1% FDR and an ion score ≥ 50 and exported as Microsoft Excel files.

Sample Preparation for MALDI MS Imaging, Soaking, Embedding, and Sectioning. Chickpeas and crab's eye vine seeds were soaked in 30% aqueous ethylene glycol at room temperature (RT) for 1 week, which led to slight swelling of the seeds. Seed shape and color did not change substantially upon sample preparation. Prior to embedding in 5% gelatin, seeds were dried using a lint-free wipe. The bottom of a cryomold (Tissue-Tek, Sakura, Alphen aan den Rijn, the Netherlands) was covered with warm gelatin and precooled to 0 $^{\circ}\text{C}$. Samples were frozen at -80 $^{\circ}\text{C}$ for 45 min and then placed into the cryomold, which was filled up with gelatin and frozen at -80 $^{\circ}\text{C}$ for 2 h. Cryosectioning was performed in a cryomicrotome (Leica CM3050S, Wetzlar, Germany) at -40 $^{\circ}\text{C}$ chamber and object temperature and a section thickness of 25 μm with the germ facing upward, away from the cutting blade. Sections were thaw-mounted on glass slides (Menzel-Gläser Superfrost Plus, Thermo Scientific, Bremen, Germany) and stored at -80 $^{\circ}\text{C}$ until further preparation.

Tissue Washing, Water Spray, and In Situ Tryptic Digestion. Sections were brought to RT for 10 min in a desiccator. Excessive gelatin surrounding the sections was removed with a pointed cotton swab. For tissue washing, the protocol by Grassl et al. was adopted.²⁸ In brief, sections were washed in ice-cold 70% 2-propanol twice for 30 s, followed by 15 s submersion in ice-cold 95% 2-propanol. Sections were allowed to dry for 10 min in a desiccator. Subsequently, a short spray of pure water was conducted by using an HTX MS sprayer (HTX Technologies, Chapel Hill) equipped with an isocratic HPLC pump (Knauer, Berlin, Germany). Immediately after the water spray, 180 $\mu\text{g}/\text{mL}$ trypsin solution was

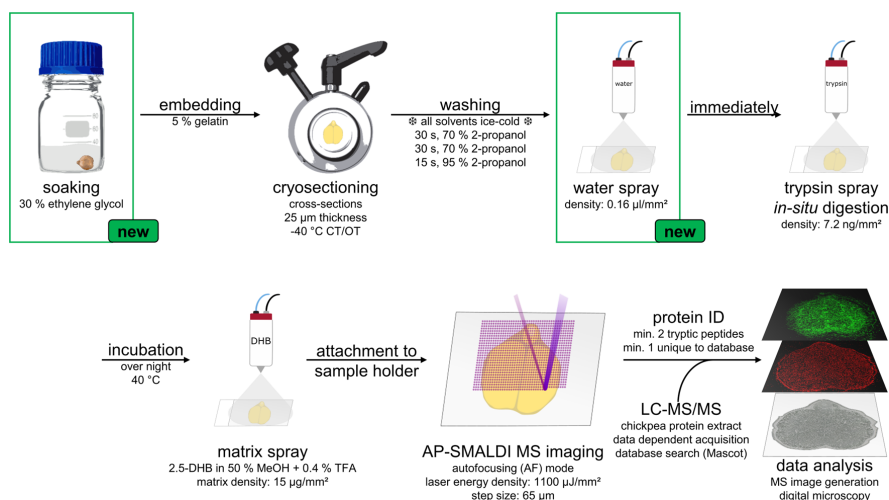


Figure 1. Sample preparation workflow for bottom-up MALDI MS imaging of plant proteins. Sample soaking and water spray are newly introduced steps in the standard sample preparation protocol. CT/OT: chamber and object temperature.

sprayed onto the sections with the HTX MS sprayer and an AL-300 isocratic syringe pump (WPI Europe, Friedberg, Germany). Spray parameters for water and trypsin are listed in Table S2 and discussed in the Results and Discussion Section. Sprayed samples were placed into an incubator at 40 °C overnight, while during daytime, hot water (70 °C) was repeatedly placed into the chamber. For quality control, temperature and humidity during incubation were monitored with sensors connected to a Raspberry Pi 3 (Raspberry Pi Trading Ltd., Cambridge, U.K.).

Matrix Application and MS Imaging Measurement. A solution of 30 mg/mL 2.5-DHB was prepared in 50% aqueous methanol and 0.4% TFA. Prior to injection into the spraying device, the solution was sonicated for 20 min at RT. For the matrix spray, an HTX MS sprayer was used. The spray parameters are listed in Table S2 and discussed in the Results and Discussion Section. MALDI MS imaging measurements were conducted using a quadrupole-orbitrap mass spectrometer Q Exactive HF (Thermo Scientific, Bremen, Germany) coupled to the atmospheric pressure autofocusing MALDI imaging source AP-SMALDIS AF (TransMIT GmbH, Gießen, Germany),³² which we have already successfully used for autofocusing MS imaging of food of plant origin.³³ All measurements were carried out in positive ion mode with a fixed C-trap injection time of 500 ms and 50 laser shots per pixel at a mass resolution of 240,000 at m/z 200 full width at half-maximum (FWHM). Mass calibration before each measurement was conducted using a mixture of DHB and Ultramark 1621.

In addition, internal mass calibration was performed during the measurement using homogeneously distributed matrix cluster ions.³⁴ Laser step size was set to 65 μm with a calculated target energy density of approximately 1100 $\mu\text{J}/\text{mm}^2$.

Data Analysis. Proprietary Thermo “RAW” data were converted into “imzML” data format³⁵ using an open access imzML Converter v2.1.0.³⁶ Validation of imzML files was done using imzML Validator v1.0.2.³⁷ The identification of proteins

was based on Huber et al.²³ and partly supported by a program which is currently being developed in our group to facilitate this process. The exported list of proteins detected in LC-MS/MS was used as a database for in silico digestion. Ion images of all putative peptides were generated, allowing a maximum of 2 missed cleavages and an image generation tolerance of ± 3 ppm. Apart from protonated adducts, sodium, potassium, and ammonium adducts were considered, since all of them are commonly detected in MALDI MS imaging with atmospheric pressure ionization and DHB matrix.²³ The results were filtered by mass deviation (± 1.5 ppm) and measure of spatial chaos metric³⁸ (≥ 0.96). In the next step, autolytic trypsin peptides (see Table S3) were excluded. The remaining peptides were assigned to their corresponding proteins and sorted into groups based on their distribution pattern.

For the calculation of monoisotopic masses and mass-to-charge ratios of putative peptides, Microsoft Excel with integrated Pep-Calc add-in was used.³⁹ Generation of single ion images and mass measurement accuracy (MMA) plots as well as the calculation of root-mean-square errors (RMSEs) of the $\Delta m/z$ values were conducted using in-house programmed imzML Analyzer v2.3.3 software. (Multi-)colored ion images were generated using Mirion 3D v3.3.64.11.⁴⁰ The bin width of all shown ion images is ± 3.0 ppm. For the interpretation of MS/MS spectra, mMass v5.5.0 was used.⁴¹

RESULTS AND DISCUSSION

Development of Sample Preparation Workflow.

In the following, the preparation of plant samples for MALDI MS imaging of tryptic peptides is described by means of chickpea seeds as a model for a protein-rich plant organ (18.6% in the dry seed).⁴² A schematic overview of the workflow is given in Figure 1. Cryosectioning of plant samples in general is not trivial because of an increased risk of shrinkage or section flaking and therefore requires thorough development.^{5,43} The sectioning method described by Kawamoto,⁴⁴ which uses an adhesive film for the preparation of thin sections from a carboxymethylcellulose (CMC) block containing the sample, is

commonly applied for delicate samples such as most plant organs. However, it is not applicable for in situ digestion because of the required tissue washing steps; sections fall off the slides when the tape comes into contact with organic solvents. Instead, in our study, entire chickpea seeds were soaked prior to cryosectioning to reduce the risk of flaking and/or breakage. To minimize the risk of analyte loss, soaking medium was not added excessively, but only for the samples being just immersed. To avoid cell breakage, no heat was applied during soaking. Several soaking media were tested, and representative microscopy images are given in Figure S1. While soaking in water led to uneven swelling of the seeds and increased formation of cracks within sections, the use of 50% ethanol produced more stable sections at first. Yet, during subsequent sample preparation steps, these sections turned out to dry very quickly, peel off, or even fall off the slides. Better results were achieved by soaking in aqueous ethylene glycol. Mixtures from 15 to 35% ethylene glycol were tested, and 25–30% were found to produce intact and stable sections. Keeping samples moist overnight, as proposed by a study on edible nuts,⁴⁵ did not suffice for chickpea seeds. Irrespective of the soaking medium, the necessary time period for complete soaking was around 1 week. Shorter periods produced samples with a dry center; longer periods (up to 4 weeks were tested) are not beneficial for sectioning. Entire seeds were wiped dry and frozen at $-80\text{ }^{\circ}\text{C}$ for 45 min. Rapid deep-freezing using liquid nitrogen caused breakage of the sample, which has also been described previously.⁴⁵ Gelatin is recommended as an embedding medium for plants^{9,28} and was used with a concentration of 5%. Chickpea seeds were placed into the embedding well with the radicle facing toward the bottom and allowed to freeze for another 2 h at $-80\text{ }^{\circ}\text{C}$. The use of gelatin showed better retention of the fragile seed coat than CMC, which also tended to thaw quickly and be absorbed by the section. The correlation between the glycol concentration for soaking and section thickness is depicted in Figure S2. Best sections were acquired with a thickness of 25–30 μm after soaking samples in 25–30% glycol. Due to the reduced freezing point of the glycol solution, both chamber (CT) and object temperature (OT) of the cryostat needed to be set to $-40\text{ }^{\circ}\text{C}$ to prevent detachment of the seed coat. Also, the orientation of the seed toward the cutting blade is crucial for successful sectioning. With the radicle facing away from the cutting blade, the loss of the radicle could be prevented, and stable, complete chickpea sections were acquired.

Owing to the complexity of biological tissues, the removal of salts, lipids, and saccharides by washing is commonly applied to prevent suppression effects and to ensure fixation of the sections.⁴⁵ The extent of washing protocols should, however, be kept at a minimum to avoid loss of analytes from hydrophilic plant tissue.⁴³ In general, the influence of soaking entire seeds (with an intact cell structure) as well as the water spray (for details, see Table S4) regarding delocalization of (hydrophilic) proteins is considered much lower compared to the tissue washing step. Due to the necessity of washing for successful MS imaging of tryptic peptides, delocalization cannot be avoided completely. Thus, the choice of a suitable washing protocol is crucial to achieve an acceptable trade-off between the effective removal of interfering substances and minimal analyte delocalization. In contrast to animal tissue, saccharides play a major role in plant tissue and effective removal thereof should be considered. For chickpea sections, two different washing protocols were tested: The first,

according to Grassl et al.,²⁸ includes two washing steps for 30 s with 70% ice-cold 2-propanol and a 15 s step with 95% ice-cold 2-propanol. The second was modified from Enthaler et al.,⁴⁶ using two cycles of 70 and 100% ice-cold ethanol for 30 s each, with 5 dips in ammonium bicarbonate buffer at pH 4.5 in between.⁴⁷ The buffer was introduced instead of pure water for better protein fixation due to the isoelectric point of most chickpea proteins. The comparison showed that with the latter protocol, some proteins are washed off the section, and the corresponding tryptic peptides could not be detected, as demonstrated for tryptic peptides of 40S ribosomal protein S4 (Accession No. A0A1S2YYM1) in Figure S3A. With the 2-propanol-based protocol, this was not observed (Figure S3B), so we considered this protocol suitable for our purpose.

Since plant tissues in general tend to absorb liquids, it is difficult to restrict tryptic digestion to the sample surface. Suction of trypsin into the inner parts of the section would lead to a reduced formation of peptides on the surface and, thus, reduced peptide signal intensities. Therefore, a short spray of pure water was inserted into the workflow prior to trypsin application to saturate the plant tissue and, thus, prevent trypsin absorption. This water spray treatment was investigated thoroughly, and the final parameters are listed in Table S2. They were chosen to balance between a visibly dry sample and excessive moisture, i.e., sections should “darken” with moisture but must not appear shiny on the surface. More details on the evaluation of water spray parameters are given in Table S4. The application of water as a spray is preferable compared to a short dip because applying excessive liquid is avoided, and thus, delocalization or even loss of hydrophilic proteins is minimized (see Figure S4 for more details). Immediately after the water spray, an aqueous solution of trypsin was applied to the chickpea section. Parameters for the automated trypsin spray are given in Table S2; evaluation results on trypsin density can be found in Figure S5. As a quality control measure to prevent application of inactive enzyme, trypsin activity was checked photometrically prior to each spray (Figure S6). Activity scores in the presented measurements ranged between 2.0 and 2.3 U/mg. Digestion was performed overnight in a $40\text{ }^{\circ}\text{C}$ tempered humid chamber. Overnight digestion yielded a higher number of detected peptides than only 3.5 h digestion, although with a lower average number of amino acids per peptide. After removal from the tempered chamber, digestion was stopped by applying the MALDI matrix at low pH. Here, we compared the matrices DHB and CHCA. Significantly higher signals for chickpea tryptic peptides were achieved using DHB (see Figure S7), so this matrix was chosen for further measurements. Parameters for the automated matrix spray are listed in Table S2; the final calculated matrix density was $15\text{ }\mu\text{g}/\text{mm}^2$. The procedure for data conversion and untargeted protein identification from MS imaging data is described in detail in the Materials and Methods Section. A protein was only marked as identified if more than 50% of its corresponding peptides show consistent distribution (“predominant distribution”) and two or more peptides could be assigned with at least one peptide being unique in the entire data set (all in silico digested proteins from the LC-MS/MS database).²³

The described workflow for MALDI MS imaging of tryptic peptides in plants required substantial method development, including new steps in sample preparation. Most plants differ greatly in their composition compared to mammalian tissues, resulting in the need, e.g., for sample soaking. Due to the

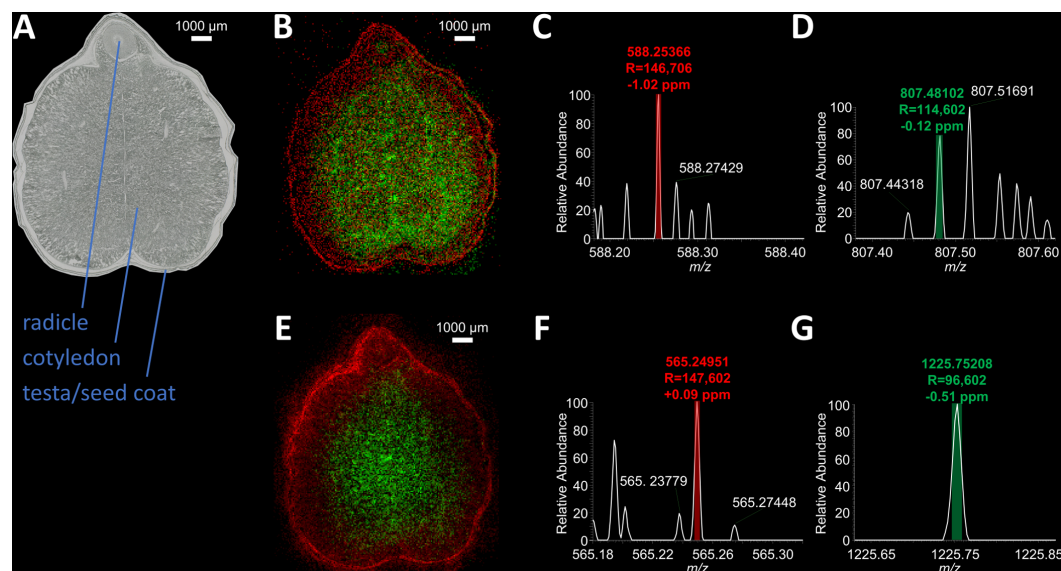


Figure 2. Ion images and MS data of tryptic peptides with different distributions in chickpea seeds. (A) Optical image of the measured chickpea section with assigned anatomical features. (B) Overlay of m/z 588.25426 (red), corresponding to tryptic peptide EFVR (K adduct) of protein A0A1S2XHJ1 and m/z 807.48112 (green), corresponding to tryptic peptide VGVKIKNR (Na adduct) of protein A0A1S2YYM1. (C) Single-pixel mass spectrum of m/z 588.25426 with mass resolution R , mass deviation, and bin width (red bar). (D) Single-pixel mass spectrum of m/z 807.48112 with R , mass deviation, and bin width (green bar). (E) Overlay of m/z 565.24946 (red), corresponding to tryptic peptide SHGVK (K adduct) of protein A0A1S2YX55 and m/z 1225.75283 (green), corresponding to tryptic peptide KKWVIHIER (NH₄ adduct) of protein A0A1S2XNPS. (F) Single-pixel mass spectrum of m/z 565.24946 with R , mass deviation, and bin width (red bar). (G) Single-pixel mass spectrum of m/z 1225.75283 with R , mass deviation, and bin width (green bar). Single-channel MS images are depicted in Figure S15.

soaking medium, the sectioning temperature needed to be reduced. Water-rich plant sections stored at -80 °C tend to dehydrate and sometimes shrink; in our case, fresh preparation of sections is required for each measurement. The higher amount of carbohydrates in plant tissue must be considered for the choice of suitable wash protocols. Finally, the stronger tendency of plant sections to absorb liquids leads to technical differences in the application of enzyme (such as an additional water spray) and the MALDI matrix.

Based on this protocol for chickpea seeds, new workflows for other plant organs and species can be developed for MS imaging of tryptic peptides. An application for crab's eye vine seeds is presented further on.

MS Imaging of Tryptic Peptides for Identification of Chickpea Seed Proteins. In the optical image of the chickpea cross section (Figure 2A), different anatomical features can be distinguished, such as cotyledons, testa, and radicle.⁴⁸ By MS imaging, tryptic peptides from chickpea seed proteins were detected with different distributions including the anatomical compartments visible in microscopy. In Figure 2B,E, two overlays of selected ion images of tryptic peptides from different chickpea seed proteins illustrate the detected distribution patterns. Tryptic peptide EFVR (K adduct) of α -1,4 glucan phosphorylase (Accession No. A0A1S2XHJ1, 111.3 kDa) is depicted in red in Figure 2B. It is evenly distributed throughout all seed compartments, including the testa. A mass spectrum from a single 65 μ m pixel showing this peptide's signal at high mass resolution (R (FWHM) = 146,706) and high mass accuracy (mass deviation -1.02 ppm)

is given in Figure 2C. All MS measurements of peptides shown in this study were of similar quality, i.e., a mass resolution higher than 60,000 and a mass accuracy better than 1.5 ppm RMSE (see also Figure 2D,F,G).

Tryptic peptide VGVKIKNR (Na adduct) of 40S ribosomal protein S4 (Accession No. A0A1S2YYM1, 29.9 kDa) is localized in the cotyledons and the radicle, as depicted in green in Figure 2B; a single-pixel mass spectrum is shown in Figure 2D. The MS image shows a characteristic ring-shaped distribution within the cotyledons, possibly due to vascular bundles or a fold in the cotyledons. As shown in Figure 2E, tryptic peptide SHGVK (K adduct) of heat shock 70 kDa protein 8 (Accession No. A0A1S2YX55, 62.2 kDa) is concentrated around the testa with low intensities within the cotyledons; a single-pixel mass spectrum is provided in Figure 2F. Complementarily, tryptic peptide KKWVIHIER (NH₄ adduct) of 60S ribosomal protein L26–2-like (Accession No. A0A1S2XNPS, 16.6 kDa), depicted in green in Figure 2E, is located only within the cotyledons. A corresponding single-pixel mass spectrum is given in Figure 2G. The mass accuracy for each signal across all individual spectra is described as RMSE. In the case of tryptic peptide EFVR (K adduct) at m/z 565.24946, the calculated RMSE is 1.04 ppm (28,938 spectra). MMA plots, RMSE values, and the respective pixel counts for all signals are provided in Figure S8. In Schober et al., we published the first MS imaging experiment using an orbital trapping mass spectrometer for the detection of tryptic peptides with accurate mass and pointed out that high mass resolution and mass accuracy are crucial for selective detection

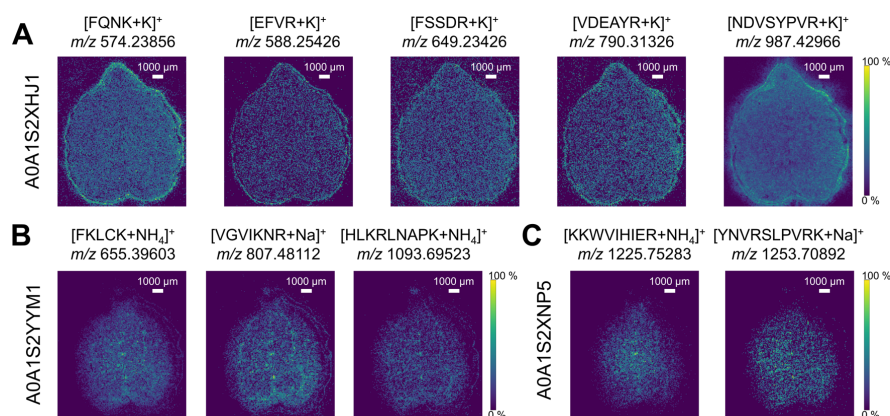


Figure 3. MS imaging of tryptic peptides of three chickpea seed proteins. (A) MS images of tryptic peptides from protein A0A1S2XHJ1. (B) MS images of tryptic peptides from protein A0A1S2YYM1. (C) MS images of tryptic peptides from protein A0A1S2XNP5. All ion images are generated with 0–100% intensity scaling of the respective m/z .

and the presentation of spatial features in MS imaging of mammalian tissue.²¹ We can confirm and emphasize this for MS imaging of plants, where, in many cases, high mass resolution and mass accuracy are essential, considering the increased molecular complexity of the sample due to the generation of cleavage peptides during enzymatic digestion. Figure S9 demonstrates this aspect in the present measurement by means of tryptic peptide CPGR (NH_4 adduct) at m/z 449.22893, which has a close neighboring peak (Figure S9A,B) with a different spatial distribution (Figure S9C,D). With low-resolution instruments, the distribution of the peptide would have been distorted by the inclusion of the neighboring signal. Further details regarding the identification of proteins in plant sections are discussed in the following. The MS images depicted in Figure 2 are only a small proportion of all detected tryptic peptide signals; for the presented distribution patterns, with the exception of the distribution with higher concentrations around the testa (tryptic peptide SHGVK (K adduct)), multiple tryptic peptides could be found for several proteins. Since there is no generally agreed procedure for the identification of proteins in MS imaging so far, we discussed relevant requirements in a previous study and proposed a minimum number of two detected peptides per protein with consistent “predominant” spatial distribution and at least one peptide unique to the data set (see also previous section).²³ Based on these recommendations, MS images of tryptic peptides corresponding to three representative identified chickpea seed proteins are shown in Figure 3. Next to tryptic peptide EFVR (K adduct) from Figure 2B (red), four additional tryptic peptides with consistent distribution across the entire section were found for the protein α -1,4 glucan phosphorylase (Accession No. A0A1S2XHJ1) and are depicted in Figure 3A. The assignment of this protein is also supported by a recent LC-MS/MS-based study of chickpea seeds.⁴⁹ In addition to tryptic peptide VGVKNR (Na adduct) from Figure 2B (green) showing a distribution across the radicle and the cotyledons with the characteristic ring-shaped structure, two more tryptic peptides with matching distributions were detected for 40S ribosomal protein S4 (Accession No. A0A1S2YYM1) and are shown in Figure 3B. Apart from tryptic peptide KKWVIHIER (NH_4 adduct) depicted in Figure

2E (green), another similarly distributed tryptic peptide of 60S ribosomal protein L26–2-like (Accession No. A0A1S2XNP5) was found within the cotyledons (Figure 3C). High mass accuracy is ensured in all presented MS images, with RMSE values lower than 1.5 ppm (Table S5).

In order to further support the identification of peptides by MALDI MS imaging, we conducted MALDI-MS/MS experiments on the tissue section after the MS imaging measurement. MALDI-MS/MS spectra are provided in Figure S12 for tryptic peptide NDVSYR (K adduct) shown in Figure 3A, and four additional tryptic peptides shown in Figure S10. In addition, MS/MS spectra of tryptic peptides, which were also directly detected in the complementary LC-MS/MS measurements, are provided in Figure S13.

The number of presented proteins in Figure 3 is not exhaustive. In total, based on the aforementioned identification requirements by Huber et al.,²³ 16 proteins could be identified in chickpea seeds. Thereof, 7 proteins show distributions across the entire section (Figure S10). Another 8 proteins are distributed throughout the cotyledons and the radicle (Figure S11), and one protein was identified for the cotyledon distribution pattern. A high number of additional peptides corresponding to other chickpea proteins were detected as well; however, our identification requirements of two peptides per protein with matching distribution (minimum one unique) were not met. By applying less strict criteria, the number of identified proteins would increase substantially. For example, with the requirement of only one peptide assigned to a protein in our database (“unique”), we would report 189 proteins as “identified” in our measurement. However, in this case, the probability of false positive assignments would be much higher. Notably, 69% of the identified proteins in our study are larger than 30 kDa (see Table S6) and would thus not be readily detected or identified by direct top-down protein MS imaging analysis without digestion. Moreover, using top-down protein MS imaging, typically only a few proteins are identified,^{16–18} or potential protein signals cannot be assigned to a protein. In a study that used smaller protein fragments (<10 kDa) as indirect markers, 22 proteins were assigned.¹⁹ In comparison to studies on mammalian tissues, which have been developed for more than a decade,⁵⁰ it is not surprising that the number

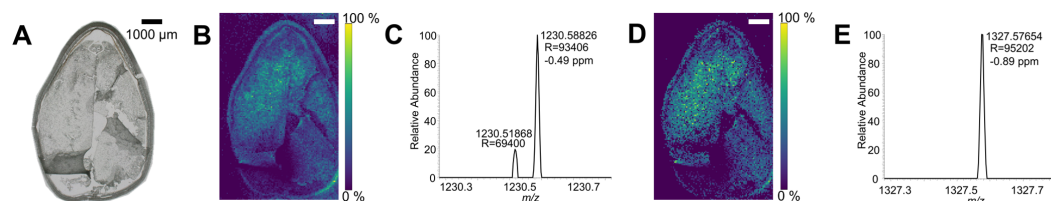


Figure 4. MS imaging of abrin-a (Accession No. P11140) peptides in crab's eye vine seed. (A) Optical image of the section prior to digestion. (B) Ion image of m/z 1230.58886, corresponding to tryptic peptide IIMWKCKDR (K adduct). (C) Single-pixel mass spectrum of m/z 1230.58886, with mass resolution and mass deviation. (D) Ion image of m/z 1327.57772, corresponding to tryptic peptide FSTEGATSQSYK (Na adduct). (E) Single-pixel mass spectrum of m/z 1327.57772, with mass resolution and mass deviation.

of identified proteins is much lower in plant tissue so far. In addition, animal tissue often contains (locally) higher amounts of proteins (e.g., in muscle strains) and much less carbohydrates. Furthermore, plant cells have a more rigid cell structure than animal cells, which makes the preparation of plant tissue for MS imaging more challenging.

In order to show the reproducibility of our workflow, results from a replicate measurement of another section at a different cutting plane in the same chickpea seed are given in Figure S14. Results are comparable to those shown in Figure 3 regarding the distribution patterns of tryptic peptides. Two additional measurements were conducted under almost identical conditions. Single-channel ion images of tryptic peptides depicted in Figure 2 are shown for all four measurements in Figures S15–S18. The presented results demonstrate that by MS imaging, proteins in plant samples can be identified and localized based on their tryptic peptides. The spatial resolution ($65 \mu\text{m}$ pixel size) in our study is higher compared with previous MS imaging studies of proteins in plants. At the same time, tryptic peptides were detected with high mass resolution and mass accuracy. The application of untargeted bottom-up protein MS imaging holds great potential for plant science. In a variety of biological processes, the distribution of proteins is of utmost importance, e.g., for studies on plant infection by molds.⁵ Moreover, the spatial distribution of proteins can also be relevant for (food) safety purposes, as shown in the following application.

MS Imaging of Abrin-a Peptides in *Abrus precatorius* Seeds. Abrin is a collective term for four toxic high-mass protein isoforms (~ 60 kDa), which are present in crab's eye vine and pose a severe health risk when ingested.^{51,52} There are several case reports on abrin intoxication and subsequent medical treatment of humans following ingestion of crab's eye vine seeds^{53–58} and a recent report on the presence of these seeds in pepper mixtures,⁵⁹ which all demonstrate the importance of the topic in the light of health and food safety. In the respective case reports, different methods of ingestion were described with varying outcomes. On the one hand, ingestion of 7 crushed seeds was fatal for a 28-year-old woman⁵⁷ and a freshly prepared “drink” of 20 blended seeds resulted in the death of a 25-year-old male.⁵⁶ On the other hand, ingestion of few damaged seeds⁵³ and seeds, which had been drilled or powdered, led to a full recovery.^{51,56,60} Although these case reports suggest a possible influence, only a few discuss the correlation between the form of ingestion and toxicity. Discussions focus merely on the potentially protective seed coat^{51,56} and proteolysis of abrin in the gastrointestinal tract.⁵¹ Other potential ways of detoxification, e.g., through penetration/removal of abrin “hotspots” after drilling or

peeling of the seeds, have not been investigated so far, but they have recently been mentioned in the context of “preprocessing” of seeds (e.g., drilling).⁵⁹ A particular distribution of abrin within crab's eye vine seeds could therefore be a conceivable explanation for detoxification. Thus, comparing the spatial distribution of abrin to the seed parts typically penetrated during processing could contribute to answering this question.

We addressed this task by applying our developed sample preparation and MS imaging workflow to a targeted measurement of abrin in crab's eye vine seeds. Samples were prepared and measured in the same way as chickpea seeds; however, instead of an untargeted data analysis approach, we directly searched for peptides of abrin-a (Accession No. P11140, 59.2 kDa). As depicted in Figure 4, two tryptic peptides of abrin-a could be detected: tryptic peptide IIMWKCKDR (K adduct) at m/z 1230.58886 is depicted in Figure 4B with an RMSE of 0.82 ppm (11,823 spectra, exemplary single-pixel spectrum in Figure 4C) and tryptic peptide FSTEGATSQSYK (Na adduct) at m/z 1327.57772 is shown in Figure 4D with an RMSE of 1.35 ppm (7771 spectra, exemplary single-pixel spectrum in Figure 4E). MMA plots for both signals are provided in Figure S19. Both tryptic peptides are unique for abrin-a within the data set of proteins of the *Abrus precatorius* organism detected by LC-MS/MS. In addition, tryptic peptide FSTEGATSQSYK was also found in our LC-MS/MS data (see Figure S20) and had already been detected in *A. precatorius* extract after tryptic digestion in a previous study.⁶¹ In our measurement, both peptides are evenly distributed throughout all seed compartments, including the seed coat. Analogous MS images from a replicate measurement of abrin-a in a different section of a crab's eye vine seed are provided in Figure S21. Our results show that MALDI MS imaging following in situ tryptic digestion is a suitable approach for the targeted investigation of the abrin distribution in crab's eye vine seeds. Abrin-a is present throughout the entire tissue including germ and seed coat. Although signal intensities are slightly higher within the cotyledons than those in other regions, there are no distinct “hotspots” of abrin; thus, they do not seem to play a major role in detoxification of “preprocessed” seeds. Possibly, it is rather the number of ingested beans and/or the individual clinical treatment that seem to influence the patients' recovery substantially. Moreover, the state of ripeness of the seeds is mentioned in cases of intoxication because unripe seeds have a softer seed coat, which can be easily chewed.⁵³ Nonetheless, our experiment shows that since abrin has also been detected in the seed coat and not only in the interior, a certain exposure to abrin released from intact seeds during gastrointestinal passage or sucking cannot be precluded. As long as studies on

abrin migration from intact seeds into saliva and intestinal fluids are lacking, recommendations to withhold "natural" jewelry containing crab's eye vine from children should be maintained.⁶²

CONCLUSIONS

In this study, we show the first results of MALDI MS imaging with accurate mass detection of plant proteins after in situ tryptic digestion. Due to the substantially different properties of plant tissue compared to mammalian tissue, the sample preparation workflow needed to be extended and modified. Tryptic peptide signals were detected with high mass accuracy as well as high mass resolution and matched to in silico digestion results from complementary LC-MS/MS data; 16 proteins were visualized and identified in chickpea seeds using strict identification criteria. In contrast to the top-down approach, MALDI MS imaging after tryptic digestion is not restricted in the analysis of larger proteins. Furthermore, unlike MALDI-IHC (and other antibody-based techniques), it is an untargeted approach. Consequently, bottom-up protein MS imaging provides unique information, as it makes the distribution and identification of larger proteins (≥ 30 kDa) in plant tissues accessible in an untargeted manner. In terms of the number of identified proteins and obtained spatial resolution, current results still lag behind studies on mammalian tissue, which have been developed for decades. The quality of results will most likely increase with further development in sample preparation (e.g., alternative enzymes); our results thus lay the basis for future studies on distributions of proteins in plants. Proteins play important roles in many biochemical processes in plants, so a vast range of research fields might profit from new insights into the spatial distribution of plant proteins. Also, changes in protein distributions over time can be investigated using this technique, which might be of particular interest in developmental biology and phytopathology. From a food science perspective, MS imaging of plant proteins may complement established analytical methods to assess the nutritional quality and/or safety of crop plants (as exemplified by our data on abrin).

ASSOCIATED CONTENT

Supporting Information

The Supporting Information is available free of charge at <https://pubs.acs.org/doi/10.1021/acs.analchem.3c02428>.

Additional experimental details on LC-MS/MS measurements; automated spray parameters for MALDI MS imaging sample preparation; microscopic images and descriptions of samples during preparation steps; supporting LC-MS/MS and MALDI-MS/MS spectra; diagrams for comparison of trypsin concentration and the MALDI matrix; MS imaging data of additional tryptic peptides and replicate measurements; details on the trypsin activity test; mass measurement accuracy tables and plots for detected ion signals; and table of all proteins marked as identified (PDF)

AUTHOR INFORMATION

Corresponding Author

Andreas Römpp – *Bioanalytical Sciences and Food Analysis, University of Bayreuth, D-95447 Bayreuth, Germany;*

orcid.org/0000-0001-8384-9250;
Email: andreas.roempp@uni-bayreuth.de

Authors

Oliver Wittek – *Bioanalytical Sciences and Food Analysis, University of Bayreuth, D-95447 Bayreuth, Germany;*
Present Address: Department of Physiology and Biochemistry of Nutrition, Max Rubner-Institute, Haid-und-Neu-Strasse 9, D-76131 Karlsruhe, Germany;
orcid.org/0000-0002-8872-6791

Bastian Jahreis – *Bioanalytical Sciences and Food Analysis, University of Bayreuth, D-95447 Bayreuth, Germany*

Complete contact information is available at:

<https://pubs.acs.org/10.1021/acs.analchem.3c02428>

Author Contributions

A.R. initiated the study. O.W. and A.R. designed the experiments and developed methodology and data analysis approaches. Sample preparation, method development, MS imaging measurements, and data processing were performed by O.W. B.J. established the trypsin activity test and the digestion workflow for mammalian tissue, which served as a basis for this study. Images for Table S4 and data for Figure S13 and Table S3 were generated by B.J. O.W. created all figures and tables. The manuscript was written by O.W. and A.R. All authors reviewed the manuscript. A.R. acquired funding and managed and supervised the project.

Notes

The authors declare no competing financial interest.

ACKNOWLEDGMENTS

The authors are grateful to Magdalena V. Wilde and Thomas Fröhlich from the Gene Center Munich (LAFUGA), LMU Munich, for conducting LC-MS/MS measurements. Thanks go to Dirk Lachenmeier from CVUA Karlsruhe for providing seeds of crab's eye vine. The authors' appreciation goes to Florian Stübinger for initial work on in situ tryptic digestion for MALDI MS imaging and to Marius Kolodziej for his work on chickpea section washing. Special thanks go to Verena Wallner for her valuable support on sample preparation and method development. This study was supported by the Deutsche Forschungsgemeinschaft (DFG, German Research Foundation) Project Number RO 3421/6-1, 391977956-SFB 1357, INST 91/373-1-FUGG, and the TechnologieAllianzOberfranken (TAO).

REFERENCES

- (1) Spengler, B. *Anal. Chem.* **2015**, *87* (1), 64–82.
- (2) Mullen, A. K.; Clench, M. R.; Crosland, S.; Sharples, K. R. *Rapid Commun. Mass Spectrom.* **2005**, *19* (18), 2507–2516.
- (3) Liu, B.; Meng, X.; Li, K.; Guo, J.; Cai, Z. *Talanta* **2021**, *221*, No. 121614.
- (4) Bednarz, H.; Roloff, N.; Niehaus, K. *J. Agric. Food Chem.* **2019**, *67* (49), 13470–13477.
- (5) Bhandari, D. R.; Wang, Q.; Friedt, W.; Spengler, B.; Gottwald, S.; Römpp, A. *Analyst* **2015**, *140* (22), 7696–7709.
- (6) Bhandari, D. R.; Wang, Q.; Li, B.; Friedt, W.; Römpp, A.; Spengler, B.; Gottwald, S. *Plant Methods* **2018**, *14* (1), No. 103.
- (7) Kokesch-Himmelreich, J.; Wittek, O.; Race, A. M.; Rakete, S.; Schlicht, C.; Busch, U.; Römpp, A. *Food Chem.* **2022**, *385*, No. 132529.
- (8) Boughton, B. A.; Thinagaran, D.; Sarabia, D.; Bacic, A.; Roessner, U. *Phytochem. Rev.* **2016**, *15*, 445–488.

- (9) Hu, W.; Han, Y.; Sheng, Y.; Wang, Y.; Pan, Q.; Nie, H. *J. Sep. Sci.* **2021**, *44* (18), 3462–3476.
- (10) Kaspar, S.; Peukert, M.; Svatos, A.; Matros, A.; Mock, H.-P. *Proteomics* **2011**, *11* (9), 1840–1850.
- (11) Yoshimura, Y.; Zaima, N. *Foods* **2020**, *9* (5), No. 575.
- (12) Aebersold, R.; Mann, M. *Nature* **2016**, *537* (7620), 347–355.
- (13) Yan, S.; Bhawal, R.; Yin, Z.; Thannhauser, T. W.; Zhang, S. *Mol. Hort.* **2022**, *2* (1), No. 17.
- (14) Mergner, J.; Frejino, M.; List, M.; Papacek, M.; Chen, X.; Chaudhary, A.; Samaras, P.; Richter, S.; Shikata, H.; Messerer, M.; et al. *Nature* **2020**, *579* (7799), 409–414.
- (15) Han, J.; Permentier, H.; Bischoff, R.; Groothuis, G.; Casini, A.; Horvatovich, P. *TrAC, Trends Anal. Chem.* **2019**, *112*, 13–28.
- (16) Bencivenni, M.; Faccini, A.; Zecchi, R.; Boscaro, F.; Moneti, G.; Dossena, A.; Sforza, S. *J. Mass Spectrom.* **2014**, *49* (12), 1264–1271.
- (17) Cavatorta, V.; Sforza, S.; Mastrobuoni, G.; Pieraccini, G.; Francese, S.; Moneti, G.; Dossena, A.; Pastorello, E. A.; Marchelli, R. *J. Mass Spectrom.* **2009**, *44* (6), 891–897.
- (18) Liu, H.; Han, M.; Li, J.; Qin, L.; Chen, L.; Hao, Q.; Jiang, D.; Chen, D.; Ji, Y.; Han, H.; et al. *Anal. Chem.* **2021**, *93* (35), 11920–11928.
- (19) Yin, Y.; Ren, Z.; Zhang, L.; Qin, L.; Chen, L.; Liu, J.; Jia, R.; Xue, K.; Liu, B.; Wang, X. *J. Agric. Food Chem.* **2023**, *71* (18), 7140–7151.
- (20) Claes, B. S. R.; Krestensen, K. K.; Yagnik, G.; Grgic, A.; Kuik, C.; Lim, M. J.; Rothschild, K. J.; Vandenbosch, M.; Heeren, R. M. A. *Anal. Chem.* **2023**, *95* (4), 2329–2338.
- (21) Schober, Y.; Guenther, S.; Spengler, B.; Römpp, A. *Rapid Commun. Mass Spectrom.* **2012**, *26* (9), 1141–1146.
- (22) Schober, Y.; Schramm, T.; Spengler, B.; Römpp, A. *Rapid Commun. Mass Spectrom.* **2011**, *25* (17), 2475–2483.
- (23) Huber, K.; Khamehgir-Silz, P.; Schramm, T.; Gorshkov, V.; Spengler, B.; Römpp, A. *Anal. Bioanal. Chem.* **2018**, *410* (23), 5825–5837.
- (24) Phillips, L.; Gill, A. J.; Baxter, R. C. *Front. Oncol.* **2019**, *9*, No. 379.
- (25) Gemperline, E.; Keller, C.; Jayaraman, D.; Maeda, J.; Sussman, M. R.; Ané, J.-M.; Li, L. *J. Proteome Res.* **2016**, *15* (12), 4403–4411.
- (26) Poth, A. G.; Mylne, J. S.; Grassl, J.; Lyons, R. E.; Millar, A. H.; Colgrave, M. L.; Craik, D. J. *J. Biol. Chem.* **2012**, *287* (32), 27033–27046.
- (27) Niyompany, P.; Sangvanich, P. *Int. J. Mass Spectrom.* **2022**, *477*, No. 116857.
- (28) Grassl, J.; Taylor, N. L.; Millar, A. H. *Plant Methods* **2011**, *7* (1), No. 21.
- (29) Peukert, M.; Matros, A.; Lattanzio, G.; Kaspar, S.; Abadia, J.; Mock, H.-P. *New Phytol.* **2012**, *193* (3), 806–815.
- (30) Matros, A.; Mock, H.-P. *Front. Plant Sci.* **2013**, *4*, No. 89.
- (31) Bose, U.; Broadbent, J. A.; Byrne, K.; Hasan, S.; Howitt, C. A.; Colgrave, M. L. *J. Proteomics* **2019**, *197*, 23–33.
- (32) Kompauer, M.; Heiles, S.; Spengler, B. *Nat. Methods* **2017**, *14* (12), 1156–1158.
- (33) Wittek, O.; Römpp, A. *Sci. Rep.* **2023**, *13* (1), No. 5400.
- (34) Treu, A.; Römpp, A. *Rapid Commun. Mass Spectrom.* **2021**, *35* (16), No. e9110.
- (35) Schramm, T.; Hester, Z.; Klinkert, I.; Both, J.-P.; Heeren, R. M. A.; Brunelle, A.; Laprévotte, O.; Desbenoit, N.; Robbe, M.-F.; Stoeckli, M.; et al. *J. Proteomics* **2012**, *75* (16), 5106–5110.
- (36) Race, A. M.; Styles, I. B.; Bunch, J. *J. Proteomics* **2012**, *75* (16), 5111–5112.
- (37) Race, A. M.; Römpp, A. *Anal. Chem.* **2018**, *90* (22), 13378–13384.
- (38) Alexandrov, T.; Bartels, A. *Bioinformatics* **2013**, *29* (18), 2335–2342.
- (39) Lear, S.; Cobb, S. L. *J. Comput.-Aided Mol. Des.* **2016**, *30* (3), 271–277.
- (40) Paschke, C.; Leisner, A.; Hester, A.; Maass, K.; Guenther, S.; Bouschen, W.; Spengler, B. *J. Am. Soc. Mass Spectrom.* **2013**, *24* (8), 1296–1306.
- (41) Strohalm, M.; Kavan, D.; Novák, P.; Volný, M.; Havlíček, V. *Anal. Chem.* **2010**, *82* (11), 4648–4651.
- (42) Souci, S. W.; Fachmann, W.; Kraut, H.; Kirchoff, E. *Food Composition and Nutrition Tables: Die Zusammensetzung der Lebensmittel, Nährwert-Tabellen*; Medpharm Scientific Publ: Stuttgart, 2008; p 1364.
- (43) Dong, Y.; Li, B.; Malitsky, S.; Rogachev, I.; Aharoni, A.; Kaftan, E.; Svatoš, A.; Franceschi, P. *Front. Plant Sci.* **2016**, *7*, No. 60.
- (44) Kawamoto, T. *Arch. Histol. Cytol.* **2003**, *66* (2), 123–143.
- (45) Hou, J.; Zhang, Z.; Zhang, L.; Wu, W.; Huang, Y.; Jia, Z.; Zhou, L.; Gao, L.; Long, H.; Lei, M.; et al. *Food Chem.* **2022**, *371*, No. 130893.
- (46) Enthaler, B.; Bussmann, T.; Pruns, J. K.; Rapp, C.; Fischer, M.; Vietzke, J.-P. *Rapid Commun. Mass Spectrom.* **2013**, *27* (8), 878–884.
- (47) Lahiri, S.; Walenta, L.; Aftab, W.; Strauss, L.; Poutanen, M.; Mayerhofer, A.; Imhof, A. Imaging mass spectrometry and shotgun proteomics reveal dysregulated pathways in hormone induced male infertility *bioRxiv* 2020.
- (48) Finch-Savage, W. E.; Leubner-Metzger, G. *New Phytol.* **2006**, *171* (3), 501–523.
- (49) Glusac, J.; Isaschar-Ovdat, S.; Fishman, A. *Food Chem.* **2020**, *315*, No. 126301.
- (50) Guo, G.; Papanicolaou, M.; Demarais, N. J.; Wang, Z.; Schey, K. L.; Timpson, P.; Cox, T. R.; Grey, A. C. *Nat. Commun.* **2021**, *12* (1), No. 3241.
- (51) Dickers, K. J.; Bradberry, S. M.; Rice, P.; Griffiths, G. D.; Vale, J. A. *Toxicol. Rev.* **2003**, *22* (3), 137–142.
- (52) Lin, J. Y.; Lee, T. C.; Hu, S. T.; Tung, T. C. *Toxicol.* **1981**, *19* (1), 41–51.
- (53) Fernando, C. *Anaesthesia* **2001**, *56* (12), 1178–1180.
- (54) Kinamore, P. A.; Jaeger, R. W.; DeCastro, F. J.; Peck, K. O. *Clin. Toxicol.* **1980**, *17* (3), 401–405.
- (55) Kobert, R. *Lehrbuch der Intoxikationen*; Verlag von Ferdinand Enke: Stuttgart, 1906.
- (56) Reedman, L.; Shih, R. D.; Hung, O. *West J. Emerg. Med.* **2008**, *9* (3), 157–159.
- (57) Subrahmanyam, D.; Mathew, J.; Raj, M. *Clin. Toxicol.* **2008**, *46* (2), 173–175.
- (58) Wooten, J. V.; Pittman, C. T.; Blake, T. A.; Thomas, J. D.; Devlin, J. J.; Higgerson, R. A.; Johnson, R. C. *J. Med. Toxicol.* **2014**, *10* (4), 392–394.
- (59) Habel, S.; Lachenmeier, D. W. *Lebensmittelchemie* **2019**, *73* (3), 71–72.
- (60) Robb, C. S. *TrAC, Trends Anal. Chem.* **2015**, *67*, 100–106.
- (61) Hansbauer, E.-M.; Worbs, S.; Volland, H.; Simon, S.; Junot, C.; Fenaille, F.; Dörner, B. G.; Becher, F. *Anal. Chem.* **2017**, *89* (21), 11719–11727.
- (62) *Schmuck aus Paternosterbohnsensamen nicht für Kinder geeignet*; Bundesinstitut für Risikobewertung: Berlin, 2012.

Supporting information

MALDI MS imaging of chickpea seeds (*Cicer arietinum*) and crab's eye vine (*Abrus precatorius*) after tryptic digestion allows spatially resolved identification of plant proteins

Oliver Wittek[†], Bastian Jahreis, Andreas Römpf*

Bioanalytical Sciences and Food Analysis, University of Bayreuth, Universitaetsstrasse. 30, D-95447 Bayreuth, Germany

[†] present address: Max Rubner-Institute, Department of Physiology and Biochemistry of Nutrition, Haid-und-Neu-Strasse 9, D-76131 Karlsruhe, Germany

PROCEDURE FOR PROTEIN EXTRACTION AND IN-SOLUTION DIGESTION^{1,2}

Samples were frozen in liquid nitrogen and processed into fine flour using a ball mill (Retsch GmbH, Haan, Germany). 10 mg of flour was weighed into a reaction tube, 200 μ l of aqueous extraction buffer (50 mM TRIS-HCl and 2 % DTT, pH 8.5) were added and the suspension was mixed until complete dispersion. After sonication for 5 min, the suspension was shaken for 45 min at 800 rpm and eventually centrifuged at 17,000 G for 15 min. 180 μ l of the extract were transferred into a 10 kDa MWCO tube (Vivaspin 500, Sartorius, Göttingen, Germany). Proteins were washed twice with 200 μ l ice-cold wash buffer consisting of 8 M urea and 50 mM TRIS-HCl (pH 8.5); centrifugation each time for 20 min at 17,000 G. For cysteine alkylation, 100 μ l of a 50 mM iodoacetamide solution in wash buffer were pipetted onto the filter and incubated for 20 min in the dark before centrifugation for 20 min at 17,000 G, followed by two subsequent wash and centrifugation steps with 100 μ l of a 100 mM ammonium bicarbonate buffer (pH 8.0). Then, 200 μ l of a 100 μ g/ml trypsin solution (in 10 mM ammonium bicarbonate buffer) were added to the filter and incubated over night at 37 °C. After attachment of fresh collection tubes, the peptide extract was centrifuged for 30 min at 17,000 G and washed twice with 200 μ l of 100 mM ammonium bicarbonate buffer (pH 8.0). The combined filtrate was lyophilized and redissolved in 100 μ l of 1 % aqueous formic acid for LC-MS/MS analysis.

Table S1: Parameters for liquid chromatography and mass spectrometric detection of tryptic peptides in chickpea seeds and crab's eye vine.

Trap column	Acclaim PepMap C18 (3 μ m, 20 x 0.1 mm)
Analytical column	EASY-Spray PepMap RSLC C18 (3 μ m, 500 x 0.075 mm)
Solvent A	0.1 % aqueous formic acid
Solvent B	0.1 % formic acid in acetonitrile
Flow rate	250 nl/min
Gradient	30 min / 3 % \rightarrow 25 % B 5 min / 25 % \rightarrow 40 % B
DDA cycles	1 full scan \rightarrow max. 12 MS/MS scans
Full scan mass range	m/z 350-1600
Mass resolution	Full scan: 60,000 MS/MS: 15,000
LC-MS/MS data analysis	Database: UniProtKB, organism „CICAR“ / „ABRPR“ (accessed on May 19, 2021) Modifications: „carbamidomethyl (C)“ (fixed) „oxidation (M)“ (variable) Monoisotopic mass tolerance: \pm 10 ppm (parent ions) \pm 0.02 Da (fragment ions)

Table S2: Parameters for the automated sprays of water, trypsin and the MALDI matrix DHB on chickpea sections using a HTX M5 Sprayer.

	water	trypsin	DHB
nozzle temperature (°C)	40	40	70
tray temperature (°C)	20	20	40
# passes	6	6	20
flow rate (µl/min)	40	10	75
nozzle velocity (mm/min)	750	750	1200
track spacing (mm)	2	2	2.5
spray pattern	vertical (VV)	criss-cross (CC)	vertical (VV)
nitrogen pressure (psi)	10	10	10
drying time between passes (s)	0	0	0
nozzle height (mm)	40	40	40

Table S3: Autoproteolytic peptides and corresponding mass adducts of porcine trypsin (*Sus scrofa*) in the mass range of m/z 500-2000 in positive ion mode. Peptide sequences were generated from Uniprot ID P00761 based on a maximum of two missed cleavages (#MC).

Peptide sequence	position	#MC	M (Da)	[M+H] ⁺	[M+NH ₄] ⁺	[M+Na] ⁺	[M+K] ⁺
IQVR	54-57	0	514.32273	515.33001	532.35656	537.31195	553.28589
SRIQVR	52-57	1	757.45587	758.46315	775.48970	780.44509	796.41903
VATVSLPR	108-115	0	841.50215	842.50943	859.53598	864.49137	880.46531
NKPGVYTK	209-216	0	905.49707	906.50435	923.53090	928.48629	944.46023
APVLSRSSCK	148-157	0	1005.48010	1006.48738	1023.51393	1028.46932	1044.44326
LSSPATLNSR	98-107	0	1044.55637	1045.56365	1062.59020	1067.54559	1083.51953
SSGSSYPSSLQCLK	134-147	0	1468.72318	1469.73046	1486.75701	1491.71240	1507.68634
VCNYVNIQQTIAAN	217-231	0	1735.83519	1736.84247	1753.86902	1758.82441	1774.79835
SCAAAGTECLISGWGNTK	116-133	0	1767.79201	1768.79929	1785.82584	1790.78123	1806.75517
LSSPATLNSRVATVSLPR	98-115	1	1868.04796	1869.05524	1886.08179	1891.03718	1907.01112

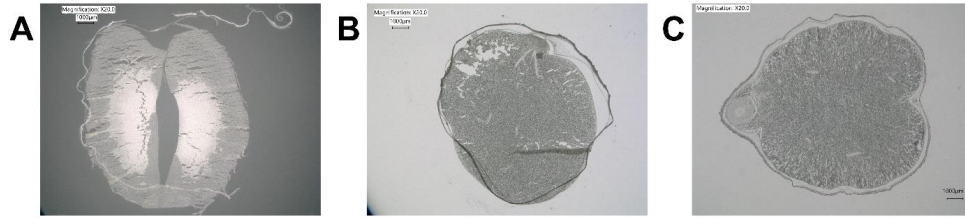


Figure S1: Representative microscopic images for different soaking media (7 days time period each). (A) Soaking in pure deionized water. Central parts of the sample are still dry, seed coat is removed easily and crack formation across the entire section. (B) Soaking in 50 % ethanol. Less crack formation, sections are stable at first; however, they dry quickly, peel off or fall off the slide easily. (C) Soaking in 30 % ethylene glycol. Sections are complete and stable during sample preparation and thin sections (25 µm) can be prepared.

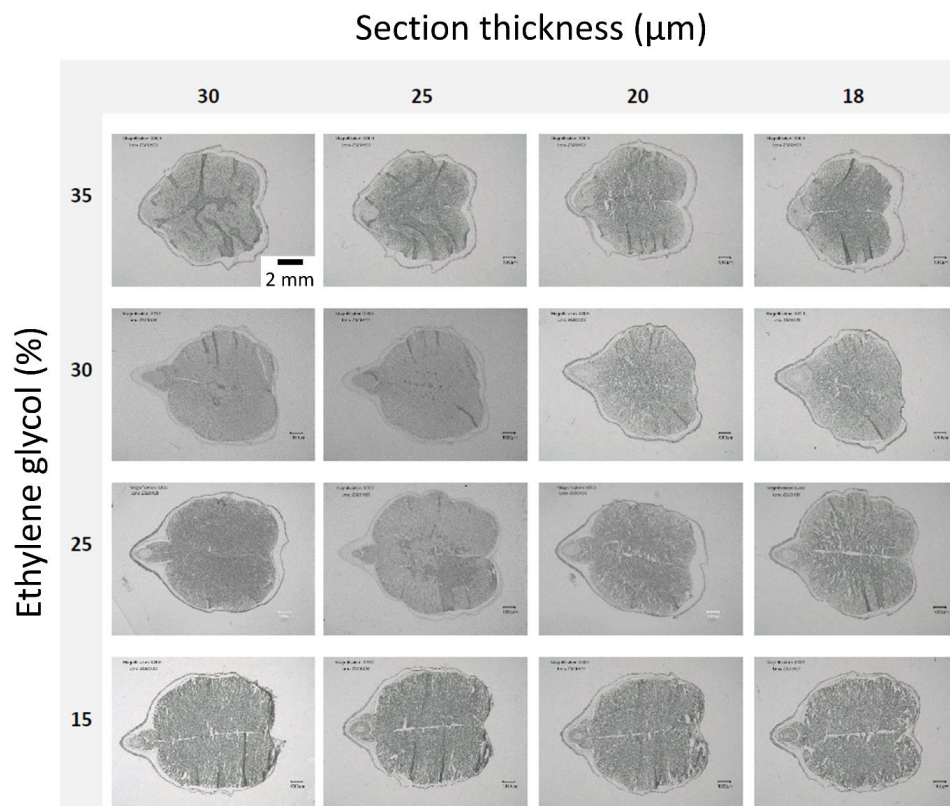
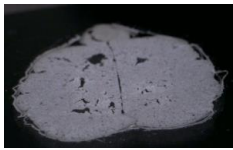




Figure S2: Matrix of microscopic images for different section thicknesses and concentrations of ethylene glycol for soaking. All images were taken in transmitted light mode with a X20 magnification. Evaluation was undertaken under consideration of wrinkling, removal of sample parts and crack formation.

3.3 MALDI MS imaging of chickpea seeds (*Cicer arietinum*) and crab's eye vine (*Abrus precatorius*) after tryptic digestion allows spatially resolved identification of plant proteins

Table S4: Experiments for water spray parameter evaluation. Pictures were captured using a USB digital microscope (DST-1028 5MP, Bresser GmbH, Rhede, Germany).

	Parameters				Result	Optical image of section after water spray
	Nozzle temp (°C)	Tray temp (°C)	# passes	Flow rate (µl/min)		
1	40	40	6	10	Section stays visibly dry independent of the number of spray passes; air flow of the spray causes tissue damage → no discernable rehydration of tissue section	
2	40	20	6	50	Visibly saturated with water after first pass; shiny appearance of section surface after following passes → excessive amount of liquid	
3	40	20	6	40	Visibly saturated with water; no excessive liquid; no visible change during trypsin spray → efficient rehydration without excessive moisture → protocol was used for MS imaging experiments in this study	

Optical images represent tissue appearance directly after the last pass of the water spray. Differences described above were apparent by visual inspection with the naked eye. It was difficult to capture these subtle – but important – differences with a camera.

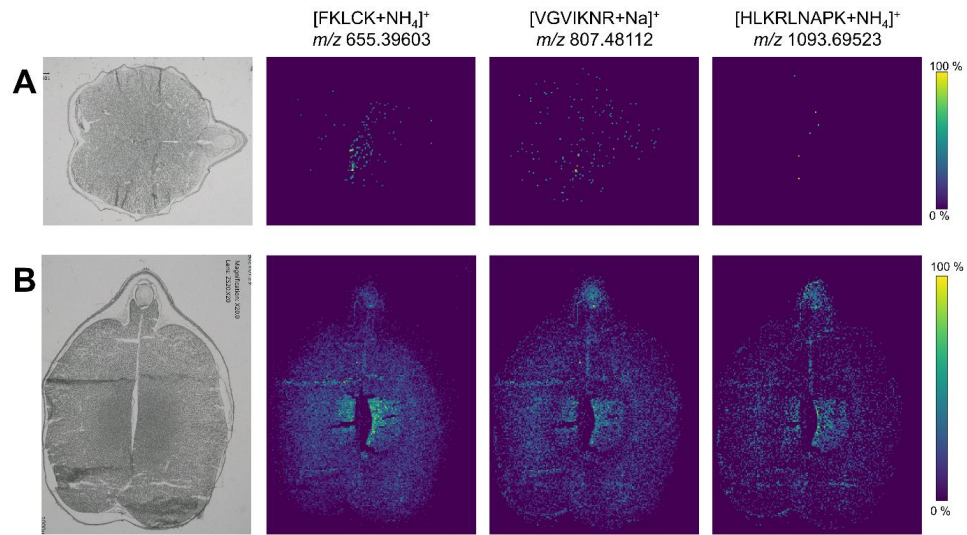


Figure S3: Comparison of wash protocols by means of three tryptic peptides from 40S ribosomal protein S4 (UniProt ID: A0A1S2YYM1). (A) Water-containing protocol modified based on Enthaler et al. 2013.³ (B) Wash protocol without water step adopted from Grassl et al. 2011.⁴

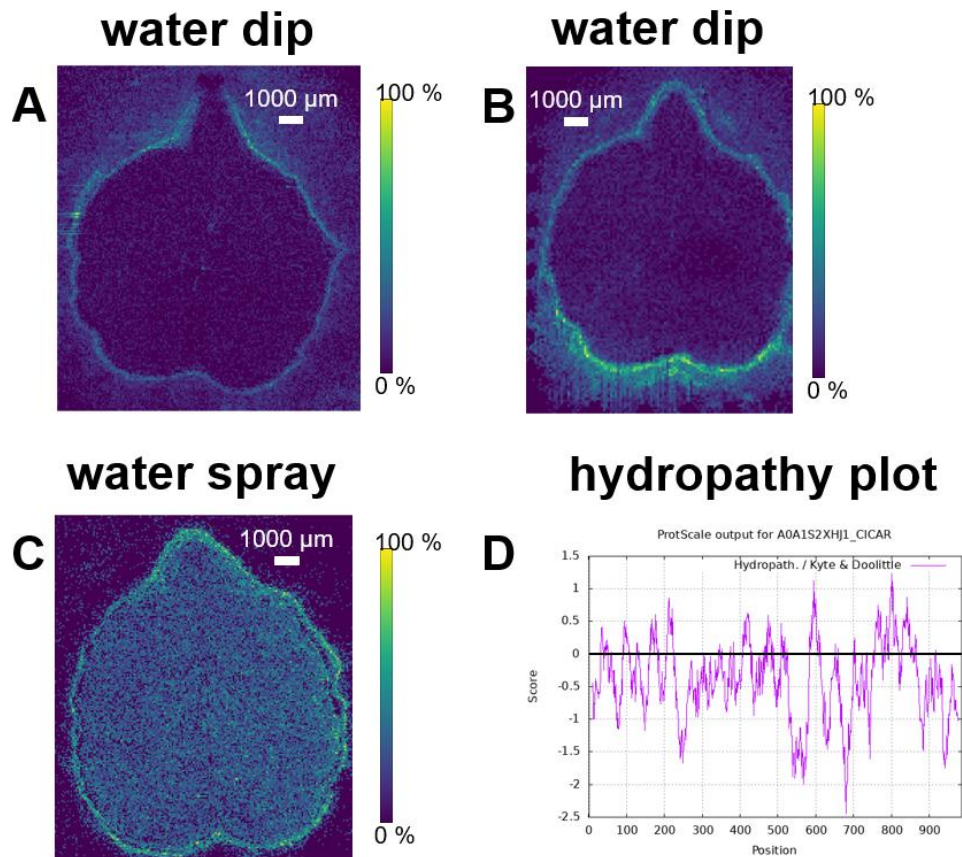


Figure S4. Exemplary MS imaging measurements after water dip instead of water spray prior to trypsin spray. All ion images show m/z 574.23856, corresponding to tryptic peptide FQNK (K adduct) of protein A0A1S2XHJ1. (A) MS image in measurement after water dip. Step size: 65 μm . (B) MS image in a second measurement after water dip. Step size: 100 μm . (C) MS image in measurement after water spray; also depicted in manuscript Figure 3A. (D) Hydropathy plot carried out on the complete sequence of this protein (window size: 21) shows vast hydrophilic regions (negative score) across the entire protein, suggesting that the protein is hydrophilic and prone to delocalization through water. The plot was created using the ExPASy ProtScale tool (<http://web.expasy.org/protscale/>).

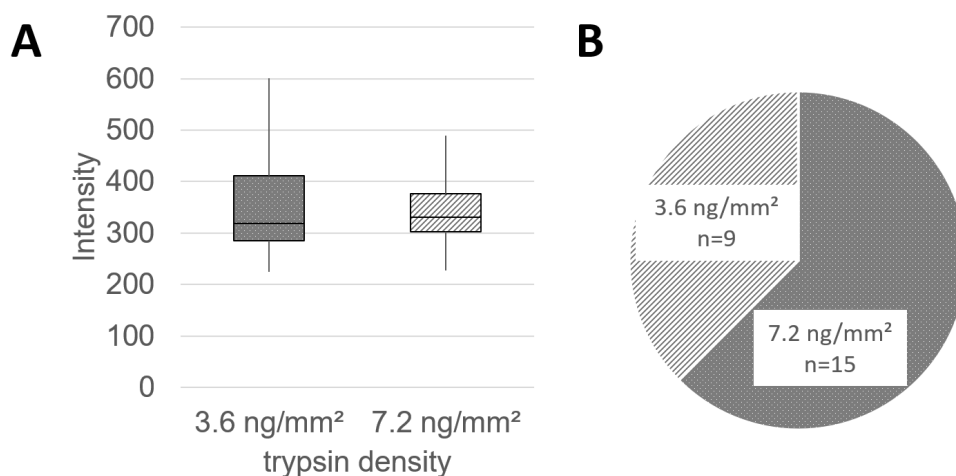


Figure S5: Comparison of trypsin concentrations. Two measurements were conducted with otherwise equal sample preparation parameters. One sample was sprayed with 90 ng/ μ l trypsin solution, yielding a final calculated trypsin density of 3.6 ng/mm²; the second sample was sprayed with 180 ng/ μ l trypsin solution yielding 7.2 ng/mm² density. (A) Intensity boxplot of n=24 tryptic peptides detected in both measurements. Median peptide intensity was 318 at 3.6 ng/mm² and 331 at 7.2 ng/mm². (B) Qualitative comparison of intensities according to trypsin concentration. 62.5 % of peptides showed higher intensity with 7.2 ng/mm² trypsin; 37.5 % showed higher intensity with 3.6 ng/mm² trypsin.

Multiple sprays with short intermediary digestion intervals, as conducted for mammalian tissues^{2,5}, were found unsuitable for chickpea seeds, because sections would dry out quickly during handling. We compared the two trypsin concentrations 90 ng/ μ l and 180 ng/ μ l, corresponding to calculated surface densities of 3.6 ng/mm² and 7.2 ng/mm², respectively. As shown in Figure S5A, trypsin concentration had no substantial effect on the average peptide intensity; however, on a qualitative level, the majority of peptides showed an increase in intensity at 7.2 ng/mm² (Figure S5B). In comparison to animal tissue (4.0 ng/mm² on mouse testis)⁶, trypsin density was slightly higher, probably due to some remaining absorption effect of plant tissue.

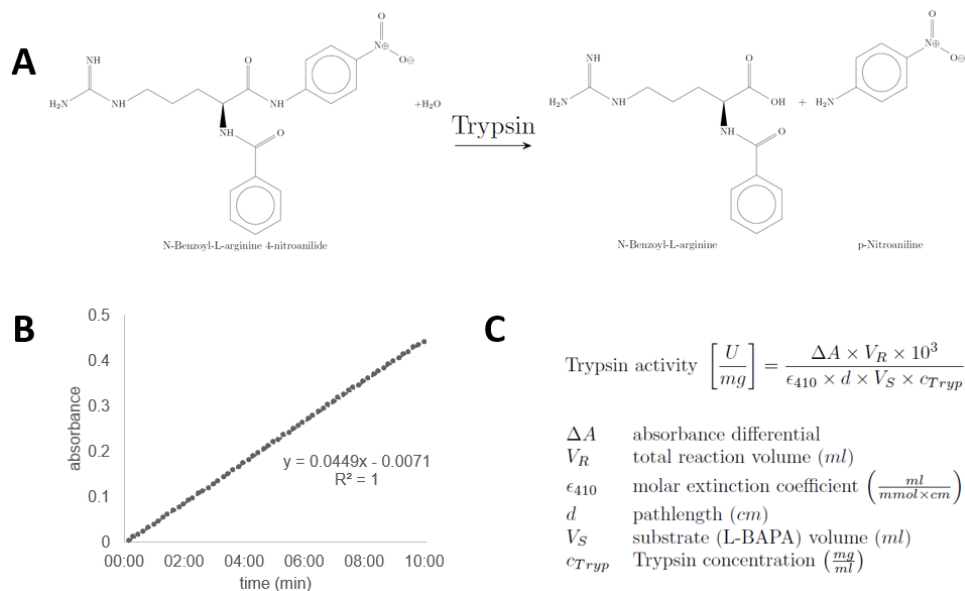


Figure S6: Photometric assay for verification of trypsin activity based on the method by Erlanger et al. 1961.⁷ (A) N α -benzoyl-L-arginine 4-nitroanilide hydrochloride (L-BAPA) used as trypsin substrate is cleaved by the enzyme to form p-nitroaniline, which is monitored at $\lambda=410$ nm for 10 min. Based on the slope of the linear regression (B), The enzyme activity is calculated according to Lambert-Beer's law (C) with a molar extinction coefficient of 8800 ml/(mmol cm).

For the photometric assay, a cuvette ($d = 1$ cm) was filled with 0.25 ml L-BAPA-solution (V_S), water and trypsin ($c_{Tryp} = 0.003$ mg/ml) to a total reaction volume (V_R) of 0.30 ml. The measured absorbance differential per minute was 0.0449 min^{-1} . Using the equation provided in Figure S6C, a trypsin activity of 2.04 U/mg results from the given variables.

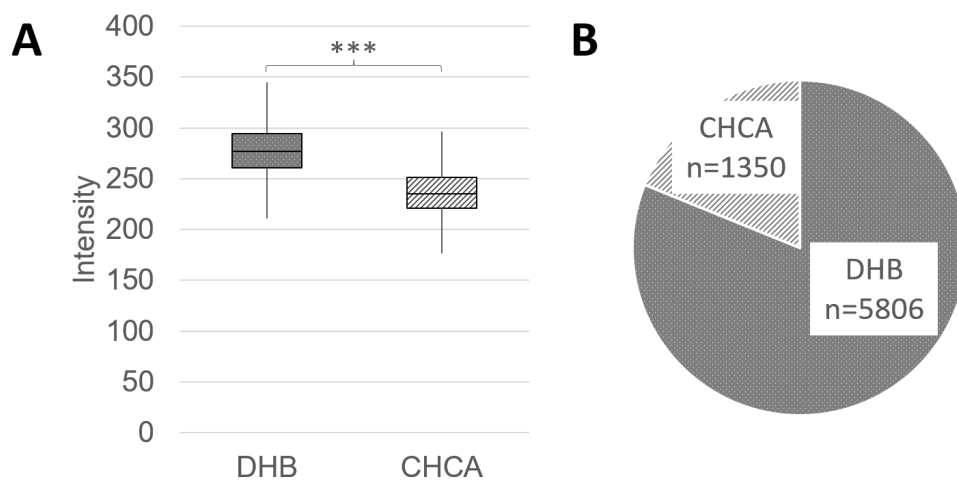


Figure S7: Comparison of MALDI-matrices. (A) Intensity boxplots of all detected peptides in a drop of 3x1 µl chickpea peptide solution (in-solution digestion) on a chickpea section (N(DHB)=6,064; N(CHCA)=6,203). *** t-test significance of independent datasets, $p < .001$. (B) Qualitative distribution of higher-intensity peptides across the matrices. 81 % of detected peptides had higher mean intensities with DHB matrix, 19 % had a higher mean intensity with CHCA matrix.

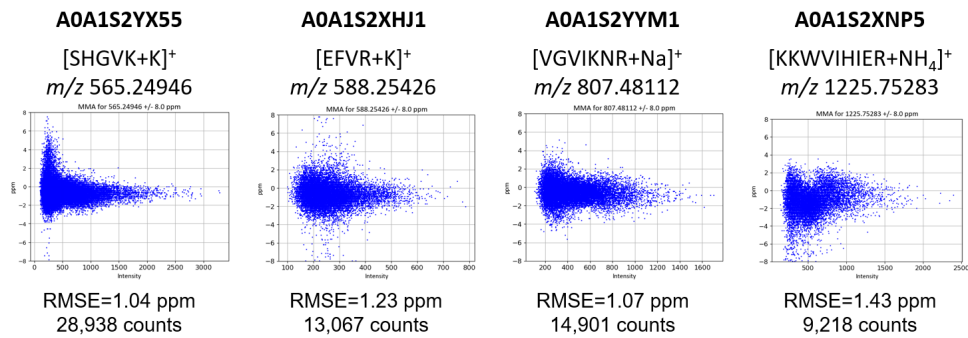


Figure S8: Mass measurement accuracy plots, root-mean square errors and pixel counts (number of spectra with detected peak) for all signals displayed in Figure 2.

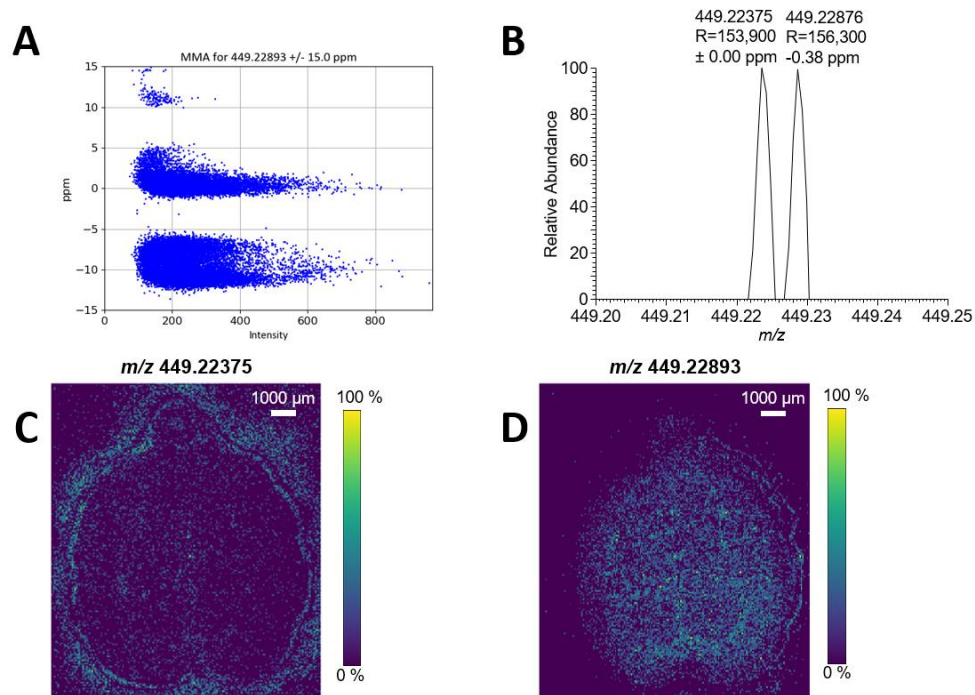


Figure S9: Necessity of high-resolution mass spectrometry for selective peptide detection exemplified by the tryptic peptide CPGR (NH_4 adduct) with a theoretical m/z 449.22893, corresponding to the protein A0A1S2YD23. (A) Mass measurement accuracy plot of the peptide showing a close, however entirely separated, neighboring signal. (B) Single-pixel mass spectrum (zoom) of the respective signals with mass resolution R. (C) Spatial distribution of the neighboring signal m/z 449.22375. (D) Spatial distribution of the peptide signal m/z 449.22893. All bin widths were set to 3 ppm.

Table S5: Mass measurement accuracy of peptides displayed in Figure 3. Root-mean square errors are given together with the mean detected m/z , the corresponding standard deviation and the number of pixels, in which the respective signal was detected (counts).

Input m/z	RMSE [ppm]	Mean m/z	StDev m/z	Counts
565.24946	1.04	565.24912	0.00048	28938
574.23856	0.85	574.23837	0.00045	25626
588.25426	1.23	588.25388	0.00062	13067
649.23426	0.87	649.23437	0.00055	20946
655.39603	1.31	655.39678	0.00041	16746
790.31326	1.03	790.31305	0.00078	17759
987.42966	0.89	987.42909	0.00067	34146
1225.75283	1.43	1225.7518	0.00141	9218
1253.70892	1.31	1253.71007	0.00117	7325
1093.69523	0.99	1093.69543	0.00106	11159

3.3 MALDI MS imaging of chickpea seeds (*Cicer arietinum*) and crab's eye vine (*Abrus precatorius*) after tryptic digestion allows spatially resolved identification of plant proteins

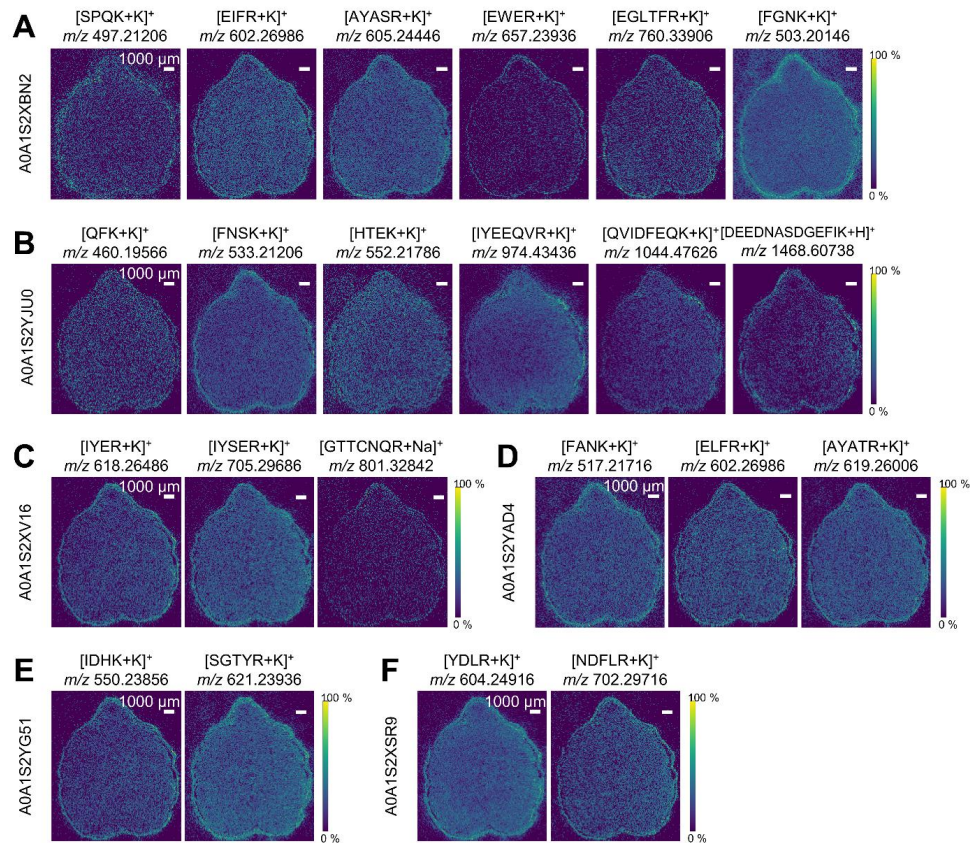


Figure S10: Identified proteins distributed throughout the entire section (in addition to protein AOA1S2XHJ1 depicted in Figure 3A). All ion images are generated with 0–100 % intensity scaling of the respective m/z .

3.3 MALDI MS imaging of chickpea seeds (*Cicer arietinum*) and crab's eye vine (*Abrus precatorius*) after tryptic digestion allows spatially resolved identification of plant proteins

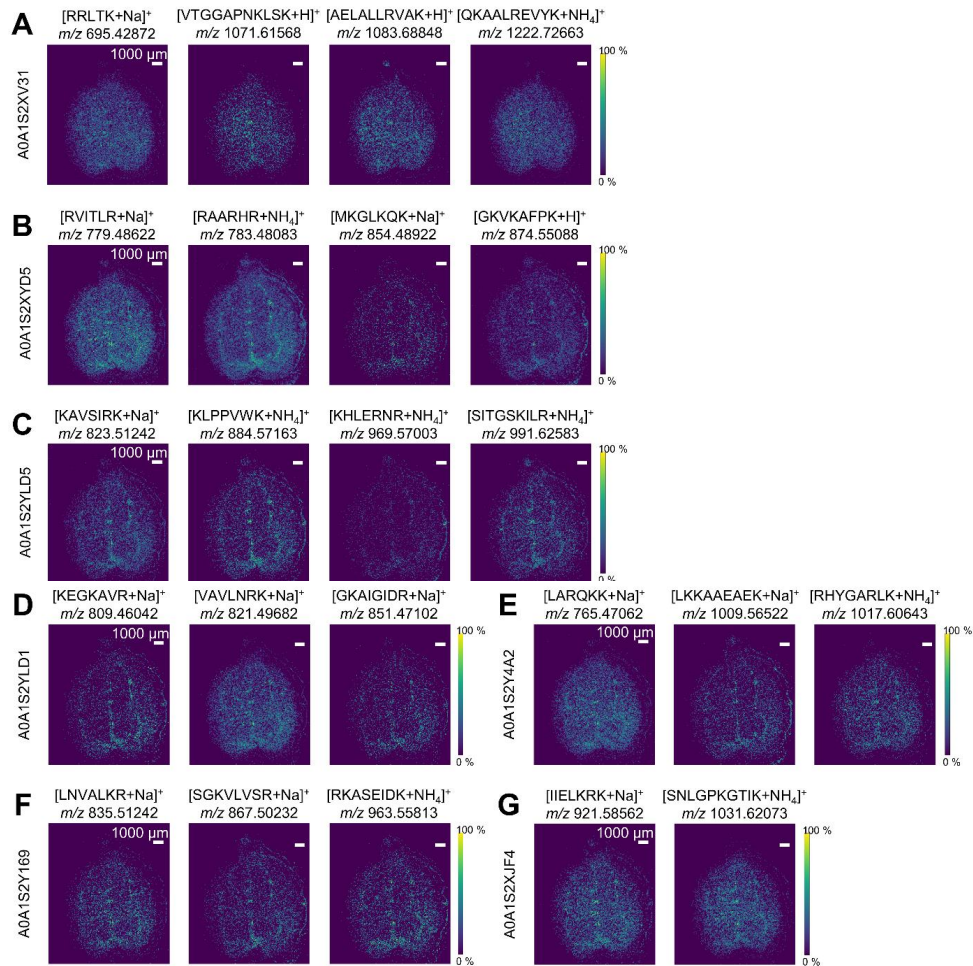


Figure S11: Identified proteins distributed across cotyledons and radicle (in addition to protein A0A1S2YYM1 depicted in Figure 3B). All ion images are generated with 0–100 % intensity scaling of the respective m/z .

3.3 MALDI MS imaging of chickpea ceeds (*Cicer arietinum*) and crab's eye vine (*Abrus precatorius*) after tryptic digestion allows spatially resolved identification of plant proteins

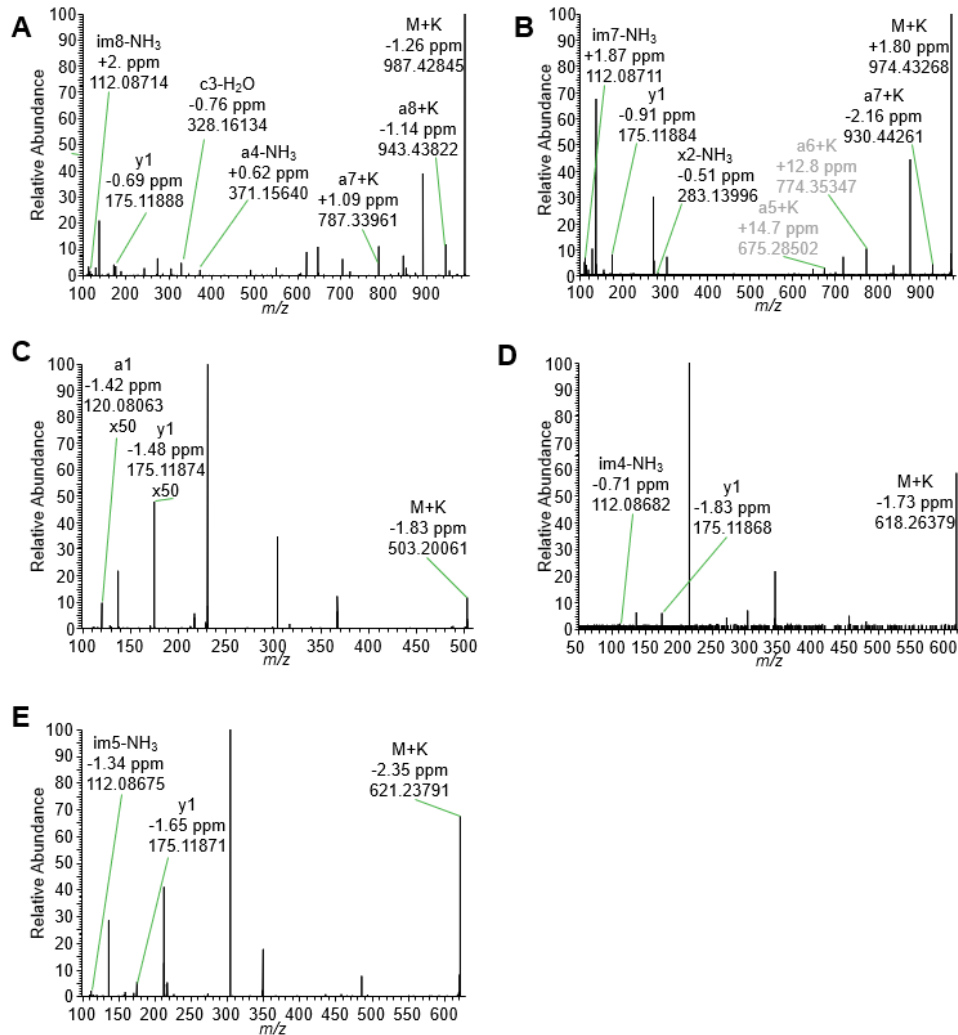


Figure S12: MALDI-MS/MS experiments on chickpea tissue section after the MALDI MS imaging measurement shown in Figures 2 and 3. (A) Mean spectrum (n=34) of tryptic peptide NDVSYVVR [M+K]⁺, m/z 987.42966, HCD 35. (B) Mean spectrum (n=58) of tryptic peptide IYEEQVR [M+K]⁺, m/z 974.43436, HCD 35. Fragments a5 and a6 are excluded due to unexpectedly high fragment mass deviation, though the neutral loss matches the mass of valine. (C) Mean spectrum (n=257) of tryptic peptide FGNK [M+K]⁺, m/z 503.20146, HCD 35. (D) Mean spectrum (n=9) of tryptic peptide IYER [M+K]⁺, m/z 618.26486, HCD 30. (E) Mean spectrum (n=217) of tryptic peptide SGTYR [M+K]⁺, m/z 621.23936, HCD 32.

Digestion conditions were identical to MALDI MS imaging measurement. To enhance recrystallization of the peptides, one 2 μ L droplet of 50% acetonitrile/water (v/v) was applied to the section surface before MS/MS measurement. Common interfering signals from DHB-matrix clusters at m/z 137.02332 and m/z 273.03937 as well as m/z 304.26160 resulting from electric interference are commonly detected and unrelated to peptide fragment signals.

3.3 MALDI MS imaging of chickpea seeds (*Cicer arietinum*) and crab's eye vine (*Abrus precatorius*) after tryptic digestion allows spatially resolved identification of plant proteins

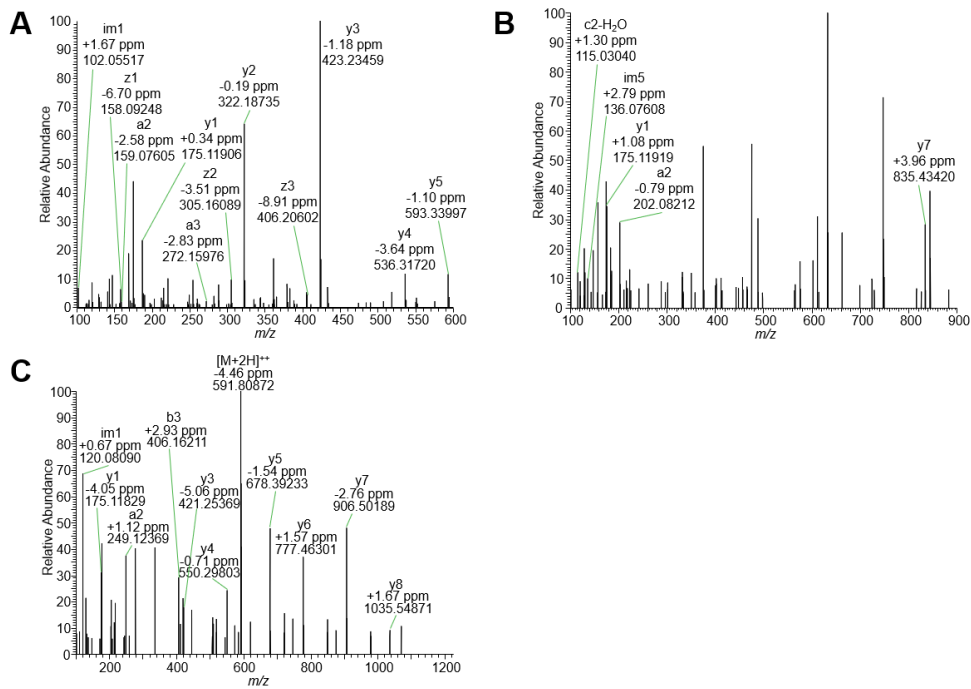


Figure S13: LC-MS/MS single spectra of tryptic peptides shown in images of MALDI MS imaging experiments of chickpea. (A) Tryptic peptide EGLTFR [M+2H]⁺⁺, *m/z* 361.6952, corresponding to MS image shown in Figure S10A. (B) Tryptic peptide NDVSYFVR [M+2H]⁺⁺, *m/z* 475.2427, corresponding to MS image shown in Figure 3A. (C) Tryptic peptide FEEVKEFVR [M+2H]⁺⁺, *m/z* 591.8111, corresponding to tryptic peptide EFVR (K adduct) from Figure 2B and Figure 3A with one missed cleavage. All MS/MS spectra were acquired with isolation window ± 0.8 Da, HCD 28.

3.3 MALDI MS imaging of chickpea seeds (*Cicer arietinum*) and crab's eye vine (*Abrus precatorius*) after tryptic digestion allows spatially resolved identification of plant proteins

Table S6: Overview of chickpea proteins identified by MALDI-MS imaging after *in-situ* tryptic digestion.

Entry	Protein names	Length (# amino acids)	Mass (Da)
<i>All section compartments</i>			
A0A1S2YJU0	myosin-9 isoform X2	1356	153115
A0A1S2XBN2	Lipoxygenase (EC 1.13.11.-)	861	97493
A0A1S2XHJ1	Alpha-1,4 glucan phosphorylase (EC 2.4.1.1)	986	111311
A0A1S2XSR9	translin	284	32890
A0A1S2XV16	Sucrose synthase (EC 2.4.1.13)	812	92456
A0A1S2YG51	Tubulin alpha chain	449	49513
A0A3Q7YAD4	Lipoxygenase (EC 1.13.11.-)	859	96937
<i>Cotyledons + Radicle</i>			
A0A1S2XJF4	T-complex protein 1 subunit zeta 2	535	59270
A0A1S2XV31	60S ribosomal protein L35-like	123	14292
A0A1S2XYD5	60S ribosomal protein L3-1	389	44558
A0A1S2Y169	Coatomer subunit delta	530	58388
A0A1S2Y4A2	60S ribosomal protein L13	207	23956
A0A1S2YLD1	transketolase (EC 2.2.1.1)	735	79556
A0A1S2YLD5	40S ribosomal protein S13	151	17169
A0A1S2YYM1	40S ribosomal protein S4	264	29871
<i>Cotyledons</i>			
A0A1S2XNP5	60S ribosomal protein L26-2-like	146	16615

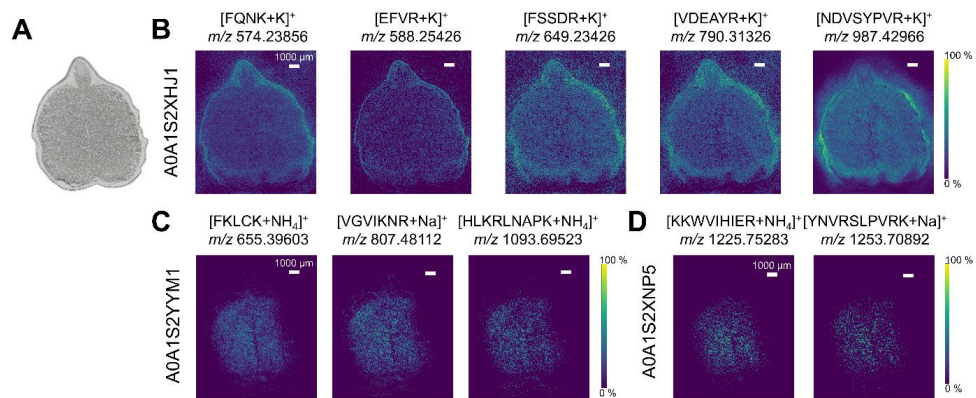


Figure S14: Replicate measurement of chickpea seed analogous to Figure 3. (A) Optical image of the measured section. (B) MS images of tryptic peptides from protein A0A1S2XHJ1. (C) MS images of tryptic peptides from protein A0A1S2YYM1. (D) MS images of tryptic peptides from protein A0A1S2XNP5. All ion images are generated with 0–100% intensity scaling of the respective m/z .

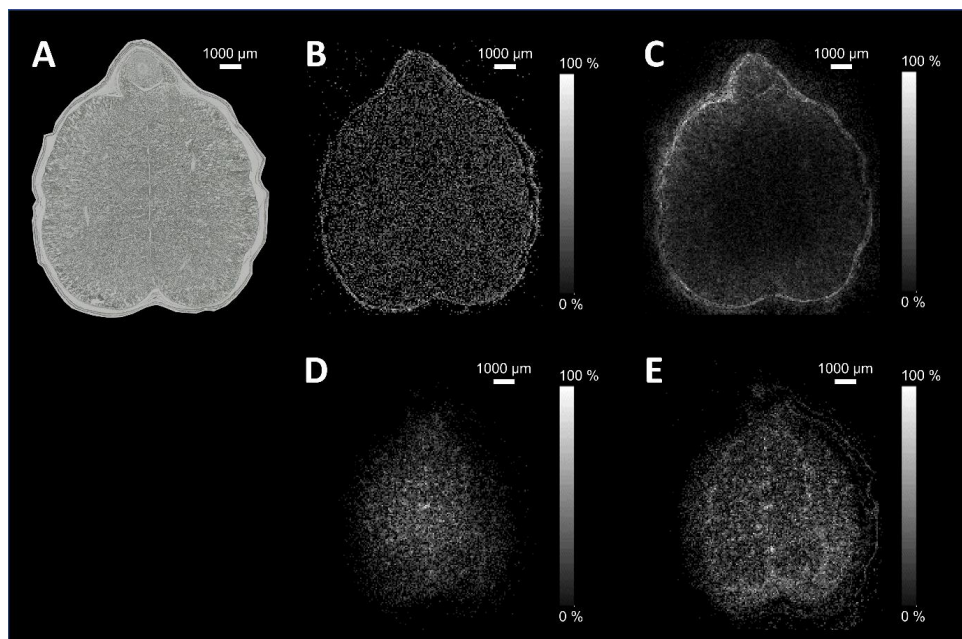


Figure S15: Single-channel MS images of tryptic peptides with different distributions across chickpea seed sections. (A) Optical image of the measured chickpea section. (B) MS image of m/z 588.25426, corresponding to tryptic peptide EFVR (K adduct) from A0A1S2XHJ1. (C) MS image of m/z 565.24946, corresponding to tryptic peptide SHGVK (K adduct) from A0A1S2YX55. (D) MS image of m/z 1225.75283, corresponding to tryptic peptide KKWVIHIER (NH_4 adduct) from A0A1S2XNP5. (E) MS image of m/z 807.48112, corresponding to tryptic peptide VGVKNR (Na adduct) from A0A1S2YYM1.

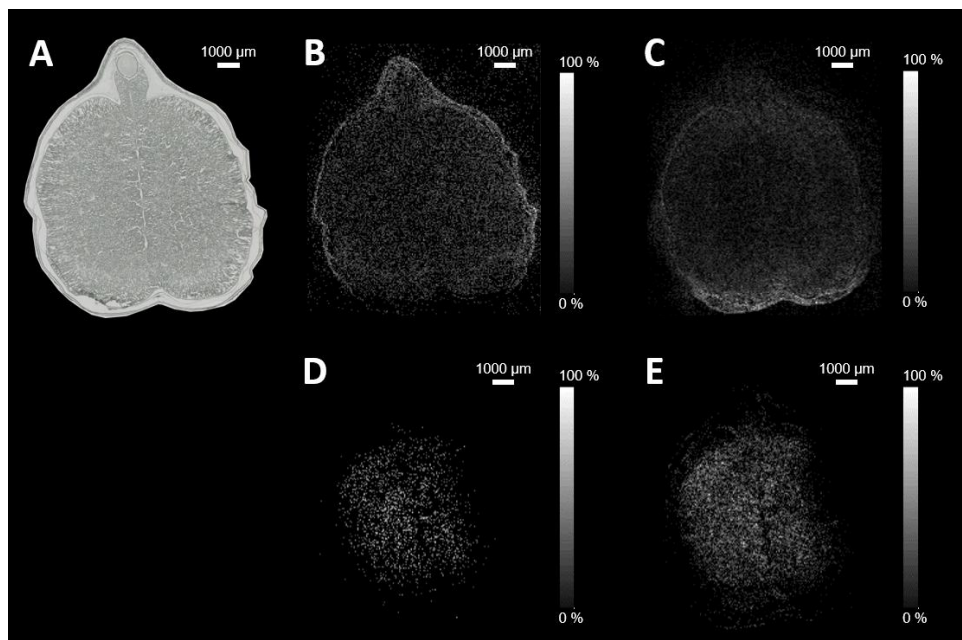


Figure S16: Single-channel MS images of tryptic peptides in replicate measurement shown in Figure S14 with different distributions across chickpea seed sections. Descriptions of figure parts are equivalent to Figure S15.

S23

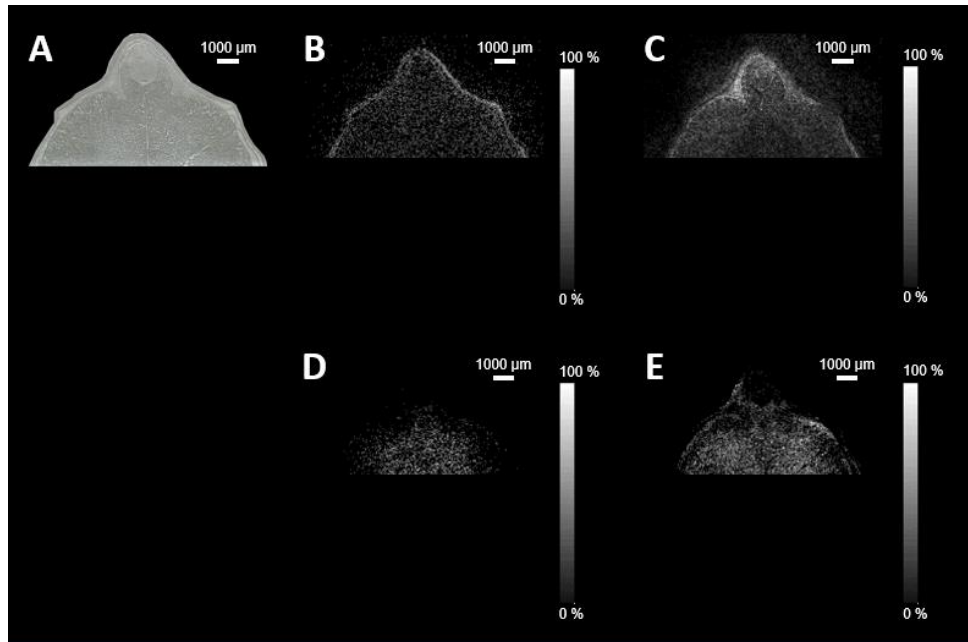


Figure S17. Single-channel MS images of tryptic peptides in a replicate measurement with different distributions across chickpea seed sections. Only technical difference to other measurements: One night storage of the section at -80 °C. Descriptions of figure parts are equivalent to Figure S15.

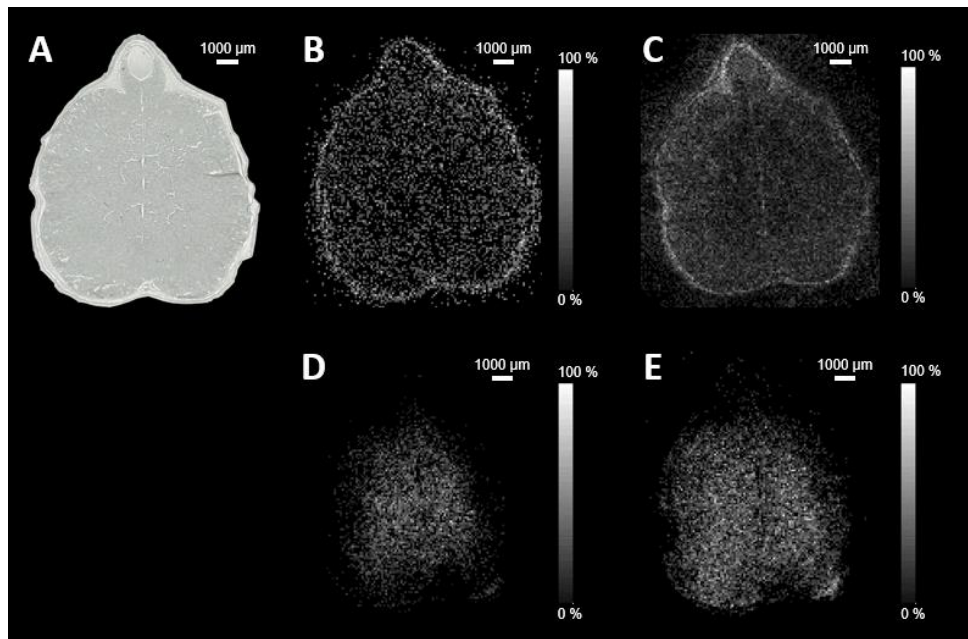


Figure S18. Single-channel MS images of tryptic peptides in a replicate measurement with different distributions across chickpea seed sections. Technical differences to other measurements: One night storage of the section at -80 °C. Pixel size: 100 μm. Descriptions of figure parts are equivalent to Figure S15.

S24

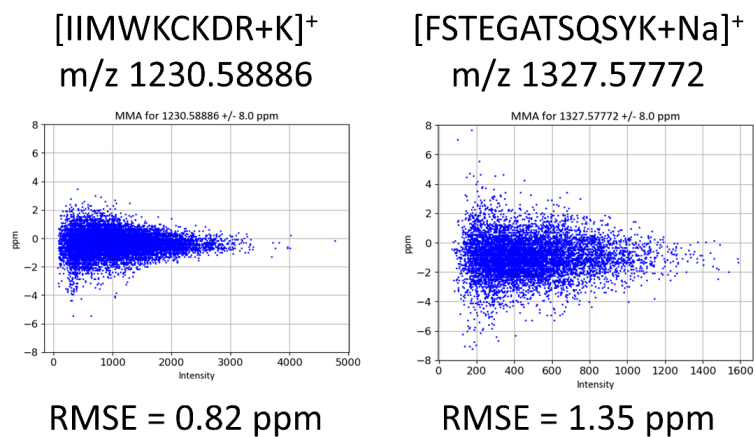


Figure S19: Mass measurement accuracy plots and root-mean square errors for peptide signals of abrin-a, displayed in Figure 4.

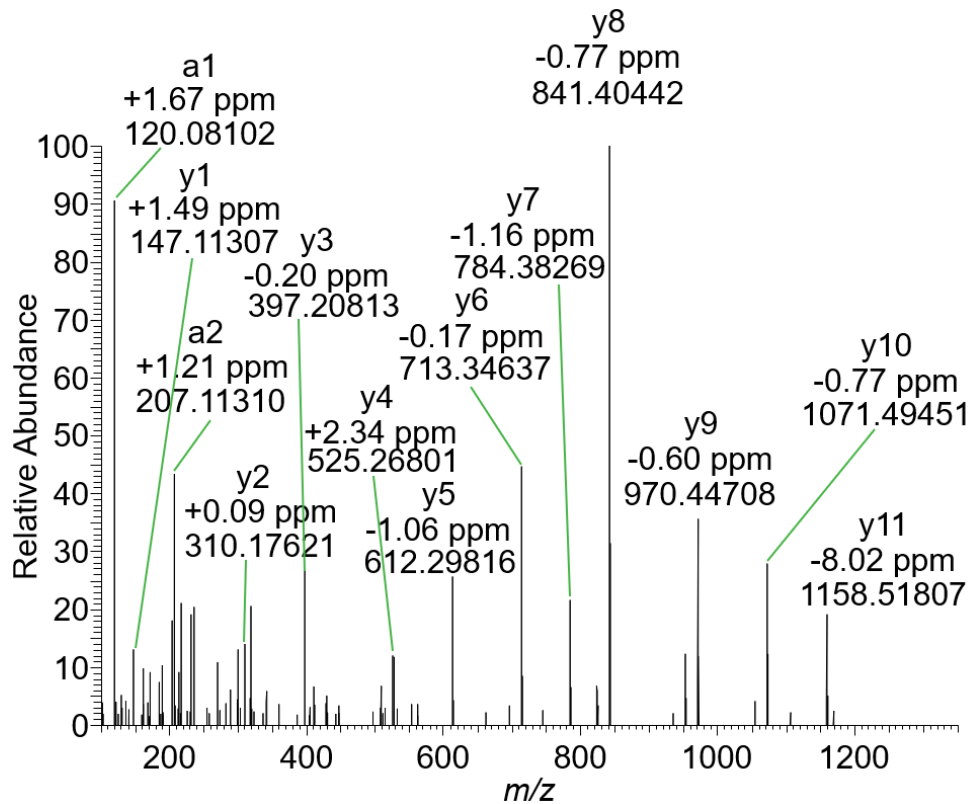


Figure S20: LC-MS/MS single spectrum of tryptic peptide FSTEGATSQSYK [M+2H]⁺⁺, m/z 653.3010, corresponding to MS image shown in Figure 4D. MS/MS spectrum was acquired with isolation window ± 0.8 Da, HCD 28

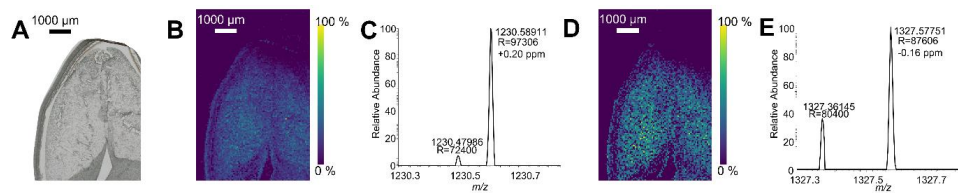


Figure S21: Replicate measurement of crab's eye vine. The presented sample section is cut off due to a technical error with the sample stage. (A) Optical image of the sample section. (B) Ion image of m/z 1230.58886, corresponding to tryptic peptide IIMWKCKDR (K adduct). C: Single-pixel mass spectrum of m/z 1230.58886, with R and mass deviation. D: Ion image of m/z 1327.57772, corresponding to tryptic peptide FSTEGATSQSYK (Na adduct). E: Single-pixel mass spectrum of m/z 1327.57772, with R and mass deviation.

- (1) Bose, U.; Broadbent, J. A.; Byrne, K.; Hasan, S.; Howitt, C. A.; Colgrave, M. L. Optimisation of protein extraction for in-depth profiling of the cereal grain proteome. *J Proteomics* **2019**, *197*, 23–33.
- (2) Schober, Y.; Guenther, S.; Spengler, B.; Römpf, A. High-resolution matrix-assisted laser desorption/ionization imaging of tryptic peptides from tissue. *Rapid Commun Mass Spectrom* **2012**, *26* (9), 1141–1146.
- (3) Enthaler, B.; Bussmann, T.; Pruns, J. K.; Rapp, C.; Fischer, M.; Vietzke, J.-P. Influence of various on-tissue washing procedures on the entire protein quantity and the quality of matrix-assisted laser desorption/ionization spectra. *Rapid Commun Mass Spectrom* **2013**, *27* (8), 878–884.
- (4) Grassl, J.; Taylor, N. L.; Millar, A. H. Matrix-assisted laser desorption/ionisation mass spectrometry imaging and its development for plant protein imaging. *Plant Methods* **2011**, *7* (1), 21.
- (5) Huber, K.; Khamehgar-Silz, P.; Schramm, T.; Gorshkov, V.; Spengler, B.; Römpf, A. Approaching cellular resolution and reliable identification in mass spectrometry imaging of tryptic peptides. *Anal Bioanal Chem* **2018**, *410* (23), 5825–5837.
- (6) Lahiri, S.; Walenta, L.; Aftab, W.; Strauss, L.; Poutanen, M.; Mayerhofer, A.; Imhof, A. *Imaging mass spectrometry and shotgun proteomics reveal dysregulated pathways in hormone induced male infertility*; 2020.
- (7) Erlanger, B. F.; Cohen, W.; Kokowsky, N. The preparation and properties of two new chromogenic substrates of trypsin. *Arch Biochem Biophys* **1961**, *95* (2), 271-278.

4 Conclusions and outlook

The main goal of this dissertation was to push the boundaries of MALDI MS imaging analysis for food to demonstrate its analytical value and its potential for both scientific pursuits as well as food monitoring by manufacturers and food authorities.

Looking at the developments as part of the first publication, they showed that MS imaging can be applied to various food matrices, i.e., fresh/raw food or food crops as well as processed food which might be of altered texture and/or consist of multiple ingredients. Within these food matrices, both major and minor compounds could be detected and visualized: Besides typical constituents, such as carbohydrates, lipids or polyphenols, which had already been successfully visualized in existing studies, this work has shown that – given dedicated method development – also low-abundant exogenous compounds, such as acrylamide as a contaminant or natamycin as a food additive can be reliably traced using MALDI MS imaging. With increasing complexity of food samples, new approaches in sample preparation (e.g., sectioning with a cutting disk) and measurement (e.g., autofocusing MALDI) need to be found and validated for successful analysis, which was a main challenge for MS imaging of gingerbread samples in the second publication. Going beyond the mere display of distributions in ion images, the development of in-depth data analysis protocols for natamycin in the first publication and acrylamide in the second publication highlight the potential for practical use in product development or quality control by manufacturers and authorities. The detection and spatially resolved identification of proteins as challenging analytes in plant (food) matrix has been given extensive consideration in the third publication. While protocols for bottom-up identification and visualization of proteins had already been developed and optimized for animal tissue, the first dedicated method development for plant tissue was conducted in this work. The results showed that with an extended and modified sample preparation workflow together with accurate mass detection, plant proteins can be identified and visualized with high selectivity based on their tryptic peptides. This approach can be used for untargeted protein identification and is independent of the original protein size. With regard to plants in particular, the development status of spatially resolved protein identification strategies is still at a very early stage. The third publication’s results thus serve as a valuable basis for further experiments (e.g., the use of alternative enzymes), for optimization of workflow parameters for achieving a higher number of protein identifications and/or higher lateral resolution as well as for method transfer to other plant species and organs. Understanding protein distribution patterns and changes thereof can be of high interest for various fields in plant or food science investigating biological processes in plants.

Many previous food MS imaging studies focused on highly abundant ‘model’ analytes in ‘model’ samples. This procedure is absolutely adequate for methodological development purposes, most of which are currently performed by trained analytical chemists. To gain meaningful insights into other than such ‘model’ analytes in ‘real-life’ samples, however, MS imaging as an analytical technique needs to take the next step towards the life sciences, to food scientists with a specific research question at hand, for which MS imaging is the appropriate method. In all these endeavors, there is no doubt that it is impossible to apply the same yardstick to novel ‘real-life’ applications and model setups with regards to, e.g., sensitivity or spatial resolution. Well-standardized and reproducible MS imaging methods always require significant development and validation efforts and often depend on a specific type of instrument, which is also the primary factor determining measurement speed. Still, in a well-chosen setup, MS imaging has the potential to answer ‘real-life’ questions; the results of all three publications presented in this work support this process by the development of MS imaging solutions for challenging food samples.

In the current EU food legislation, spatial distributions of whichever compound play a subordinate role, not to say that there are hardly any regulations. Certain pesticides are permitted only in fruit peels, which, however, does not require spatially resolved analysis if the fruit can be easily peeled. The very recent Regulation (EU) 2023/915 on Food Contaminants^{f13}, for instance, strongly focuses on contaminants’ concentrations in the homogenized food matrix – which is doubtlessly important. Yet, it scarcely considers contaminant distributions, the only exception being certain mycotoxins on the surface of cereal grains. Besides that, natamycin as preservative E235, for which a penetration limit of 5 *mm* from the

^{f13}Commission Regulation (EU) 2023/915 of 25 April 2023 on maximum levels for certain contaminants in food and repealing Regulation (EC) 1881/2006

surface has been laid down in Regulation (EC) 1333/2008^{f14} for certain cheeses and dried cured sausages, is the only example for a food ingredient underlying an official requirement regarding its spatial distribution in the EU. In the first publication, it was discussed how this spatial requirement poses a challenge to established analytical methods and the potential of MS imaging to practically complement such approaches for effective process control and verification of conformity with legal distribution requirements. Considering the variety of scientific perspectives and motivations for food analysis, spatial distributions of substances in food can be of high relevance and complement quantitative chromatography-based analyses of homogenated samples. Conceivable applications for food MS imaging are numerous: From the agricultural science perspective, imaging reverse genetics approaches could for instance reveal spatial changes in the metabolome/proteome after genetic modification. Food microbiological applications could improve spatially resolved identification and counting of bacteria colonies directly on tissue and don't need streaking/plating as well as lengthy colony forming. Lastly, immediate challenges in food safety and authenticity could make use of MS imaging, for example to assess the possibility of post-harvest removal of contaminated food parts or the detection of restructured meat using spatially resolved (un-)targeted proteomics.

This work as a whole has shown that MS imaging can be useful not only for scientific pursuits, but also for (process) monitoring by food manufacturers or official analyses by food safety authorities. It is quite understandable and correct that the EU legislation generally considers current analytical capabilities when defining legal requirements for food. Therefore, equipping food safety authorities with MS imaging instruments and expertise should be fostered in the upcoming decade. Then, alongside further development of sophisticated food imaging techniques including MS imaging, but also mapping/imaging Raman spectroscopy, magnetic resonance imaging (MRI) and hyperspectral imaging, spatial requirements (in addition to maximum concentration levels) should be implemented into future food legislation where applicable.

^{f14}Regulation (EC) 1333/2008 of the European Parliament and of the Council of 16 December 2008 on food additives

5 Publication list

Peer-reviewed publications included in this dissertation

Kokesch-Himmelreich, J.*; **Wittek, O.***; Race, A. M.; Rakete, S.; Schlicht, C.; Busch, U.; Römpp, A. MALDI mass spectrometry imaging: From constituents in fresh food to ingredients, contaminants and additives in processed food. *Food Chemistry* **2022**, *385*, 132529. (* equal contribution)

Wittek, O.; Römpp, A. Autofocusing MALDI MS imaging of processed food exemplified by the contaminant acrylamide in German gingerbread. *Scientific Reports* **2023**, *13*, 5400.

Wittek, O.; Jahreis, B.; Römpp, A. MALDI MS imaging of chickpea ceeds (*Cicer arietinum*) and crab's eye vine (*Abrus precatorius*) after tryptic digestion allows spatially resolved identification of plant proteins. *Analytical Chemistry* **2023**, *95*, 14972–1498.

Peer-reviewed publication not included in this dissertation

Wittek, O.; Messinger, J.; Römpp, A. Carotenoids and chlorophyll derivatives in lulo fruit (*Solanum quitoense* Lam.) — Characterization and quantification by UHPLC-DAD and high-resolution MS/MS. *in preparation*.

Press articles

Römpp, A.; Treu, A.; **Wittek, O.**: Molecular images for the life sciences — From food to pharmaceutical compounds. In: *Spektrum — The Science Magazine of the University of Bayreuth* **2020** *16* (2), 20.

Römpp, A.; Treu, A.; **Wittek, O.**: Molekulare Bilder für die Life Sciences — Den Inhaltsstoffen von Lebensmitteln auf der Spur. In: *Zeit Online* **2020**. URL: <https://www.zeit.de/campus/angebote/forschungskosmos/forschen-fuer-die-gesellschaft/uni-bayreuth/lebensmittelanalytik/index>

Kokesch-Himmelreich, J.; **Wittek, O.**; Römpp, A. Lebensmittel untersuchen — Bildgebende Massenspektrometrie in der Lebensmittelanalytik. In: *LABO* **2022**. URL: <https://www.labo.de/spektroskopie/bildgebende-massenspektrometrie-in-der-lebensmittelanalytik.htm>

Wittek, O.; Römpp, A. Kontaminante Acrylamid in Eisenlebkuchen — Autofokussierendes MALDI MS Imaging von prozessierten Lebensmitteln. In: *Lebensmittelchemie* **2023** *77* (5), S. 140. DOI: 10.1002/lemi.202300504 .

Conference participations

Wittek, O.; Messinger, J.; Römpp, A. Analysis of carotenoids and chlorophyll derivatives in Lulo (*Solanum quitoense*) fruit by UHPLC DAD(-APCI)-MS. *Arbeitstagung des Regionalverbandes Bayern am 12. März 2019, Erlangen* **2019** (Poster).

Wittek, O.; Kokesch-Himmelreich, J.; Römpf, A. MS Imaging von prozessierten pflanzlichen Lebensmitteln am Beispiel von Acrylamid in Elisenlebkuchen. *48. Deutscher Lebensmittelchemikertag, Dresden 2019* (Poster).

Wittek, O.; Kokesch-Himmelreich, J.; Römpf, A. MS Imaging of processed food of plant origin exemplified by the contaminant acrylamide in gingerbread. *OurCon VII, St. Malo 2019* (Poster).

Wittek, O.; Kokesch-Himmelreich, J.; Römpf, A. MS Imaging of processed food of plant origin exemplified by the contaminant acrylamide in gingerbread. *53rd Annual Conference of the DGMS, Münster 2020* (Poster).

Wittek, O.; Kokesch-Himmelreich, J.; Römpf, A. MS Imaging von prozessierten Lebensmitteln am Beispiel von Acrylamid in Elisenlebkuchen. *Arbeitstagung des Regionalverbandes Bayern am 9./10. März 2020, Würzburg 2020* (Poster). DOI: 10.1002/lemi.202051025 .

Wittek, O.; Messinger, J.; Römpf, A. Orangefarbene Schale und grünes Fruchtfleisch — Identifizierung und Quantifizierung der Carotinoide und Chlorophyllderivate in der exotischen Lulo Frucht (*Solanum quitoense* Lam.). *Arbeitstagung des Regionalverbandes Bayern am 9. März 2021, online 2021* (Poster-Flashtalk). DOI: 10.1002/lemi.202151007 .

Wittek, O.; Römpf, A. Autofokus MS Imaging von Acrylamid in prozessierten pflanzlichen Lebensmitteln nach on-tissue Derivatisierung. *49. Deutscher Lebensmittelchemikertag, online 2021* (Poster-Flashtalk). DOI: 10.1002/lemi.202158031 .

Römpf, A.; Jahreis, B.; **Wittek, O.** Advances in MALDI imaging of tryptic peptides: improve spatial resolution in mammalian tissue and first results for plant proteins. *Annual Conference of the ASMS 2023, Houston 2023* (Poster).

Wittek, O.; Jahreis, B.; Römpf, A. MALDI MS imaging von Kichererbsen (*Cicer arietinum*) und Paternostererbsen (*Abrus precatorius*) nach tryptischem Verdau erlaubt orts aufgelöste Identifizierung von Pflanzenproteinen. *51. Deutsche Lebensmittelchemietage 2023* (Poster). DOI: 10.1002/lemi.202359124.

6 Danksagung

Diese Dissertation und die damit verbundenen Aufgaben und Herausforderungen wären ohne die Unterstützung einiger Personen nicht möglich gewesen, denen ich hier ausdrücklich danken möchte.

Zunächst möchte ich Prof. Dr. Andreas Römpf danken, dass er mir ermöglicht hat, an seinem Lehrstuhl über ein so spannendes und zukunftsgerichtetes Thema zu promovieren. Seine Hilfe und sein wertvoller Rat haben sich stets positiv auf die Qualität meiner Arbeit ausgewirkt. Insbesondere bin ich dankbar für seine Offenheit gegenüber eigenen Ideen, die ich in meine Arbeit einbringen durfte („ein gewisser Anteil *Freestyle*“).

Weiterhin danke ich meinen ehemaligen Kolleginnen und Kollegen der Arbeitsgruppe am Lehrstuhl für Bioanalytik und Lebensmittelanalytik für die angenehme und konstruktive Atmosphäre. Insbesondere gilt dieser

...Bastian Jahreis, meinem fantastischen Bürokollegen „am anderen Gang“ in Kulmbach

...Julia Kokesch-Himmelreich und Heinar Schmidt für die vielen Gespräche und Ratschläge,

...sowie Axel Treu für das gewissenhafte Korrekturlesen dieser Arbeit.

Die Lehre als Bestandteil des Promotionsstudiums hat mir immer besonders Spaß gemacht. Dazu gehört die dankenswerte Unterstützung durch die Studierenden, die meine Projekte als Hiwi oder im Rahmen ihrer Forschungsmodule/Abschlussarbeiten tatkräftig vorangebracht haben.

Die Agilis Verkehrsgesellschaft mbH & Co. KG hat an dieser Stelle ebenso lobende Erwähnung verdient, da ihre Züge mich, entgegen ursprünglicher Erwartungen, über mehrere Jahre von Bayreuth nach Kulmbach und zurück gebracht haben und das stets sicher und zuverlässig.

Zu meinem Leben in Bayreuth gehörte in besonderem Maße das erweiterte universitäre Umfeld, einschließlich dem Hochschulsport, dem Sprachenzentrum, dem Aufstrichzirkel sowie dem Glashaus. Diese Einrichtungen und die vielen fantastischen Menschen, die ich dort kennenlernen durfte, haben maßgeblich dazu beigetragen, dass ich mich in Bayreuth immer sehr wohl gefühlt habe.

Bei meinen Eltern Günther und Claire sowie meiner Schwester Julia möchte ich mich für die großartige Unterstützung über all die Jahre und in allen Belangen bedanken. Nicht zuletzt gilt Merle mein besonderer Dank und mein höchster Respekt für ihre grenzenlose Unterstützung, Geduld und Motivation.

7 (Eidesstattliche) Versicherungen und Erklärungen

(§ 9 Satz 2 Nr. 3 PromO BayNAT)

Hiermit versichere ich eidesstattlich, dass ich die Arbeit selbstständig verfasst und keine anderen als die von mir angegebenen Quellen und Hilfsmittel benutzt habe (vgl. Art. 97 Abs. 1 Satz 8 BayHIG).

(§ 9 Satz 2 Nr. 3 PromO BayNAT)

Hiermit erkläre ich, dass ich die Dissertation nicht bereits zur Erlangung eines akademischen Grades eingereicht habe und dass ich nicht bereits diese oder eine gleichartige Doktorprüfung endgültig nicht bestanden habe.

(§ 9 Satz 2 Nr. 4 PromO BayNAT)

Hiermit erkläre ich, dass ich Hilfe von gewerblichen Promotionsberatern bzw. -vermittlern oder ähnlichen Dienstleistern weder bisher in Anspruch genommen habe noch künftig in Anspruch nehmen werde.

(§ 9 Satz 2 Nr. 7 PromO BayNAT)

Hiermit erkläre ich mein Einverständnis, dass die elektronische Fassung meiner Dissertation unter Wahrung meiner Urheberrechte und des Datenschutzes einer gesonderten Überprüfung unterzogen werden kann.

(§ 9 Satz 2 Nr. 8 PromO BayNAT)

Hiermit erkläre ich mein Einverständnis, dass bei Verdacht wissenschaftlichen Fehlverhaltens Ermittlungen durch universitätsinterne Organe der wissenschaftlichen Selbstkontrolle stattfinden können.

.....
Ort, Datum, Unterschrift